The glyoxylate shunt as a target for antibacterial intervention in *Pseudomonas aeruginosa*

Alyssa C. McVey

Department of Biochemistry

Gonville & Caius College

University of Cambridge

This dissertation is submitted for the degree of *Doctor of Philosophy*

May 2019

Declaration

This dissertation is the result of my own work conducted under the supervision of Dr Martin Welch in the Department of Biochemistry and includes nothing which is the outcome of work done in collaboration except as specified in the text.

This work is not substantially the same as any I have submitted, or, is being concurrently submitted for a degree or diploma or other qualification at the University of Cambridge or any other University or similar institution except as declared in the Preface and specified in the text. I further state that no substantial part of my dissertation has already been submitted, or, is being concurrently submitted for any such degree, diploma or other qualification at the University of Cambridge or any other University or similar institution except as declared in the Preface and specified in the text.

The work presented in chapter 3 of this dissertation has been adapted from a published research article; 'Structural and Functional Characterization of Malate Synthase G from Opportunistic Pathogen *Pseudomonas aeruginosa'* by A. C. McVey, P. Medarametla, X. Chee, S. Bartlett, T. Rahman, D. R. Spring, A. Poso, and M. Welch, 2017. This original research article was authored by myself and edited by my supervisor, Dr Martin Welch.

The length of this dissertation does not exceed the word limit prescribed by the Biology Degree Committee.

Summary

The glyoxylate shunt as a target for antibacterial intervention in *Pseudomonas aeruginosa*

Alyssa C. McVey

Pseudomonas aeruginosa is an opportunistic human pathogen responsible for a large proportion of drug-resistant, hospital-acquired infections worldwide. These infections are notoriously difficult to treat due to *P. aeruginosa*'s many intrinsic and acquired resistance mechanisms. Despite the critical need for new antibiotics against *P. aeruginosa*, the current pipeline is unable to meet the demand for treating these infections. *P. aeruginosa* can thrive in diverse infection scenarios by rewiring its central metabolism, and an example of this is in the lungs of cystic fibrosis patients, where this bacterium metabolises fatty acids into acetyl coenzyme A for biomass production via the glyoxylate shunt. The glyoxylate shunt is comprised of two enzymes: isocitrate lyase and malate synthase G, and allows the synthesis of cellular constituents from C_2 nutrient sources, bypassing the decarboxylation steps of the citric acid cycle when glucose is not available. The glyoxylate shunt has potential as a new antibacterial target in *P. aeruginosa* as there is evidence to support that, besides carbon fixation, the glyoxylate shunt is implicated in virulence and is essential for establishing pulmonary infections.

In this dissertation, the glyoxylate shunt was investigated as an antibacterial target in *Pseudomonas aeruginosa*. The biochemical characterisation of malate synthase G resulted in the first reported crystal structure solved to 1.6 Å resolution. Computational evaluation of the crystal structure revealed two promising binding sites suitable for future *in silico* drug design, which confirmed malate synthase as an apt drug target. Two 2-aminopyridine derivatives were found that displayed dual inhibition of the glyoxylate shunt enzyme activities as well as *P. aeruginosa* growth with low micromolar potencies. Insights into the different mechanisms of action on the target enzymes were explored using kinetic analysis and isothermal titration calorimetry. Hit to lead optimisation experiments of the hit compounds provided awareness of their potential for any future development as antibacterial agents. Although the compounds showed promising efficacies, *in vitro* drug metabolism and safety profiles, I also found that they displayed possible "off-target" effects and had issues in chemical stability. Together, these data indicate that the compounds warrant further chemical modification to improve these characteristics.

Acknowledgements

First and foremost, I would like to thank Dr Martin Welch for the opportunity to work in his group. I appreciate his straightforward and understanding approach as a supervisor, and his training in scientific writing was invaluable throughout the project. Thanks to Dr Päivi Tammela from the University of Helsinki and Dr Antonio Felici from Aptuit for hosting me on my research secondments. I thank Heidi Mäkkylä for training me in cell culture, and Dr Mahmud Kajbaf and Dr Annalisa Pellacani for their expertise in DMPK. Huge appreciation is also deserved by Dr Dima Chirgadze, Dr Paul Brear, and Professor Ben Luisi for their training and consultation in X-ray crystallography.

I am tremendously appreciative of the European Commission's Marie Skłodowska-Curie Actions Innovative Training Network scheme for funding this PhD project for the first three years and to the University of Cambridge, Gonville & Caius College, and The Cambridge Philosophical Society for funding me during the final year.

Collaboration with my peers has been vital for this project. Dr Sean Bartlett, Dr Xavier Chee, and Prashanthi Medarametla have all been influential in this work. Additional thanks to my INTEGRATE colleagues for all the fun and productive meetings.

Thank you to the members of the Welch group for creating a great working environment; Dr Eve Maunders, Dr Audrey Crousilles, Lærøld C. Grimes, Dr Stephen Dolan, Dr Yassmin Abdelhamid, Dr Shunsuke Numata, Andre Wijaya, Rory Triniman, Stephen Trigg, Tom O'Brien, Suzie Forrest, and Veena Mohan. The debates and general foolishness have created many fond memories. Thanks also to Dr Rita Monson for being a wealth of advice and humour.

This dissertation would not have been possible without the love and support from Shivam and our families. Many thanks to my friends, old and new, for enriching my life and encouraging me in so many ways throughout the PhD. I particularly want to thank Andrea for starting and ending this journey with me in Cambridge. I also want to thank the Holy Mondays crew, as well as KT and Nikki, for their unwavering friendships.

Table of contents

List of figures

Chapter 1.

Chapter 2.

Chapter 3.

Chapter 4.

Chapter 5.

List of tables

Chapter 2.

Chapter 3.

Chapter 4.

Chapter 5.

Abbreviations and acronyms

AcCoA	Acetyl coenzyme A
Ac	Acetate
aceA	Gene encoding isocitrate lyase
ATCC	American type culture collection
ATP	Adenosine triphosphate
BLAST	Basic local alignment search tool
Boc	*tert*-butyloxycarbonyl protecting group
CF	Cystic fibrosis
CFU	Colony forming units
CV	Column volume
CoA	Coenzyme A
D	Deuterium
Δ	Difference or deletion (genetics)
dH_2O	Deionised water
DMSO	Dimethyl sulphoxide
DMPK	Drug metabolism and pharmacokinetics
DNA	Deoxynucleic acid
DTNB	5, 5-dithio-bis-(2-nitrobenzoic acid)
DRI	Drug-resistant infection
DTT	Dithiothreitol
EDP	Entner-Doudoroff pathway
EDTA	Ethylenediamine tetraacetic acid
EMP	Embden-Meyerhof-Parnas
EtOH	Ethanol
EWG	Electron withdrawing group
$FADH_2$	Flavin adenine dinucleotide
FAT	Fatty acid transporter
FBS	Fetal bovine serum
GST	Glutathione *S*-Transferase
glcB	Gene encoding malate synthase G
HAI	Hospital-acquired infection
HTS	High throughput screening
IC_{50}	Inhibitory concentration at 50%
ICD	Isocitrate dehydrogenase
IDH	Isocitrate dehydrogenase
ICL	Isocitrate lyase
IPTG	Isopropyl β-D-1-thiogalactopyranoside
ITC	Isothermal titration calorimetry
kDa	KiloDalton
λ_{max}	Wavelength of maximum absorbance
LB	Luria-Bertani broth
LC-MS/MS	Liquid chromatography-tandem mass spectrometry
LDH	Lactate dehydrogenase
LPS	Lipopolysaccharide
LMW	Low molecular weight
MBC	Minimum bactericidal concentration
MDR	Multidrug resistant/resistance
MeOH	Methanol

MIC	Minimum inhibitory concentration
MHB	Mueller Hinton broth
MOA	Mechanism of action
MOI	Mode of inhibition
MS	Malate synthase G
MWCO	Molecular weight cut-off
NAD(H)	Nicotinamide adenine dinucleotide
NADP(H)	Nicotinamide adenine dinucleotide phosphate
NBCS	New born calf serum
Ni-NTA	Nickel-nitrilotriacetic acid
OD	Optical density
ORF	Open reading frame
PBS	Phosphate buffer saline
PDKA	Phenyldiketoacid
PDB	Protein databank
PEG	Polyethylene glycol
RFU	Relative fluorescence unit
Rmsd	Root mean square deviation
Rpm	Rotations per minute
SAD	Single wavelength anomalous dispersion
SDS-PAGE	Sodium dodecyl sulphate-polyacrylamide gel electrophoresis
SEC	Size exclusion chromatography
TCA	Trichloroacetic acid cycle
TEMED	Tetramethylethylenediamine
Tris	Tris(hydroxymethyl)aminomethane
v/v	Volume-to-volume ratio
w/v	Weight-to-volume ratio
WT	Wild-type

Standard one and three letter codes denote the natural amino acids.

1. Introduction

1.1 Drug-resistant bacterial infections are a global crisis

Hospital-acquired infections (HAIs) are the most frequent adverse events in healthcare worldwide.[1] More than 720,000 HAIs in the United States and 300,000 HAIs in England are reported every year.[2,3] HAIs are a risk for vulnerable patient populations including the elderly, the immunocompromised, and the chronically ill.[4] One of the main risk factors associated with obtaining HAIs is being hospitalised longer than two days, while the risk of developing drug-resistant HAIs is associated with hospitalisations longer than five days.[5]

The main culprit behind HAIs is the "ESKAPE" panel of multidrug-resistant bacteria; a group of six pathogens that exhibit widespread resistance to clinical antibiotics including; *Enterococcus faecium, Staphylococcus aureus*, *Klebsiella pneumonia*, *Acinetobacter baumannii*, *Pseudomonas aeruginosa* and *Enterobacter* species.[6,7] The ESKAPE pathogens already cause serious infections, but treating these infections is a growing challenge in the face of multidrug resistance. Four out of the six ESKAPE pathogens are Gram-negative bacteria, which represent the greatest unmet clinical need in drug-resistant HAIs.[8]

An estimated 700,000 deaths are attributed to drug-resistant infections (DRIs) globally every year.[9,10] In the United States, more than two million cases of DRIs and 23,000 deaths are reported each year.[11] In Europe, 700,000 DRIs resulting in 33,000 deaths were reported in 2015.[12] Across Asia, the collective occurrence of DRIs is estimated to be more than double that of the United States and Europe combined, with particularly alarming rates of multidrug resistance developing in countries like India.[13] A report commissioned by the UK government predicted that by 2050, more people will die from drug-resistant bacterial infections than from cancer, which is currently estimated at 10 million per year.[14] DRIs not only prolong hospitalisations and increase unnecessary deaths, but also escalate the costs of healthcare. It is projected that by 2050, DRIs will add an economic burden of $100 trillion to the world's economy.[10]

The discovery of antibiotics in the first half of the 20th century revolutionised modern medicine and drastically improved the quality of human life. Antibiotics have increased the average person's life expectancy by 30 years in developed nations and have been essential in supporting medical advancements, such as neonatal care, surgical procedures and cancer treatments.[15,16] Despite these successes, antibiotics are among the only types of medicines that lose their effectiveness and value over time. As a result, we are now in a time where resistance to every antibiotic class used clinically has been observed.[17,18] Antibiotics are also different from other types

of drugs, unfortunately, in that the negative effects of resistance extend far beyond individual patients.

1.1.1 The rise of antibiotic resistance

The first antibiotic, penicillin, was discovered serendipitously by Alexander Fleming 90 years ago.[19] Antibiotics usage has intensified since their introduction into society in the early 1940s, and a rising trend of resistance has swiftly followed.[20] Clinical resistance actually pre-dates penicillin, where the first resistance to the antibacterial drug[i], Salvarsan (used to treat syphilis before penicillin), was reported in 1924.[21,22]

It seems as though antibiotic resistance is a modern phenomenon in response to human consumption, but this is just one (anthropocentric) interpretation of history. Investigations have shown the prevalence of genetic operons encoding the synthesis of antibiotics in bacteria, alongside several self-protection measures against said antibiotics, and that these antibiotic-producing gene clusters are ancient.[23–25] This suggests that the capacity for resistance should be as old as the capacity for producing antibiotics. Indeed, an analysis of 30,000-year-old DNA from permafrost sediments in the Canadian Yukon detected resistance genes to modern antibiotic classes, such as β-lactam, tetracycline and vancomycin.[26] These findings establish that bacteria have attained the tools needed to cultivate, acquire and spread resistance genes long ago without human influence.[27]

Antibiotic resistance mechanisms, once developed, remain among bacteria even if the selective pressure to survive subsides as the antibiotic concentration decreases.[28] Instead, resistance elements are integrated into the antibiotic resistome, a shared reservoir of resistance that has developed over the last 3.5 billion years that is accessible by all bacteria—pathogenic or non-pathogenic.[29,30] Its discovery highlighted the enormous diversity of resistance elements in environmental bacteria, and a large fraction of the resistome is believed to be comprised of silent and proto-resistant genes, which are present in the genome, but a mutation or mobilisation is required to express a resistant phenotype.[31–33] While antibiotic resistance is a natural and primordial process, human usage of antibiotics over the last century has been artificially imposed on the process, accelerating the capture of resistance from the resistome by providing Darwinian selective pressures.[34] Our antibiotic consumption has been the single largest driver behind the antibiotic resistance crisis.[11]

---

[i]The distinction between *antibiotic* and *antibacterial drug* refers to the compound's source. A compound isolated from nature is an *antibiotic*, and a compound discovered by chemical synthesis is an *antibacterial agent* or *drug*. However, *antibiotic* has become synonymous with *antibacterial drug*, so they are used interchangeably throughout this dissertation.

Most antibiotic usage has been deemed improper; *i.e.* overused or inappropriately used in clinical medicine and agricultural practice.[35] In the United States, analyses revealed that 22 standard doses (*e.g.* a pill or capsule) were prescribed per person per year, but that this inpatient antibiotic usage only represented 39% of the total US antibiotic market.[36,37] Data from China show an antibiotic prescription rate twice that of the World Health Organization's recommended rate for a middle-income country.[38] Antibiotics prescribed by physicians are largely driven by patient treatment expectations, coupled with diagnostic uncertainties, and incentives to overprescribe for drug reimbursements.[39] Improvements in manufacturing over time have also provided less expensive drugs that embolden non-prescription and off-label uses.[40] It is estimated that non-prescription use accounts for anywhere from 19-100% of antibiotic use outside of Europe and North America, which is aggravated by the lack of regulations.[41] Public misconception about antibiotics has also led to their overuse. A recent survey revealed that only a slim majority (56%) of people in the European Union understand that antibiotics do not kill viruses.[42]

Antibiotic underuse is another contributing factor to the crisis, which refers to bacterial exposure to sub-lethal concentrations of antibiotics as they are recycled from hospitals, clinics, farms, and manufacturing plants into the environment.[43] An estimation of 20-80% of antibiotics excreted by humans and animals are in their chemically stable and active forms, which contaminate environmental reservoirs such as rivers, lakes and soil, where they can remain for months or years at sub-therapeutic levels.[44]

Inappropriate use is characterised by improper treatment regimens prescribed by clinicians, such as the extensive use of broad-spectrum antibiotics as monotherapies. Even more egregious is the use of antibiotics for non-curative purposes by the food industry. It has been estimated in the United States that in the early 2000s, 11.2 million kilograms of antibiotic doses were given to livestock for non-therapeutic purposes, compared with only 900,000 kilograms given for therapeutic purposes.[45] Examples of non-curative uses include prophylaxis, such as spraying antibiotics on fruit and vegetable crops or using antibiotics to promote animal growth.[46]

It is clear that how we have used antibiotics historically has resulted in accelerated bacterial resistance to all of the current classes in our arsenal.[47] The rise and dissemination of antibiotic resistance over the past several decades have led to multidrug resistant (MDR), and extensively drug-resistant (XDR) strains of bacteria that are responsible for severe infections, especially in hospitals. An example is the New Delhi metallo-β-lactamase-containing bacteria (NDM-1), identified in India in 2009, that display broad resistance to carbapenems.[48] Five years later, NDM-1 was detected on every habitable continent.[49] Moreover, bacterial strains have been isolated from hospitals that exhibit pan-drug resistance (PDR) to all antibiotics, such as *Mycobacterium tuberculosis*,

Pseudomonas aeruginosa, and *Klebsiella pneumoniae*.[50–53] The potential for the rapid, global transmission of these PDR strains and their extreme resistance profiles warrants close patient monitoring and prudent antibiotic administration in hospitals.

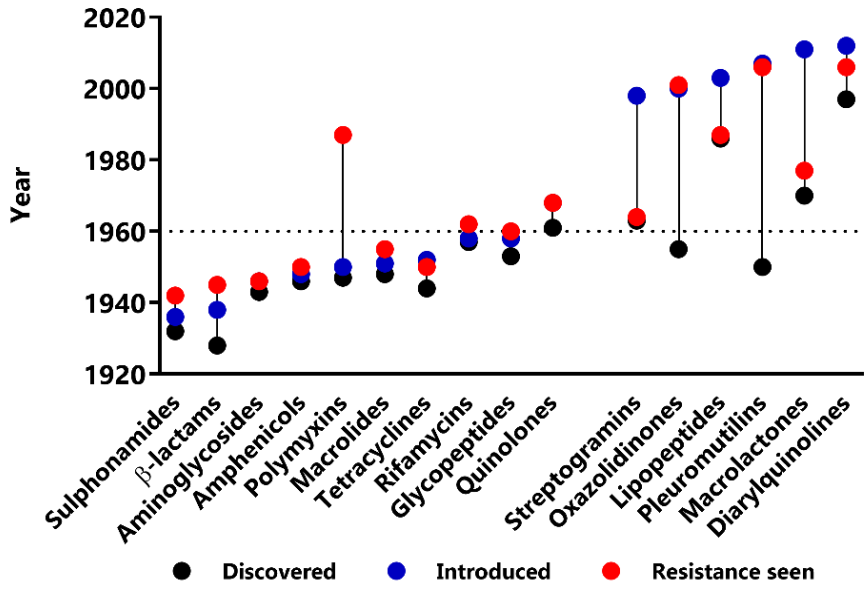

Figure 1. Timeline of antibiotic innovations. This graph shows the years when all major antibiotic classes were discovered, introduced into the clinic, and resistances were first observed. All instances of resistance have been seen within ten years of discovery or introduction into the market, except the polymyxins, which were used sparingly due to toxicity issues. A dotted black line indicates the end of the golden era of antibiotic drug discovery (1960). Data obtained from Lewis, 2013.[47]

1.1.2 Bacterial resistance mechanisms

Beyond the basic cellular requirements for survival and proliferation, bacteria harbour intrinsic genetic determinants of resistance.[54] This allows bacteria to escape the detrimental effects of certain antibiotics over others. An example is that Gram-negative bacteria are intrinsically less permeable to many antibiotics than Gram-positive bacteria, which is due to the presence of the lipopolysaccharide outer membrane. The outer membrane encapsulates the periplasm and filters out large, hydrophobic molecules.[55] An example of intrinsic resistance is to the glycopeptide antibiotics, like vancomycin, which cannot pass the outer membrane and are thus not effective against most Gram-negative species.[56] Intrinsic resistance unquestionably prompts careful consideration of appropriate treatments by clinicians and complicates infection outcomes; however, the crux of the present resistance crisis is attributed to the continuous development and acquisition of resistance mechanisms between all bacteria.[57] Resistance is acquired (**figure 2A**) through resistance genes in portable DNA sequences, such as plasmids or transposons, spreading

from one bacteria to another through horizontal gene transfer (HGT) in a process known as conjugation.[58,59] HGT accomplished through bacteriophages is known as transduction.[60] Chromosomal genes can also be transmitted to a bacterium by the uptake of naked DNA released from a nearby microorganism in a process called transformation.[61]

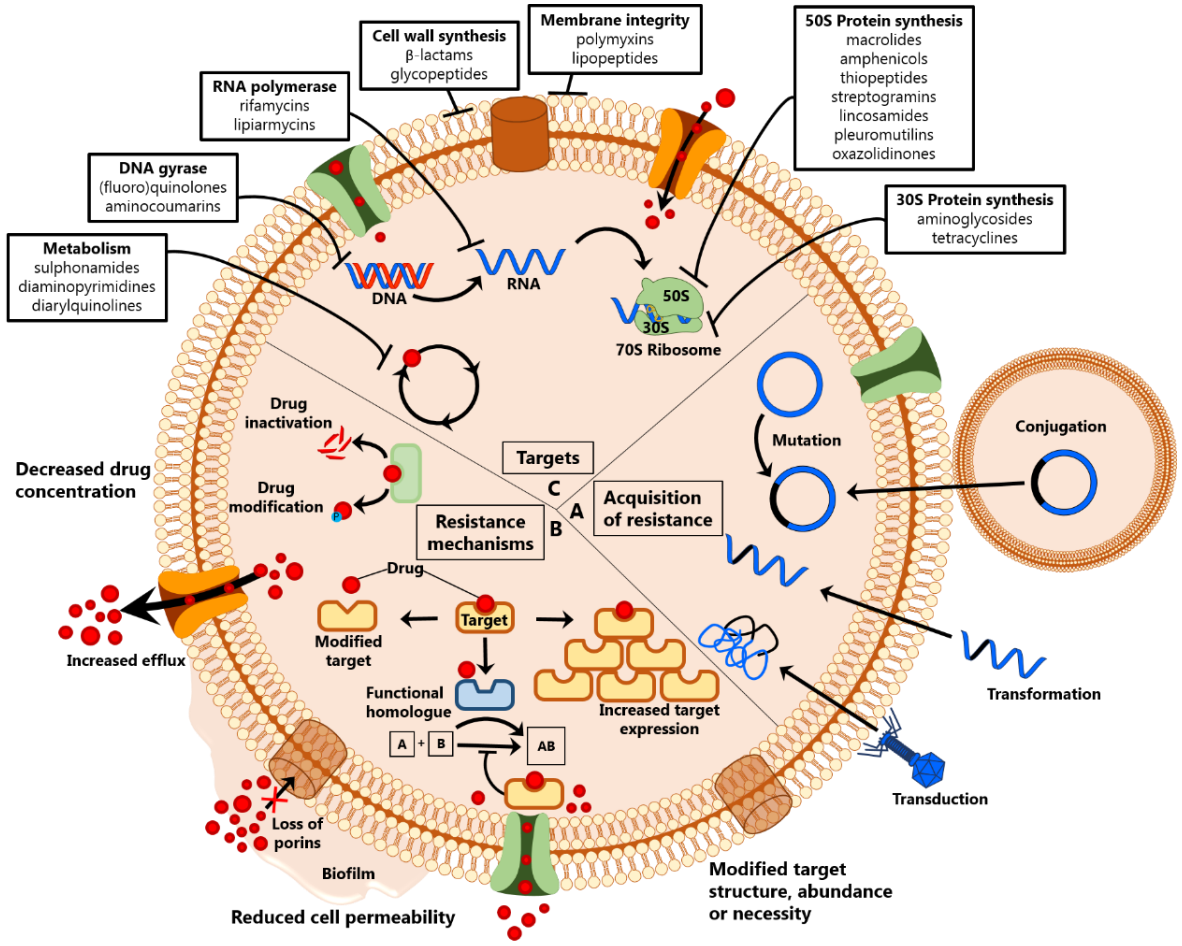

Figure 2. Overview of antibacterial targets and resistance mechanisms. A) Resistance to antibiotics is acquired through processes including horizontal gene transfers and point mutations in chromosomal DNA. **B)** Primary antibiotic resistance mechanisms include decreasing intracellular drug concentration, reducing drug penetration, or by circumventing drug inhibition through alterations in the biological target structure, target necessity, or target abundance. **C)** Approved antibiotic classes act upon relatively few bacterial targets, meaning that once resistance arises, it affects multiple classes with shared mechanisms of action. Figure created from information from Coates, 2002.[79]

Antibiotic resistance occurs through three general mechanisms, as shown in **figure 2B**. These include altering the structure, abundance or necessity of the drug target,[62] lowering the intracellular drug concentration,[63,64] and decreasing drug entry into the cell.[65,66] First, altering the target structure can be achieved through single nucleotide polymorphisms, or point mutations,

which result in amino acid substitutions that lower the target's affinity for the drug without compromising the target's function.[67] A common clinical example is point mutations in DNA gyrase that yield quinolone resistance.[68] Increasing a drug target's abundance from upstream point mutations, promoter acquisitions or gene amplification can also render a drug ineffective.[69] As a last line of defence, bacteria can employ functional homologues in metabolic pathways acquired through HGT or *de novo* genome changes that supersede the original target.[70] A notable example of this is in methicillin-resistant *S. aureus*, in which the β-lactam-insensitive protein, PBP2a, enables cell wall synthesis to occur as the β-lactam inhibits the native PBP.[71]

Second, to lower the intracellular drug concentration, bacteria exploit mechanisms to alter or destroy the drug. A classic example is the hydrolysis of β-lactam antibiotics by β-lactamase enzymes.[72] Aminoglycosides are also susceptible to modification by acetyltransferases, phosphotransferases and nucleotidyltransferases in bacteria as they are large molecules with exposed hydroxyl and amide groups.[73] Another mechanism to lower intracellular drug concentrations is to physically remove the drug via efflux pumps that span the cell envelope. Efflux pumps extrude hydrophobic cations and amphipathic compounds across the outer membrane that are unneeded by the cell.[74] Efflux pump expression can be increased in response to environmental signals, such as iron limitation, or acquired through mutations in the regulatory network controls efflux pump expression.[75]

Finally, bacteria rely on the cell envelope to act as a barrier to prevent the drug from entering the cell. However, some species further decrease their susceptibilities to antibiotics by modifying the cell surface through biofilm production or by reducing the expression of membrane porins, which allow for nutrient transport.[76] Point mutations in efflux pumps genes can change substrate specificities and similarly preclude drug entry.[77] Bacteria can also export molecules that sequester antibiotics extracellularly.[78]

1.1.3 Current antibacterial targets

Antibiotics and their targets need to meet strict criteria in order to be successful, thus delivering a new drug to market is a significant challenge.[80] It is estimated that 80% of drugs fail in clinical trials during drug development, and the two main reasons for failure are a lack of efficacy and toxicity.[81,82] A successful antibacterial drug needs to combine efficacy, specificity and bioavailability with suitable chemical and pharmaceutical properties for chemical optimisation and effective dosing.[83] Meanwhile, a good antibacterial target needs to be essential for infection and sufficiently different from human orthologues, ideally absent from the human genome entirely, to minimise side effects.[84]

Successful antibacterial agents exploit the fundamental differences between prokaryotic and eukaryotic cells. The majority of antibacterial drugs that are used today have nonprotein targets and prevent or subvert just five essential cellular processes conserved across bacteria.[85] Current antibiotic classes (**figure 2C**) are limited to mechanisms as cell wall inhibitors, which target the synthesis and cross-linking of peptidoglycan; folate metabolism inhibitors, which target the metabolic pathway needed to synthesise nucleobases and DNA; nucleic acid synthesis inhibitors, which target the DNA gyrase, topoisomerase and RNA polymerase enzymes involved in DNA replication; protein synthesis inhibitors, which target the ribosome to arrest protein translation; and membrane inhibitors, which disrupt the integrity and function of the cell membrane.[86]

As shown by decades of clinical successes, these antibacterial drugs and their targets make excellent use of the physiological differences between human and bacterial cells. There are multiple classes at our disposal for each validated drug target; however, it is an unfortunate reality that resistance to one antibiotic soon spreads to the whole class, and the more a class of antibiotics is used, it seems that resistance is more likely to develop as a result of selective pressure.[87] Awareness of resistance can lead to more responsible antibiotic stewardship and medical practices, which can help to prolong a drug's therapeutic value, but resistance will eventually defeat all antibiotics. Therefore, as long as they are required, we need to prioritise scientific innovation to find novel antibacterial agents as old antibiotics are lost to resistance.

1.2 Antibacterial drug discovery in the resistance era

The need for new antibiotics is evident; however, the shortage of unique targets in clinical use and the bare research and development (R&D) pipeline threaten our ability to combat antibiotic resistance in the future. The World Economic Forum concluded in an annual report on global risks of antibiotic-resistant bacteria that, "We live in a bacterial world where we will never be able to stay ahead of the mutation curve. A test of our resilience is how far behind the curve we allow ourselves to fall."[88] In the past 20 years, only five novel antibiotic classes were launched: oxazolidinone (2000), lipopeptide (2003), pleuromutilin (2007), fidaxomicin (2011), and diarylquinoline (2012).[89] Most of these classes were discovered decades ago and are only being revisited out of need. These classes also do not possess activity against Gram-negative bacteria. From this, it is clear that industry is struggling to replace antibiotics as they become obsolete.[90–94]

The growing deficit of antibacterial R&D stems from economic, regulatory and scientific problems that have been exacerbated by antibiotic resistance. Policy changes to incentivise the reformation of antibiotic misuse have been enacted by government agencies including the World

Health Organisation (WHO), the European Centre for Disease Prevention and Control (ECDC), and the Infectious Diseases Society of America (IDSA).[95] Public education campaigns, such as the UK's One Health Initiative, highlight the need for improved antibiotic stewardship, which encourages a more cautious approach towards medical and veterinary antibiotic usage.[96] The US and EU governments have been collectively investing nearly $1 billion to stimulate new antibacterial R&D.[97,98] However, most of this funding is for early stages of preclinical development, leaving gaps in funding for clinical development and the commercialisation of new antibiotics. There is also a lack of international coordination across these active initiatives, which could hinder future progress.[99,100]

Just as government agencies are issuing calls and providing funding for antibiotic development to evade a looming public health crisis, significant players in the pharmaceutical industry are pulling out of the antibacterial discovery space. As of 2019, there are only four multinational pharmaceutical companies with active antibiotic programmes: Merck & Co., Roche, GlaxoSmithKline, and Pfizer.[101] For industry, the economic incentives are too weak, and returns on investment are too low as drug reimbursement is based on the volume of drugs sold, which is lower for antibiotics because they are prescribed for short-term use.[102]

Additionally, the rigid regulatory hurdles currently in place have stifled antibacterial drug discovery. Recruiting the required amount of patients for antibacterial clinical trials is difficult sometimes if the antibacterial agent is addressing specific pathogens or emerging resistance.[103] Also, under the current FDA application process, demonstrating a clinical benefit in a reasonable timeframe is challenging due to the sporadic nature of antibiotic resistance and the difficulty in demonstrating the superiority of a novel agent over an existing, curative antibiotic.[104]

1.2.1 Scientific approaches to antibacterial drug discovery

While economic and regulatory issues are complex factors impinging on the shrunken R&D pipeline, they can ultimately be influenced in the long term by the trajectory of quality science. The infectious disease community can continue to contribute to antibacterial drug discovery by identifying new targets and new drug candidates in innovative ways. Scientists have made several advances in understanding microbial physiology in the past few decades, such as acquiring knowledge that bacteria form biofilms,[105] that pathogens inject effectors into host cells,[106] and the mechanisms underlying horizontal gene transfer.[107] However, there are several shortcomings in historical approaches towards antibacterial R&D that have resulted in a dearth of new antibiotics reaching the market.

Briefly, the first shortfall is a lack of chemical novelty. Natural product drug discovery, rich in chemical diversity, was abandoned as the rate of rediscovery became too high after the golden

era of antibacterial drug discovery in the 1960s.[108] Fortunately, advancements in synthetic chemistry made it possible to study semi-synthetic derivatives of antibiotics, which caused the field to focus on a few good antibiotic scaffolds and their targets.[109] As established previously, a resistance that emerges towards a particular mechanism of action or target will usually extend to all the derivatives in the class, and scientists have been focused on improving or modifying the same few chemical scaffolds for decades.

Another more complex shortfall is the use of target-based screening for the past several decades to identify new antibacterial hit compounds. Pharmaceutical companies have historically responded to the rise in antibiotic resistance by focusing on high-tech discovery approaches (genomics and high-throughput screening) on novel genetically-essential, isolated targets to find new antibacterial agents.[87] Two notable examples of this in industry are analyses on R&D efforts by GlaxoSmithKline and AstraZeneca, which both had immense genome platforms in the late 1990s that ultimately yielded no new tractable leads. The reasons for these failures were credited to too many self-imposed restrictions placed on screening, such as rejecting targets with unknown function and seeking compounds with broad-spectrum activity. Another reason for these target-based screening failures was that the hits were biased towards more lipophilic physicochemical properties than the hits from whole-cell screens.[110,111]

A final shortfall is improper target validation, which results in poor *in vivo* efficacy of antibacterial drug candidates.[112] Target validation techniques range from measuring the target's expression levels in disease states to modulating target genes and observing phenotypic endpoints. Biological targets that are found to be intractable at later stages in drug development is expensive; therefore, a thoroughly performed, multi-validation approach is necessary during early stages of drug development to reduce attrition rates.[113]

Although some believe that novel and diverse chemistry is the best way forward to tackle the discovery void,[114] others believe that a parallel strategy is required as well that adjusts traditional screening methods to better reflect *in vivo* infection conditions.[113] An example is a study from Pfizer that found inhibitors of Gram-negative bacteria by targeting Lipid A biosynthesis. Not only was this a novel target, but it was also an opportunity to probe with inhibitors to gain a better biochemical understanding of the pathway and unravel its importance *in vivo*. This included testing for the spontaneous generation of resistance to the inhibitors.[115]

Other logical strategies include focussing on finding narrow-spectrum antibiotics that act against a specific bacterial strain. This has been explored in *Mycobacterium tuberculosis*, where the ability to kill the pathogen (not just inhibit replication) is crucial for treating *M. tuberculosis* infections.[116] An encouraging example is a study in which the target, aminotransferase BioA,

involved in the biosynthesis of biotin, was identified in *M. tuberculosis*. Then, three different screening approaches were employed; first, BioA was demonstrated as genetically essential and vulnerable *in vivo* and *in vitro,* and chemical libraries were screened against the enzyme. Second, the same libraries were screened in a whole-cell assay with biotin added to the medium to identify which hits contained whole-cell activity that was biotin-dependent. Third, an assay was done on a BioA-depleted bacterial strain, which allowed for the identification of weaker hits that would have been otherwise missed in the wild-type strain.[117]

However, it is essential that strain-specific antibiotics are coupled with rapid diagnostics in order for this strategy to be successful in hospitals. The current regulatory framework would also have to change to allow strain-based clinical trials and approvals. There have been minimal improvements in the diagnostics of bacterial infections over the years, which contrasts the progress made in other diseases, such as diabetes or cardiovascular disease.[118]

There is also a strong case for moving the search for antibiotics to compounds that have more than one cellular target.[119,120] Some of the most successful antibiotics are broad spectrum and hit multiple cellular targets, diminishing the probability of developing resistance. An example is ciprofloxacin, a fluoroquinolone that targets DNA gyrase and DNA topoisomerase.[94] Another example is augmentin, a combination antibiotic of amoxicillin and clavulanic acid, which are β-lactam and β-lactamase inhibitors, respectively. A more recent example is the *S. aureus* inhibitor kibdelomycin, which targets both gyrase B and topoisomerases IV proteins.[121] The justification for this approach is that many single gene knockouts in model organisms show no (or small) phenotypic effects by themselves. Compounds that hit multiple targets simultaneously can explore "synthetic lethal" interactions that further expand the number of available targets in an organism.[122] These are just a few examples of how the scientific paradigm for developing antibiotics is shifting in response to unmet needs. One of the multidrug-resistant pathogens where there is a tremendous unmet need for new antibacterial agents is *Pseudomonas aeruginosa.*

1.3 *Pseudomonas aeruginosa*

Pseudomonas aeruginosa is a Gram-negative, mono-flagellated bacillus of the Pseudomonadaceae family and the γ-proteobacteria class. *Pseudomonas* is derived from a combination of the Greek word, *ψευδής* (*pseudes*), meaning false, and the Greek word, *μονάς* (*monas*), meaning a single unit. The word, *aeruginosa*, is derived from the Latin, *verdigris*, meaning copper rust.[123] *P. aeruginosa* is an obligate aerobe and has been isolated from a wide range of ecological niches, including soil and fresh water, and is also an opportunistic pathogen with a variety of plants, animals and humans among its target hosts.[124]

P. aeruginosa is unique because it contains one of the largest genomes among bacteria, with between 5.5 and 7 million base-pairs and a G-C content of around 65%.[125] The vast genome is divided between the core genome and the accessory genome. The core genome is conserved among *P. aeruginosa* strains, even among samples obtained from patients,[126] while the accessory genome varies greatly between clones of the same species and contributes to the overall genetic plasticity, which is central to *P. aeruginosa* evolution. Genes for lipopolysaccharide O antigen, iron-scavenging pyoverdine, resistance to various antibiotics, and virulence factors have been traced to the accessory genome, which provides profound advantages for the survival of this species.[127–129]

Generally, *P. aeruginosa* does not affect healthy individuals but is a notorious opportunistic pathogen that colonises and displays pathogenic behaviour in immunocompromised hospital patients, accounting for 10% of HAIs in the European Union.[130] It is renowned for its metabolic versatility and subsequent widespread distribution, which results in potent and persistent infections that escalate the need for surgical intervention, increase the overall length and costs of hospitalisation stays and can carry an average mortality rate in hospitals of 40-60%.[131] *P. aeruginosa* is exceptionally difficult to overcome by chemotherapy due to its ability to develop resistance mechanisms to multiple drug classes, often during the course of treatment, and most notably during combination antibiotic treatment.[131,132] Its aggressive nature and broad adaptability can be attributed to its nutritional adaptability and both endogenous and acquired antibiotic resistance mechanisms.

1.3.1 Infection scenarios

Of the Gram-negative bacteria responsible for HAIs, *P. aeruginosa* ranks as the second most problematic.[133] One of the largest patient groups affected by *P. aeruginosa*'s opportunism is burn victims. The skin is the body's first line of immune defence, and when this barrier is breached whilst in hospital, *P. aeruginosa* can very easily colonise the wounds. Once an infection is detected, medical staff must move quickly to prevent the infection from spreading. These acute infections are associated with haemorrhaging and lung tissue necrosis as a result of *P. aeruginosa* producing several exotoxins and proteases.[134] Despite the high risk of infection in burn victims, lung infections are associated with the highest mortality rates, particularly hospital-acquired and ventilator-associated pneumonia.[135]

Probably the most prominent example of *P. aeruginosa* opportunism is seen in its ability to infect the pulmonary airways of cystic fibrosis (CF) patients. CF is a hereditary disease caused by mutations in the gene encoding the cystic fibrosis transmembrane conductance regulator. This results in defects in the membrane-associated chloride channels, which are expressed primarily in epithelial tissues and serve multiple roles, including the coordination of fluid secretion. In the

pulmonary airways, enhanced sodium absorption and impaired chloride transport lead to mucosal thickening and inefficient mucociliary clearance.[136,137] This situation provides an environment depleted in salt, iron and proteins, whilst rich in lipids that is highly conducive to bacterial proliferation.[138,139] Once bacteria colonise the lungs, several species can thrive, and this leads to a diverse microflora in CF patients at what is the start of a chronic infection. Despite this diversity, *P. aeruginosa* eventually dominates due to its superior adaptability and establishes chronic infections correlated with declining lung function from scarred tissues and eventual mortality.[140]

Although the prognosis of CF patients has greatly improved over the years, life expectancy still ranges from 12-40 years old in Europe while the patients are plagued with chronic *P. aeruginosa* infections.[141] One way that *P. aeruginosa* is suited to the unique physiological environment in CF airways is through anaerobiosis. As the lungs are colonised with bacteria, free oxygen is consumed, and oxygen gradients form within the mucus. Under these microaerobic or aerobic conditions, *P. aeruginosa* employs nitrate and nitrite as alternative electron acceptors to oxygen.[142] In cases where iron availability is limited, *P. aeruginosa* secretes a greater number of virulence factors such as proteases and elastases and increases its production of alginate, which provides further protection from the host immune system and may also confer an advantage in terms of iron utilisation.[143,144] When typical nutrient sources are scarce in the lungs, the conservation of metabolites is essential for cell proliferation. *P. aeruginosa* isolated from CF lungs are often auxotrophic for various amino acids and display chemotaxis towards phosphatidylcholine (PC), which is the main component (80%) of lung surfactant.[145] PC is cleaved by *P. aeruginosa* lipases and phospholipase C into fatty acids, glycerol and phosphorylcholine, which are then transported into the cell by the fatty acids transporter (FAT), where they undergo β-oxidation.[146]

1.3.2 Intrinsic resistance

Unfortunately, *P. aeruginosa* infections are especially difficult to resolve because of the high intrinsic antibiotic resistance of *P. aeruginosa*. As already discussed, the outer membrane is a feature of all Gram-negative bacteria and is highly impermeable to antibiotics. What is unique about *P. aeruginosa* is that its outer membrane has been estimated to have 1-3% of the diffusion rates for carbapenems and zwitterionic compounds as the *Escherichia coli* outer membrane.[147] In *P. aeruginosa* laboratory strain PAO1, the completed genome sequence revealed that there are nearly 300 outer membrane transport systems known as porins.[148] Porins are water-filled channels that are selective for hydrophilic, charged compounds and have size limitations (<600 Da) on which molecules can pass. These porin proteins form cylindrical openings in the outer membrane with polar amino acid side chains lining the inside of the opening. The water molecules interacting with the channel-lining amino acids have to be removed and replaced temporarily by the drug molecule in order to

gain entry.[149] There are three major families of porins in *P. aeruginosa*. The OprF family accounts for the majority of nonspecific permeation through the outer membrane. The OprB family allows for the diffusion of glucose and other antibiotic-like molecules. The OprD family is part of a larger family and is responsible for the uptake of nutrients like cationic amino acids.[148] These latter porins are narrower and less efficient than the OprF family.[150] Loss of OprD through a point mutation confers resistance to the β-lactam imipenem.[151]

Other intrinsic antibiotic resistance mechanisms in *P. aeruginosa* include the multidrug efflux pumps, belonging to the resistance-nodulation-cell division (RND) superfamily. These pumps are composed of an energy-dependent pump in the cytoplasmic membrane (Mex component), an outer membrane porin (Opr component), and another Mex component joining the three together.[152] Four RND systems have been studied in *P. aeruginosa*: MexAB-OprM, MexXY-OprM, MexCD-OprJ and MexEF-OprN.[153] Small and hydrophobic or large and zwitterionic compounds are often recognised as multidrug efflux pump substrates. Examples include MexAB-OprM, which recognises and extrudes β-lactam and quinolone antibiotics, while MexXY-OprM extrudes aminoglycosides.[154]

1.3.3 Acquired resistance

P. aeruginosa has acquired resistance to many antibiotics in the β-lactam and aminoglycoside classes through the horizontal transfer of plasmids.[155] Other than acquiring resistance mechanisms, bacteria can spontaneously mutate. If a random mutation is beneficial for survival, then it will remain in that organism's genome and be passed down to its progeny. The normal mutation rate is 10^{-6} to 10^{-9} per nucleotide per generation in response to antibiotic selective pressure. *P. aeruginosa* has been observed to develop mutations 100x faster than this normal mutation rate towards ciprofloxacin in certain infections, such as in the CF airways.[156] Certainly, these extreme endogenous and acquired resistance mechanisms combined with the lack of new anti-Pseudomonal drugs available to the clinical community has driven the WHO to classify *P. aeruginosa* recently as a critical priority pathogen for the development of new antibiotics.[9]

1.3.4 Central metabolism

The tricarboxylic acid (TCA) cycle, first discovered in bacteria in the 1950s by Krebs, Kornberg and Monod, is positioned in the centre of cellular metabolic pathways where the biosynthesis of key intermediates are produced.[157,158] The main function of the TCA cycle is to generate electron carriers that can be used in the final stage of cellular respiration, oxidative phosphorylation. Cellular respiration is a metabolic process that occurs in three stages; (1) organic fuel molecules, *e.g.* glucose, fatty acids, and amino acids, are oxidised to yield two-carbon (C_2) fragments in the form of the acetyl group of acetyl coenzyme A. (2) These C_2 groups are fed into

the TCA cycle, which enzymatically oxidises them to carbon dioxide (CO_2). The energy released by this oxidation is conserved in the reduced electron carriers, NADH and $FADH_2$. (3) NADH and $FADH_2$ are then oxidised themselves, releasing protons and electrons. The electrons are transferred along a chain of electron-carrying molecules to O_2, where they are reduced to form H_2O. During electron transfer, large amounts of energy are released and conserved in the form of ATP.[159]

The TCA cycle was first discovered in *Pseudomonas aeruginosa* in 1951.[160] The presence of oxygen and glucose in the environment allows for the complete oxidation of glucose via cellular respiration. In *P. aeruginosa*, sugars are catabolised mostly by the Entner-Doudoroff pathway (EDP) pathway, which cleaves glucose into two molecules of pyruvate in stage 1 of cellular respiration. There are two other glucose-catabolising pathways in bacteria: the oxidative pentose phosphate pathway and the Embden-Meyerhof Parnas (EMP) pathway. The EMP pathway also yields two molecules of pyruvate from one molecule of glucose.[161–163] Before entering the TCA cycle, pyruvate is converted to acetyl coenzyme A by pyruvate dehydrogenase.

Once metabolites are fed into the TCA cycle, eight catalytic reactions occur; (1) **acetyl coenzyme A** reacts with oxaloacetate to form **citrate** and coenzyme A; (2) **citrate** is restructured to form **isocitrate**; (3) **isocitrate** is oxidised to form **α-ketoglutarate**, losing a molecule of CO_2 in the process; (4) **α-ketoglutarate** is oxidised to form **succinyl coenzyme A,** losing another molecule of CO_2 in the process; (5) **succinyl coenzyme A** is enzymatically converted to **succinate**; (6) **succinate** is oxidised to form **fumarate**; (7) **fumarate** is hydrated to yield **malate**; and finally, (8) **malate** is oxidised to **oxaloacetate**. Each completion of the cycle results in the regeneration of oxaloacetate and the formation of two CO_2 molecules, two ATP molecules, and reducing equivalents for electron transport, or stage 3, in cellular respiration.[164]

Acetyl coenzyme A plays a pivotal role in central metabolism as the end product of glycolysis, fatty acid β-oxidation and amino acid degradation; however, the synthesis of gluconeogenic precursors from acetyl coenzyme A alone is not possible. This means that when the surrounding environment is depleted of metabolic inputs complementary to acetyl coenzyme A like sugars, bacteria are unable to generate biomass. Nonetheless, we have seen from the range of environments in which *P. aeruginosa* can thrive and cause infections, that glucose is not always present, yet *P. aeruginosa* can rewire its central metabolism depending on nutrient availability.[165]

The solution to this bacterial problem is a modified TCA cycle. This modification is known as the glyoxylate shunt, which is an anaplerotic, or replenishing pathway, which allows for the net conversion of acetyl coenzyme A into malate without glucose, see **figure 3**.[166] The glyoxylate shunt was first discovered in *Pseudomonas* KB1 in 1957 by Kornberg and Krebs.[167] When *P. aeruginosa*'s

only access to nutrients is limited to carbon-poor sources, such as fatty acids, the bacterium employs lipases and transporters in the outer membrane to liberate and transport the fatty acids into the cell.[168] Once inside the cell, the fatty acids undergo β-oxidation, where they are oxidised into molecules of acetyl coenzyme A by acetyl coenzyme A synthetase. Acetyl coenzyme A then feeds into the TCA cycle where the first two reactions occur, as described previously. However, instead of undergoing oxidative decarboxylation to yield α-ketoglutarate, isocitrate is diverted away from the TCA cycle reactions and provided a direct route to malate, thereby circumventing the two CO_2-producing steps that would normally preclude growth on fatty acids.[169]

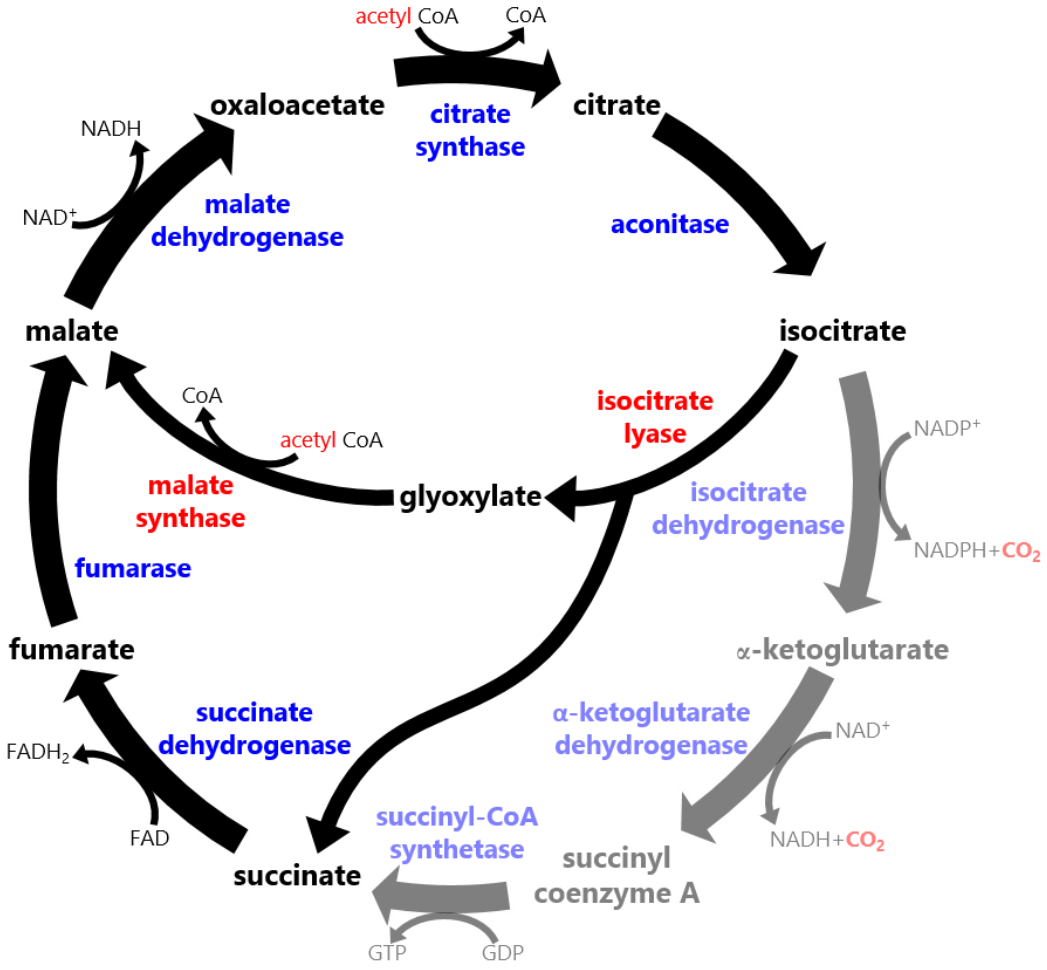

Figure 3. Glyoxylate shunt schematic. The two metabolic reactions catalysed by the glyoxylate shunt are shown within the eight catalytic steps of the TCA cycle. The glyoxylate shunt allows the bypassing of the CO_2-producing reactions of the TCA cycle. This gives a substantial advantage when the bacteria grow on limited carbon sources such as acetate.

The glyoxylate shunt is composed of two enzymes: isocitrate lyase (ICL) and malate synthase (MS), see **figure 3**. ICL enzymatically cleaves isocitrate to yield glyoxylate and succinate

in a reversible reaction. This reaction is then followed by an irreversible condensation of glyoxylate and acetyl coenzyme A yielding the formation of malate and CoA by MS.[170–172] The glyoxylate shunt is present in a wide range of prokaryotic and lower eukaryotic organisms, and it enables these microorganisms to grow on carbon sources with a C_2 backbone, such as short-chained fatty acids, like acetate or ethanol.[169,173]

Isocitrate is the substrate for ICL but is also the substrate for two isocitrate dehydrogenases (ICD/IDH) present in *P. aeruginosa*, which together, mandate carbon flux either through the glyoxylate shunt or around the TCA cycle.[174] Thus, there is a competition between these enzymes for isocitrate. Despite its initial discovery in *P. aeruginosa*, much of what is understood about the regulation of the glyoxylate shunt has been studied in *E. coli*.[175] Carbon flux in *E. coli* is controlled based on isocitrate dehydrogenase kinase/phosphatase (AceK) phosphorylating or dephosphorylating ICD in the presence of acetate or glucose, respectively. Phosphorylation deactivates ICD, directing isocitrate through the shunt to ICL.[176] Because the *P. aeruginosa* genome also encodes a second isocitrate dehydrogenase isoform (IDH), which is not a substrate for AceK-dependent inhibition, the *E. coli* model of metabolic regulation of the glyoxylate shunt is probably an over-simplification of what is happening in *P. aeruginosa*.[174]

1.3.4.1 Isocitrate lyase

Isocitrate lyase (ICL) is responsible for cleaving isocitrate into succinate and glyoxylate as the first enzyme of the glyoxylate shunt in what is inferred as a Claisen-type condensation from an enolic intermediate.[177] ICL has been structurally characterised in one eukaryotic species: *Aspergillus nidulans* (PDB entry 1DQU), and three prokaryotic species: *M. tuberculosis* (PDB entry 1F61), *E. coli* (PDB entry 1IGW), and more recently in the Welch laboratory, *P. aeruginosa* (PDB entry 6G1O). These studies all concurred that the oligomeric status of ICL is a tetramer.[174,178–180] However, the amino acid sequences of the enzymes differ. *M. tuberculosis* ICL (ICL_{Mt}) and *E. coli* ICL (ICL_{Ec}) have a predicted molecular mass of 48 kDa, while *A. nidulans* ICL (ICL_{An}) has a predicted mass of 67 kDa and *P. aeruginosa* ICL (ICL_{Pa}) has a predicted mass of 59 kDa. These differences in secondary sequence manifest in the tertiary and quaternary structures. For example, ICL_{Pa} has more than 100 extra amino acids in its sequence than ICL_{Ec} or ICL_{Mt}, which results in elongated α-helices and extends the contacts between the four protomers in the tetramer.

The four ICL structures all share a conserved TIM-barrel domain, which contains the active site that is also highly conserved between organisms. Acetate has been shown to upregulate ICL_{Pa} transcription, and carbon flux between the TCA cycle (ICD_{Pa}/IDH_{Pa}) and the glyoxylate shunt (ICL_{Pa}) is rheostatically regulated, depending on the concentration of various metabolic intermediates present in the cell. This is because ICL_{Pa} and ICD_{Pa}/IDH_{Pa} have similar affinities

towards isocitrate. For example, pyruvate was shown reciprocally to inhibit ICL_{Pa} and activate IDH_{Pa}.[174]

1.3.4.2 Malate synthase G

Malate synthase is responsible for catalysing the final step in the glyoxylate shunt: the condensation of glyoxylate and acetyl coenzyme A to yield malate and coenzyme A. All malate synthases described in the literature to date are found either as isoform A or isoform G. The monomeric malate synthase isoform G (MSG) has been found only in bacteria, whereas the oligomeric malate synthase isoform A (MSA) occurs in plants and fungi, as well as some species of bacteria.[169] Both are represented in pathogenic organisms. For example, MSG occurs in *M. tuberculosis,* and MSA is present in *C. albicans*.[181,182] *E. coli* is unique because it contains the genes for both isoforms: *aceB* for MSA, where the expression is regulated by the presence of fatty acids; and *glcB* for MSG, where the expression is regulated by the presence of glycolate.[183] Although the G isoform is predominantly monomeric, one study has suggested that *M. tuberculosis* MSG acts as both a monomer and dimer under physiological conditions and proposed that the dimeric form is more stable.[184]

X-ray crystal structures have been solved for *E. coli* MSA (PDB entries: 3CUZ and 3CV1). The structure of MSG from four prokaryotic species has been resolved by X-ray crystallography: *E. coli* (PDB entries 1P7T and 1D8C), *M. tuberculosis* (PDB entries for apo and substrate-bound structures include 1N8W, 1N8I, 2GQ3, 5H8P, and 5H8U), *Mycobacterium marinum* (PDB entry 6AXE), and *Mycobacterium leprae* (PDB entry 4EX4). Also, the *E. coli* MSG structure has been solved by NMR (PDB entries 1Y8B and 2JQX). These structural studies of MSG reveal that there are four structural domains: an 8α/8β TIM barrel fold centred by an N-terminal helical clasp and an α/β domain insertion. Several α-helices comprise the C-terminal domain, which borders the active site along with the TIM barrel.[181,182,185–188] The structural difference between MSG and MSA is that the α/β insertion is missing in MSA.[185,187] *Pseudomonas aeruginosa* MSG (MS_{Pa}) has a predicted mass of 78 kDa with overall amino acid sequence identities of 56% and 70% to *E. coli* and *M. tuberculosis*, respectively.[187] Since the 8α/8β TIM barrel and helical C-terminus are shared among the malate synthase superfamily; the only variability would be expected to be in the N-terminal domain.

1.4 The glyoxylate shunt as a target for antibacterial intervention

Beyond their role in carbon fixation, ICL and MS have been implicated in virulence, persistence, and antibiotic resistance in medically relevant organisms. Expression levels of the glyoxylate shunt enzymes are upregulated in chronic *P. aeruginosa* infections of cystic fibrosis patients.[189] ICL_{Pa} has also been linked with the induction of Type III Secretion System (T3SS) expression, an important virulence mechanism during infections. Under oxygen-limited conditions, a ΔICL_{Pa} mutant significantly reduced the expression of the four main structural components of the T3SS machinery, PcrV, PopN, ExoS, and ExsD.[190]

Additionally, an MS_{Mt} deletion mutant resulted in decreased severity of lung lesions in a mouse infection model and MS was shown to be essential for the bacteria to resist fatty acid-associated toxicity.[191] An ICL_{Mt} deletion mutant has shown an increased susceptibility to clinical tuberculosis drugs than WT strain.[192] In another study, an ICL_{Mt} deletion mutant displayed an increased rate of clearance from the lung and a reduced level of tissue damage in a rat pulmonary infection model.[193] Likewise, a *P. aeruginosa* double deletion mutant (ΔICL ΔMS) was found to be completely avirulent in a mouse pulmonary infection model, and the glyoxylate shunt was discovered to be conditionally essential for survival in mammalian systems as there were no recoverable colonies from the lung tissue after 48 hours.[194] Thus, both ICL and MS are attractive targets for drug discovery because they are essential during infection situations.

1.4.1 Project aims

In this dissertation, I propose to investigate the glyoxylate shunt as a target for antibacterial intervention in *Pseudomonas aeruginosa*. This proposition is supported by the critical need for new antibacterial agents against *P. aeruginosa* and the looming threat of antibiotic resistance to current treatments. Targeting the glyoxylate shunt in *P. aeruginosa* could potentially be efficacious as the shunt is a part of central metabolism and therefore, conditionally important. Also, the glyoxylate shunt is essential in many hospital-acquired infection situations that impact large patient populations. The glyoxylate shunt as an antibacterial target would also be selective because there are no mammalian orthologues of either enzyme known. It could further be potentially broad spectrum as the glyoxylate shunt is present in many pathogenic bacteria. Finally, simultaneously targeting both enzymes could provide a successful antibacterial agent that theoretically delays the development of resistance due to the multi-targeted approach. To investigate this further, I pursued the following objectives:

- To biochemically characterise MS from *P. aeruginosa* by resolving the X-ray crystal structure, studying the kinetic properties, and analysing the target enzyme to assess its suitability as a drug target.
- To test small molecules against both purified enzymes of the glyoxylate from *P. aeruginosa* as well as against *P. aeruginosa* cultures to assess and validate their potential as dual inhibitors.
- To determine the suitability of any hit compounds as lead candidates by evaluating their cytotoxicity, hepatotoxicity, and antibacterial activity in response to various conditions.

2. Experimental

2.1 Microbiological procedures

2.1.1 Bacterial strains

Bacterial strains used in this work (see **table 1**) were stored at -80°C in growth medium containing 25% (v/v) glycerol. Viable bacteria were stored on agar media plates at room temperature for up to five days.

Table 1. List of bacterial strains and plasmids used in this study.

Strain	Description	Source
Pseudomonas aeruginosa		
PAO1	Wild-type prototroph	B. Iglewski
YM64	*⊿mexAB-oprM ⊿mexCD-oprJ ⊿mexEF-oprN ⊿mexXY*	Morita *et al.*[153]
Boston 41501	Clinical isolate, isolated from blood	ATCC 27853
Escherichia coli		
BL21	BL21 derivative of *E. coli* B	Miroux *et al.*[195]
Rosetta	Derivative of *E. coli* BL21	Novagen
FDA strain Seattle 1946	Clinical isolate, reference strain for antimicrobial susceptibility testing	ATCC 25922
Klebsiella pneumoniae K6	Clinical isolate from urine, produces beta-lactamase SHV18	ATTC 700603
Acinetobacter baumannii 2208	Type strain isolated from urine	ATCC 19606
Staphylococcus aureus Rosenbach	Clinical isolate from a wound (Wichita)	ATTC 29213
Enterococcus faecium Orla Jensen	Quality control strain	ATTC 35667
Enterobacter aerogenes NCDC 819-56	Type strain isolated from lung sputum	ATTC 13048
Plasmid	**Description**	**Source**
pGEX-6P-1::*glcB*	Vector for inducible expression of *N*-terminally glutathione *S*-transferase-tagged *glcB,* Cb^R	Roucourt *et al.*[196]
pET19m::*aceA*	Vector for inducible expression of *N*-terminally His_{6x} -tagged *aceA*, Cb^R	S. Dolan

2.1.2 Bacterial growth media

Growth media and constituents are listed in **table 2**. Media and solutions were sterilised either by autoclaving at 121°C for 15 minutes in glass bottles or by filtering with 0.22 μm membrane stericups (Millipore).

Table 2. Media and solutions used to grow and assay bacteria.

Media and solutions	**Components per litre**
Luria Bertani broth	10 g peptone 5 g yeast extract 5 g sodium chloride
2×TY broth	16 g tryptone 10 g yeast extract 5 g sodium chloride
MHB medium	22 g Mueller Hinton II Broth powder (cation-adjusted) (Becton Dickinson)
1x M9 minimal medium	200 mL 5x M9 minimal salts solution (Difco) 0.2% (w/v) magnesium sulphate 0.01% (w/v) calcium chloride 0.5% (w/v) carbon source
1x MOPS minimal medium	100 mL of 10x MOPS minimal salt solution 20-60 mM carbon source 32 μM calcium chloride 0.29 mM potassium sulphate 1.32 mM dipotassium phosphate 8 μM iron(II) chloride
Solid agar plates	Growth media containing 1.5% (w/v) agar
Solutions	**Components per litre**
M9 minimal salts, 5x (Difco)	33.9 g disodium phosphate 15 g monopotassium phosphate 2.5 g sodium chloride 5 g ammonium chloride
MOPS minimal salts, 10x	40 mM MOPS, pH 7.5 4 mM Tricine, pH 7.5 0.01 mM iron(II) sulphate 9.52 mM ammonium chloride 0.5 μM calcium chloride 0.52 mM magnesium chloride (hexahydrate) 50 mM sodium chloride 1x micronutrients
Micronutrients, 100x	3 mg ammonium molybdate tetrahydrate 24 mg boric acid 7 mg cobalt chloride 3 mg cupric sulphate 16 mg manganese chloride 3 mg zinc sulphate

2.1.3 Bacterial growth on solid media

Colonies were grown in 10 cm diameter Petri-dishes containing 25 mL of suitable growth media (see **table 2**) and incubated at 37°C overnight. When growing cells from frozen stocks, cells were defrosted on the surface of the agar at room temperature. A sterile inoculation loop was used to spread the cells across the agar using the streaking method to produce single colonies.

2.1.4 Bacterial overnight cultures

A single bacterial colony was inoculated in 10 mL of required growth medium in a 25 mL plastic universal tube. The culture was grown at 37°C for approximately 18 hours on a rotating wheel. If appropriate, the antibiotic selection was maintained throughout the incubation. Unless otherwise stated, experiments were conducted in triplicate using three biological replicates from three independent bacterial colonies.

2.1.5 Antibiotics

The antibiotics used in this work are listed in **table 3**. Antibiotics were either solubilised in water and stored at 4°C, or were solubilised in a 50% (v/v) ethanol solution and stored at -20°C for up to one month. All antibiotics were filter-sterilised before use with 0.22 μm membrane filters (Millipore).

Table 3. Antibiotics used in this work.

	Working antibiotic concentrations (μg mL^{-1})			
Bacteria	Carbenicillin[a]	Ciprofloxacin[b]	Gentamicin[b]	Linezolid[b]
P. aeruginosa	250	1	50	-
E. coli	50	0.015	10	-
S. aureus	-	0.5	-	-
K. pneumoniae	-	0.5	-	-
A. baumannii	-	1.2	-	-
E. faecium	-	0.5	-	4
E. aerogenes	-	0.04	-	-

Antibiotics were either dissolved in [a] 50% (v/v) ethanol or [b] deionised water.

2.1.6 Minimal inhibitory concentrations and growth curves

Bacterial overnight cultures were inoculated to a starting optical density at 600 nm ($OD_{600\ nm}$) of 0.05 in the relevant medium. Diluted bacterial suspensions (198 μL) were added in triplicate to 96-well, sterile, clear U-bottom plates (Thermo Fisher Scientific). Stock concentrations (100x) of test compounds (2 μL) were added to the plates in two-fold dilutions, and the plates were covered with gas-permeable adhesive seals (Scientific Laboratory Supplies). Assay controls

included 1% DMSO, a positive antibiotic control, and media-only wells as a control for background absorbance.

For minimum inhibitory concentration (MIC) assays and growth curves, plates were incubated in a FLUOstar® Omega microplate reader (BMG Labtech) for 18 hours at 37°C with 200 rpm agitation, and automatic $OD_{600\ nm}$ well scans were recorded of individual wells every 60 minutes. For MIC assays on the ESKAPE pathogens, plates were incubated at 37°C with 500 rpm agitation between measurements at $OD_{620\ nm}$ at 0, 4, 8 and 24-hour intervals using a Multiskan Go plate reader, according to CLSI and EUCAST guidelines.[197,198] MICs were determined as the lowest concentration in which more than 75% of bacterial growth (calculated from $\Delta OD_{600\ nm}$ using untreated and media wells) was inhibited. MICs were also determined and confirmed by visual inspection of wells.

2.1.7 Minimal bactericidal concentrations and viable cell counts

After MIC determination in 96-well plates, 100 μL from each well was serially diluted with sterile deionised water. The diluted samples (10^{-1}-10^{-9}) were added in 2 μL spots to agar plates of corresponding media.[199] The lowest concentration that resulted in no viable colonies after 48 hours of incubation at 37°C was determined as the minimum bactericidal concentration (MBC).

2.2 Purification of target enzymes

The glyoxylate shunt enzymes from *Pseudomonas aeruginosa* were overexpressed and purified in order to yield sufficient amounts of purified protein for biochemical characterisation and to study protein-ligand interactions. **Table 4** consists of the protein purification buffers and solutions used in this study.

2.2.1 Overexpression of malate synthase G

The gene encoding malate synthase G (*glcB,* PA0482) from *P. aeruginosa* strain PAO1 was overexpressed with a PreScission protease-cleavable, *N*-terminal Glutathione *S*-Transferase tag. A 2 L culture of *E. coli* strain BL21 containing the plasmid [pGEX-6P-1 (*glcB*)] in 2×TY medium was inoculated with 3 mL of an overnight culture grown in LB medium with carbenicillin (50 μg mL^{-1}). The culture was grown at 37°C with 250 rpm agitation to an approximate $OD_{600\ nm}$ of 0.6. The flasks were cooled to 16°C, and isopropyl-β-thiogalactopyranoside (IPTG) was added to a final concentration of 0.2 mM to induce overexpression of the cloned *glcB* open reading frame (ORF). Protein expression was continued for a further 16 hours at 16°C.

Table 4. List of the protein purification buffers used in this study.

Buffer	Components per litre
10x phosphate buffered saline (PBS)	10 PBS tablets (Dulbecco A)
Lysis buffer (GST-tagged)	1x PBS 1 mM DTT 1 cOmplete Mini EDTA-free protease tablets (Roche) pH 7.0
Protein purification buffer (GST-tagged)	50 mM Tris-HCl 150 mM sodium chloride 1 mM EDTA 0.1 mM TCEP pH 7.5
Protein purification buffer (Ni-tagged)	50 mM sodium phosphate 200 mM sodium chloride 10% (v/v) glycerol 10 mM imidazole pH 8.0
Elution buffer (GST-tagged)	50 mM Tris-HCl 150 mM sodium chloride 10 mM reduced glutathione 1 mM DTT pH 8.0
Elution buffer (Ni-tagged)	50 mM sodium phosphate 200 mM sodium chloride 10% (v/v) glycerol 250 mM imidazole pH 8.0
Dialysis buffer	50 mM Tris-HCl 150 mM sodium chloride pH 7.5
Protein loading dye	50 mM Tris-HCl 2% (w/v) SDS 0.1% (w/v) bromophenol blue 10% (v/v) glycerol 10 mM DTT
SDS-PAGE stacking buffer, 5x	60 g Tris-HCl 0.5% (w/v) SDS pH 6.8
SDS-PAGE resolving buffer, 5x	151 g Tris-HCl 0.5% (w/v) SDS pH 8.8
SDS-PAGE running buffer, 10x	30 g Tris-HCl 150 g glycine 0.1% (w/v) SDS pH 8.0

2.2.2 Malate synthase G protein purification

The *E. coli* BL21 cells were harvested by centrifugation (3430×*g* for 30 minutes at 4°C). The cell pellets were resuspended in 30-40 mL of ice-cold lysis buffer, see **table 4**. The bacterial suspension was lysed to completion by sonication with continuous cooling on ice (10 pulses of 30 seconds, 13 A, with 1 minute pauses between pulses). The cellular debris was removed by ultracentrifugation (9900×*g* for 30 minutes at 4 °C), and the clarified supernatant was filtered through 0.45 μm membrane filters (Sartorius). Subsequent purification was performed using an ÄKTA FPLC system where the filtered sample was loaded immediately onto a 5 mL Glutathione Sepharose column (GSTrapFF) pre-equilibrated with lysis buffer, see **table 4**. The column was washed with 10 column volumes of protein purification buffer, and the bound protein was eluted with 2 column volumes of elution buffer.

Meanwhile, 5 mL of slurried Glutathione Sepharose 4B resin (GE Healthcare) was equilibrated with protein purification buffer in a 50 mL polypropylene tube. The GST-tagged MS fusion protein was added to the Glutathione Sepharose 4B resin along with 100 units of PreScission Protease (GE Healthcare). The mixture was then incubated for 48 hours at 4°C with gentle mixing to allow the cleavage of the fusion protein from the immobilised GST tag at the recognition sequence (LeuGluValLeuPheGln↓GlyPro).

The Glutathione Sepharose 4B resin was sedimented by centrifugation, and the supernatant was loaded directly onto a 16-600 Superdex 200 preparatory grade column (GE Healthcare) equilibrated at room temperature with de-gassed purification buffer. The flow rate was 0.8 mL min^{-1}. The elution profile was monitored with a multi-wavelength UV-vis display (UPC-900) at 230, 260, and 280 nm, and UV-active fractions were collected in 2 mL vials.

Fractions containing purified MS (confirmed by SDS-PAGE) were pooled and concentrated to 18 mg mL^{-1} using a Vivaspin with a molecular weight cut-off of 30 kDa (Sartorius). This mixture was divided into 100 μL aliquots, snap-frozen in liquid nitrogen, and stored at −80°C. Before freezing, I determined the protein concentration by measuring the absorbance at 280 nm and calculating the concentration, based on a modified Beer-Lambert law,[200] with the molar extinction coefficient for MS_{Pa} (ε_{calc} = 75,985 M^{-1} cm^{-1}) predicted from the amino acid sequence by the ExPASy ProtParam tool.[201]

$$\boldsymbol{c = \left(\frac{A}{(\varepsilon \times L)}\right) \times MW \times dilution\ factor} \quad \textbf{(1)}$$

Where c is the molar concentration of the protein; A is the absorbance at 280 nm; ε is the molar extinction coefficient of the protein (M^{-1} cm^{-1}); L is the path length of the cuvette (cm); MW is molecular weight of the protein (g mol^{-1}).

2.2.3 Preparation of Mg^{2+}-depleted malate synthase G

After purification, 50 mM EDTA (pH 8.0) was added to a portion of purified MS to remove bound metals for fluorescence studies, see **section 2.9**. MS was then dialysed extensively (4 × 1 L) at 4°C in 50 mM Tris-HCl, pH 7.5 containing 100 mM NaCl and 10 mM EDTA. The EDTA was then removed from the sample by dialysing at 4°C against 3 × 1 L of 50 mM Tris-HCl, pH 7.5 containing 100 mM NaCl. The final protein concentration was adjusted to 175 μM using **equation 1**.

2.2.4 Overexpression of isocitrate lyase

Isocitrate lyase (ICL, *aceA,* PA2634) from *P. aeruginosa* strain PAO1 was overexpressed with a TEV protease-cleavable, *N*-terminal $Histidine_{6x}$ tag kindly provided by Dr Stephen Dolan from the Welch laboratory. A 2 L culture of *E. coli* Rosetta strain containing plasmid [pET19m (*aceA*)] was grown at 37°C in LB medium with 250 rpm agitation to an $OD_{600\ nm}$ of 0.5-0.6. The temperature was then decreased to 20°C, and IPTG was added to a final concentration of 1 mM to induce overexpression of the cloned *aceA* ORF, and protein expression was continued for a further 16 hours at 20°C.

2.2.5 Isocitrate lyase protein purification

The *E. coli* Rosetta cells were harvested by centrifugation (3430×*g* for 30 minutes at 4°C), and the cell pellets were resuspended in 30 mL of ice-cold lysis buffer without DTT. The bacterial suspension was lysed to completion by sonication with continuous cooling on ice (10 pulses of 30 seconds, 13 A, with 1 minute pauses between pulses). The cellular debris was removed by ultracentrifugation (9900×*g* for 30 minutes at 4 °C), and the clarified supernatant was filtered through 0.45 μm membrane filters (Sartorius). Subsequent purification was performed using an ÄKTA FPLC system. The filtered sample was loaded immediately onto a 5 mL Ni-NTA superflow cartridge (Qiagen) pre-equilibrated with protein purification buffer, see **table 4.** The column was washed with 10 column volumes of the purification buffer, and the bound protein was eluted with 2 column volumes of elution buffer. The eluted protein sample was added with 1 mg of TEV protease in dialysis tubing with a 10-12 kDa MWCO (Thermo Fisher), and was dialysed extensively (3 × 2 L) at 4°C with gentle stirring for 24 hours to allow for the complete cleavage of the His_6 tag and removal of residual imidazole from the protein sample.

Meanwhile, 5 mL of slurried Ni-NTA resin (BioRad) was equilibrated with dialysis buffer in a 50 mL polypropylene tube. The cleaved protein sample was added to the resin and was incubated for 2 hours at 4°C while being gently mixed to allow for the removal of the TEV protease and any remaining fusion protein from the sample. UV-active (estimated by $A_{280\ nm}$) fractions containing purified ICL (confirmed by SDS-PAGE) were pooled and concentrated to 20

mg mL^{-1} using a Vivaspin with an MWCO of 10 kDa (Sartorius). This mixture was divided into 100 μL aliquots, snap-frozen in liquid nitrogen, and stored at −80°C. The protein concentration was determined by spectrophotometry using the calculated molar extinction coefficient for ICL_{Pa} (ε_{calc} = 54,820 M^{-1} cm^{-1}), predicted by the ExPASy ProtParam tool,[201] see **equation 1**.

2.2.6 SDS-PAGE preparations and staining

Protein samples (10 μL) were diluted with deionised water and 4x concentrated loading dye and denatured by heating at 95°C for 10 minutes. Samples were separated on 12% poly(acrylamide) separating gel, prepared as described in **table 5**. SDS-PAGE gels were run at 10 V cm^{-1} for three hours. Gels were incubated overnight in Coomassie stain [1 g/L Coomassie Brilliant Blue G (Sigma), 50% (v/v) methanol, 10% (v/v) methanol, 10% (v/v) acetic acid] and destained for three hours with Destain I [50% (v/v) methanol, 7% (v/v) acetic acid] and for destained a second time for three hours with Destain II [10% (v/v) methanol, 7% (v/v) acetic acid]. Protein samples sizes were determined by comparing migration against a Precision Plus Protein Standard (BioRad).

Table 5. Preparations for a 12% SDS-PAGE gel.

Gel Phase	Components per 10 mL
6% Stacking gel	2 mL 30% Bis-Acrylamide solution (Severn Biotech) 1 mL 5x stacking buffer 7 mL dH_2O 50 μL 20% (v/v) SDS 100 μL 8% (v/v) APS 5 μL TEMED
12% Resolving gel	4 mL 30% Bis-Acrylamide solution (Severn Biotech) 5 mL 5x stacking buffer 50 μL 20% (v/v) SDS 100 μL 8% (v/v) APS 5 μL TEMED

2.3 Data fitting and processing

All data fitting was performed with GraphPad Prism version 7.04 (GraphPad 7 Software, Inc., USA). The solid lines are the result of fitting the data to the equations denoted in relevant experimental sections. In all graphs, unless otherwise stated, the data points are the mean of experimental triplicates, and all error bars correspond to ±1 standard deviation. For all bar graphs, the statistical significance of the results was determined using a standard unpaired *t*-test unless otherwise stated.[202]

2.4 Kinetic measurements of malate synthase G

The enzymatic activity of purified MS was measured using a modified coupled assay in which the amount of free thiol (present in the reaction product, coenzyme A) was titrated using 5,5'-dithio(2-nitrobenzoic acid) (DTNB).[203] Reaction mixtures contained 50 mM potassium phosphate and 10 mM $MgCl_2$ buffer, pH 7.5 supplemented with 0.2 mM DTNB, acetyl coenzyme A, and glyoxylate (as indicated in results). The mixture was equilibrated at 37°C for 1 minute before the reaction was initiated by the addition of 1 µL of MS (final concentration, 25 nM). The initial linear change in absorbance (ΔAbs.) was recorded at 412 nm using a Biospectrometer (Eppendorf). Reaction rates were calculated using the molar extinction coefficient of the assay product 2-nitro-5-thiobenzoic acid (TNB) (14,150 M^{-1} cm^{-1}).[204] Initial velocity studies were conducted at fixed, saturating concentrations of glyoxylate and varying concentrations of acetyl coenzyme A and *vice versa*. The kinetic parameters were calculated from the best-fit nonlinear regression based on the Michaelis-Menten equation.[205]

$$\boldsymbol{v = \frac{V_{max} \times [S]}{(K_M + [S])}} \quad \textbf{(2)}$$

Where v is enzymatic reaction velocity, V_{max} is the maximum reaction velocity; K_M is the Michaelis-Menten constant, or the substrate concentration needed to achieve half-maximal enzyme velocity; $[S]$ is the substrate concentration. k_{cat}, the turnover that each enzyme site converts substrate to product per unit of time, was calculated using the following equation.[206]

$$\boldsymbol{v = \frac{E_t \times k_{cat} \times [S]}{(K_M + [S])}} \quad \textbf{(3)}$$

Where v is enzyme velocity; $[S]$ is the substrate concentration; E_t is the concentration of catalytic sites in the enzyme in the same units as $[S]$ and K_M. If the enzyme has multiple subunits, the value of E_t will be higher than the concentration of the enzyme.

In the case of non-Michaelis-Menten kinetics, or when an allosteric sigmoidal data distribution was observed, the following equation was applied to determine the best fit nonlinear regression.[207]

$$v = \frac{V_{max} \times [S]^h}{\left(K_{half}{}^h + [S]^h\right)} \quad \textbf{(4)}$$

Where v is enzyme velocity; V_{max} is the maximum reaction velocity; $[S]$ is the substrate concentration; K_{half} is the concentration of substrate needed to achieve a half-maximal enzyme velocity; h is the Hill slope. When h=1, this equation is identical to the Michaelis-Menten equation. When h>1, the curve is sigmoidal due to positive cooperativity.[208]

2.5 Kinetic measurements of isocitrate lyase

The enzymatic activity of isocitrate lyase (ICL) was measured using a modified coupled assay in which the number of exposed ketones (present in the reaction product, glyoxylate) was titrated using phenylhydrazine HCl.[209] Reaction mixtures contained 30 mM imidazole buffer, pH 6.8 and 5 mM $MgCl_2$ supplemented with D-L-isocitric acid (as indicated in results), 1 mM EDTA, and 4 mM phenylhydrazine. The mixture was equilibrated at 37°C for 1 minute before the reaction was initiated by addition of 1 μL of ICL (final concentration, 170 nM). The initial linear rate was recorded at $A_{324\ nm}$ using a Biospectrometer (Eppendorf). Rates were calculated using the molar extinction coefficient of the assay product, glyoxylate-phenylhydrazone (16,800 M^{-1} cm^{-1}). Kinetic parameters were calculated for ICL from the best-fit nonlinear regression using **equations 2** and **3**.

2.6 IC_{50} determinations of enzyme inhibition

Test compounds were assessed for their ability to reduce or impede the enzymatic activities of ICL and MS. Test compounds were solvated in DMSO, added to the respective reaction mixtures (concentrations indicated in results **chapter 4**) with a total DMSO concentration of 1%, and were allowed to incubate with the enzymes for 5 minutes at 37°C. Reactions were initiated by adding the enzyme's substrate (as indicated in results **chapter 4**), and the initial linear change in absorbance at appropriate wavelengths were measured (detailed previously in the kinetics sections). Dose-response curves were generated as normalised percentages of the initial linear reaction rates, and the concentrations which yielded 50% inhibition (IC_{50} values) were calculated from the best-fit logistic regression using the following equation from GraphPad Prism v. 7.04.

$$\boldsymbol{Response} = \frac{\mathbf{100}}{\mathbf{1} + \left(\mathbf{100}^{\left((\mathbf{logIC_{50}} - [I]) \times \boldsymbol{Hill\ slope}\right)}\right)} \quad \textbf{(5)}$$

Where *Response*, in this context, is the per cent enzyme activity in the presence of inhibitors; the denominator of the fraction is the per cent response at the bottom plateau of the sigmoidal curve; the numerator of the fraction is the per cent response at the top plateau of the sigmoidal curve, or 100; *[I]* is the concentration of inhibitor added; $LogIC_{50}$ is the dose when the inhibition is halfway between the top and bottom plateaus. *Hill slope* describes the steepness of the curve and has no units.

2.7 Determining the mode of inhibition kinetically

Kinetic assays were conducted on MS and ICL by titrating their respective substrates in the presence of fixed concentrations of inhibitors to see how they influenced the rate of enzymatic reactions. Concentrations of the inhibitors near to calculated IC_{50} values were added to reaction mixtures with the enzyme present and allowed to incubate for 5 minutes at 37°C. Reactions were initiated with pH-adjusted substrate solutions (concentrations specified in results **chapter 4**). The initial linear change in absorbance was measured, and kinetic parameters were calculated using the best-fit nonlinear regression. The enzyme activity *versus* substrate concentration plots were transformed into Lineweaver-Burk or double reciprocal plots as denoted in the following equation.

$$\frac{\mathbf{1}}{\boldsymbol{v}} = \frac{\boldsymbol{K_M}}{\boldsymbol{V_{max}}} \times \frac{\mathbf{1}}{[\boldsymbol{S}]} + \frac{\mathbf{1}}{\boldsymbol{V_{max}}} \quad \textbf{(6)}$$

Where *v* is enzymatic reaction velocity; V_{max} is the maximal reaction velocity; K_M is the Michaelis-Menten constant; *[S]* is the substrate concentration. The parameters of the linear regressions (x- and y-intercepts and slopes) of the double reciprocal plots were analysed along with apparent changes observed in K_M, V_{max} and k_{cat} values (**equations 2** and **3**) in the presence and absence of inhibitors to determine whether the mode of inhibition was competitive, uncompetitive, or displayed any of the three types of mixed inhibition. The inhibition constants were calculated differently, depending on the type of inhibition observed. The following equation for the best fit nonlinear regression is a modification of **equation 2** and was used as a mathematical starting point to solve for all kinetic constants in the presence of inhibitors.[210]

$$v = \frac{(V_{max}{}^{app} \times [S])}{(K_M{}^{app} + [S])} \quad (7)$$

Where $K_M{}^{app}$ and $V_{max}{}^{app}$ are defined as apparent values calculated in the presence of inhibitors.

2.7.1 Mixed inhibition

Mixed inhibition is when the inhibitor can bind to both the enzyme and the enzyme-substrate complex, but usually has a binding preference for one state over the other.[211] There were three types of mixed inhibition visually observed from the Lineweaver-Burk plots.

- In type 1 mixed inhibition, [-I] and [+I] lines intersected between the x- and y-axes in the second quadrant of the graph. This type indicates that [I] binds to [E] with greater affinity than to [ES]; Thus, $K_i < K_i'$, $K_M{}^{app} > K_M$ and $V_{max}{}^{app} = V_{max}$. This type mimics competitive inhibition.
- In type 2 mixed inhibition, [-I] and [+I] lines intersect at the x-axis between the second and third quadrants of the graph. This type indicates that [I] binds with equal affinity to [E] and [ES]; Thus, $K_i = K_i'$, $K_M{}^{app} = K_M$, and $V_{max}{}^{app} < V_{max}$. This type is traditional non-competitive inhibition.
- In type 3 mixed inhibition, [-I] and [+I] lines intersect below the x-axis in the third quadrant of the graph. This type indicates that [I] binds to [ES] with greater affinity than to [E]; Thus, $K_i > K_i'$, $K_M{}^{app} < K_M$, and $V_{max}{}^{app} < V_{max}$. This type mimics uncompetitive inhibition.

Where [-I] and [+I] are the linear regressions without and with inhibitor added, respectively; [E] is the free enzyme; [ES] is the enzyme-substrate complex; $K_M{}^{app}$ and $V_{max}{}^{app}$ are apparent K_M and V_{max} values calculated in the presence of inhibitors; K_i is the inhibition constant with respect to binding to the free enzyme; and K_i' is the inhibition constant for binding to the enzyme-substrate complex. In types 1 and 3 mixed inhibition, both V_{max} and K_M are altered in the presence of an inhibitor.[212] $V_{max}{}^{app}$ is altered by the value of K_i', which depending on the value, can decrease $V_{max}{}^{app}$. This is portrayed in the following equation.

$$V_{max}{}^{app} = \frac{V_{max}}{\left(1 + \frac{[I]}{K_i'}\right)}$$

(8)

$K_M{}^{app}$ is influenced by the ratio of K_i and K_i' inhibition constants. If the inhibition constant for [E] is larger than the inhibition constant for [ES], then ($K_i' > K_i$), $K_M{}^{app} < K_M$, and [I] has a stronger affinity for [E]. If $K_i' < K_i$, then $K_M{}^{app} > K_M$ and [I] has a stronger affinity for [ES]. This phenomenon is illustrated in the following equation:

$$K_M{}^{app} = \frac{K_M \times \left(1 + \frac{[I]}{K_i}\right)}{\left(1 + \frac{[I]}{K_i'}\right)}$$

(9)

Combining the changes to $V_{max}{}^{app}$ and $K_M{}^{app}$ in the presence of an inhibitor from **equations 8** and **9** into **equation 7** algebraically, a final equation representing all types of mixed inhibition is attained:

$$v = \frac{V_{max} \times [S]}{\left(\left(K_M \times \left(1 + \frac{[I]}{K_i}\right)\right) + \left([S] \times \left(1 + \frac{[I]}{K_i'}\right)\right)\right)}$$

(10)

2.7.2 Uncompetitive inhibition

In some cases, the nonlinear regression best fit an uncompetitive mode of inhibition (see results **chapter 4**), despite being visually declared as mixed inhibition by linear regression analysis. **Equation 7** can be used to analyse an uncompetitive inhibitor. In typical uncompetitive inhibition, the inhibitor exclusively binds to [ES]. As a result, $V_{max}{}^{app}$ and $K_M{}^{app}$ are both influenced by K_i', displayed in the following equations:

$$K_M{}^{app} = \frac{K_M}{\left(\frac{1 + [I]}{K_i{}'}\right)} \quad (11)$$

$$V_{max}{}^{app} = \frac{V_{max}}{\left(\frac{1 + [I]}{K_i{}'}\right)} \quad (12)$$

The modifications to $V_{max}{}^{app}$ and $K_M{}^{app}$ in the presence of an inhibitor from **equations 11** and **12** can be substituted into **equation 7** for a final equation representing uncompetitive inhibition:

$$v = \frac{V_{max} \times [S]}{\left(K_M + \left([S]\left(\frac{1 + [I]}{K_i{}'}\right)\right)\right)} \quad (13)$$

2.7.3 Competitive inhibition

In some cases, the nonlinear regression best fit a competitive mode of inhibition, despite being visually declared as mixed inhibition by linear regression analysis. As **equation 7** is a modified Michaelis-Menten equation (derived from **equation 2**), it can be used to analyse a competitive inhibitor. In competitive inhibition, the inhibitor exclusively binds to [E], and inhibition can be overcome when high concentrations of the substrate are added. As a result, $V_{max}{}^{app} = V_{max}$ and only $K_M{}^{app}$ is influenced by K_i, see the following equation:

$$K_M{}^{app} = K_M \times \left(1 + \frac{[I]}{K_i}\right) \quad (14)$$

In this type of inhibition, $K_M{}^{app} > K_M$, which reduces the enzyme's catalytic efficiency. **Equation 14** can be substituted into **equation 7** for a final equation representing competitive inhibition:

$$v = \frac{V_{max} \times [S]}{\left(K_M\left(\frac{1 + [I]}{K_i}\right) + [S]\right)} \quad (15)$$

From **equations 6, 10, 13** and **15**, $V_{max}{}^{app}$, $K_M{}^{app}$, K_i, and K_i', were all calculated for individual concentrations of inhibitor added for both MS and ICL. K_i and K_i' values common to all the concentrations were calculated using GraphPad Prism version 7.04. These calculated

constants, along with visual analysis of Lineweaver-Burk plots, were taken into consideration when identifying the mode of inhibition of hit compounds.

2.8 Isothermal titration calorimetry

Isothermal titration calorimetry (ITC) was performed on both MS and ICL to validate the hit compounds and to establish the thermodynamics of binding. Protein samples were dialysed (2 × 1 L) in a D-tube dialyzer (Merck) for three hours in dialysis buffer (25 mM Tris-HCl, 100 mM NaCl, and 0.1 mM TCEP). Adjustments to the concentrations were made using the same dialysis buffer before sample loading. Samples were degassed and loaded under a vacuum pump. MS (110 μM) or ICL (202 μM) were titrated into the calorimeter cell containing 11 μM of the hit compound using a VP-ITC (Malvern Panalytical) at 25°C with 200 rpm stirring. The syringe and the cell both contained a final concentration of 0.1% DMSO.

The injection parameters for MS were set with a reference power of 15 μcal sec^{-1}, an initial injection of 3 μL over 3.6 seconds, and subsequent injections of 10 μL throughout 12 seconds. Injections were spaced by 150 seconds with a filter period of two seconds. The injection parameters for ICL were set with a reference power of 15 μcal sec^{-1}, an initial injection of 3 μL over 3.6 seconds, followed by subsequent injections of 8 μL over 10 seconds. Injections were spaced by 170 seconds with a filter period of two seconds. Data were analysed first in NITPIC[213] for baseline calculations and then fit for thermodynamic parameters using the OneSite model in Origin 7.0 software. The parameters were analysed using the following equations.[214]

$$\boldsymbol{\Delta G = \Delta H - T\Delta S} \tag{16}$$

Where ΔG is the total free binding energy. ΔH is the measure of the energy of bonds broken and created, known as enthalpy. T is the temperature in Kelvin, and ΔS is the entropic term of binding, which is driven by hydrophobic interactions. Favourable or spontaneous interactions include a $\Delta H < 0$ and a $\Delta S > 0$. Because of the way the free energy of the system is defined, if both the enthalpic and entropic terms favour a reaction, then $\Delta G < 0$. Free binding energy can also be defined by:

$$\boldsymbol{\Delta G = -RT \ln K_a} \tag{17}$$

In which R is the gas constant; T is the absolute temperature; K_a is the equilibrium association constant. Other parameters derived from the ITC binding isotherm include the equilibrium dissociation constant, K_d, and the stoichiometry between protein and ligand, n, which

indicates how many binding sites are in the protein. In order to confirm the accuracy of *n*, I used the following equation:

$$\boldsymbol{n = st \times \frac{AF_{cell}}{AF_{syringe}}} \quad \textbf{(18)}$$

Where *n* is the value of stoichiometry of the interacting species; *st* is the stoichiometry and indicates the number of binding sites on the protein; AF_{cell} is the active fraction of contents in the main cell, denoted as [active cell content]/ [total cell content]; $AF_{syringe}$ is the active fraction of content in the syringe, denoted as [active syringe content]/ [total syringe content]. When concentrations of the cell and syringe are 100% accurate and contain 100% active species, *n* and *st* will be the same.

2.9 Fluorimetry

Fluorescence spectra were recorded on a PerkinElmer LS55 luminescence spectrometer using an optical cuvette with a 1 cm path length. Mg^{2+}-depleted MS was added to a buffer composed of 50 mM Tris-HCl, pH 7.5 and 100 mM NaCl, giving a final MS concentration of 0.88 μM. $MgCl_2$, glyoxylate, and acetyl coenzyme A were added to give the final concentrations (indicated in results **chapter 3**). The mixtures were equilibrated at 25°C using a water bath for two minutes before measurements were taken. An excitation wavelength of 295 nm was used for measuring intrinsic tryptophan fluorescence, and the emission spectra were recorded between 300 and 400 nm. The excitation and emission slit widths were 2.5 nm each.

Quenching experiments were performed as described above with the addition of increasing the concentrations of neutral quencher, acrylamide. The data presented are the mean of three independent repeats and were analysed using the Stern Volmer equation.[215]

$$\boldsymbol{\frac{I}{I_0} = (1 + K_{sv}[Q])(1 + K_a[Q])} \quad \textbf{(19)}$$

Where I_0 is the intensity or rate of fluorescence without a quencher; *I* is the intensity or rate of fluorescence with a quencher; *[Q]* is the concentration of quencher added; K_a is the association constant; K_{sv} is the Stern Volmer constant, derived from the slope of the plot of [Q] *versus* I/I_0. Mg^{2+} titrations were performed as described above, and data were fit to hyperbolic binding curves using GraphPad Prism version 7.04. The data presented are the mean of three independent repeats and were analysed using the Scatchard equation.[216]

$$\frac{r}{[L]_{free}} = nK_a - rK_a \quad \textbf{(20)}$$

Where r is the concentration of bound ligand to total available binding sites; $[L]_{free}$ is the concentration of unbound ligand; n is the number of binding sites in the protein. K_a is the association constant derived from the concentrations of the ligand-protein binding complex per the individual concentrations of ligand and protein.

2.10 Protein crystallisation

Crystallisation conditions for purified proteins were screened in high-throughput industry screening plates using sitting drop vapour diffusion. A sparse matrix approach was used on both MS and ICL in initial crystallisation trials, see **table 6**. First, 2-drop 96-well industry screening plates were thawed, and 200 nL of purified protein and either 200 nL or 100 nL of reservoir solution were deposited per drop using a Mosquito crystal liquid handling robot (TTP Labtech).

Table 6. Sparse matrix industry screens used in protein crystallisation.

Supplier	Screening plate	Protein screened
Qiagen	$AmSO_4$ Suite	MS
Qiagen	Classics Suite	MS
Molecular Dimensions	JCSG+	MS & ICL
Molecular Dimensions	MIDAS	MS
Molecular Dimensions	PACT *premier* Suite	MS & ICL
Qiagen	PEGS Suite I	MS & ICL
Qiagen	PEGS Suite II	MS & ICL
Qiagen	PH Clear I	MS
Molecular Dimensions	Wizard I & II	MS
Molecular Dimensions	Wizard III & IV	MS

Abbreviations: $AmSO_4$, ammonium sulphate; JCSG, Joint Centre for Structural Genomics; ICL, isocitrate lyase; MS, malate synthase G; PACT, pH-, anion- and cation-testing; PEGS, polyethylene glycol.

Crystallisation optimisations were performed using fine-grid matrices, which were created by designing concentration gradients of the precipitating agents in the original crystallisation condition. Stock solutions of precipitants and salts were prepared using high-purity chemicals (Sigma) and water produced by a Milli-Q system (Millipore) and were then syringe-filtered through 0.22 μm filters (BioRad). These solutions were deposited into the wells (80 μL) of Polystyrene MRC 2-drop 96-well plates (Molecular Dimensions) using a Dragonfly crystal liquid handler (TTP Labtech). Then, the protein samples were deposited by Mosquito, as mentioned above. All plates

were carefully sealed using clear packing tape and a roller and were placed into a Rock Imager 1000 automated imaging and hotel system (Formulatrix) to equilibrate at 19°C. Images were checked daily using the protein crystallisation software Rock Maker Web (Formulatrix). Plates were discarded after three weeks if no crystals were observed.

For drops which contained good quality single crystals with the largest dimension of >100 μm in length, the sealed tape over the drop of interest was opened using a scalpel and removed using tweezers. The crystals in the drop were quickly treated with 0.5 μL of a cryoprotectant solution [24% (v/v) ethylene glycol and 76% (v/v) mother liquor], gingerly mounted in nylon loops of the corresponding crystal size to minimise the formation of ice crystals and thermal damage to the crystals, and flash-frozen in liquid nitrogen prior to data collection.

2.10.1 Crystallisation of native malate synthase G

A sparse matrix screening approach was used on native MS, and the best crystals were obtained after 3-6 days with a 1:1 mixture of ≥11 mg mL^{-1} purified protein and reservoir solution. The optimised condition (JCSG+ screen, well D9) contained concentration gradients of 0−25 mM ammonium sulphate, 13−17% (v/v) glycerol, and 20−27% (w/ v) PEG 4000 that resulted in several single crystals suitable for harvesting.

2.10.2 Soaking malate synthase G

Soaking experiments were undertaken on MS crystallised as detailed in the previous section. A stock concentration of hit compounds in DMSO was diluted in the cryoprotectant solution, and 0.5 μL of this mixture was added directly to the drop, giving a final concentration of 1 mM SB002 in 6.25% DMSO. Depending on the soaking times, drops were quickly sealed to prevent crystal dehydration, or crystals were mounted directly into nylon loops.

2.10.3 Co-crystallisation of malate synthase G and SB002

Co-crystallisation was first attempted with the optimised native MS condition detailed previously. Additional sparse matrix screens were attempted with industry plates using sitting drop vapour diffusion with 75 μM or 146 μM purified protein. MS was pre-incubated for ≥60 minutes on ice with different concentrations of SB002 and other additives like $MgCl_2$ or glyoxylate. The mixture was then centrifuged at 11,363×*g* for 5 minutes at 4°C to sediment possible protein aggregates or ligand precipitation before setting up the crystallisation plates. Images of drops were monitored daily for signs of precipitation, crystalline nucleation or crystal growth.

2.10.4 Co-crystallisation of isocitrate lyase and SB002

A sparse matrix screening approach was attempted using sitting drop vapour diffusion with 340 μM or 170 μM of purified ICL. The protein was incubated with different concentrations

of SB002 as well as product glyoxylate for ≥60 minutes on ice and then centrifuged at 11,363×*g* for 5 minutes at 4°C to sediment possible protein aggregates or ligand precipitation. The crystallisation mixture from the reservoir (200 nL) was added to the 200 nL of protein in the drop in the crystallisation plates. Images of drops were monitored daily for signs of nucleation, precipitant, crystals and crystalline growth.

2.11 X-ray diffraction, structure determination, and refinement

All diffraction data were collected remotely on the MX-I03, I04, and I04-1, beamlines at the Diamond Light Source Synchrotron (DLS, Didcot, UK) equipped with multi-axis goniometers and P3-6M, Eiger2 × 16M, and P6M-F detectors, respectively. Diffraction data were processed using Xia3 DIALS,[217] and data statistics were examined for quality. Structures were determined by molecular replacement using CCP4's Phaser.[218] I used an apo MS structure from *Mycobacterium tuberculosis* (PDB entry 1N8I) as a model for phasing native *Pseudomonas aeruginosa* MS, and then later I used my model (PDB entry 5AOS) of native MS as a template for molecular replacement with MS-ligand complexes. I used the apo ICL structure from *Pseudomonas aeruginosa* (PDB entry 6G1O) as a template for co-crystallised ICL.[174] Automated refinement was performed using PHENIX.refine or CCP4's Refmac.[219] Iterative runs of manual modelling and refinement were performed in COOT.[220]

2.12 Computational analysis of malate synthase G

All computational analyses of the native MS crystal structure were completed by Prashanthi Medarametla, an early stage researcher in the Marie Skłodowska Curie Actions project consortium, from the University of Eastern Finland in Kuopio, Finland. The Schrödinger suite (Schrödinger LLC, New York, NY) was used for all computations. Protein Preparation Wizard with default parameters was used to prepare the MS structure for downstream *in silico* analyses.[221]

2.12.1 Analysis of potential drug binding sites

SiteMap was used to predict putative binding pockets in MS. SiteMap's algorithm predicts binding pockets in proteins based on the geometry, size, volume, and the hydrophilicity/hydrophobicity character of amino acid residues.[222] SiteMap predicts druggable pockets and ranks them using two parameters: the SiteScore and the druggability, or "Dscore." SiteScores reveal the highly promising binding sites in the protein that can potentially be targeted

with drug-like molecules, and the Dscores indicate the druggability of the predicted site. SiteMap was run using a fine grid option with a more restrictive definition of hydrophobicity to exclude solvent-exposed regions during binding site prediction.

2.12.2 Analysis of hydration sites

The solvation network available to a protein plays an essential role in the protein to ligand binding affinity. It is useful to understand the effects of the solvation network when designing or conducting virtual screens of potential inhibitors. Theoretical hydration sites and associated thermodynamic properties were predicted using the WaterMap module.[223] WaterMap predicts probable hydration sites and their properties in user-defined regions based on molecular dynamics. WaterMap was run using default parameters to understand the druggability of MS through its solvation network.

2.13 Mammalian cell lines

Mammalian cell lines used in this work were obtained from the American Type Culture Collection (ATTC) and are displayed in **table 7**. Cell lines were stored in liquid nitrogen in cryovials containing growth medium and 5% (v/v) DMSO. Cell lines were subcultured from frozen stocks and passaged for 2-3 weeks prior to performing cytotoxicity assays. All media was stored at 4°C for no longer than three weeks.

Table 7. List of mammalian cell lines used in this work.

Cell line	Description	Source
A-375	*Homo sapiens* skin epithelia; malignant melanoma cells	ATTC CRL-1619
A549	*Homo sapiens* lung epithelia; carcinoma cells	ATCC CCL-185
BALB/c 3T3 Clone A31	*Mus musculus,* embryo fibroblast; normal cells	ATTC CCL-163
Hs27	*Homo sapiens* foreskin fibroblast; normal cells	ATTC CRL-1634
U937	*Homo sapiens* lymphocyte; histiocytic lymphoma cells	ATTC CRL-1593.2

Five mammalian cell lines were used to assess cytotoxicity. A-375 was selected because it is robust.[224] Hs27 was selected as a representative for normal human cells. BALB/c 3T3 Clone A31 (BALB/c) mouse cells were selected as a representation of the potential viability of future *in vivo* work. A549 was selected as a representative of the prospective clinical applications of this work regarding clinical *P. aeruginosa* lung infections. U937 was selected as the only suspension cell line.

2.14 Mammalian cell culture maintenance

All mammalian cells were grown from frozen stocks by quickly thawing in a 37°C water bath, and then transferring into a 15 mL centrifugation tube (Falcon) containing 10 mL of pre-warmed growth medium. The cells were centrifuged at 125×*g* for 7 minutes. The supernatant was discarded, cells were resuspended with 1 mL of pre-warmed medium and then were transferred into 25 cm^2 culture flasks (Greiner) containing 5 mL of pre-warmed media. The flasks were kept in an incubator (Thermo Fisher Scientific) at 37°C, 5% CO_2, 95% humidity.

Table 8. Media used in mammalian cell culturing and cytotoxicity assays.

Media	Components per litre
Growth medium for A-375, A549, and Hs27 cells	900 mL Glutamax DMEM, high glucose (Gibco) 100 mL FBS (Gibco)
Growth medium for BALB/c 3T3 Clone A31 cells	900 mL Glutamax DMEM, high glucose (Gibco) 50 mL NBCS (Gibco) 50 mL FBS (Gibco)
Growth medium for U937 cells	980 mL RPMI1640 (2 mM Glutamine) (Sigma) 20 mL FBS, heat inactivated (Sigma) 10 mL of 10,000 units penicillin and 10 mg streptomycin mL^{-1}
Assay medium for A-375 and Hs27 cells	950 mL Glutamax DMEM, high glucose (Gibco) 50 mL FBS (Gibco)
Assay medium for A549 cells	900 mL DMEM, phenol red-free (Thermo Fisher) 100 mL FBS, heat-inactivated (Sigma)
Assay medium for BALB/c 3T3 Clone A31 cells	950 mL Glutamax DMEM, high glucose (Gibco) 25 mL NBCS (Gibco) 25 mL FBS (Gibco)
Assay medium for U937 cells	980 mL RPMI-1640, phenol red-free (Sigma) 20 mL FBS, heat inactivated (Sigma)

2.14.1 Subculturing adherent cell lines

Before subculturing, the flasks were viewed under a light microscope (100x magnification) to assess the degree of confluence and to confirm the absence of microbial or other cell line contaminants. When the cells were 70-90% confluent, the old medium was discarded by suction with a vacuum pump, and the cell monolayer was washed with 10 mL of sterile 1x PBS. 1x TrypLE trypsin with no phenol red (Gibco) (1 mL) was added to the washed monolayer, and the flask was

manually tilted to ensure the monolayer was covered with trypsin. The flask was incubated for 5 minutes at 25°C until the cells were visibly detached under the microscope from the bottom of the flask.

Growth medium pre-warmed at 37°C in a water bath was added (10 mL), and any clumps of cells were dispersed by gently pipetting. The cells were transferred to a 15 mL centrifugation tube (Falcon) and centrifuged at 125×*g* for 7 minutes. The supernatant was discarded, and the cells were rewashed with pre-warmed media before being transferred into a 75 cm^2 cell culture flask (Greiner) containing 20 mL of pre-warmed medium. The culture to fresh media ratios were 1:8, 1:4, 1:10, and 1:8 for A-375, Hs27, A549, and BALB/c 3T3 Clone 31A, respectively. The cell lines were subcultured every 2-4 days, depending on the degree of confluency, or the number of adherent cells in the flask.

2.14.2 Subculturing suspension cell lines

Before subculturing U937 culture, the flasks were viewed under a light microscope (100x magnification) to visualise the number of live cells and confirm the absence of microbial or other cell line contaminants. A 1:1 mixture of 10 μL of the cell suspension and 10 μL of Trypan blue solution (Sigma) was placed into the chamber of a single use haemocytometer. Cells were counted in each of the counting grids (0.10 μL) in the four corners of the haemocytometer under a microscope at 100x magnification. Cells were considered dead if they were dyed blue by the Trypan solution.[224] The number of cells per μL was calculated as:

$$\boldsymbol{cells\ \mu L^{-1} = \frac{Sum\ of\ 4\ squares}{4} \times 2 \times 10} \quad \textbf{(21)}$$

Where the average of cells counted is obtained and then multiplied by two because of the dilution with Trypan blue and then multiplied by a factor of 10 to obtain units in μL. The suspension culture was diluted by 20 mL of fresh, pre-warmed growth medium. Typically, a 1:40 dilution was suitable for a weekly subculture, and a 1:4 dilution was suitable for use in an assay later in the week.

2.15 Determining cytotoxicity using luminescence

The CellTiter-Glo® Luminescent Cell Viability Assay (Promega; Lot# 0000200446) was performed as a homogeneous method of determining the number of viable cells in a culture based on quantifying the amount of ATP present, which signals the presence of metabolically active cells. The A-375, Hs27, and BALB/c 3T3 Clone A31 cells lines were used to assess the cytotoxicity of

hit compounds using a luminescence-based assay. The measurement of ATP present is based on the luciferase reaction.

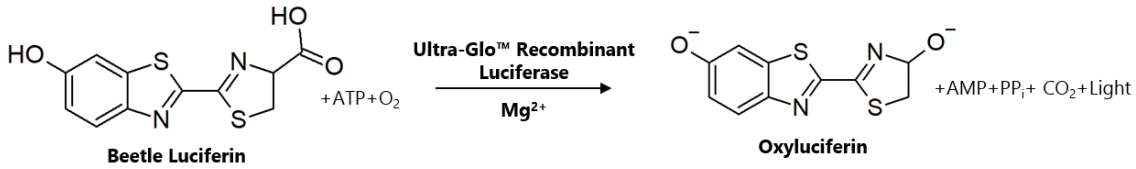

Figure 4. The luciferase reaction. The oxygenation of Beetle luciferin is catalysed by luciferase in the presence of magnesium, ATP, and molecular oxygen to form oxyluciferin, carbon dioxide, AMP, and light.

2.15.1 Seeding into microtitre plates

Cells were harvested from 75 cm^2 culture flasks according to the adherent cell subculturing protocol detailed in **section 2.14.1** and were counted before they were seeded into sterile, white-framed 96-well plates with clear bottomed wells (PerkinElmer). Briefly, a mixture of 50 µL of sample cells and 50 µL of Trypan blue was prepared in an Eppendorf tube. 10 µL of the sample was placed into each of the two chambers of a single-use haemocytometer, and the number of live cells was determined with Countless II automated cell counter (Thermo Fisher Scientific).

After counting, the cells were diluted with fresh growth medium to the appropriate density for each cell line. A-375 cells were seeded at a density of 10,000 cells $well^{-1}$, and Hs27 and BALB/c 3T3 Clone A31 were added at a density of 7,500 cells $well^{-1}$ in 100 µL of growth media per well. The last column in the microplate was filled with growth medium instead of cells as a control. Cell culture plates were incubated for 20-24 hours at 37°C, 5% CO_2, 95% humidity. Plates were checked before performing the assay for a consistent, confluent monolayer in the wells.

2.15.2 Luminescence-based cell viability assay

The growth medium was removed from the assay plates by turning the plate upside down and firmly tapping the plate into a waste reservoir. Cells were washed with assay medium twice before 200x stock solutions of test compounds and controls (diluted in assay medium) were added in triplicate to the assay plate. Controls included 0.5% DMSO and positive controls; *e.g.* Camptothecin for A-375 and Hs27, and Polymyxin B for BALB/c 3T3 Clone A31. Camptothecin induces apoptosis by inhibiting DNA topoisomerase I and preventing DNA re-ligation.[208] Polymyxin B is a polycationic antibiotic which interacts with lipopolysaccharide, an anionic molecule, in cell membranes, which results in membrane permeability and cell leakage.[225] Plates were incubated at 37°C, 5% CO_2, 95% humidity for 48 hours.

The CellTiter-Glo® substrate (Promega) was thawed and added to the CellTiter-Glo® reagent (Promega). Cells were washed with 100 µL of 1x PBS twice. Both 50 µL of assay media and 50 µL of the CellTiter-Glo® mixture were added into each well. The contents were mixed for two minutes on a plate shaker at 25°C, and then the plate was incubated for 10 minutes at 25°C to stabilise the luminescent signal. Air bubbles in the wells were popped using a sterile needle to prevent interference with the absorbance signal. The luminescence was measured using a VarioSkan LUX multimode microplate reader (Thermo Fisher Scientific), and the percentage of cytotoxicity of each sample was calculated relative to controls.

2.16 Determining cytotoxicity using colourimetry

The CytoTox 96® Non-Radioactive Cytotoxicity Assay (Promega) is a colourimetric-based cytotoxicity assay that was used to determine the total number of cells affected by necrosis after exposure to test compounds. Cell lines A549 and U937 were assessed for cytotoxicity using the colourimetric assay. Lactate dehydrogenase (LDH) is a stable cytosolic enzyme that is released upon cell lysis. Released LDH in culture supernatants was measured with a coupled enzymatic assay, which results in the conversion of a tetrazolium salt into a red formazan product that can be detected at 492 nm, see **figure 5**.

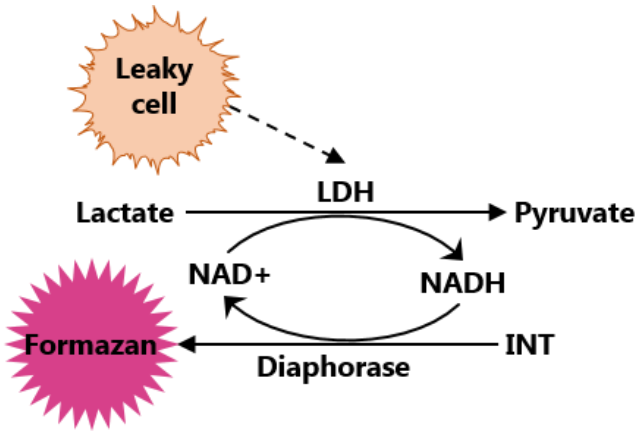

Figure 5. The LDH reaction. The release of lactate dehydrogenase (LDH) from damaged cells is proportional to the quantity of red formazan measured at absorbance 412 nm. Formazan is created by supplying lactate, NAD+ and INT dye as substrates in the presence of lactate dehydrogenase and diaphorase.

2.16.1 Preparation of an A549 cell monolayer

A549 cells were detached from a culture flask according to the adherent cell subculturing protocol, as outlined in **section 2.14.1**. A sample of the cell suspension was mixed with 4% Trypan blue solution (1:1 ratio) and counted via a haemocytometer under the microscope at 100x

magnification. The cell suspension was diluted to 5×10^5 cells mL^{-1} with fresh, pre-warmed growth medium, and 100 μL of the cell suspension was dispensed into each well of a clear, 96-well flat-bottomed sterile plate (Thermo Fisher) to yield 50,000 cells $well^{-1}$. The plates were incubated at 37°C, 5% CO_2 overnight.

2.16.2 Preparation of a U937 cell suspension

A sample of U937 cells was counted via a haemocytometer as described above, and the entire contents of the flask were collected by centrifugation at 425×*g* for two minutes. The supernatant was discarded, and cells were resuspended with 5 mL of assay medium and washed twice more. The cells were then resuspended in assay medium to produce a cell suspension with a density of 5×10^5 cells mL^{-1}.

2.16.3 Lactate dehydrogenase measurement

For A549 cells, the growth medium was removed from the assay plate before adding test compounds by turning the plate upside down and firmly tapping it over a waste reservoir. The cells in the assay plate were washed twice with assay medium, and a final volume of 99.5 μL of assay medium was added to each well of the assay plate. For U937 cells, 99.5 μL of the prepared cell suspension was added to the wells of a clear, 96-well sterile U-bottomed plate (Greiner). Then, 0.5 μL of 200x stock solutions of test compounds and controls were added in triplicate to both of the assay plates. Controls included 0.5% DMSO, cells reserved for total lysis, and a media-only background. The plates were shaken for 1 minute at 100 rpm on a plate shaker and were then incubated for 4 hours at 37°C and 5% CO_2.

After 3.5 hours of incubation, CytoTox 96® 10x lysis solution was added to the wells reserved as lysis controls, which represented maximum LDH release, and the plates were left to incubate at 37°C for another 30 minutes. After, 50 μL of supernatant from each assay plate was transferred to a clear, 96-well sterile flat-bottomed plate (Thermo Fisher). Pre-thawed CytoTox 96® buffer (Promega) was added to the CytoTox 96® substrate (Promega), and 50 μL of this CytoTox 96® mixture was added into each well. The plates were incubated for 10 minutes in darkness at 25°C to allow the enzyme reaction to occur. CytoTox 96® stop buffer (50 μL) was added to stop the enzymatic reaction, and the plates were left to incubate for another 15 minutes at 25°C. Any air bubbles were popped using a sterile needle. The absorbance was measured at 492 nm using a CLARIOstar® multimode microplate reader (BMG Labtech), and the percentage of cytotoxicity of each sample was calculated from the fully lysed cells as:

$$\%\ \boldsymbol{Cytotoxicity} = \mathbf{100} \times \frac{\boldsymbol{Experimental\ LDH\ release\ (OD_{492\ nm})}}{\boldsymbol{Maximum\ LDH\ relase\ (OD_{492\ nm})}} \quad \textbf{(22)}$$

2.17 Determining CYP450 activity in liver microsomes

The metabolic stability of hit compounds was performed at Aptuit (Verona, Italy) using liver microsomes from humans and preclinical species, and evaluation of intrinsic clearance was completed using liquid chromatography-tandem mass spectrometry. Verapamil (metabolised by cytochrome P450 3A4) and dextromethorphan (metabolised by cytochrome P450 2D6) were used as positive controls and guaranteed the appropriate test system performance during the experiments. Acceptance clearance criteria for verapamil and dextromethorphan, based on Aptuit's historical data, was ≥100 and ≥10 μL minute^{-1} mg^{-1} of microsomal proteins, respectively. All compounds were dissolved in methanol to obtain 10 mM stocks.

Table 9. Commercially available liver microsomes used in this study.

Organism	Description	Source
Human	Mixed gender, 50-donor, 20 mg mL^{-1}	BioreclamationIVT (Lot# IHG)
Rat	Male Sprague-Dawley, 20 mg mL^{-1}	BD Gentest (Lot# 60614)
Mouse	Male CD-1, 20 mg mL^{-1}	Xenotech (Lot# 1610148)

2.17.1 Preparing microsomal incubations

An automated incubation procedure was performed using the RSP Freedom Evo liquid dispensing and incubation system (TECAN). Five microlitres of 50 μM test compounds or positive controls were added to 445 μL of microsomal solution (comprised of pooled and homogenised liver microsomes at 0.56 mg mL^{-1} in 50 mM potassium phosphate, pH 7.4) in 96 deep well 1 mL plates and incubated at 37°C for 5 minutes.

The enzymatic reactions were initiated by adding 50 μL of pre-warmed NADPH regenerating buffer (prepared by adding 1.7 mg of NADP, 7.8 mg of Glucose-6-phosphate, and 6 units of Glucose-6-phosphate dehydrogenase per mL of 2% sodium bicarbonate solution) per well. Reaction plates were incubated at 37°C, and 50 μL aliquots were taken from the plates and dispensed into quenching plates at 0, 3, 10, 15, 30 and 45-minute intervals to precipitate protein and quench the reactions.

Quenching plates were prepared in advance by dispensing 150 μL of acetonitrile into each well of 96-deep well 1 mL plates. Quenching plates were centrifuged at 825×*g* for 10 minutes, and 100 μL of the supernatant was added to a plate with 200 μL of internal standard (100 ng mL^{-1} Rolipram in water), which was optimal for LC-MS/MS analysis. All the incubations were carried out in duplicate.

2.17.2 LC-MS/MS analysis

Dr Mahmud Kajbaf from Aptuit performed the tandem mass spectrometry tuning method to create methods for the hit compounds' analyses. Tuning included establishing selected ion monitoring transitions that were specific to the compounds, as well as optimising the collision energy to induce fragmentation of the selected ions in the gas phase, the declustering potential, and the collision exit potential.

Measurements were performed using an API4000 Qtrap mass spectrometer (Applied Biosystems/MDS SCIEX) coupled with an HP1100 series HPLC system (Agilent Technologies) and a CTC-PAL auto-injector (CTC Analytics AG). The analytical column was a Synergi "Max-RP" reverse phase C12 with TMS endcapping (30 mm × 2 mm, 4 μm particle size) (Phenomenex, Inc.), selected for the best separation of hydrophobic compounds in neutral pH values. The column temperature was maintained at 60°C. The injected sample volume was 10 μL, and analytes were eluted at a flow rate of 800 μL min^{-1} by a linear gradient with a mobile phase, which consisted of a mixture of mobile phase A (water with 0.1% formic acid) and mobile phase B (acetonitrile with 0.1% formic acid). The gradient conditions for elution were 5% B (0.00–0.20 minutes); 5–95% B (0.20–1.00 minutes); 95% B (1.00–1.30 minutes); 95–5% B (1.30–1.31 minutes); 5% B (1.31–1.50 minutes). The mass spectrometer was operated in positive electrospray mode with an ion source temperature of 650°C. The analytes were quantified in multiple reaction-monitoring mode. The mass transitions used for positive controls and test compounds are listed in **table 10**.

Table 10. Mass spectrometry ionisation of test and control compounds.

Analyte	Precursor ion (m/z)	Product ion (m/z)	Polarity
SB002	371.0	259.0	Positive
SB023	362.2	145.1	Positive
4-chloro-2-aminopyridine	129.0	85.0	Positive
Rolipram (internal standard)	276.1	208.2	Positive
Verapamil (positive control)	455.1	165.1	Positive
Dextromethorphan (positive control)	272.1	171.1	Positive

Metabolic stability was calculated from the peak area ratio of the test and control items with the internal standard *versus* time. Peak areas were integrated using Integrator Software from Agilent. The integrated peak areas of the test and control items at selected time points were divided by the respective peak areas of the internal standard (IS), and the percentage of parent compound remaining was calculated by normalising the peak area ratio of the parent compound to that of the IS at time 0. The half-life of the compounds' metabolism was derived from the initial linear portion of the slope of the natural log of per cent parent compound remaining over time. Intrinsic clearance in liver microsomes was estimated from the following equation.[226]

$$Cl_{int} = k \times \left(\frac{V}{M}\right)$$

(23)

Where k in mL min^{-1} is the rate of depletion of the parent compound; V is the volume of the incubation in mL; M is the number of microsomal proteins in the incubation in mg mL^{-1}. The amount of protein in the incubations was also scaled relative to average liver and body masses of each species to obtain intrinsic hepatic clearance in an *in vitro* to *in vivo* correlation.

Table 11. Species-specific body and liver masses, hepatic blood flows, and scaling factors used to calculate intrinsic clearance.

	Liver microsomes species		
	Human	**Rat**	**Mouse**
Scaling factor 1[a] (g)	52.5	52.5	52.5
Average liver weight (g)	1800	11.0	1.75
Average body weight (kg)	70	0.25	0.025
Scaling factor 2[b] (g kg^{-1})	25.7	44.0	70.0
Blood flow (mL min^{-1})	20.7	85.0	95.0

[a] Aptuit's generic scaling factor for liver microsomal protein (mg) to liver (g).
[b] Scaling factor for liver mass (g) to body mass (kg) that is used to predict *in vivo* drug clearance.

Hepatic intrinsic clearance of the compounds was estimated from the following equation.

$$Cl_{h,int} = \left(\left(\left(k \times \frac{V}{M}\right) \times 1^{st}\ Scaling\ factor\right) \times 2^{nd} Scaling\ factor\right)$$

(24)

Where $Cl_{h,\ int}$ is intrinsic hepatic clearance in mg min^{-1} kg^{-1}. k (in mL min^{-1}) is the rate of depletion of the parent compound; V is the volume of the incubation in mL; M is the number of microsomal proteins in the incubation in mg mL^{-1}. The microsomes to liver and liver to body weight scaling factors are depicted in **table 11**. These scaling factors were used along with the average hepatic blood flow of each species to obtain *in vivo* correlations using the well-stirred model.[227]

$$Cl_h = \frac{(Q \times Cl_{h,int})}{(Q + Cl_{h,int})}$$

(25)

Where Cl_h is *in vivo* hepatic clearance in mL min^{-1} kg^{-1}. $Cl_{h,\ int}$ is intrinsic hepatic clearance (in mg min^{1} kg^{-1}) calculated from the previous two **equations 23** and **24**. Q is the median hepatic blood flow (in mL min^{-1}) and is species-specific, the values of which are shown in **table 11**.

2.18 Evaluation of hit compounds as CYP450 inhibitors in human liver microsomes

2.18.1 Preparing microsomal incubation

The cytochrome P450 (CYP450) inhibition was determined by measuring the reaction products of known CYP450 substrates called probes. Probe substrate solutions were prepared by diluting probe stock solutions to final indicated concentrations, see **table 12**, with buffer (100 mM Tris-HCl, pH 7.5 and 0.5 mM EDTA) and 180 μL of pooled human liver microsomes at 20 mg mL^{-1} (BioreclamationIVT).

Table 12. CYP450s, their respective substrate probes, and positive controls used in this work.

CYP450	Substrate probe	Solvent	Positive controls[a]
CYP1A2	Phenacetin	acetonitrile	Fluvoxamine
CYP2C8	Rosiglitazone	methanol	Quercetin
CYP2C9	Diclofenac	water	Sulfaphenazole
CYP2C19	S-Mephenytoin	methanol	Ticlopidine
CYP2D6	Bufuralol	water	Quinidine
CYP3A4	Atorvastatin	methanol	Ketoconazole
	Midazolam	methanol	
	Nifedipine	acetonitrile	

[a] Positive controls were all dissolved in methanol.

First, the probe substrate solutions (195 μL) were dispensed into 96-well plates with low evaporation lids (Falcon) and were pre-warmed to 37°C in a thermomixer (Hamilton). Next, 5 μL of the test compounds and positive controls were added to the plates and incubated for a further 5 minutes at 37°C. Then, 50 μL of NADPH regenerating solution (prepared by adding 1.7 mg of NADP, 7.8 mg D-Glucose-6-phosphate, and six units of Glucose-6-phosphate dehydrogenase in 1 mL of a 2% sodium bicarbonate solution) was dispensed into the incubation plates using a Microlab STAR liquid handling system (Hamilton).

CYP450 mixtures with phenacetin, rosiglitazone, mephenytoin, atorvastatin and nifedipine as probes were incubated for 10 minutes at 37°C, while those with midazolam and diclofenac were incubated for only 5 minutes at 37°C, see **table 13**. Aliquots (100 μL) from each incubation mixture and acetonitrile (200 μL) were added using the liquid handling system to a 96-deep well plate to quench the reactions. The plates were centrifuged at 3000×*g* for 10 minutes at 4°C and supernatants were automatically transferred to a new plate and further diluted in water containing 5 ng mL^{-1} Rolipram as an internal standard for LC-MS/MS analysis. All incubations were carried out in triplicate.

Table 13. Final effective concentrations of test compounds, substrate probes, and positive controls incubated with CYP450s.

CYP450	Substrate probes	Positive controls (μM)	Test compounds (μM)
CYP1A2	35 μM Phenacetin	Fluvoxamine (0, 0.01, 0.03, 0.1, 0.33, 1, 3.3, 10)	• SB002 • SB023 • 2-amino-4-chloropyridine (0, 0.1, 0.33, 1, 3.3, 10, 33, 100)
CYP2C8	3 μM Rosiglitazone	Quercetin (0, 0.01, 0.03, 0.1, 0.33, 1, 3.3, 10)	
CYP2C9	8 μM Diclofenac	Sulfaphenazole (0, 0.1, 0.33, 1, 3.3, 10, 33, 100)	
CYP2C19	50 μM S-Mephenytoin	Ticlopidine (0, 0.01, 0.03, 0.1, 0.33, 1, 3.3, 10)	
CYP2D6	5 μM Bufuralol	Quinidine (0, 0.01, 0.03, 0.1, 0.33, 1, 3.3, 10)	
CYP3A4	50 μM Atorvastatin 2.5 μM Midazolam 10 μM Nifedipine	Ketoconazole (0, 0.01, 0.03, 0.1, 0.33, 1, 3.3, 10)	

2.18.2 Substrate probe depletion by LC-MS/MS analysis

During metabolism by CYP450s, the probe substrates received a hydroxyl functional group as a first step to increase the aqueous solubility for further hepatic metabolism.[228] Therefore, the analytes detected by liquid chromatography-tandem mass spectrometry (LC-MS/MS) were the products of the CYP450 enzymatic reactions.

Table 14. List of the probe products measured in this study.

CYP450	Substrate probes	Probe product
CYP1A2	35 μM Phenacetin	paracetamol
CYP2C8	3 μM Rosiglitazone	Par-hydroxyrosiglitazone
CYP2C9	8 μM Diclofenac	4'-hydroxydiclofenac
CYP2C19	50 μM S-Mephenytoin	4-hydroxymephenytoin
CYP2D6	5 μM Bufuralol	1-hydroxybufuralol
CYP3A4	50 μM Atorvastatin 2.5 μM Midazolam 10 μM Nifedipine	o-Hydroxyatorvastatin 1'-hydroxymidazolm oxidised nifedipine

The probe products were separated by different Ultra Performance Liquid Chromatography (UPLC) methods validated by Aptuit, which depended on the probe's chemistry. **Table 15** shows the UPLC instrumentation, analytical column, and conditions for analysing probe

products from CYP2C8 and CYP3A4 reactions. **Table 16** shows the UPLC separation method and gradient profiles for CYP2C8 and CYP3A4 probe products.

Table 15. UPLC conditions for o-Hydroxyatorvastatin, 1'-hydroxymidazolm, oxidised nifedipine, and Par-hydroxyrosiglitazone.

Instrument	Waters Acquity UPLC system
Strong wash solvent	Acetonitrile/methanol/isopropanol (50:30:20)
Weak wash solvent	Water/acetonitrile (50:50)
Typical injection volume	10 μL
Flow rate	800 μL min^{-1}
Analytical column	Acquity BEH C18 (50 × 2.1 mm, 1.7 μm particle size)
Column temperature	60°C
Mobile phase A	Water with 0.1% formic acid
Mobile phase B	Acetonitrile with 0.1% formic acid

Table 16. UPLC gradient profile for o-Hydroxyatorvastatin, 1'-hydroxymidazolm, oxidised nifedipine, and Par-hydroxyrosiglitazone.

Time (min)	Flow (mL min^{-1})	Mobile phase A (%)	Mobile phase B (%)
0.00	0.8	95	5
0.20	0.8	95	5
1.50	0.8	5	95
1.75	0.8	5	95
1.80	0.8	95	5
2.00	0.8	95	5

Table 17 shows the UPLC instrumentation, analytical column, and conditions for analysing probe products for CYP1A2, CYP2C9, CYP2C19 and CYP2D6 reactions. **Table 18** shows the UPLC separation method and gradient profiles for CYP1A2, CYP2C9, CYP2C19 and CYP2D6 probe products.

Table 17. UPLC conditions for paracetamol, 4'-hydroxydiclofenac, 4-hydroxymephenytoin and 1-hydroxybufuralol.

Instrument	Waters Acquity UPLC system
Strong wash solvent	Acetonitrile/methanol/isopropanol (50:30:20)
Weak wash solvent	Water/acetonitrile (50:50)
Typical injection volume	10 μL
Flow rate	700 μL min^{-1}
Analytical column	Acquity BEH phenyl (50 × 2.1 mm, 1.7 μm particle size)
Column temperature	45°C
Mobile phase A	Water with 0.1% formic acid
Mobile phase B	Acetonitrile with 0.1% formic acid

Table 18. UPLC gradient profile for paracetamol, 4'-hydroxydiclofenac, 4-hydroxymephenytoin and 1-hydroxybufuralol.

Time (min)	Flow (mL min^{-1})	Mobile phase A (%)	Mobile phase B (%)
0.00	0.7	0	100
0.10	0.7	0	100
2.30	0.7	80	20
2.40	0.8	80	20
2.90	0.8	80	20
3.00	0.7	0	100
3.80	0.7	0	100

The tandem mass spectrometry conditions for probe analysis were the same for all CYP450 enzymes and are displayed in the following **table 19**. The mass transitions used to analyse the probe products are depicted in **table 20**.

Table 19. Mass spectrometry conditions for probe products.

Mass spectrometer	Applied Biosystems 4000QTrap
Ionisation/interface	TurboIonSpray at 650°C
Pause time	5 ms
Curtain gas setting	15
Collision gas setting	4
Ion source Gas 1	60
Ion source Gas 2	40

Rolipram was used as an internal standard (IS) to gauge the performance of the LC-MS/MS analysis. Data were processed to give triplicate mean values, and the IC_{50} values were determined using nonlinear regression analysis of the plot of percentage control activity *versus* concentration of the test compounds (**equation 5**). The percentage control activity was calculated based on a comparison between the peak area ratio of the sample and the peak area ratio of the control sample.

Table 20. Mass spectrometry ionisation of probe products.

Analyte	Precursor ion (m/z)	Product ion (m/z)	Polarity
o-Hydroxyatorvastatin	575.10	440.40	Positive
Oxidised nifedipine	345.00	284.00	Positive
1'-Hydroxymidazolam	342.10	203.00	Positive
Paracetamol	152.00	110.20	Positive
Para-hydroxyrosiglitazone	374.00	151.00	Positive
4'-Hydroxydiclofenac	312.00	150.00	Positive
4-Hydroxymephenytoin	235.01	150.20	Positive
1-Hydroxybufuralol	278.40	186.00	Positive
Rolipram (internal standard)	276.10	208.20	Positive

3. Results and discussion

Biochemical characterisation of malate synthase G

3.1 Background

Malate synthase isoform G (MS) is the second enzyme of the glyoxylate shunt and is encoded by *glcB* in *Pseudomonas aeruginosa*. MS catalyses the irreversible condensation of glyoxylate and acetyl coenzyme A into malate and coenzyme A. Glyoxylate is generated for MS by the cleavage of isocitrate in a reversible reaction catalysed by isocitrate lyase (ICL). Isocitrate is diverted into the glyoxylate shunt from the TCA cycle during bacterial growth on fatty acids, which allows for the production of gluconeogenic precursors from metabolic inputs with only a C_2 backbone.[173] The glyoxylate shunt replenishes biosynthetic intermediates, generates biomass and appears to be vital for *P. aeruginosa* to survive in infection scenarios. For example, expression levels of the enzymes are upregulated in chronic *P. aeruginosa* infections of cystic fibrosis patients.[189] ICL and MS are also vital for *P. aeruginosa* fitness in mammalian infection models. For instance, a double deletion mutant of the shunt enzymes (ΔICL ΔMS) was found to be completely avirulent in a mouse pulmonary infection model.[194] Thus, MS is an attractive target for drug discovery efforts but has never been fully characterised before in *P. aeruginosa*.

In this chapter, I investigate the structure and biochemical function of MS from *Pseudomonas aeruginosa* (MS_{Pa}). The SDS-PAGE and size exclusion chromatography (SEC) analysis of MS assesses the quality of the enzyme after purification. I will present the enzyme kinetics, the first published crystal structure of MS_{Pa}, and results from intrinsic fluorescent experiments that detail magnesium co-factor binding. Then, I will present the binding pockets in the MS_{Pa} crystal structure that are most suitable for drug development based on the druggability of the pockets, which were determined computationally from the result of a collaboration. These results will be discussed in the context of other medically relevant pathogens. Lastly, I will present results from a molecular dynamics simulation that predicts the likely physiological hydration network of the protein by calculating free energies of bound water molecules.

3.2 Protein purification

The investigation of MS_{Pa} began with the purification of the enzyme. First, the *glcB* gene was PCR-amplified from the PAO1 genome and cloned into a pGEX-6P-1 plasmid. The vector carrying *glcB* was introduced into *E. coli* BL21 to overexpress the protein. A previous laboratory member in 2015 performed this cloning. I then purified MS_{Pa} using the following workflow: the first step involved affinity chromatography, which used a glutathione sepharose column to purify the construct according to the affinity between the fusion protein's GST tag and the resin. The second step involved PreScission Protease digestion to cleave the GST tag from the N-terminus of purified MS_{Pa}. The final step was SEC, see **figure 6**, which required a 16-600 Superdex 200 preparatory grade column to separate the native protein, any uncleaved fusion protein, the cleaved GST tag, and any other impurities from the sample.

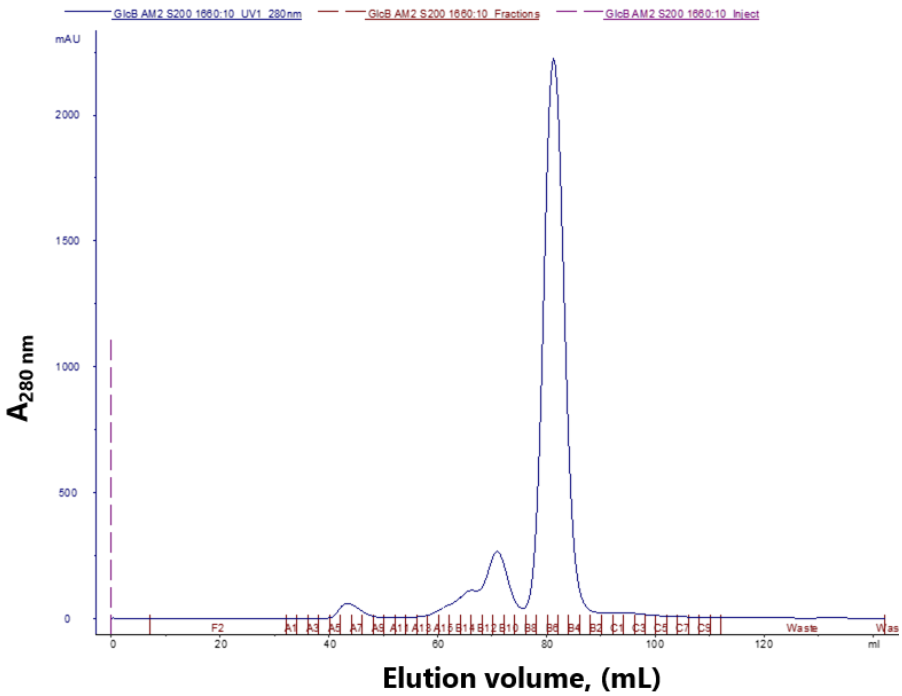

Figure 6. Size exclusion chromatogram of MS_{Pa} elution. The single large peak corresponds to purified untagged MS_{Pa}, and the smaller shoulder peak could be indicative of a dimer or larger aggregates from purification due to high loading concentration. The first small peak is most likely contaminants or degradation products.

SEC revealed a tall and narrow single elution peak measured by UV (at 280 nm), which is indicative of pure protein. The small, rounded peak that eluted first could be resulting from impurities like keratin contamination, degraded protein fragments, or DNA.[229] The second elution was a shoulder peak to the purified MS_{Pa} and could designate a dimer or larger order aggregates

from the purification due to high loading concentrations. The purity of a protein batch is important for applications like protein crystallisation,[230] so an SDS-PAGE analysis was performed to determine the protein size and purity. The SDS-PAGE gel (**figure 7**) was prepared with a protein sample after SEC. The image of the gel shows a band of purified MS_{Pa} that migrated with an apparent molecular mass between 75 and 100 kDa. This corresponds to a monomeric molecular mass of 78.66 kDa predicted from the MS_{Pa} amino acid sequence by the ExPASy ProtParam tool.[201] MS_{Pa} was successfully expressed and purified to homogeneity with adequate yields (~25 mg L^{-1}), determined from protein concentration calculations (**equation 1**).

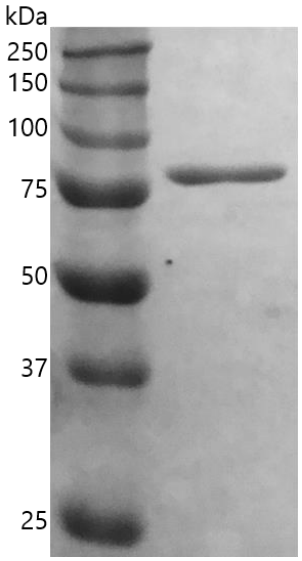

Figure 7. Coomassie blue-stained SDS-PAGE analysis after MS_{Pa} purification. This gel shows the final untagged protein after protein purification. A clear single band is visible just above 75 kDa, compared with the molecular mass ladder displayed on the left. This mass correlates with the actual predicted molecular mass of 78.66 kDa.

3.3 Amino acid sequence alignments

Amino acid sequence alignments of other pathogenic bacteria revealed that MS is remarkably well conserved among species, see **figure 8**. MS amino acid sequences sourced from the UniProt database (*Pseudomonas aeruginosa*, Q9I636; *Escherichia coli*, P37330; *Mycobacterium tuberculosis*, P9WK17; *Mycobacterium leprae*, O32913) were aligned using ClustalOmega[231,232] and were displayed with Jalview.[233]

There is a 60% amino acid sequence identity between MS_{Pa} and *E. coli* MS (MS_{Ec}), and a 70% amino acid sequence identity between MS_{Pa} and *M. tuberculosis* MS (MS_{Mt}). The amino acids identical among all four species are highlighted in purple in **figure 8**, and the known catalytic amino acid residues in MS_{Mt} and MS_{Ec} are highlighted in orange.

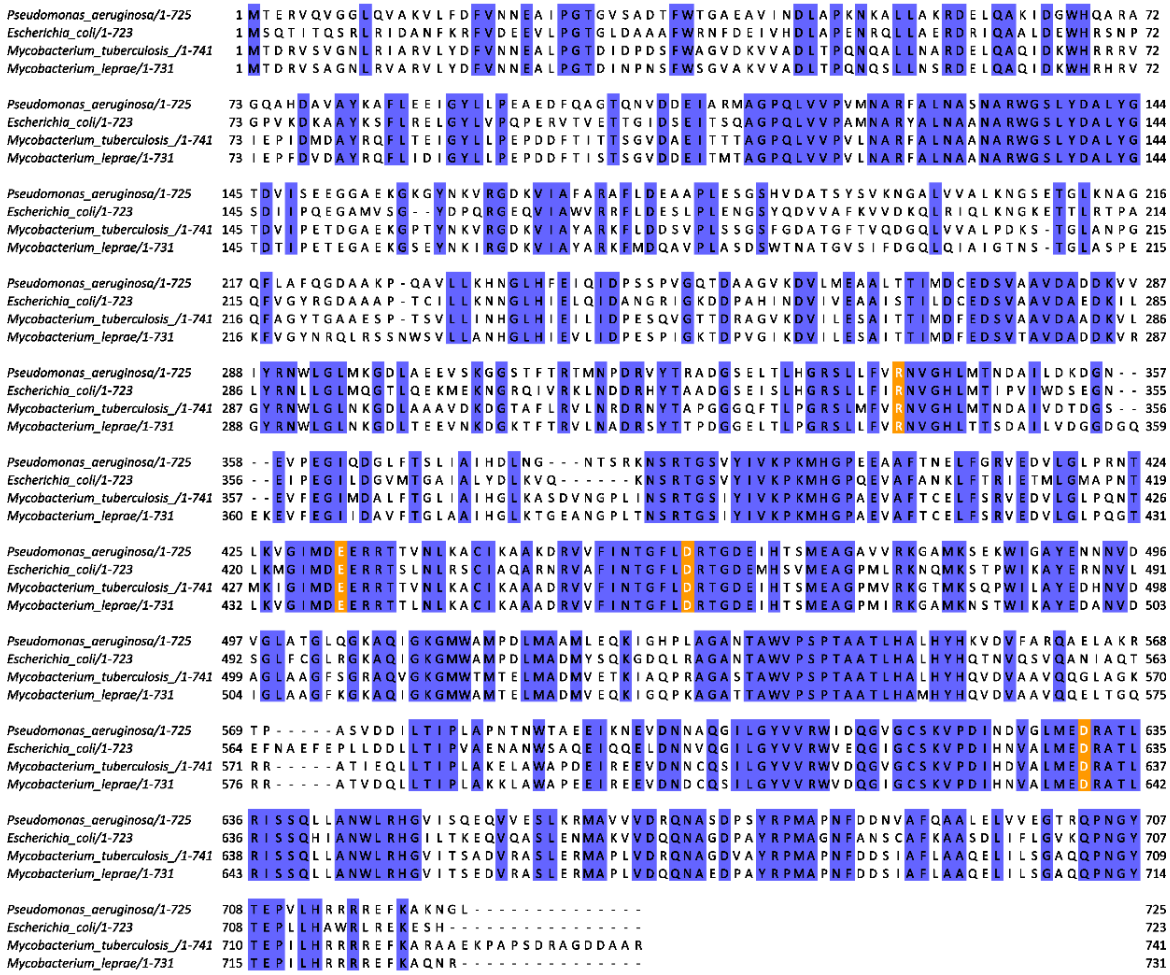

Figure 8. Amino acid sequence alignment of MS_{Pa} with MS homologues. Amino acid sequences from pathogens whose structures have been determined by X-ray crystallography were aligned with MS_{Pa}: *E. coli*, P37330 (PDB entry 1P7T); *M. tuberculosis*, P9WK17 (PDB entry 1N8I); and *M. leprae*, O32913 (PDB entry 4EX4). Amino acids are coloured by sequence identity, where regions of 100% identity are highlighted in purple. Amino acids known to be involved in catalysis in MS_{Ec} and MS_{Mt} are highlighted in orange, and these amino acids are conserved among all four organisms shown.

3.4 Kinetic analysis

Purified MS_{Pa} exhibited Michaelis−Menten kinetics, see **figure 9**. The kinetic analysis at variable concentrations of substrates revealed that the K_M values were 34 μM and 48 μM for glyoxylate and acetyl coenzyme A (AcCoA), respectively. V_{max} was determined as 2.36 μM s^{-1} for glyoxylate and 1.64 μM s^{-1} for AcCoA. Glyoxylate is the conjugate base of glycolic acid and chiefly exists as a gem-diol, which is highly reactive.[191] This means that glyoxylate will readily react with Tris buffer, forms of reactive oxygen species, and cellular metabolites at physiological pH.[191,234,235] This type of chemical reactivity, while excess glyoxylate (200 μM) was present, could account for the lower V_{max} when AcCoA was titrated.

The first order rate catalytic turnover (k_{cat}) for glyoxylate, calculated for monomeric MS_{Pa}, was 94 second^{-1}. MS is a central metabolism enzyme, and it has been suggested that these enzymes operate with increased catalytic turnover and are under strong selective pressures to perform efficiently.[236] Kinetic analysis of purified MS_{Pa} has been performed in just one study prior to this investigation, which reported a lower substrate affinity for glyoxylate (70 μM) and a higher substrate affinity for acetyl coenzyme A (12 μM) than is reported here.[196]

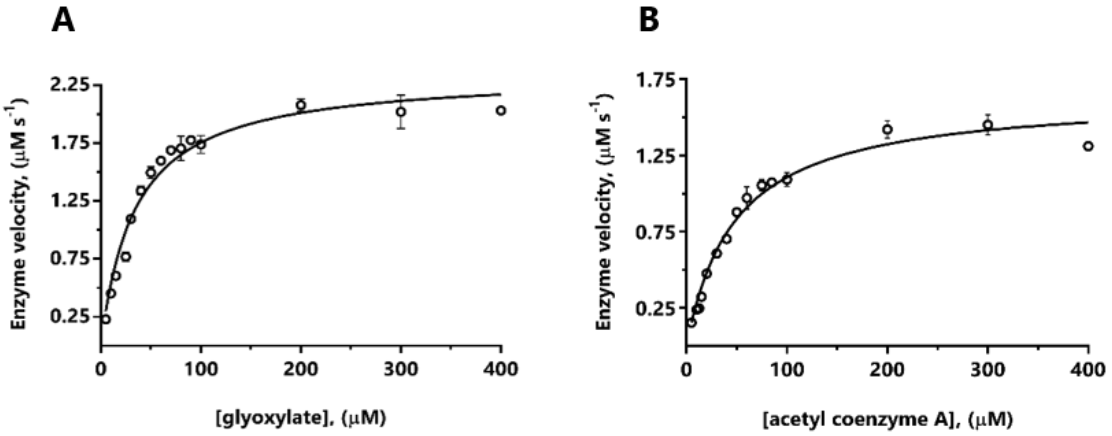

Figure 9. Kinetic analysis of MS_{Pa}. Michaelis-Menten plots of enzyme velocity measured by **(A)** fixing the concentration of acetyl coenzyme A at 0.2 mM while varying the concentration of glyoxylate as indicated; or by **(B)** fixing the concentration of glyoxylate at 0.2 mM while varying the concentration of acetyl coenzyme A as indicated.

Kinetic studies of MS from other pathogenic bacteria have been performed as well, including *M. tuberculosis*, *E. coli*, and *Corynebacterium glutamicum*. Results from these analyses were comparable to that of MS_{Pa} and are displayed in **table 21**. Additionally, the MS_{Pa} enzymatic reaction has been determined to proceed through a sequential, bi-bi mechanism in a ternary complex with both substrates binding before the reaction is catalysed, as opposed to a substituted enzyme mechanism.[196,237] This is common for enzymes with two substrates catalysing a group transfer.[238]

Table 21. Comparison of MS kinetic parameters from pathogenic bacteria.

Organism	$K_{M,\ gly}$ (μM)	$K_{M,\ AcCoA}$ (μM)	V_{max} (μmol mg^{-1} s^{-1})	k_{cat} (s^{-1})	Reference
P. aeruginosa	34	48	1200	94	This work
P. aeruginosa	70	12	990	-	[196]
M. tuberculosis	30	10	-	23	[239]
M. tuberculosis	57	30	360	-	[187]
E. coli	21	9	2160	48	[186]
C. glutamicum	30	12	-	-	[240]

Abbreviations: gly, glyoxylate; AcCoA, acetyl coenzyme A.

3.5 Crystal structure of MS

The three-dimensional structure of MS_{Pa} was determined by molecular replacement using MS_{Mt} (PDB entry 1N8I) as a template. The MS_{Pa} crystal diffracted to 1.6 Å resolution, and it crystallised with one molecule in the asymmetric unit composed of 725 amino acids. The final model is presented in **figure 10** in the apo form. The full statistics for data collection and refinement are listed in **appendix 1**. The atomic coordinates and structure factors obtained in this work are available in the PDB under the accession code 5OAS, and **appendix 1** contains a few of the validation elements from PDB submission, including the Ramachandran plot and Polygon analysis. The model was optimised with an R_{work} of 16.7% and an R_{free} of 19.6%. The Ramachandran distribution of all amino acid dihedral angles in the protein structure indicates that 98% of the amino acids are in favoured or allowed regions.

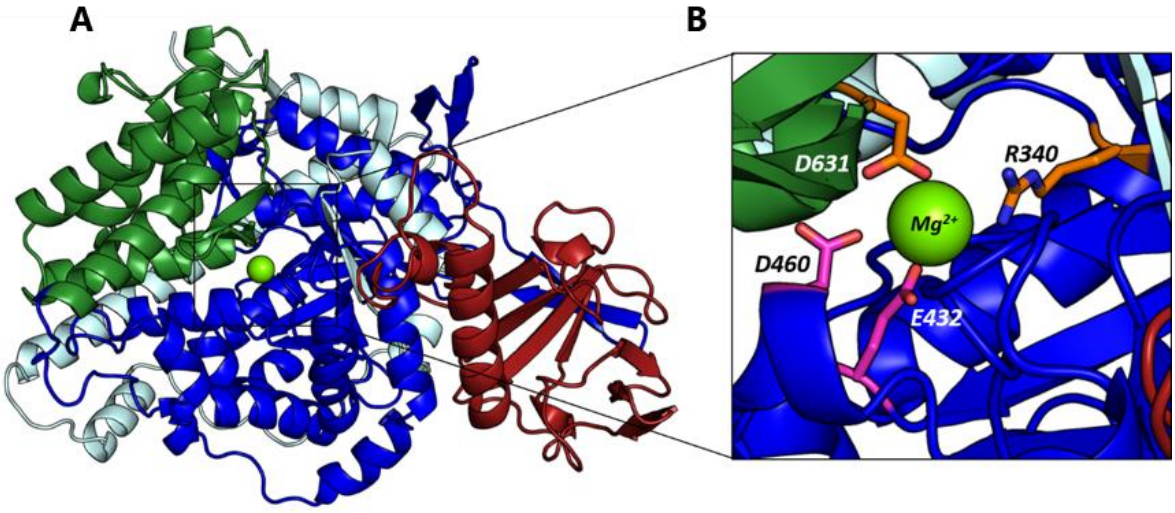

Figure 10. Cartoon representation of the MS_{Pa} crystal structure. (A) The structural domains in MS_{Pa} include a TIM barrel fold (blue), α-helical domain (green), and a β-sheet-rich domain (red). The N-terminal helices (amino acids 2−115) are coloured light cyan. **(B)** A closer look at the active site shows the proposed substrate-binding residues, Glu432 and Asp460 (magenta sticks), and the proposed catalytic residues, Asp631 and Arg340 (orange sticks). The residues involved in catalysis are oriented around the Mg^{2+} ion, which is depicted as a chartreuse sphere.

The first MS structure to be elucidated by X-ray crystallography in 2000 was from *E. coli* and contained magnesium and glyoxylate bound (PDB entry 1D8C).[185] Now, there are several structures in the PDB of MS in apo, substrate-bound, and product-bound forms from four prokaryotic species: *E. coli* (PDB entries 1P7T and 1D8C); *M. leprae* (PDB entry 4EX4), deposited in 2012; *M. marinum* (PDB entry 6AXE), deposited in 2017; and *M. tuberculosis* (PDB entries 1N8I, 1N8W, 2GQ3, 5H8P, and 5H8U), first deposited in 2003. Also, while the manuscript on which this chapter is based was in preparation, I became aware that a structure of MS_{Pa} with glyoxylate

bound had been deposited in the PDB in April 2017 (entry 5VFB). However, to the best of my knowledge, this structure has not been described in the literature.

In common with these previously reported MS structures, MS_{Pa} is composed of three domains: a TIM barrel domain with eight α-helices and eight β-strands (amino acids 116−135 and 266−589), a second α-helical domain (amino acids 590−725), and a third β-sheet-rich domain (amino acids 136−265) inserted between the first α-helix and second β-sheet of the TIM barrel domain. Near the N-terminus of the protein is a strikingly long α-helix (amino acids 32−71) that partially wraps around the TIM barrel domain (**figure 10A**). Comparison of the structure presented here with known MS structures from other organisms revealed that the protein is highly conserved across species. For example, the backbone rmsd of the superposition between the MS_{Mt} (used as the molecular replacement template; PDB entry 1N8I) and MS_{Pa} is 0.94 Å over 682 Cα atoms.

In particular, comparison of the MS_{Pa} structure with other MS structures revealed that the active site residues and the Mg^{2+} ion are highly conserved across species. The active site pocket in MS_{Mt} and MS_{Ec} sits between the TIM barrel and a loop (amino acids 615−631 in MS_{Pa}) from domain II.[185,187] Known active site residues in MS_{Mt} and MS_{Ec} are also present in the MS_{Pa} crystal structure, and they occupy the same positions (not shown). The MS_{Pa} active site, when aligned with the MS_{Mt} active site, has an rmsd of 0.20 Å. The active sites compared between the apo (PDB entry 5H8P) and a substrate-bound (PDB entry 1N8W) MS_{Mt} crystal structures are also practically identical, except for the tightening of the aforementioned loop from domain II when glyoxylate is bound. This means that MS generally does not undergo major conformational changes during catalysis. Additionally, comparison of the apo MS_{Pa} structure presented here with the glyoxylate-bound structure of MS_{Pa} recently deposited in the PDB (entry 5VFB) revealed no conformational differences except for a small shift in a solvent-exposed loop (amino acids 305−312) far from the active site.

3.6 Influence of Mg^{2+} on substrate binding

The $F_0 - F_c$ difference map for the MS_{Pa} crystal structure uncovered electron density in the active site for an Mg^{2+} ion and a molecule of ethylene glycol (referred as EDO), which was the cryoprotectant used during crystal harvesting. Mg^{2+} is reportedly essential for the enzymatic function of MS and is present in every MS crystal structure published thus far.[181,185,187,241,242] In these other structures, the Mg^{2+} is coordinated by four water molecules and conserved Glu and Asp residues in an octahedral conformation. However, in my structure, the Mg^{2+} appears to be coordinated by the EDO molecule, one water molecule, and the carboxylate side chains of Glu432, Asp460, Glu274, and Asp275, as shown in **figure 11**. These side chains are all located within 3.5

Å of the metal ion and could be interacting to decrease the overall energy. A conserved tryptophan residue, Trp539, was noticed nearby (~6 Å), which could be useful as a fluorescent reporter to monitor binding events in the active site.

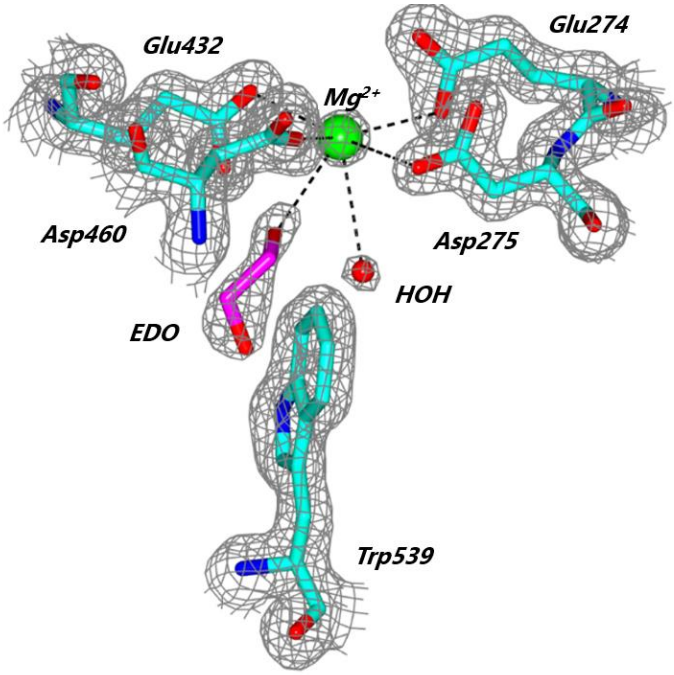

Figure 11. Mg^{2+} coordination in the MS_{Pa} crystal structure. The magnesium ion is coordinated by Glu274, Asp275, Glu432, Asp460, ethylene glycol, and a single water molecule in the active site. Trp539 is located 6.0 Å from the magnesium ion. The electron density map is contoured at 1.5σ.

I measured the intrinsic tryptophan fluorescence of MS_{Pa} to examine the effect of Mg^{2+} on substrate(s) binding and to quantify Mg^{2+} binding affinity. In order to investigate the Mg^{2+} binding properties of MS_{Pa}, any prebound Mg^{2+} from the purified protein was first removed by dialysis with 50 mM EDTA, followed by 10 mM EDTA. There was a change in relative tryptophan fluorescence intensity and λ_{max} upon the addition of Mg^{2+} and substrates to demetallised MS_{Pa}, see **figures 12A-D**. λ_{max} for demetallised MS was determined as 340 nm, which red-shifted slightly to 342 nm upon the addition of 10 mM $MgCl_2$. This red-shift indicates that the environment around the tryptophan residue(s) became hydrophilic and exposed to more solvent in the presence of Mg^{2+}. Conversely, λ_{max} blue-shifted to 337 nm after the addition of 1 mM glyoxylate (after $MgCl_2$ was added), indicating that the environment around Trp539 and other tryptophan residues became more hydrophobic and less exposed to the bulk solvent (**figure 12A**).[243] When 1 mM glyoxylate was added to demetallised MS in the absence of Mg^{2+}, there was no deviation in λ_{max} or fluorescence intensity compared with the spectrum of the demetallised protein alone, implying that Mg^{2+} is needed in the active site for glyoxylate to bind (**figure 12B**). When a saturating

concentration of AcCoA was added to demetallised MS in the absence of Mg^{2+} or glyoxylate (**figure 12C**), no change in fluorescent intensity or λ_{max} was observed; however, once $MgCl_2$ was added alongside AcCoA, λ_{max} red-shifted again similar to when $MgCl_2$ was added to demetallised MS in **figure 12A**. This means that AcCoA does not bind to MS_{Pa} before Mg^{2+} or glyoxylate.

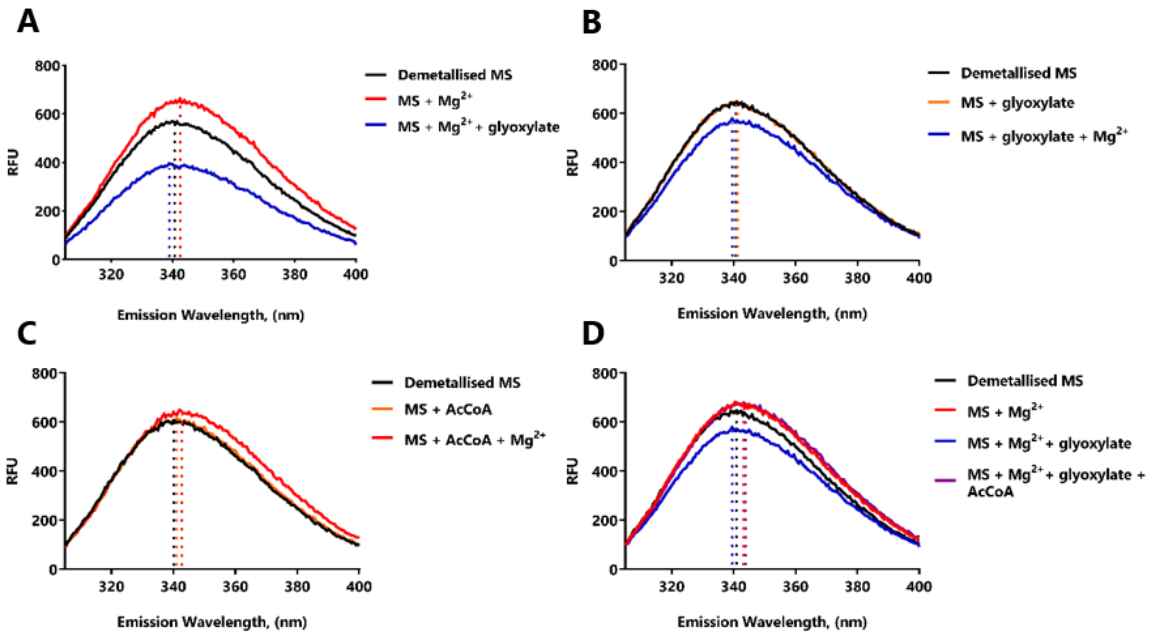

Figure 12. Intrinsic tryptophan fluorescence of demetallised MS_{Pa}. The λ_{max} for all spectra is indicated by a vertical dotted line of the corresponding colour. **(A)** Spectra of demetallised MS_{Pa} (black), demetallised MS_{Pa} with 10 mM $MgCl_2$ (red), and demetallised MS_{Pa} with 10 mM $MgCl_2$ and 1 mM glyoxylate (blue). **(B)** Spectra of demetallised MS_{Pa} (black), demetallised MS_{Pa} with 1 mM glyoxylate (orange), and demetallised MS_{Pa} with 10 mM $MgCl_2$ and 1 mM glyoxylate (blue). **(C)** Spectra of demetallised MS_{Pa} (black), demetallised MS_{Pa} with 110 µM AcCoA (orange), and demetallised MS_{Pa} with 10 mM $MgCl_2$ and 110 µM AcCoA (red). **(D)** Spectra of demetallised MS_{Pa} (black), demetallised MS_{Pa} with 10 mM $MgCl_2$ (red), demetallised MS_{Pa} with 10 mM $MgCl_2$ and 100 µM glyoxylate (blue), and demetallised MS_{Pa} with 10 mM $MgCl_2$, 100 µM glyoxylate, and 110 µM AcCoA added (violet). **Abbreviations:** AcCoA, acetyl coenzyme A; RFU, relative fluorescent units.

The order of substrate binding is further supported by **figure 12D**, which again shows λ_{max} red-shifted after the addition of Mg^{2+} and blue-shifted after the addition of Mg^{2+} and glyoxylate compared with the demetallised protein spectrum. However, when a saturating concentration of AcCoA was added after Mg^{2+} and glyoxylate, the spectrum recovered to that of the Mg^{2+}-bound spectrum. This is consistent with a sequential reaction mechanism proposed by Quartararo *et al.*,[239] in which glyoxylate binding is a prerequisite for AcCoA binding, and that Mg^{2+} remains bound in the active site upon release of the catalytic reaction products, malate and coenzyme A.

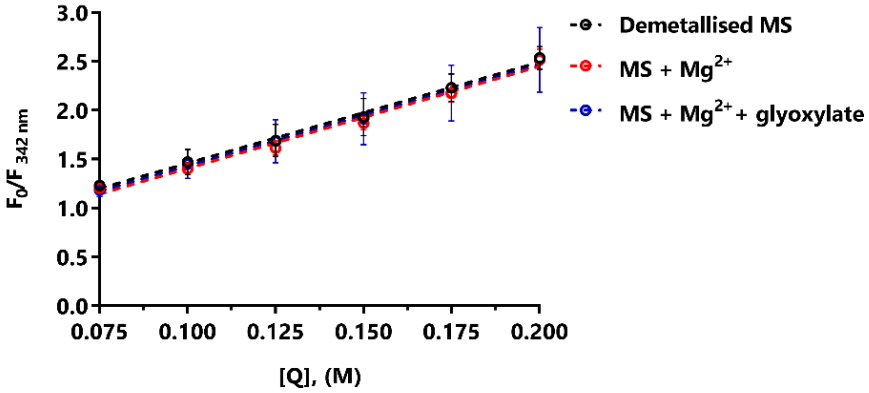

Figure 13. Stern−Volmer analysis of MS_{Pa}. No global conformational changes occur due to Mg^{2+} or glyoxylate binding to MS_{Pa} as indicated by measuring fluorescence while increasing the concentration of neutral intrinsic quenching agent, acrylamide.

Comparing the structure described here with that of the glyoxylate-bound MS_{Pa} structure (PDB entry 5VFB) reveals no apparent conformational differences between the active sites. Together with the results outlined here, this is consistent with the physical occlusion of the bulk solvent in the active site by the substrate glyoxylate. To establish whether binding of Mg^{2+} or glyoxylate to MS_{Pa} is accompanied by global conformational changes, I measured the accessibility of the tryptophan residues to an extrinsic neutral quencher, acrylamide. The presence of increasing concentrations of acrylamide caused progressively stronger quenching of tryptophan fluorescence, but the apparent dynamic quenching constant ($K_{SV} = 10.5 \pm 0.2\ M^{-1}$) was similar for Mg^{2+}-bound or glyoxylate-bound enzyme as the demetallised enzyme (**figure 13**). This indicates that the changes in tryptophan fluorescence from Mg^{2+} or glyoxylate binding arise as a consequence of changes in the local microenvironment of one or more tryptophan residues, most likely Trp539, in the active site, rather than global changes in protein conformation.

Because the tryptophan fluorescence in MS_{Pa} following the addition of Mg^{2+} was enhanced, it suggested that this spectroscopic signal might be used quantitatively to measure binding of Mg^{2+} to the enzyme. MS_{Pa} tryptophan fluorescence increased hyperbolically as the Mg^{2+} concentration increased, as is typical of a saturable binding system. In the presence of glyoxylate, the same Mg^{2+} titration also yielded a binding isotherm, except that increasing Mg^{2+} concentrations led to saturable quenching of fluorescence (**figure 14A**). Scatchard analysis of the fluorescence data from Mg^{2+} yielded apparent K_d values for the Mg^{2+}−MS_{Pa} complex of 525 and 653 μM in the absence and presence of 1 mM glyoxylate, respectively (**figure 14B**). This is comparable with the binding affinity of Mg^{2+} for other enzymes.[244]

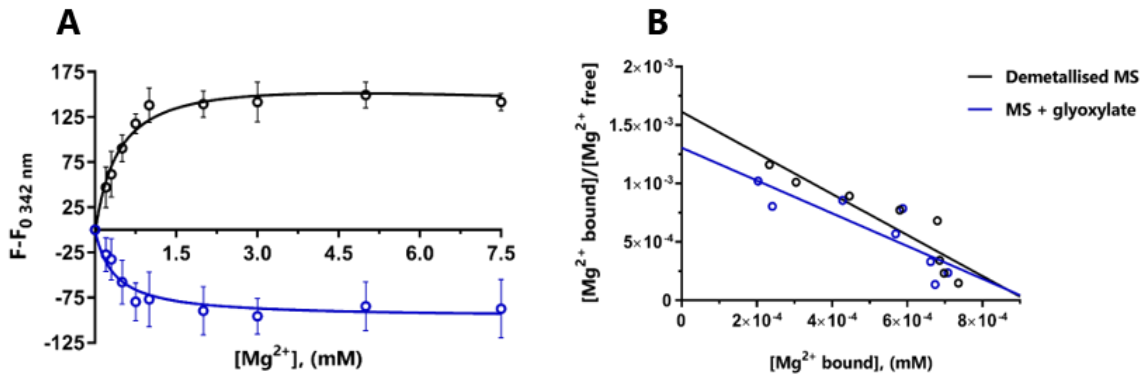

Figure 14. Magnesium binding to MS_{Pa}. (A) Mg^{2+} binding curves in the presence (blue) and absence (black) of 1 mM glyoxylate. Note that glyoxylate quenches the tryptophan fluorescence of MS_{Pa} when Mg^{2+} is added. **(B)** Scatchard analysis of Mg^{2+} binding data in the presence (blue) and absence (black) of 1 mM glyoxylate.

3.7 Identification of potential binding sites

Because *P. aeruginosa* is such a high-priority pathogen for new antibiotic discovery efforts, I collaborated with Prashanthi Medarametla and Professor Antti Poso from the University of Eastern Finland to understand the enzyme's potential as a druggable target through a computational lens. There is an important difference between the druggability of a protein and its suitability as a drug target.[245] Druggability refers to any structural features that favour interactions with drug-like small molecules, whereas useful drug targets are those that possess structural and functional features that are relevant to disease states.[246] MS_{Pa} is relevant to particular disease states, making it a suitable drug target, but I also wanted to identify any potential binding sites in MS_{Pa} that might facilitate structure-based drug design efforts. Therefore, we analysed the MS_{Pa} crystal structure using Schrödinger's SiteMap. I denoted the five top-ranking binding sites identified by SiteMap as A−E, and their SiteMap parameters are listed in **table 22**.

Table 22. Binding sites A-E in the MS_{Pa} crystal structure predicted by SiteMap.

Site	SiteScore	Size (# of site points)	Dscore	Volume (Å³)	Hydrophobic	Hydrophilic
A	1.10	123	1.16	475.01	1.60	0.72
B	0.99	188	1.02	569.03	0.58	0.95
C	0.97	163	1.02	461.24	0.59	0.89
D	0.96	110	0.97	269.12	0.50	1.06
E	0.87	80	0.87	156.53	0.79	1.04

The purpose of the SiteScore is to define and rank binding sites based on an equation that calculates druggable parameters, such as the number of site points, the enclosure score, and a hydrophilic score based on the polarity of the amino acids within the site. In a large-scale study of 538 proteins taken from the PDBbind database, SiteMap was able to correctly identify the known

binding site as the top-ranked site in 86% of cases. The SiteScore equation caps the hydrophilic variable at 1.0 to limit the impact of hydrophilicity in charged and highly polar sites when ranking the sites. The main difference between the SiteScore and the Dscore, or druggability score, is that in the Dscore equation, the hydrophilic score variable is not capped, which allows hydrophobicity to play a larger role in assessing druggability of binding sites. The Dscore should be ≥1.0 for the protein site to be considered druggable.[222]

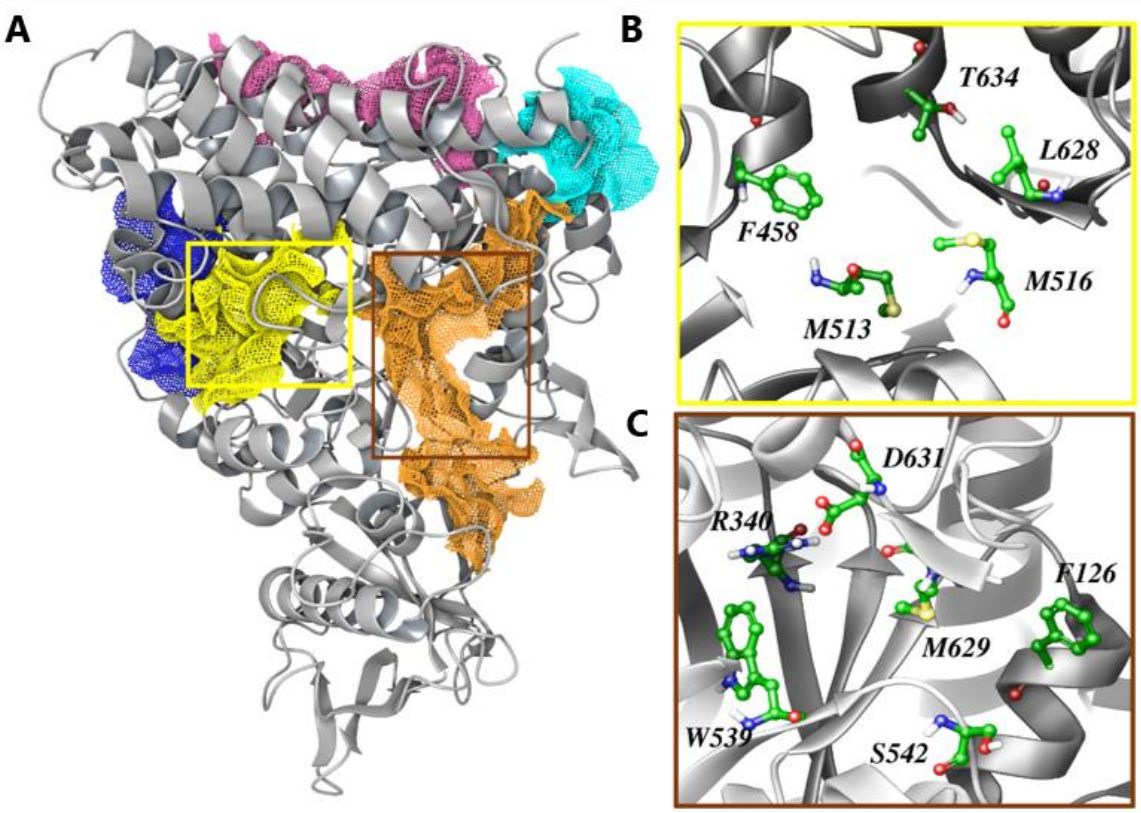

Figure 15. Predicted binding sites in MS_{Pa}. (A) Coloured mesh represents the possible binding pockets predicted by SiteMap in the MS_{Pa} structure (grey): **site A**, yellow; **site B**, orange; **site C**, magenta; **site D**, blue; **site E**, cyan. **Site A** is located between a β-hairpin (amino acids 622−628) in domain II and α-helices in the TIM barrel. **Site B** is composed of loops in the TIM barrel and domains II and III. **Site C** is located on the edge of the protein between helix α1 in the N-terminal region and the final α-helix of the protein at the C-terminus, along with a β-hairpin (amino acids 345− 350) from the TIM barrel. **Site D** is composed of a loop in the N-terminal region and α-helices in the TIM barrel. **Site E** sits near the loops of the N-terminus and C-terminus, and a flexible loop in the TIM barrel. **(B)** Site A and its hydrophobic binding site residues are shown as green sticks. **(C)** The polar and hydrophobic residues of site B are shown as green sticks. These include the Arg340 and Asp631 amino acid side chains involved in catalysis and the active site fluorophore, Trp539.

The location of each site on the MS_{Pa} crystal structure is shown in **figure 15A** as a coloured mesh (site A, yellow; site B, orange; site C, magenta; site D, blue; site E, cyan). Sites A−E all

possess a SiteScore ≥0.80, which is the minimum recommended value to distinguish between a drug binding and non-drug binding site.[222] Site A is the top-ranked potential binding site with a SiteScore of 1.10 and a Dscore of 1.16. Site B is the second-ranked site with a SiteScore of 0.99 and a Dscore of 1.02. These scores are consistent with those from earlier studies of proteins in which drugs that bind with submicromolar affinity have been identified.[247] This indicates that sites A and B are promising binding sites that could be used for structure-driven drug design.

Site A (**figure 15B**) is narrow and highly hydrophobic, with a hydrophobic-to-hydrophilic character ratio of 2.22. For reference, the mean hydrophobic-to-hydrophilic ratio for tight binding sites in proteins is 1.60.[222] This ratio, along with the suitable SiteScore and Dscores calculated by SiteMap, implies that this pocket is suitable for exploration using drug-like molecules. Also, because the pocket is located deep within the protein, small molecules could be accommodated by the site, rather than larger ones, whose entry may be hindered. Site B has the largest predicted volume (569 $Å^3$) and spreads over the entrance of the active site. Site B has a hydrophobic interior region and a hydrophilic exterior, with a hydrophobic- to-hydrophilic character ratio of 0.61. The residues in site B are displayed in **figure 15C**.

Having identified potential ligand binding sites in MS_{Pa}, I judged the likely impact of ligand binding in these sites on enzyme function. I also assessed the degree of conservation of the amino acid residues in the predicted binding sites by aligning crystal structures across species, including *M. tuberculosis* (PDB entry 5CC5), *E. coli* (PDB entry 1P7T) and *M. leprae* (PDB entry 4EX4). The protein structural alignment revealed that there were no differences in the tertiary structures of MS from the four species, except for slight orientations of a flexible loop of approximately seven amino acids in length (amino acids 305-312 in *P. aeruginosa*; not shown). Aligning the four structures of MS also revealed that predicted ligand binding site B incorporates the known substrate binding sites of MS (**figure 16**) and contains two of the amino acids predicted to be involved in catalysis in *P. aeruginosa*, Arg340 and Aps631, as well as the active site fluorophore, Trp539 (see **figure 15C** for amino acids). Site A also partially overlaps with the substrate binding pocket, surrounding the β-hairpin of domain II (amino acids 615−631 in *P. aeruginosa*), which borders the active site (not shown).

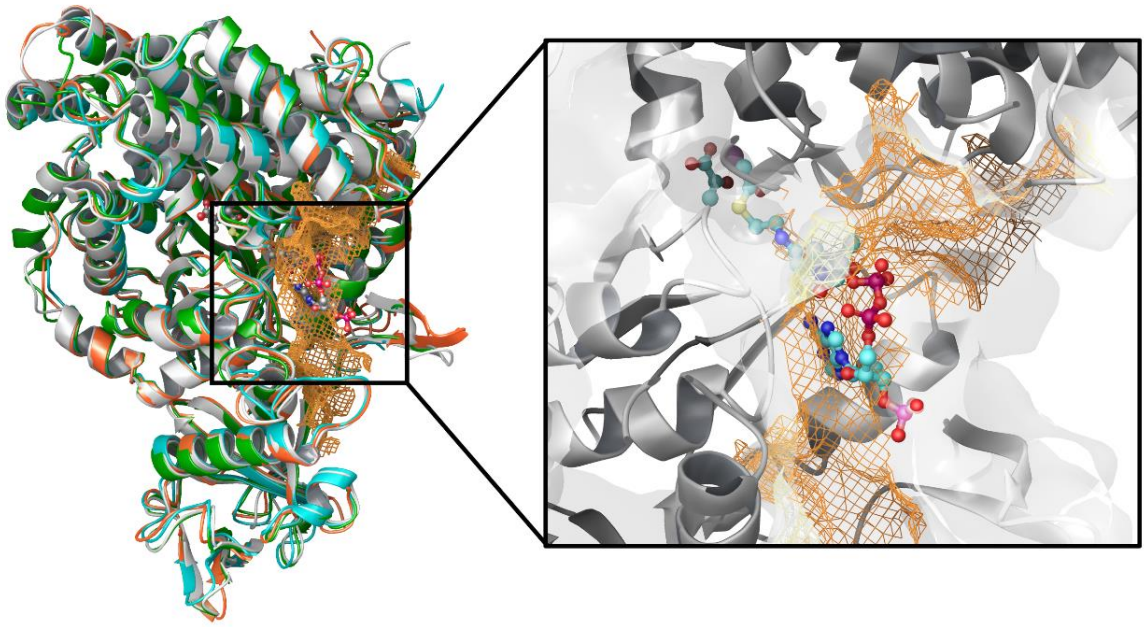

Figure 16. Alignment of MS crystal structures. The MS crystal structures of *P. aeruginosa* (grey), *E. coli* (green), *M. tuberculosis* (cyan), and *M. leprae* (orange) were aligned to locate any differences in tertiary structures. Predicted binding site B is shown as an orange mesh with substrates glyoxylate and acetyl coenzyme A present to show location (shown as sticks).

Because of the structural conservation and functional significance of sites A and B, I looked for published inhibitors of MS in other organisms that might bind in these sites. To date, however, the few known inhibitors of MS solely target the active site and are either glyoxylate analogues, Mg^{2+} chelators, or endogenous metabolic intermediates.[173,182,187,240–242] An example of a Mg^{2+} chelator is a class of compounds, phenyldiketoacids (PDKA), that was discovered to inhibit MS_{Mt}. MS_{Mt} complexed with the PDKA inhibitors did not show significant conformational changes; however, as seen for ethylene glycol in this work, the 1,2-diol moiety in these inhibitors acted as a bidentate ligand of Mg^{2+} in the MS_{Mt} active site. Another example is a study in which a high-throughput screen against *P. aeruginosa* grown on acetate identified small molecule inhibitors of MS. *In silico* binding of these hits following an induced-fit docking procedure to homology models of an MS_{Mt} crystal structure alluded to a possible interaction with the active site Mg^{2+}.[194] In a different study of MS_{Mt} complexed with chemical fragments, 18 fragments were identified that formed a hydrogen bond with the backbone carbonyl of Met631 in the active site.[241] Met631 (Met629 in MS_{Pa}) is conserved in the MS superfamily and is present in site A. Finally, a recent study has employed computer-aided drug design to predict the binding positions accurately and poses of 16 substituted PDKAs to MS_{Mt}.[248] The scarcity of MS_{Pa} inhibitors highlights the potential of targeting it through alternative binding pockets.

3.8 Computational analysis of structural waters

The solvation network in a crystal structure plays an important role in determining protein-ligand binding affinities computationally. The MS_{Pa} crystal structure incorporates 691 water molecules per molecule, as opposed to just 450 water molecules per molecule in MS_{Mt} (PDB entry 1N8I). However, hydration networks in proteins are dynamic, so Prashanthi Medarametla from the University of Eastern Finland used the molecular dynamics simulator, WaterMap by Schrödinger, to better understand the possible impact of water molecules on ligand binding. The location of the predicted stable hydration sites was consistent with the observed crystallographic waters, and the predicted hydration sites and crystal water molecules in the active site are shown in **figure 17**.

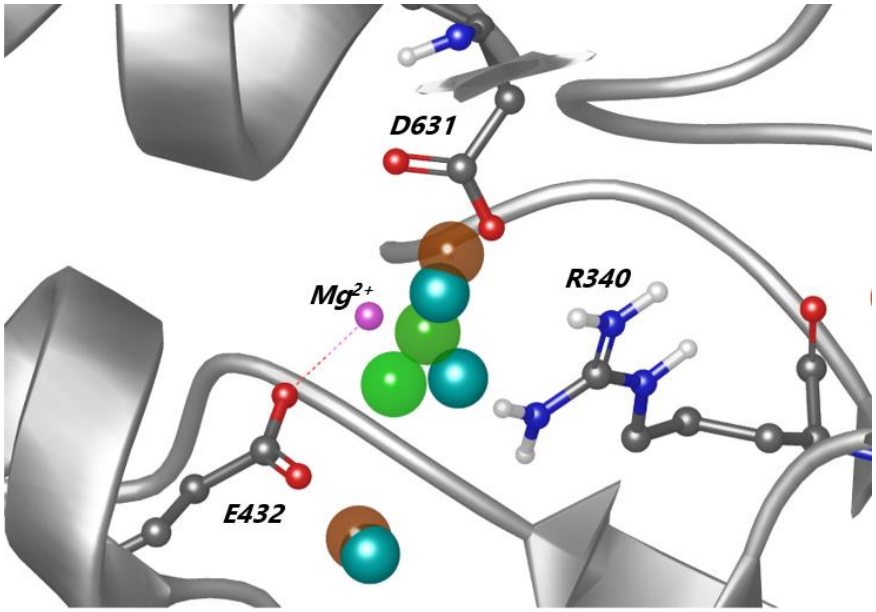

Figure 17. Comparison of predicted hydration sites with crystallographic waters. Hydration sites (brown spheres, representing unstable water molecules and green spheres, representing stable water molecules) predicted by WaterMap were superimposed with MS_{Pa} crystallographic waters (cyan spheres) and checked for spacial positions. Catalytic amino acid residues (Arg340, Glu432, and Asp631) are shown as sticks to illustrate the location.

The hydration sites predicted by WaterMap gave additional insights into the thermodynamics of the solvation network (**figure 18**). The water molecules in the hydration sites coloured green are high-energy water molecules. Typically, these water molecules are favourable for binding, and ligands that displace these water molecules must compensate for the loss in free energy. Thus, it is better to avoid these sites during ligand design. Conversely, hydration sites coloured red/brown portray lower-energy or unfavourable sites. Thus, replacing these water molecules should favour an increase in free energy. WaterMap also predicts cavity regions that are

devoid of water molecules and targeting these regions may also help in the search for high-affinity binders. The WaterMap analysis confirmed the top-ranked predicted binding sites, A and B (**table 22**), as druggable. WaterMap revealed cavity regions along with unstable hydration sites in site A (**figure 18B**) and site B (**figure 18C**).

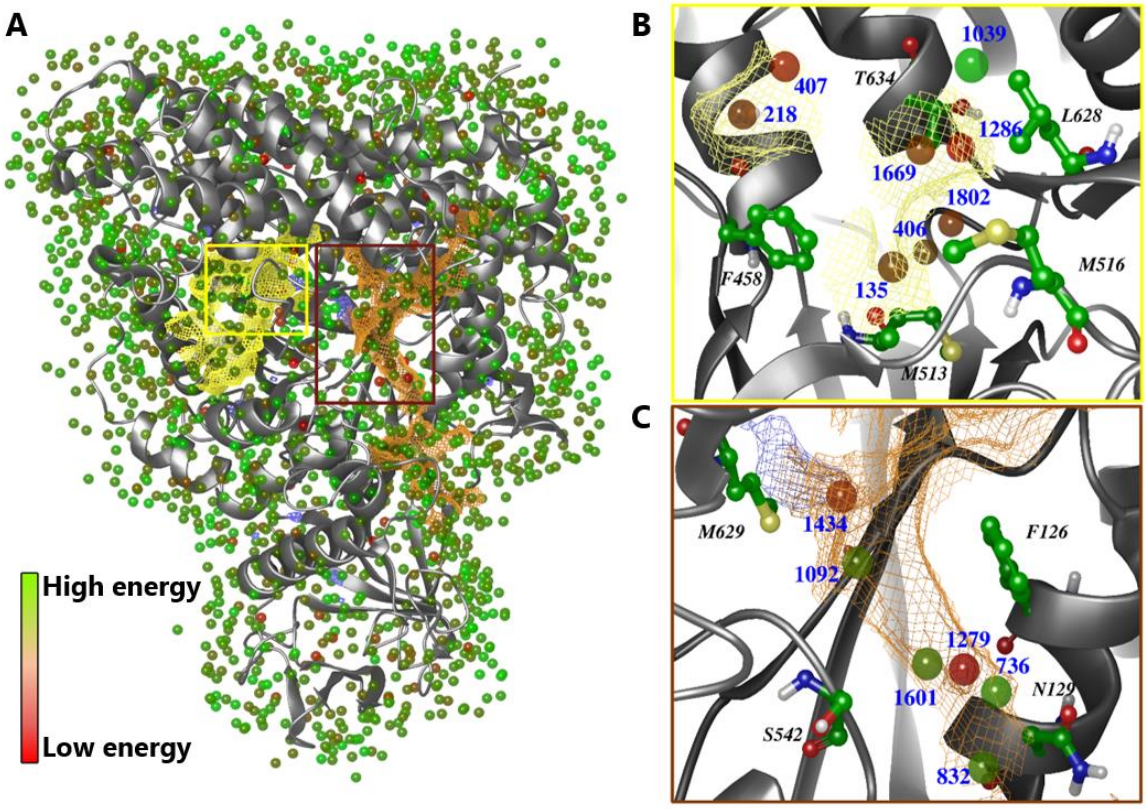

Figure 18. Computational analysis of MS_{Pa} hydration sites. (A) MS_{Pa} hydration sites predicted by WaterMap. The relative free energy of the water molecules in the hydration sites are indicated by a green (high energy) to red (low energy) colour gradient. Predicted binding sites A and B are also outlined in yellow and brown, respectively. **(B)** Site A. Yellow surface defines the site. Amino acids within the site are displayed as green sticks, and blue labels indicate hydration site numbers. **(C)** Site B. Orange surface outlines the site. A cavity region (blue mesh) partially occupies the site, along with the hydrophobic amino acids within the site (green sticks), and number hydration sites (labelled in blue).

The full thermodynamic parameters associated with the hydration sites shown in panels **B** and **C** of **figure 18** are provided in **appendix 2**. Site B has fewer unstable hydration sites than site A does, which supports the hydrophilic nature of the pocket analysed by SiteMap. In contrast, site A is more hydrophobic. However, the unstable hydration sites in site A are not contiguous, suggesting a requirement for a larger molecule with several hydrophobic regions to fit neatly in the site. One particularly interesting cavity is located near the AcCoA binding site that is so unfavourable for hydration that a void is present (shown as blue mesh in **figure 18C** and **figure**

19). Huang and colleagues' fragment screening found 18 fragments that inhibit MS activity in *M. tuberculosis* by binding to the active site.[241] Upon scrutinisation of these fragments, one particular hydrophobic fragment, indole-3-carboxylic acid (ICO), occupies the space between the glyoxylate and AcCoA binding sites, see **figure 19**, (PDB entry 5CC5), and this corresponds to the exact cavity region that we identified in our WaterMap analysis.

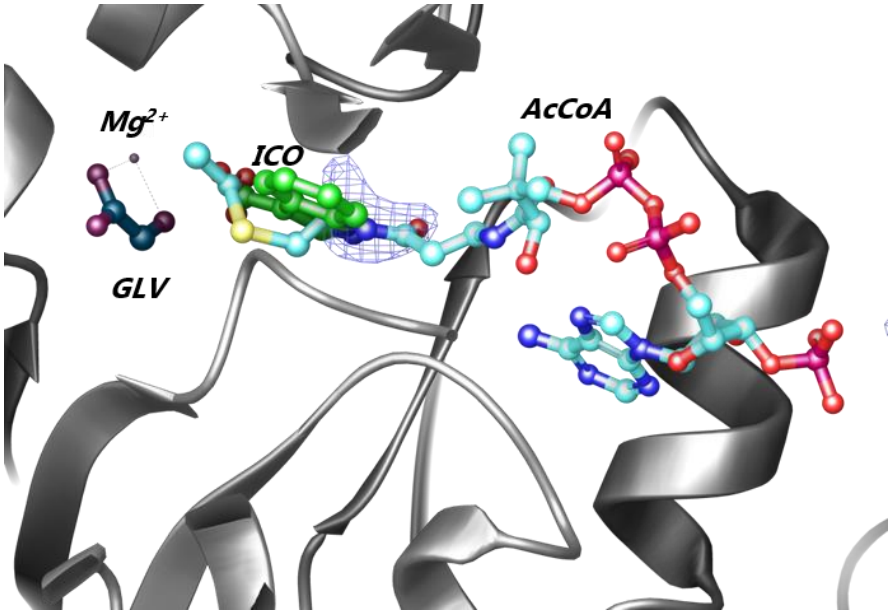

Figure 19. The MS_{Pa} cavity region predicted by WaterMap. The MS_{Mt} inhibitor, Indole-3-carboxylic acid (ICO; green sticks), partially occupies the cavity region (blue mesh) predicted in MS_{Pa} in the MS_{Mt} crystal structure (PDB entry 5CC5). Substrates glyoxylate (GLV; dark teal) and acetyl coenzyme A (AcCoA; cyan) are also presented from an MS_{Ec} crystal structure (PDB entry 1P7T) to illustrate the binding location.

Cavity regions, or "dry regions", represent an under-exploited tactic regarding the search for protein-ligand binding affinities. Typically, the computational strategy is to find a ligand of interest which displaces unfavourable waters and replaces them with groups that are complementary to the protein surface. This has been established as a principal driving force for protein-ligand binding in many systems, particularly in the pharmaceutical industry. However, if a ligand is placed in a cavity region and the ligand's chemistry is complementary to the protein surface in an appropriate region, this interaction would have to be highly favourable and result in free energy.[249]

3.9 Discussion

When establishing an infection, *Pseudomonas aeruginosa* adapts to the physiology of its environment. In the pulmonary airways of CF patients, for example, this adaptation occurs by

metabolising fatty acids as a primary source of carbon. These fatty acids are oxidised into acetyl coenzyme A and processed by the glyoxylate shunt, which bypasses the decarboxylative steps of the tricarboxylic acid cycle and enables *P. aeruginosa* to survive on short-chain fatty acids alone. Growing recognition of the important link between the glyoxylate shunt and infections has made it a prime target for the development of new antibacterial therapies. Prior work has shown that *P. aeruginosa* double shunt mutants are avirulent in a mouse pulmonary infection model, which shows that no other mechanism can bypass the loss of the glyoxylate shunt, thereby supporting the validity and tractability of this biological target.

Moreover, work from the Welch laboratory has demonstrated the association between shunt activity and increased virulence phenotypes, such as the expression of type III secretion-related virulence factors,[190,250] so understanding how to inhibit the glyoxylate shunt's function would also be useful in undermining diverse *P. aeruginosa* infections. The biochemistry of the glyoxylate shunt has been well studied in *E. coli* and *M. tuberculosis*. However, very little is known about its structure and function in *P. aeruginosa*. What is known from these model organisms about the structure and function of the shunt should not be extrapolated in *P. aeruginosa*; therefore, in this work, I generated structural and functional information to contribute to our biochemical understanding of malate synthase G in *Pseudomonas aeruginosa*.

In this chapter, I report the first X-ray crystal structure of *P. aeruginosa* malate synthase G in the apo form at 1.62 Å resolution. The first crystal structure of MS was elucidated in 2000 in *E. coli* and then in 2003 in *M. tuberculosis*. Seven years ago, interest in pursuing MS_{Mt} as a drug target emerged, and structure-based drug design efforts began. Fragment-based screenings have flourished with nearly 50 fragments available in the PDB that show binding to MS_{Mt}. The MS amino acid sequences between species indicate that they are highly conserved, and this is also visible in the crystal structures of MS_{Mt}, MS_{Ec} and MS_{Pa} when they are aligned. MS_{Pa} appears to be monomer in solution, which was suggested from SEC analysis in protein purification. This is consistent with other bacterial species in which MS isoform G has been characterised.[181,182]

Based on sequence and structural similarity, I propose that the amino acid residues involved in catalysis in MS_{Pa} are Arg340, Glu432, Asp460, and Asp631 (refer to **figures 10B and 11** for locations). I propose a mechanism, consistent with the fluorescence data as well as with previous studies on MS_{Mt} and MS_{Ec},[187,239] in which Mg^{2+} is coordinated in an octahedral conformation by the carboxylate side chains of Glu432 and Asp460, along with four water molecules. In this model (see **figure 20**), glyoxylate enters the active site and displaces two of the water molecules in the Mg^{2+} coordination sphere. Following this, acetyl coenzyme A enters the active site. Asp631 then deprotonates acetyl coenzyme A. The resulting enolate attacks glyoxylate

(activated by chelation of Mg^{2+}) to form a malyl-CoA intermediate that, in turn, deprotonates a proximal water molecule. This affords a hydroxide anion that can attack and hydrolyse the thioester. Arg340 then acts as a catalytic acid, protonating CoA, which causes CoA to leave the active site first, followed by malate.

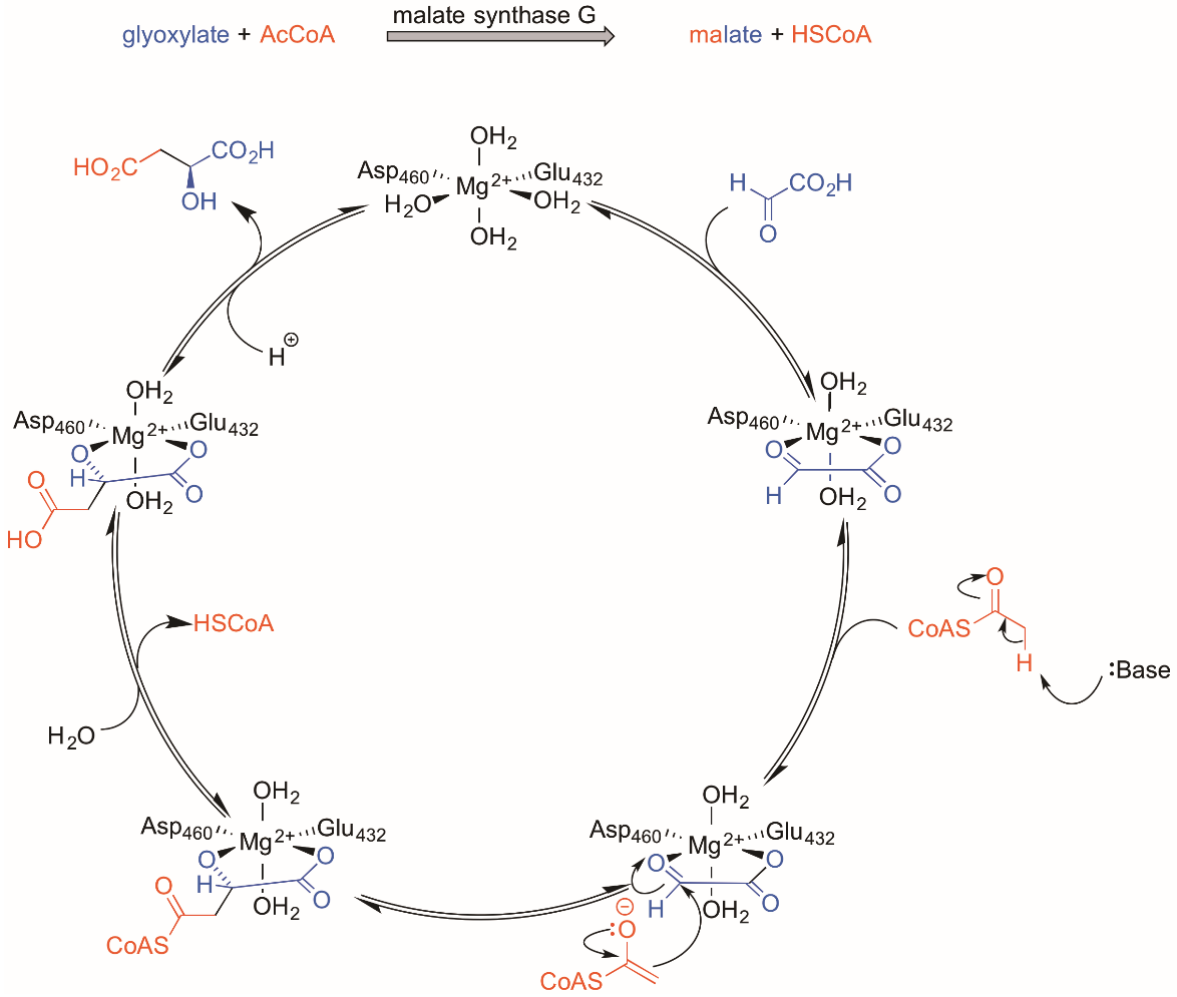

Figure 20. Schematic of the proposed catalytic cycle of MS_{Pa}. Coordination of glyoxylate by the Mg^{2+} co-factor renders it susceptible to a conjugate attack by acetyl coenzyme A. The Michael adduct is then hydrolysed by a catalytic amino acid to liberate malate and coenzyme A.

The crystal structure was useful in influencing further experimentation, where I also showed that events in the enzyme active site could be monitored non-invasively using intrinsic tryptophan fluorescence as a probe. Fluorescent studies confirmed the requirement of magnesium for substrate binding and catalysis, as well as that there were no global conformational changes during catalysis. I have characterised the structure and properties of *P. aeruginosa* malate synthase G with a particular emphasis on identifying potential drug binding sites. Computational data derived from a collaboration revealed two sites in the structure as well as the thermodynamic properties of hydration sites within the predicted binding sites that are promising starting points for drug development. Not all ligand-binding sites have the appropriate physicochemical and

topological properties to bind non-covalently to small-molecule drugs with sufficient affinity for inhibition.

These findings contribute to the growing body of evidence that MS is an amenable drug target and can provide a means for inhibitor development against *P. aeruginosa* using structure-based approaches. The findings reported here, along with the structural similarity and success in drugging malate synthase G in other pathogens instils confidence that MS is a chemically and biologically tractable target in *P. aeruginosa*.

Further work should explore whether there is a contributory network inhibition of isocitrate lyase by these small molecules inhibitors of MS. Given the functional relationship of these enzymes, it is quite possible that inhibitors of malate synthase G also act upon isocitrate lyase, which may contribute to the overall inhibition of shunt activity and minimise the risk of resistance from any single-point mutation. Building on this, more work is needed to understand the enzymatic regulation of shunt activity in *P. aeruginosa*. This is particularly important in the case of ICL as it mediates bacterial survival *in vivo* as the first enzyme of the glyoxylate shunt. Malate synthase plays a secondary role in this process, enabling glyoxylate detoxification and protecting the cell from ketoacidosis.[191] Therefore, modulating shunt expression *in vivo* represents an opportunity to disrupt shunt function simultaneously by increased expression of ICL, leading to ketoacidosis and inhibition of malate synthase G to arrest gluconeogenesis. Research in this area may pave the way for the development of novel dual-targeting inhibitors of *P. aeruginosa*.

4. Results and discussion

2-aminopyridines as dual inhibitors of the glyoxylate shunt

4.1 Background

Pseudomonas aeruginosa overcomes several metabolic challenges *in vivo,* particularly during infection scenarios where nutrients are limited. When the primary source of carbon is derived from C_2 molecules, the glyoxylate shunt is used for gluconeogenesis instead of the tricarboxylic acid cycle. Recent work has shown that carbon flux through the glyoxylate shunt plays a vital role in the pathogenicity of medically relevant microorganisms. Mutants of *Mycobacterium tuberculosis*, for example, defective in isocitrate lyase (ICL_{Mt}) activity show impaired survival *in vivo*.[193] Similarly, in *P. aeruginosa*, the glyoxylate shunt is conditionally essential for survival in mammalian systems.[194] Given their importance in pathogenicity and the fact that there are no human orthologues of the glyoxylate shunt enzymes, ICL and MS have become attractive targets for drug discovery efforts. Studies revealing the glyoxylate shunt as a potential target for antibacterial intervention are significant because *P. aeruginosa* currently occupies the second spot in the WHO's critical priority pathogens list.[9] The need for new antipseudomonal agents is dire.

Nature has already taken the opportunity to target the glyoxylate shunt as an antibacterial strategy. The human enzyme, Irg1, synthesises itaconate during macrophage activation and supports immune cells during bacterial infections by being a potent ICL inhibitor.[251,252] However, *P. aeruginosa* has seized the body's defence for its own gain to survive inside macrophages by acquiring the ability to degrade itaconate into acetyl coenzyme A and pyruvate.[253] ICL and MS from a variety of pathogens have been structurally elucidated, which have helped facilitate structure-based drug design. Examination of the active sites of the crystal structures of ICL and MS from *M. tuberculosis* suggest that the latter would provide a more "druggable" target. This implies that MS could better afford small, drug-like molecules perhaps due to its deeper, hydrophobic active site that must accommodate the pantothenate tail of acetyl coenzyme A. ICL has a smaller and highly polar active site.[179,254]

Nonetheless, several ICL inhibitors have already been identified, along with itaconate, such as 3-bromopyruvate[255] and 3-nitropropionate (3-NP)[256] (see **figure 21**). 3-NP and 3-bromopyruvate have inhibitory constants (K_i) of 3 μM and 120 μM, respectively, against ICL_{Mt}.[257] Sharma and co-workers showed evidence that Cys191 acts as the catalytic base necessary for the

cleavage of isocitrate into glyoxylate and succinate in ICL_{Mt}.[179] Another research group discovered that Cys191 serves not only in the ionisation of succinate for catalytic turnover but also in the mechanism-based inhibition by 3-NP and that Cys191 is conserved across all ICLs and methylisocitrate lyases.[258] However, these ICL inhibitors are not pharmacologically suitable for use *in vivo* because they display nonspecific hepatotoxicity.[259] Also, 3-NP is a succinate analogue and also inhibits succinate dehydrogenase, a significant enzyme of the TCA cycle.[260] A more recent compound, 2-vinyl-D-isocitrate, was developed as a mechanism-based inactivator of ICL_{Mt}. The retro-aldol cleavage of 2-vinyl-D-isocitrate by ICL reveals a Michael substrate, 2-vinylglyoxylate, which forms a covalent adduct with the thiolate form of Cys191 in the active site.[261]

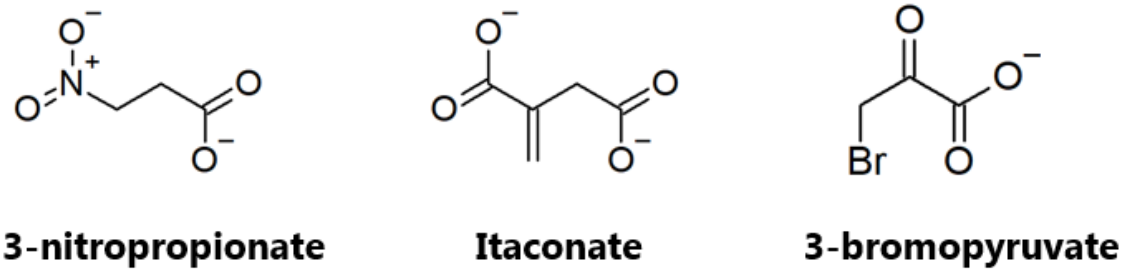

Figure 21. Chemical structures of known isocitrate lyase inhibitors. These inhibitors have been shown in *M. tuberculosis* to interfere with enzymatic cleavage of isocitrate into glyoxylate and succinate by interacting with catalytic Cys191 in the active site.

In 2012, Krieger *et al.* developed potent phenyl-diketoacid (PDKA) inhibitors of malate synthase G from *M. tuberculosis* (MS_{Mt}) through structure-based drug design.[242] They initially screened 35 substrate analogues, 19 of which exhibited inhibitory activity against MS_{Mt}. Analysis of the protein structure in complex with five of these inhibitors (PDB entries: 3S9I, 3S9Z, 3SAD, 3SAZ, and 3SB0) show no significant structural changes upon binding, but do show chelation of the magnesium co-factor in the active site by the 1-2-diol. Other common chelating agents, such as catechol, were shown to be ineffective MS_{Mt} inhibitors, suggesting a degree of specificity in the action of the PDKAs.

Further analysis of the inhibition through structure-activity relationships indicated that these PDKA compounds adopt an unusual conformational pose once bound, with the aryl substituent twisted out of coplanarity with the benzylic ketone. This allows the compound to achieve a close contact between the PDKA's aromatic ring and the carboxylic acid of a nearby aspartate (Asp633, which is one of the amino acids involved in catalysis in MS_{Mt}).[187] This pose permits the formation of an unusual face-on anion-π interaction, which is a noncovalent binding contact between an electron-deficient aromatic moiety and an anion. Intramolecular interactions of this sort are uncommon in inhibitors, but are growing in number, and are impacting our

understanding of various biological processes such as enzyme inhibition, protein-protein interactions, and macromolecular folding.[262] The aromatic ring of the PDKAs was confirmed as essential for activity as analogues carrying aliphatic chains were inactive as inhibitors of MS_{Mt}.[263] The PDKA hits were then optimised by adding various substitutions to the PKDA scaffold, although this resulted in only a modest improvement in activity. However, substitution at the ortho-position of the phenyl ring did increase stability 10-fold and improve the IC_{50} value.[242] The potency of the inhibitors improved with increasing electrophilicity of the substituent (2-F > 2-Cl > 2-Br > 2-Me > 2-H), which resulted in stronger anion-π interactions.[263]

Fahnoe and co-workers were the first to demonstrate the tractability of the glyoxylate shunt in *Pseudomonas aeruginosa* as an antibacterial target using a combined chemical and genetic approach.[194] They confirmed that the glyoxylate shunt is conditionally essential for survival on acetate, and they found that the *P. aeruginosa* double deletion mutants (ΔICL ΔMS) were completely cleared from a pulmonary infection model after 48 hours, indicating that they are also essential to establish infections in a mammalian system. The authors identified eight hits capable of preventing the growth of *P. aeruginosa* on acetate as a sole carbon source from an HTS campaign of 150,000 compounds. They confirmed the same compounds did not affect growth in glucose medium, suggesting that they are cell permeable and that they specifically target acetate metabolism. When they tested *in vitro* for their ability to inhibit purified ICL and MS, the eight compounds inhibited both enzymes from *P. aeruginosa* with IC_{50} values in a low micromolar range. These compounds were the first known dual inhibitors of ICL and MS from a HTS campaign. However, the precise mechanism of inhibition and specificity of these compounds has yet to be rigorously evaluated.

4.2 The rationale for designing a small molecule library

In collaboration with Dr Sean Bartlett from the Department of Chemistry, we designed and synthesised a small collection of structural analogues based upon the chloropyridine derivative from Fahnoe *et al.*'s work.[194] We reasoned that combining the structural and electronic features of the known inhibitors of the glyoxylate shunt could allow for more potent inhibition of *Pseudomonas aeruginosa*.

We supposed the chloropyridine derivative was a good starting point because it was an effective inhibitor according to the π-acidity of the scaffold, and it was not much larger than the PDKAs active against MS_{Mt}, see **figure 22A**. The synthesised compounds all shared the core 2-aminopyridine structure with *tert*-butyloxycarbonyl protecting groups and varied only in the electronegative substituents at the 4-position of the aromatic ring (**figure 22B**). Dr Bartlett

synthesised an isomeric 2-chloropyridine derivative as a negative control to test if inhibition was dependent on constitutional isomerism. We anticipated the new compounds would have a similar inhibitory mechanism as the PDKAs on MS_{Mt}, so we hypothesised that the IC_{50} values would decrease as the electronegativity of the substituents increased because this would favour stronger anion-π interactions.[263] We also reasoned that the same could be true of ICL_{Pa} inhibition if the mechanism of action were similar to MS_{Pa} inhibition. It is notable that the test compounds are structurally dissimilar to the endogenous substrates of the glyoxylate shunt enzymes or any of the known inhibitors of ICL.

Therefore, in this study, I set out with three experimental objectives. First, I sought to test if the small library of compounds could prevent bacterial growth of *Pseudomonas aeruginosa* in conditions relevant to the expression of the glyoxylate shunt enzymes. Second, I tested if the compounds could inhibit the activity of both of the glyoxylate shunt enzymes purified from *P. aeruginosa.* Third, I hoped to elucidate the binding mechanism and support a definitive mechanism of action on the target enzymes through enzyme kinetics, isothermal titration calorimetry and X-ray crystallography.

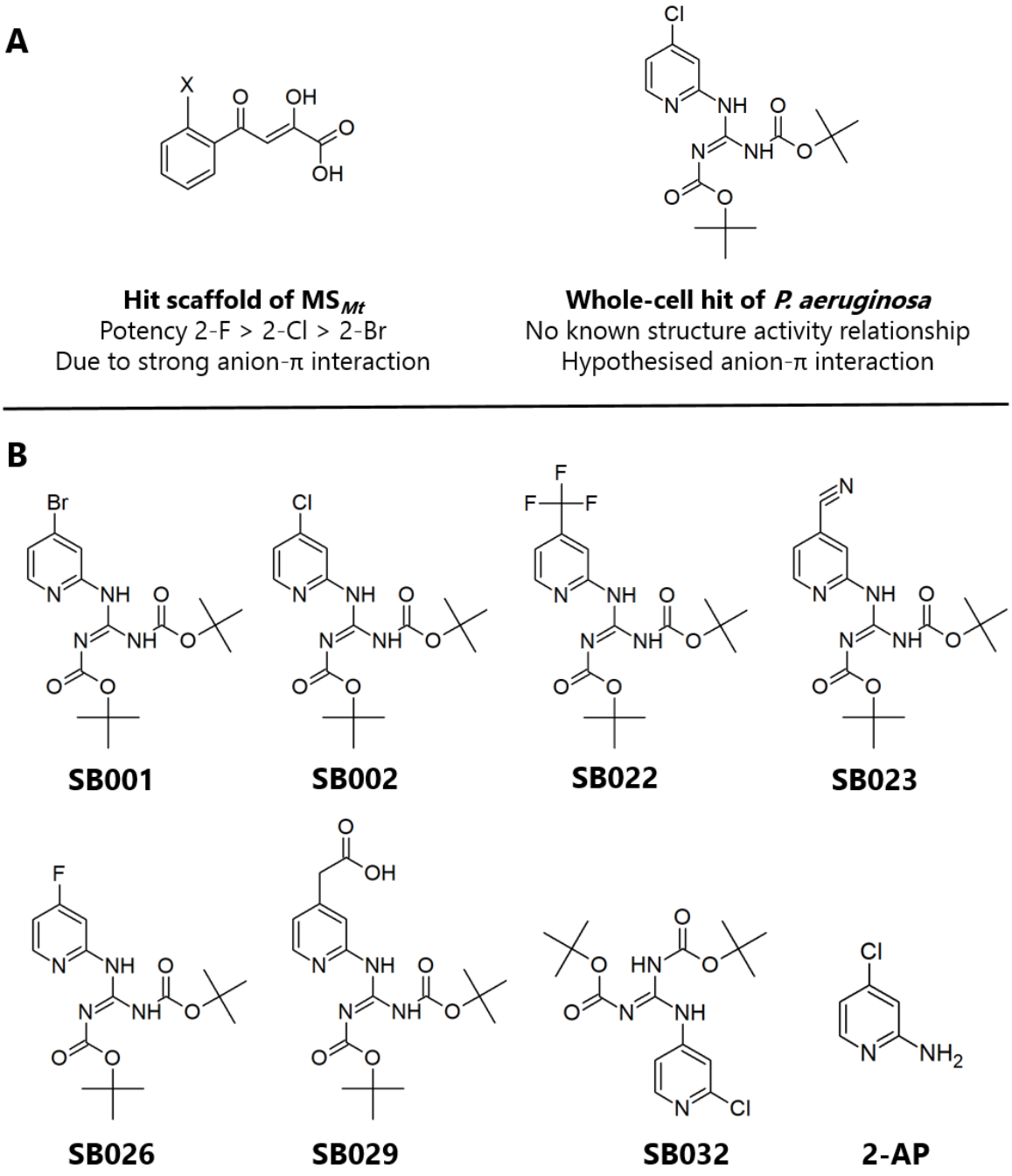

Figure 22. Analogues and controls synthesised for this study. (A) Structures of glyoxylate shunt inhibitors reported in the literature with known or proposed anion-π interactions. **(B)** The compounds (SB001-029) all shared a 2-aminopyridine core structure with *tert*-butyloxycarbonyl protecting groups, varying only in the substituent at the 4-position. SB032 and 2-amino-4-chloropyridine (2-AP) were synthesised as negative controls.

4.3 Antibacterial assessment of 2-aminopyridines against *Pseudomonas aeruginosa*

I analysed the 2-aminopyridine library to assess antipseudomonal activity through an endpoint assay. *P. aeruginosa* PAO1 culture grown overnight in LB medium was incubated with 200 μM of test compounds at a starting $OD_{600\ nm}$=0.05. After 18 hours of incubation, the wells with 2-aminopyridines added were visibly as turbid as the control wells (not shown). The optical density readings were blanked using the media-only control wells, and then the final optical density readings were subtracted from the initial readings to get $\Delta OD_{600\ nm}$. The values were normalised to that of the no inhibitor and vehicle control wells, which represented maximal growth, and bacterial growth percentage was calculated. None of the compounds affected bacterial growth of PAO1 after 18 hours in rich medium, see **figure 23**, except for SB026. It is difficult to say at this point why SB026 shows a slight inhibition (~25%) of PAO1 in LB medium, but it does point to the possibility that the growth inhibition could be due to off-target activity in PAO1.

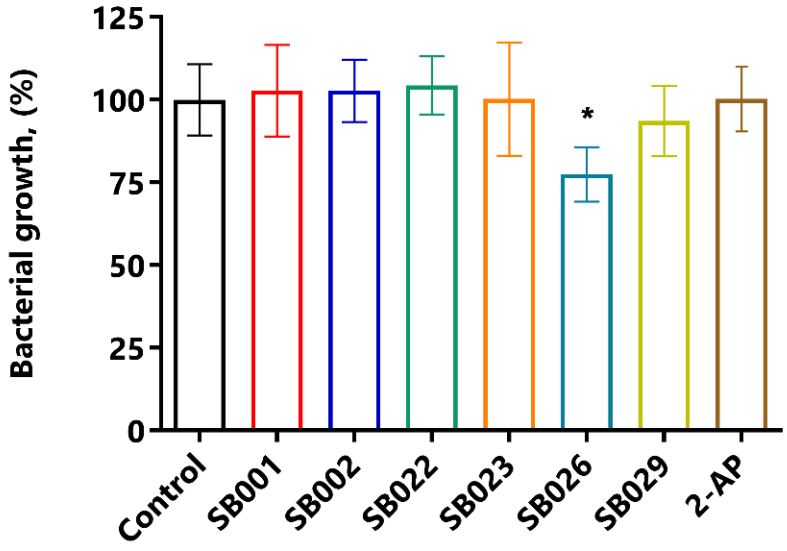

Figure 23. Screening 2-aminopyridines on *P. aeruginosa* in rich medium. The percentage of bacterial growth was calculated from $\Delta OD_{600\ nm}$ relative to that of a "no inhibitor" control. The negative control was 2-AP (2-amino-4-chloropyridine), synthesised without tert-butyloxycarbonyl protecting groups. All compounds were tested at 200 μM. Values marked with * are significantly different (* = $p<0.05$; $n=3$).

The same experiment was conducted in M9 minimal medium supplemented with 0.5% acetate as the sole carbon source. After 18 hours of incubation, wells with 2-aminopyridines added were visibly less turbid compared with control wells with no inhibitor added (not shown). SB001, SB026 and SB029 were all capable of partially inhibiting PAO1 growth (~50%), see **figure 24**. SB002 and SB023 were the only compounds to display complete inhibition of bacterial growth at 200 μM. 2-amino-4-chloropyridine was designed as a negative control due to the absence of *tert*-butyloxycarbonyl (Boc) protecting groups and displayed no inhibition. The results were in line with expectations, particularly because acetate is a C_2 carbon source that requires a functional glyoxylate shunt for its metabolism. SB022 showed no inhibition of PAO1 growth. The most logical explanation could be because it had poor aqueous solubility, which could have influenced the absorbance readings. Another explanation is that somehow the CF_3 group on the aromatic ring precluded the entry into the bacteria or binding to the target enzymes. This experiment confirmed two things. First, that SB002 and SB023 selectively target acetate metabolism via the glyoxylate shunt. Second, it shows that these compounds are cell-permeable and can pass the outer membrane, periplasm, and cell membrane of a Gram-negative bacterium.

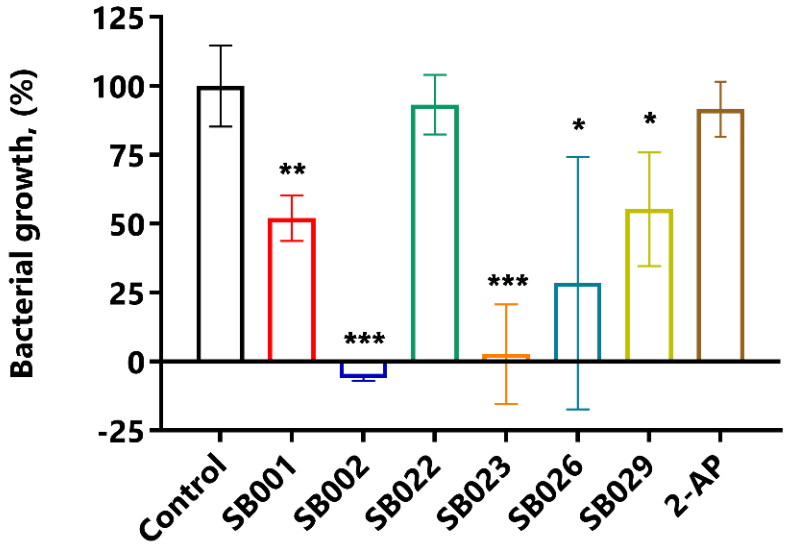

Figure 24. Screening 2-aminopyridines on *P. aeruginosa* in acetate medium. SB002 and SB023 inhibited PAO1 growth completely relative to that of a "no inhibitor" control. 2-AP (2-amino-4-chloropyridine) was the negative control. All compounds were tested at 200 μM. Values marked with *, **, and *** are significantly different (* = $p<0.05$; ** = $p<0.01$; *** = $p<0.001$; $n=3$).

Next, I tested concentrations of SB002 and SB023 to determine if a dose-dependent inhibition was possible. Again, a PAO1 overnight culture was diluted and added to 96-well plates

with two-fold dilutions of concentrations of inhibitors (0-200 μM; 1% DMSO), and the plate was incubated at 37°C with 200 rpm agitation for 18 hours. Final and initial optical density readings were blanked using the media-only control wells, and then the final optical density readings were subtracted from the initial readings to get $\Delta OD_{600\,nm}$. The values were normalised to that of the no inhibitor and vehicle control wells, and bacterial growth percentage was calculated.

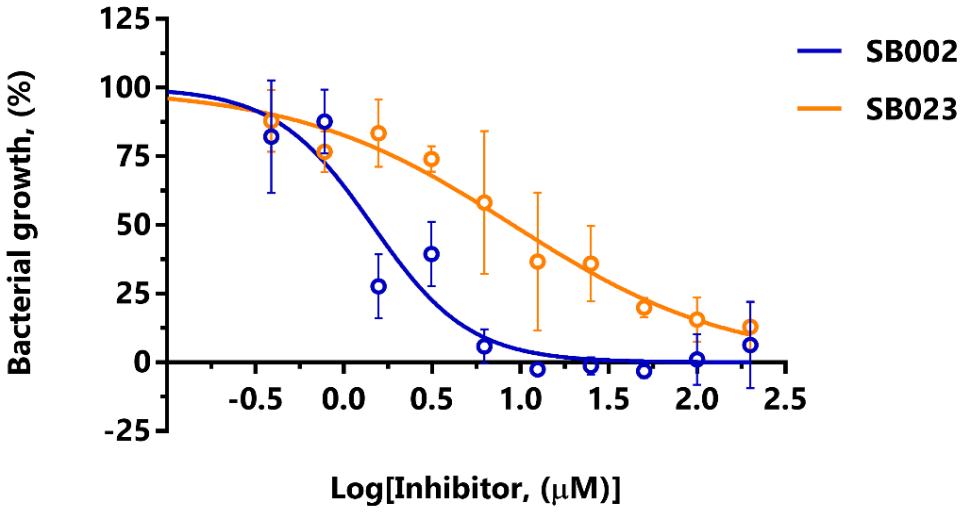

Figure 25. Dose-response inhibition of PAO1 growth by SB002 and SB023. SB002 (blue) and SB023 (orange) were added (0-200 μM) and inhibited PAO1 in M9 acetate in a dose-dependent manner.

SB002 and SB023 were able to prevent PAO1 growth in a dose-dependent manner with Hill slopes of -1.58 and -0.71, respectively. They also show promising inhibition with minimum inhibitory concentration (MIC) values of 1.16 μg mL^{-1} for SB002 and 13.48 μg mL^{-1} for SB023, see **table 23**. The MIC for SB002 is in agreement with the value found for the chloropyridine derivative in the literature.[194]

Table 23. MIC values of SB002 and SB023 on PAO1 in acetate. IC_{50} values and Hill slopes were derived from GraphPad Prism version 7.04.

	SB002	SB023
MIC (μg mL^{-1})	1.16	13.48
IC_{50} (μM)	1.45 ± 1.12	9.08 ± 1.18
Hill slope	-1.58 ± 0.26	-0.71 ± 0.08

4.4 Evaluation of 2-aminopyridines as inhibitors of malate synthase G

Next, I tested the compounds to see if they could impede or reduce the enzymatic reaction of recombinant malate synthase G from *P. aeruginosa* (MS_{Pa}). Compounds solvated in DMSO were incubated at a final concentration of 75 μM (1% DMSO) with 25 nM of purified MS. The enzymatic reaction was initiated with 200 μM of substrate glyoxylate, pH 7.5 and a modified coupled assay in which the quantity of free thiol (present in the reaction product, coenzyme A) was titrated. When the enzymatic reaction of MS_{Pa} in the presence of the compounds was compared with the control reaction, which represented the enzyme reaction at maximal velocity, there was a clear and significant inhibition for SB002 and SB023, and partial, but statistically significant inhibition (~50%) for SB026 and SB032, as well as a slight, but statistically significant inhibition (~20%) for SB001. SB022 and SB029 surprisingly show an increase in MS_{Pa} activity, but this was most likely due to their poor aqueous solubility interfering with the absorbance readings rather than them acting as enzyme activators.

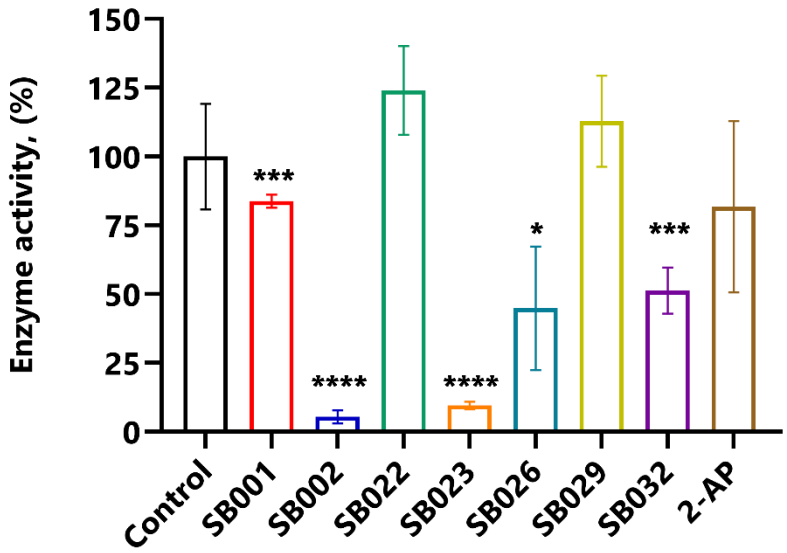

Figure 26. Screening of 2-aminopyridines on recombinant MS_{Pa}. SB002 and SB023 inhibited enzymatic activity completely relative to that of the "no inhibitor" control. 2-AP (2-amino-4-chloropyridine) was the negative control. All compounds were tested at 75 μM. Values marked with *, ***, and **** are significantly different (* = $p<0.05$; *** = $p<0.001$, and **** = $p< 0.0001$; $n=3$).

For the compounds which showed significant inhibition during the kinetic screening, I generated dose-response curves to determine the IC_{50} values and visualise complete enzyme inhibition, if possible. SB002, SB023, SB026, and SB032 all displayed a reduction in MS_{Pa} enzyme activity in a dose-dependent manner (**figure 27**), with Hill slopes of -2.1, -1.5, -1.3, and -2.3, respectively.

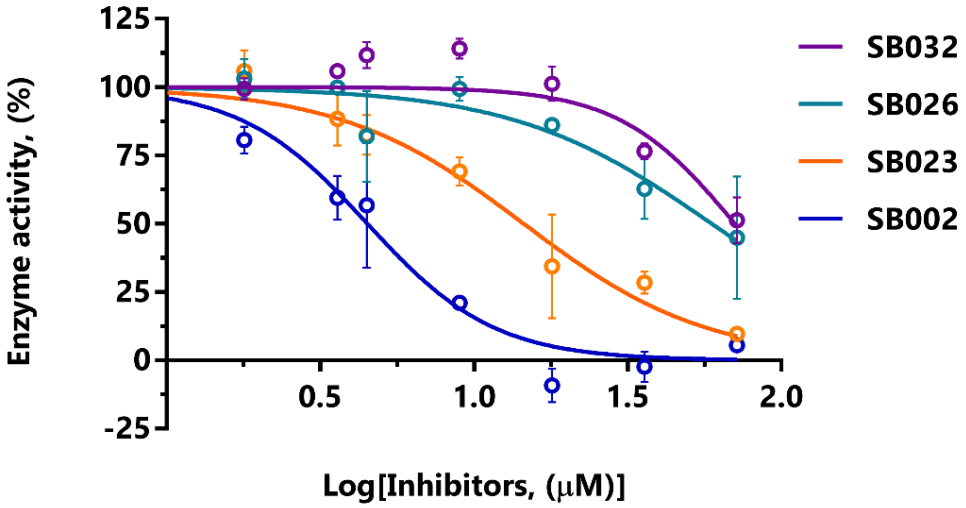

Figure 27. Dose-response inhibition of MS_{Pa}. SB002 (blue), SB023 (orange), SB026 (teal) and SB032 (violet) were tested at a range of concentrations (0-75 μM) and inhibited MS_{Pa} in a dose-dependent manner.

SB002 and SB023 were able to abolish the enzymatic activity of MS_{Pa} at 75 μM altogether and show promising inhibition with IC_{50} values in the lower micromolar range, see **table 24**. The IC_{50} value for SB002 is in agreement with the value found in the literature.[194] SB026 and SB032 do show inhibition in a dose-response manner, even though they only achieved about 50% inhibition at the highest concentration tested. 75 μM was the limit of solubility in DMSO for these compounds in these experiments, with higher concentrations visibly precipitating.

Table 24. IC_{50} and Hill slope values for 2-aminopyridine inhibitors of MS_{Pa}. Values were calculated from the dose-response inhibition curves using GraphPad Prism v. 7.04.

	SB002	SB023	SB026	SB032
IC_{50} (μM)	4.50 ± 1.12	14.49 ± 1.10	59.27 ± 1.17	70.55 ± 1.10
Hill slope	-2.1 ± 0.57	-1.4 ± 0.19	-1.3 ± 0.30	-2.3 ± 0.56

4.5 Evaluation of 2-aminopyridines as inhibitors of isocitrate lyase

The 2-aminopyridine compounds were tested to see if they could inhibit the enzymatic reaction of recombinant isocitrate lyase from *P. aeruginosa* (ICL_{Pa}). Protein purification and enzyme activity are presented in **appendix 3**. The test compounds were dissolved in DMSO at a final concentration of 75 μM and incubated with ICL_{Pa} (final concentration: 170 nM) for 5 minutes at 37°C. The enzymatic reaction was initiated with 200 μM of the substrate, D-L-isocitrate, and a modified coupled assay in which the number of ketones (present in the product, glyoxylate) was titrated using phenylhydrazine. When compared with the control enzyme reaction with no compounds added, which represented the reaction at maximal velocity, there was a full and significant inhibition observed at 75 μM for SB002, and partial inhibition for SB023, SB032, itaconate, and 3-nitropropionate, **figure 28**. SB026 and SB029 show partial decreases in enzyme activity, but the error between replicates was large and did not result in statistically significant inhibition. Like MS_{Pa}, SB001 and SB022 did not show any inhibition on ICL_{Pa}.

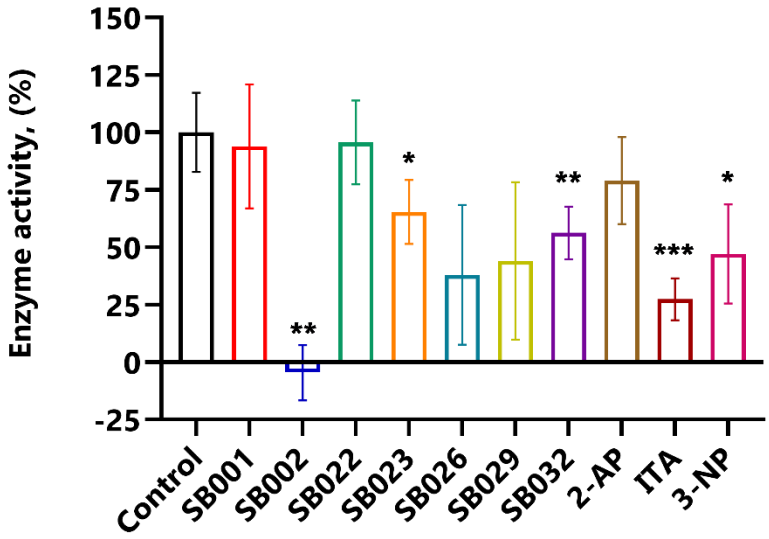

Figure 28. Screening of 2-aminopyridines on recombinant ICL_{Pa}. SB002 inhibited enzymatic activity completely relative to that of the "no inhibitor" control. 2-AP (2-amino-4-chloropyridine) was the negative control. ITA (itaconate) at 50 μ) and 3-NP (3-nitropropionate) at 100 μM were tested for comparison as positive controls. All other compounds were tested at 75 μM. Values marked with *, **, and *** are significantly different (* = $p<0.05$; ** = $p<0.01$; *** = $p<0.001$; $n=3$).

For the compounds which showed significant inhibition during the kinetic screening, I created dose-response curves to determine the IC_{50} values and visualise complete enzyme inhibition. SB002, SB023, SB032, and itaconate all displayed a reduction in ICL_{Pa} enzyme activity in a dose-dependent manner (**figure 29**), with Hill slopes of -3.6, -2.37, -1.2, and-1.3, respectively. SB002 was the only compound able to eradicate the enzymatic activity of ICL_{Pa} at 75 μM completely, and SB002 shows promising inhibition with an IC_{50} value of 13.28 μM, see **table 25**.

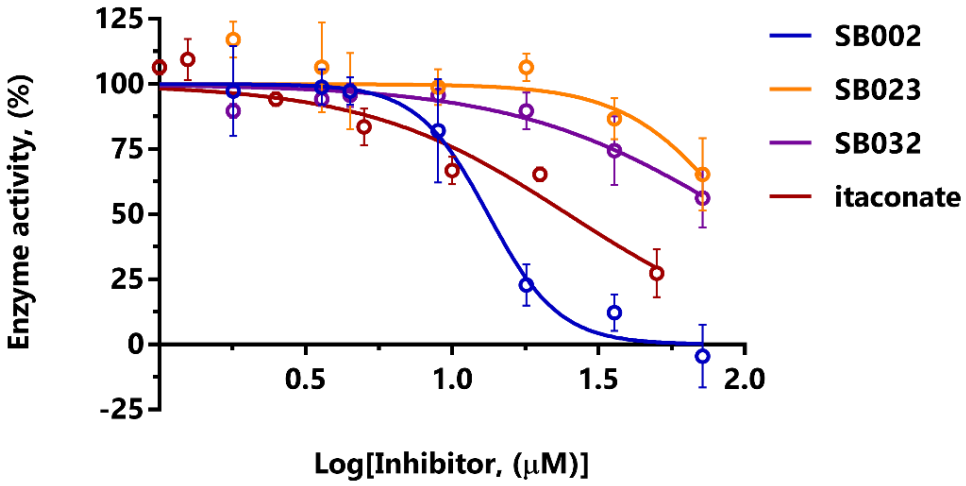

Figure 29. Dose-response inhibition of ICL_{Pa}. SB002 (blue), SB023 (orange), SB032 (violet) and itaconate (maroon) were tested at different concentrations (0-75 μM; itaconate: 0-50 μM) and inhibited ICL_{Pa} in a dose-dependent manner.

The IC_{50} value for SB002 determined in this study (13.28 μM) is nearly 80x higher than the value found in the literature (0.17 μM).[194] Fahnoe *et al.* used a final ICL concentration of 12 nM for their assessment, while I used 14x that amount (170 nM) in order to obtain a good spectroscopic signal to test for inhibition. A higher concentration of protein yielded a higher IC_{50} and a dose-response curve with a steep Hill slope (-3.5). This provides an interesting point of discussion about the possible mechanism of SB002. On the one hand, a steep Hill slope (>-1) may indicate a tight-binding inhibitor, but on the other hand, it might indicate that the inhibition is caused by aggregation or nonspecific binding, which is more discernible at higher enzyme concentrations.[264] An inhibitor can also undergo a phase transition or colloid formation as its concentration rises in the aqueous buffer. A steep Hill slope is more obvious at higher enzyme concentrations and should be approached with caution as it could give a false indication about the potency of the inhibitor.[265]

Nevertheless, SB002 was a better inhibitor of ICL_{Pa} than the positive controls at the concentrations tested. This apparent improvement in inhibition could be due, in the case of 3-NP, to the fact that the incubation time was only 5 minutes. 3-NP has been shown to display a covalent inhibition of ICL_{Mt} that requires several hours for inactivation.[258] Also, both 3-NP and itaconate possess exposed ketone groups, which could react chemically with phenylhydrazine in the presence of hydrogen atoms. Despite being present in excess (0.2 mM), a portion of phenylhydrazine could have reacted with the ketones on 3-NP and itaconate instead of any available glyoxylate, which could have reduced the spectroscopic signal for phenylhydrazone (324 nm) and distorted the results. Still, SB002 was the only compound that could reduce the enzymatic activity of both of the target enzymes completely, which means it has the potential to block the glyoxylate shunt pathway in conditions which require a functional pathway for survival.

Table 25. IC_{50} and Hill slope values for 2-aminopyridine inhibitors of ICL_{Pa}. Values were calculated from the dose-response inhibition curves using GraphPad Prism v. 7.04.

	SB002	**SB023**	**SB026**	**SB032**	**ITA**	**3-NP**
IC_{50} (μM)	13.28 ±1.08	>75	55.36 ±1.14	>75	24.55 ±1.16	>75
Hill slope	-3.6 ±0.71	-2.4 ±1.30	-2.0 ±0.54	-1.2 ±0.21	-1.3 ±0.22	-2.8 ±0.97

Abbreviations: 3-NP, 3-nitropropionate; ITA, itaconate.

The 2-aminopyridine compounds differ only in their electron withdrawing group at the 4th position, yet there is significantly different inhibition between them. For example, SB023 (4-CN) clearly inhibits MS_{Pa} but does not exhibit inhibition with nearly as much potency on ICL_{Pa}. This was surprising, particularly because of SB023's ability to completely inhibit PAO1 growth in acetate medium. Similarly, SB029 (4-CO_2Me) shows a slight inhibition against ICL_{Pa} (~50%) but shows no inhibition against MS_{Pa} and no ability to inhibit PAO1 growth. SB001 (4-Br) and SB022 (4-CF_3) should theoretically improve inhibition by encouraging a stronger anion-π interaction in the binding site, yet they were consistently ineffective in these assessments. SB002 (4-Cl) and SB032 (2-Cl) are isomers, yet there is a clear difference in their efficacy on both of the glyoxylate shunt enzymes, with SB002 exhibiting more potency. More information about the mechanism for the inhibition can be elucidated through further enzyme kinetics.

4.6 Kinetic modes of malate synthase G inhibition for SB002 and SB023

The kinetic mechanism of SB002 inhibition was investigated by determining changes to the Michaelis Menten constants (K_M^{app}) and maximum velocities (V_{max}^{app}) of MS_{Pa} in the presence of the inhibitor. Three concentrations of SB002 (3 μM, 6 μM, and 9 μM), which were near to the IC_{50} value (4.5 μM), were selected to test on MS_{Pa}. After initiating the enzymatic reactions by titrating substrate glyoxylate (5-400 μM) in the presence of fixed, saturating amounts of acetyl coenzyme A (200 μM), there was a dramatic reduction in V_{max}^{app} values concerning all three concentrations of SB002 (**figure 30A**). The K_M^{app} values for glyoxylate decreased slightly, which indicates that MS_{Pa} displayed a better affinity for glyoxylate while in the presence of 3 μM and 6 μM of SB002, **table 26**.

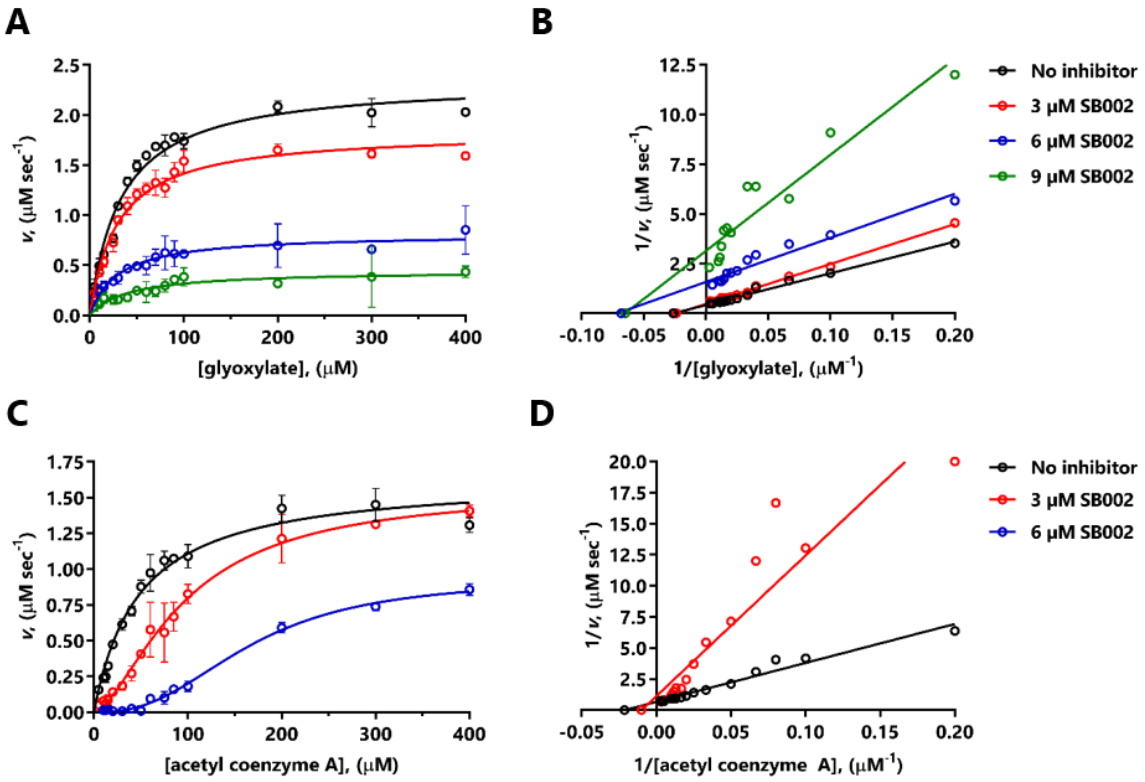

Figure 30. Mode of inhibition of MS_{Pa} by SB002. (A) Kinetic data obtained by titrating glyoxylate (5-400 μM) in the presence of no addition (black), or the presence of 3 μM (red), 6 μM (blue), or 9 μM (green) SB002. **(B)** Lineweaver-Burk plot showing that SB002 displayed mixed inhibition when glyoxylate was titrated. **(C)** Kinetic data obtained by titrating acetyl coenzyme A (5-400 μM) in the presence of no addition (black), or in the presence of 3 μM (red) or 6 μM (blue) SB002. **(D)** Lineweaver-Burk plot showing that SB002 displayed mixed inhibition when acetyl coenzyme A was titrated.

Conversely, the K_M^{app} of glyoxylate slightly increased when MS_{Pa} was incubated with 9 μM of SB002. The Lineweaver-Burk plot of 1/*velocity versus* 1/[glyoxylate] (**figure 30B**) indicates mixed

inhibition. Two types of mixed inhibition were observed concerning glyoxylate. The linear regression for the lowest concentration of SB002 (3 μM) intersected with the control line at a similar place on the x-axis, which is typical for type 2 inhibition (also known as noncompetitive inhibition).[212] Type 2 mixed inhibition is where the inhibitor, [I], has equal affinity in binding to the free enzyme, [E], as the enzyme-substrate complex, [ES]. The linear regressions for higher concentrations of SB002 (6 μM and 9 μM) appear to intersect with the control line, [-I], below the x-axis, which is characteristic of type 3 mixed inhibition. In type 3 mixed inhibition, [I] binds to both [E] and [ES], but displays a greater binding affinity for [ES]. Additionally, K_M^{app} values decrease in the presence of higher amounts of inhibitor. The inhibition binding constants of SB002 to [E] (K_i) and [ES] (K_i') were calculated (using the relevant equations denoted in **chapter 2, section 2.7**) as 4.5 μM and 3.9 μM, respectively (see **table 26**), indicating a slight preference towards [ES], which is more characteristic of uncompetitive inhibition.[266]

Varying acetyl coenzyme A concentrations (5-400 μM) in the presence of a fixed, saturating glyoxylate concentration (200 μM) resulted in sigmoidal data distribution in the presence of SB002 (**figure 30C)**. The K_{half}^{app} values of acetyl coenzyme A increased as the concentration of SB002 increased (**table 26**). There was also a noticeable decrease in V_{max}^{app} with the addition of 6 μM SB002, but no change in V_{max}^{app} with the addition of 3 μM SB002. This means that the enzyme was able to reach maximum velocity while in the presence of SB002, which is typical of competitive inhibition.[212] According to the double reciprocal plots, however, the two lines appeared to intersect between the x- and y-axes, which suggested another type of mixed inhibition: type 1 (**figure 30D**). Type 1 mixed inhibition mimics competitive inhibition, which entails that while binding to both enzyme states, [I] binds to [E] with much greater affinity than [ES].[267] Additionally, the data best fit the competitive inhibition equation in **chapter 2** (**equation 14**), resulting in a K_i value of 1.14 μM. This implies that SB002 is directly competing with acetyl coenzyme A in its binding pocket and that the inhibition is concentration-dependent. Computational analyses from chapter 3 revealed the binding pocket of acetyl coenzyme A as a druggable binding site (Site B) in MS_{Pa}. SB002 could compete with acetyl coenzyme A to interact with its binding amino acids in Site B, such as Pro543, Phe126, Arg312, or Met629 in MS_{Mt}[187], but this would need confirmation through structural information.

Table 26. Calculated kinetic parameters for SB002 and SB023 inhibition of MS_{Pa}. K_M/K_{half}, k_{cat}, and V_{max} values were derived from Michaelis-Menten or Hill sigmoidal kinetic analyses. K_i and K_i' values were determined from best-fit equations, and mode of inhibition was determined visually from linear regression analysis and inhibition constant calculations.

		K_M (μM)	V_{max} (μM s^{-1})	k_{cat}[b] (s^{-1})	K_i (μM)	K_i' (μM)	MOI Obs.[c]	MOI Calc.[d]
Fixed [acetyl coenzyme A]	**glyoxylate**	33.70	2.40	93.90	N/A	N/A	Substrate	Substrate
	3 μM SB002	29.70	1.80	73.40	12.06	12.06	Mixed (2)	Mixed (2)
	6 μM SB002	30.20	0.80	32.50	3.65	3.06	Mixed (3)	Mixed (3)
	9 μM SB002	40.60	0.50	17.80	1.63	2.03	Mixed (3)	Mixed (1)
	All SB002	N/A	N/A	N/A	**4.48**	**2.87**	N/A	**Mixed (3)**
	glyoxylate	33.70	2.40	93.90	N/A	N/A	Substrate	Substrate
	5.5μM SB023	38.60	2.20	88.80	29.60	88.36	Mixed (1)	Mixed (1)
	11 μM SB023	42.30	2.10	82.90	28.16	80.48	Mixed (1)	Mixed (1)
	22 μM SB023	52.40	1.60	63.40	32.43	32.43	Mixed (2)	Mixed (2)
	All SB023	N/A	N/A	N/A	**20.93**	**49.19**	N/A	**Mixed (1)**
Fixed [glyoxylate]	**AcCoA**	48.30	1.60	65.70	N/A	N/A	Substrate	Substrate
	3 μM SB002	97.0[a]	1.60	N/A	1.14	0.00	Mixed (1)	Competitive
	6 μM SB002	167.0[a]	0.90	N/A	N/A	N/A	N/A	N/A
	All SB002	N/A	N/A	N/A	**1.14**	**0.00**	N/A	**Competitive**
	AcCoA	62.00	2.40	98.80	N/A	N/A	Substrate	Substrate
	5.5μM SB023	40.60	2.00	78.90	48.76	0.00	Mixed (1)	Competitive
	11 μM SB023	56.10	1.80	70.80	42.17	27.98	Mixed (1)	Mixed (3)
	22 μM SB023	57.00[a]	1.30	N/A	N/A	N/A	N/A	N/A
	All SB023	N/A	N/A	N/A	**19.56**	**46.14**	N/A	**Mixed (1)**

[a] SB002 and SB023 altered the kinetics from hyperbolic to sigmoidal concerning acetyl coenzyme A, so these reported values in the table are K_{half}, instead of K_M.

[b] The value of E_t was based on the most likely oligomeric status of the native protein. MS_{Pa} was assumed to be a monomer.

[c] Three types of mixed inhibition were observed from the Lineweaver-Burk plots: (1) [-I] and [+I] lines intersected between the x- and y-axes, indicating [I] binds to [E] with greater affinity than [ES]; $K_i<K_i'$, $K_M^{app}>K_M$ and $V_{max}=V_{max}^{app}$, which mimics competitive inhibition. (2) [-I] and [+I] lines intersect at the x-axis, which indicates that [I] binds with equal affinity to [E] and [ES]; $K_i=K_i'$, $K_M^{app}=K_M$ and $V_{max}^{app}<V_{max}$, which mimics noncompetitive inhibition. (3) [-I] and [+I] lines intersect below the x-axis, indicating that [I] binds to [ES] with greater affinity than [E]; $K_i< K_i'$, $K_M^{app}<K_M$ and $V_{max}^{app}<V_{max}$, which mimics uncompetitive inhibition.

[d] The calculated mode of inhibition was determined from the best fit K_i and K_i' equations as denoted in **chapter 2**. **Abbreviations:** AcCoA, acetyl coenzyme A; MOI, mode of inhibition; N/A, not applicable.

The same experiments were completed for SB023 as the compound inhibited the activity of MS_{Pa} with micromolar potency. Three concentrations of SB023 (5.5 μM, 11 μM, and 22 μM) were selected that were near to the IC_{50} (14.5 μM) to test on MS_{Pa}. After initiating the enzymatic reactions by titrating substrate glyoxylate (5-400 μM) in the presence of a fixed, saturating acetyl coenzyme A concentration (200 μM), there were clear increases in the K_M^{app} values of glyoxylate and slight decreases in V_{max}^{app} as the concentration of SB023 increased (**figure 31A** and **table 26**).

In the double reciprocal plots, the lines for the "no inhibitor" control, [-I], and 22 μM SB023 (>IC_{50} value) intersected at the same point on the x-axis, while the lines for 5.5 μM and 11 μM SB023 intersected with the [-I] line in the second quadrant between the x- and y-axes, suggesting that SB023 is a mixed-type inhibitor (1 & 2) for MS_{Pa} (**figure 31B**). Furthermore, the calculated inhibition constants K_i and K_i' for SB023 were 20.9 and 49.2 μM, respectively. This means SB023 will bind both [E] and [ES] with a preference for [E] as $K_i < K_i'$.[211]

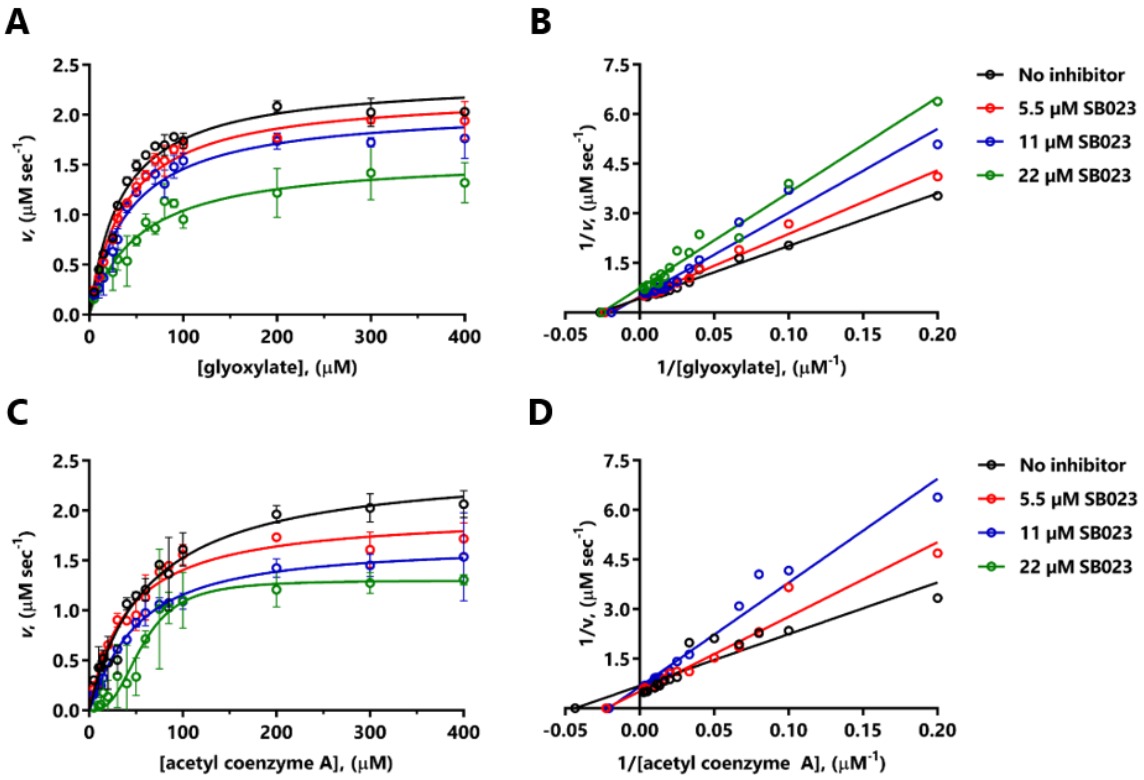

Figure 31. Mode of inhibition of MS_{Pa} by SB023. (A) Kinetic data obtained by titrating glyoxylate (5-400 μM) in the presence of no addition (black), 5.5 μM (red), 11 μM (blue), or 22 μM (green) SB023. **(B)** Lineweaver-Burk plot showing that SB023 displayed mixed inhibition when glyoxylate was titrated. **(C)** Kinetic data obtained by titrating acetyl coenzyme A (5-400 μM) in the presence of no addition (black), 5.5 μM (red), 11 μM (blue), or 22 μM (green) SB023. **(D)** Lineweaver-Burk plot showing that SB023 displays mixed inhibition when titrating acetyl coenzyme A.

When varying AcCoA concentrations (5-400 μM) in the presence of a fixed, saturating glyoxylate concentration (200 μM) (**figure 31C** and **31D**), the data displayed a sigmoidal distribution in the presence of 22 μM SB023. There were slight decreases in K_M^{app}/K_{half}^{app} values between the SB023 concentrations compared with the K_M of acetyl coenzyme A, see **table 26**. There was also a definite decrease in V_{max}^{app} with the addition of 22 μM SB023; however, V_{max}^{app} decreased more gradually in the presence of the two lower SB023 concentrations. According to the double reciprocal plots, the lines for 5.5 μM and 11 μM SB023 appear to intersect with the [-

I] line between the x- and y-axes, which suggests type 1 mixed inhibition (**figure 31D**). The inhibition constants for SB023, K_i and K_i', were determined as 19.6 μM and 46.1 μM, respectively. Additionally, the slopes and y-intercepts of the lines increased as the concentration of SB023 increased, while the x-intercepts fluctuated (**table 27**). This type of mixed inhibition mimics competitive inhibition and implies that while having the capability of binding to both [E] and [ES], SB023 favours binding to [E] due to a smaller K_i than K_i'.[211] This might suggest that the inhibitor is competing with acetyl coenzyme A in its binding pocket and that the inhibition is concentration-dependent. Much like SB002, then we can infer the potential binding pocket of SB023, but this would need confirmation through further structural evidence.

Table 27. Linear regression analysis of SB002 and SB023 inhibition of MS_{Pa}.

		Slope (K_M/V_{max})	*y*-intercept ($1/V_{max}$)	*x*-intercept ($1/K_M$)	R^2
Fixed [AcCoA]	**glyoxylate**	15.87 ± 0.47	0.42 ± 0.03	-0.027	0.9889
	3 μM SB002	19.73 ± 0.42	0.50 ± 0.03	-0.024	0.9941
	6 μM SB002	23.34 ± 1.71	1.49 ± 0.11	-0.068	0.9396
	9 μM SB002	51.45 ± 5.51	2.87 ± 0.37	-0.065	0.8882
	glyoxylate	15.87 ± 0.47	0.42 ± 0.03	-0.027	0.9889
	5.5 μM SB023	19.26 ± 0.58	0.45 ± 0.04	-0.023	0.9876
	11 μM SB023	25.38 ± 1.40	0.48 ± 0.09	-0.019	0.9588
	22 μM SB023	28.85 ± 1.14	0.74 ± 0.07	-0.026	0.9784
Fixed glyoxylate]	**AcCoA**	31.33 ± 1.56	0.64 ± 0.10	-0.021	0.9666
	3 μM SB002	113.2 ± 11.35	1.12 ± 0.73	-0.010	0.8766
	6 μM SB002	N/A	N/A	N/A	N/A
	AcCoA	19.99 ± 0.43	0.34 ± 0.03	-0.017	0.9940
	5.5 μM SB023	22.56 ± 1.29	0.51 ± 0.08	-0.022	0.9561
	11 μM SB023	31.45 ± 1.56	0.65 ± 0.10	-0.021	0.9667
	22 μM SB023	N/A	N/A	N/A	N/A

Abbreviations: AcCoA, acetyl coenzyme A; N/A, not applicable.

4.7 Kinetic mode of isocitrate lyase inhibition for SB002

To determine the kinetic mode of inhibition for SB002 on ICL_{Pa}, I again selected three concentrations (9 μM, 18 μM and 27 μM) near to the IC_{50} value determined by dose-response curves to test against ICL_{Pa}. After initiating the enzymatic reactions with increasing concentrations of substrate isocitrate (5-400 μM), there were reductions in both K_M^{app} and V_{max}^{app} values as the concentrations of SB002 increased (**figure 32A** and **table 28**).

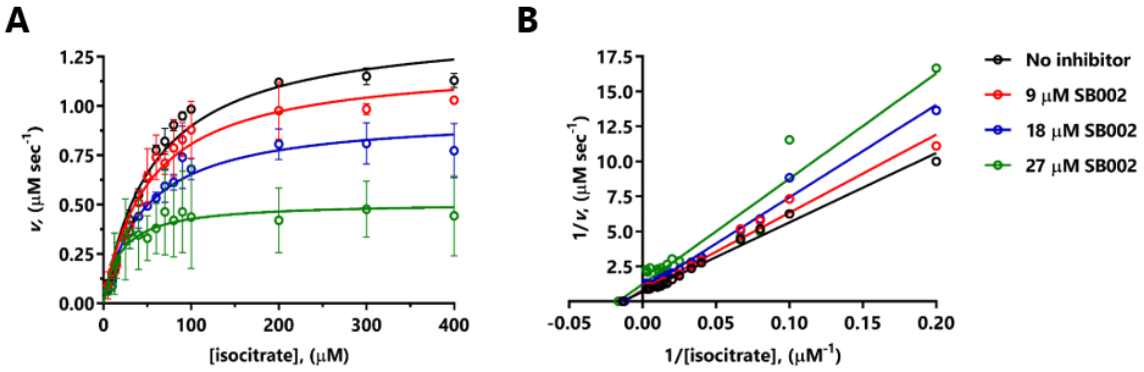

Figure 32. Mode of inhibition of ICL_{Pa} by SB002. (A) Kinetic data obtained by titrating isocitrate (5-400 μM) in the presence of no addition (black), 9 μM (red), 18 μM (blue), or 27 μM (green) SB002. **(B)** The Lineweaver-Burk plot showed that SB002 displayed mixed/noncompetitive inhibition of ICL.

Generally, this is a sign of uncompetitive inhibition, but the 1/*v versus* 1/[isocitrate] plot (**figure 32B**) consisted of all four lines converging at similar points on the x-axis.[267] Additionally, the slopes and y-intercepts of the lines increased as the concentration of SB002 increased (**table 29**), which points towards SB002 displaying type 2 mixed inhibition or classical noncompetitive inhibition of ICL_{Pa}. The linear regression for the highest concentration of SB002 (27 μM) seems to converge with the no inhibitor line below the x-axis, which indicates type 3 mixed inhibition. Therefore, SB002 has the capability of binding to both [E] and [ES]; however, the substrate *versus* velocity plots for all three concentrations best fit the equation for type 3 mixed inhibition (**equation 13** in **chapter 2**) in GraphPad Prism, simulating uncompetitive inhibition. The inhibition constant for binding to [ES], K_i', from this calculation was 21.3 μM, while K_i was equal to 0 μM. Thus, SB002 most likely binds to an allosteric site in the enzyme and favours binding to the [ES], which explains why K_M^{app} decreases for isocitrate at higher concentrations of SB002. The preferred mode of inhibition for SB002 is uncompetitive against ICL_{Pa}.

Table 28. Calculated kinetic parameters for SB002 inhibition of ICL_{Pa}. K_M, k_{cat}, and V_{max} values were derived from Michaelis-Menten kinetic analyses. K_i and K_i' values were determined from best-fit inhibition equations. Mode of inhibition was determined visually from linear regression analysis and calculated inhibition constants.

	K_M (μM)	V_{max} (μM s^{-1})	k_{cat}[a] (s^{-1})	K_i (μM)	K_i' (μM)	MOI Obs.[b]	MOI Calc.[c]
isocitrate	57.40	1.40	2.10	N/A	N/A	Substrate	Substrate
9 μM SB002	51.60	1.20	1.80	0.00	51.80	Mixed (2)	Uncompetitive
18 μM SB002	46.20	1.00	1.40	0.00	31.00	Mixed (2)	Uncompetitive
27 μM SB002	19.50	0.50	0.80	0.00	15.60	Mixed (3)	Uncompetitive
ALL SB002	**N/A**	**N/A**	**N/A**	**0.00**	**21.28**	**N/A**	**Uncompetitive**

[a] The value of E_t was based on the most likely oligomeric status of the native protein. ICL was assumed to be a tetramer.
[b] The two types of mixed inhibition observed for ICL_{Pa} from the Lineweaver-Burk plots: (2) [-I] and [+I] lines intersect at the x-axis, which indicates that [I] binds with equal affinity to [E] and [ES]; $K_i=K_i$', $K_M^{app}=K_M$, and $V_{max}^{app}<V_{max}$, which mimics noncompetitive inhibition. (3) [-I] and [+I] lines intersect below the x-axis, indicating that [I] binds to [ES] with greater affinity than [E]; $K_i< K_i$', $K_M^{app}<K_M$, and $V_{max}^{app}<V_{max}$, which mimics uncompetitive inhibition.
[c] The calculated mode of inhibition was determined from the best fit K_i and K_i' equations.
Abbreviations: MOI, mode of inhibition; N/A, not applicable.

To date, only one crystal structure of ICL_{Pa} exists (PDB entry 61GO), and in the structure, the active site is quite shallow and polar in nature.[268] An uncompetitive binding mode for SB002, a nonpolar molecule, could explain why the compound can still inhibit ICL_{Pa} with decent potency. It would be wise in the future to computationally interrogate the ICL_{Pa} crystal structure for open druggable pockets or allosteric sites in the enzyme where a ligand like SB002 could bind. 3-NP and 3-bromopyruvate, which are analogues of the enzyme product succinate, are uncompetitive inhibitors of ICL_{Mt} concerning isocitrate and have been shown to bind covalently to a catalytic cysteine residue, Cys191, which exists in ICL_{Pa} as Cys222.[259,268]

Table 29. Linear regression analysis of SB002 inhibition of ICL_{Pa}.

	Slope (K_M/V_{max})	*y*-intercept ($1/V_{max}$)	*x*-intercept ($1/K_M$)	R^2
isocitrate	49.58 ± 1.48	0.68 ± 0.09	-0.013	0.987
9 μM SB002	55.83 ± 2.09	0.75 ± 0.13	-0.014	0.980
18 μM SB002	66.13 ± 2.02	0.82 ± 0.13	-0.012	0.986
27 μM SB002	75.27 ± 5.55	1.24 ± 0.35	-0.016	0.924

4.8 Hit validation of SB002 and thermodynamics of binding

Isothermal Titration Calorimetry (ITC) is considered the gold standard for accurately determining the thermodynamics of interactions between small molecules and enzymes.[269] ITC is sensitive enough to detect thermal changes of these interactions without any labelling, immobilisation or limit on the size of either interacting entities.[270] ITC was performed to see if direct binding of SB002 to both MS_{Pa} and ICL_{Pa} was detectable. I chose SB002 as it had the highest potency of the 2-aminopyridines tested and was the only compound to inhibit both enzymes completely in the enzyme kinetic analyses. Dr Xavier Chee from the Department of Pharmacology at the University of Cambridge assisted me in the study design and data analysis.

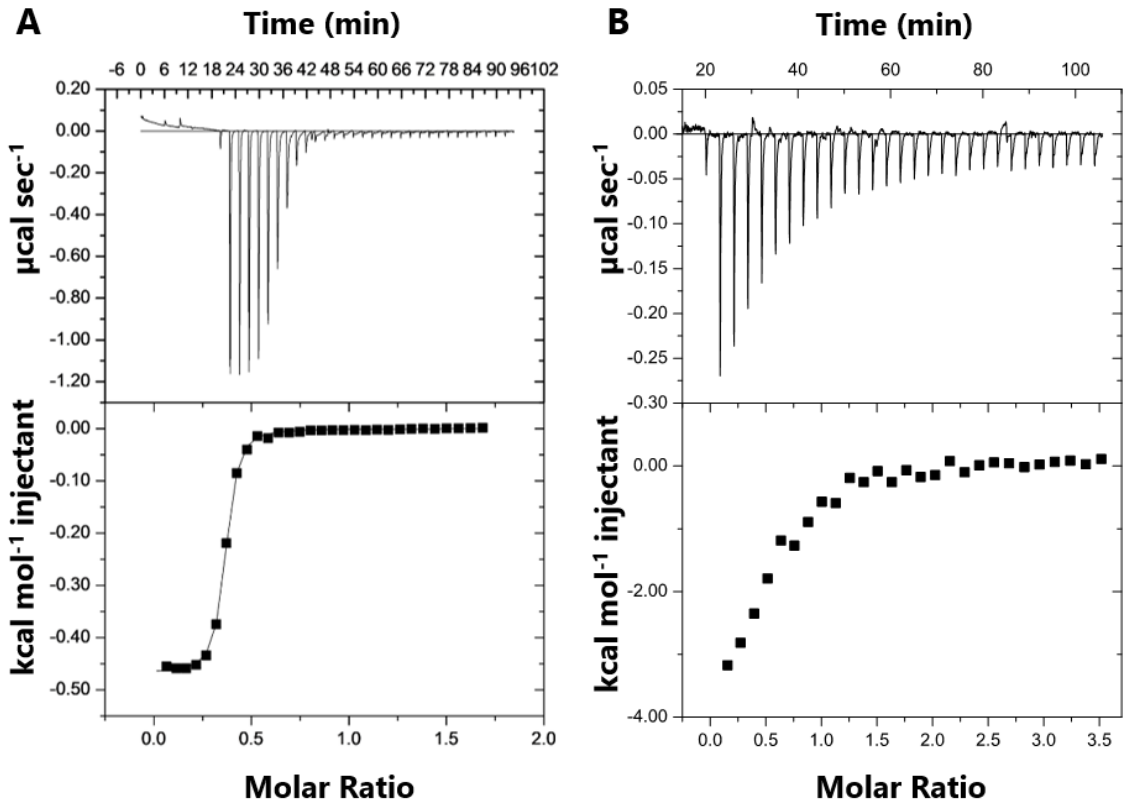

Figure 33. Isothermal titration calorimetry plots for SB002 binding to MS_{Pa} and ICL_{Pa}. The top panels illustrate the raw isothermal titration calorimetry data from 30 equal injections of either **(A)** MS_{Pa} or **(B)** ICL_{Pa} into the cell containing SB002. Both interactions are exergonic. The bottom panels illustrate the respective binding isotherms created by plotting the integrated heat peaks against the molar ratio of protein to ligand.

Purified MS_{Pa} (110 μM) or ICL_{Pa} (202 μM) were reverse titrated into the calorimeter cell containing SB002 (11 μM) using a VP-ITC at 25°C. Due to its limited working concentrations, SB002 was loaded into the cell rather than the syringe, which required lower concentrations. Protein samples were dialysed before loading in the syringe, and the dialysis buffer was used to

adjust concentrations of the protein and ligand samples to minimise heat fluctuations due to buffer exchange. The syringe and the cell contained a final concentration of 0.1% of DMSO.

The interactions between MS_{Pa}-SB002 and ICL_{Pa}-SB002 were exothermic due to the negative heat values on the y-axes of the graphs in **figure 33**. SB002 became saturated with both proteins after ten injections, after which the baselines returned to their initial heats. The raw data for ICL_{Pa} shows a sustained heat accompanying the additional injections after saturation, which is a sign of enthalpy of dilution.[270] The area of each injection peak was then integrated and plotted *versus* the molar ratio of protein to ligand. The resulting isotherms were fitted to a one-site binding model, and the thermodynamic parameters were derived from the fit, see **table 30**. The slope of the sigmoidal binding isotherm is equal to the equilibrium association constant (K_a) of the ligand-protein complex.[271] The inverse of K_a is equal to the equilibrium dissociation constant (K_d) of the protein-ligand complex, and K_a and K_d together indicate the overall binding affinity.[272] Thus, larger slopes indicate larger K_a values and smaller K_d values, meaning better binding affinities.[273] Visually, the slope of the binding isotherm for MS is steeper than for ICL_{Pa}. Based on this, SB002 has a higher binding affinity for MS_{Pa}.

Table 30. Thermodynamic parameters of SB002 binding to MS_{Pa} and ICL_{Pa}.

Thermodynamics	MS_{Pa}	ICL_{Pa}
ΔG (kcal mol^{-1})	$-10.31 \pm 1.79\times10^{-3}$	$-7.98 \pm 3.44\times10^{-1}$
ΔH (kcal mol^{-1})	$-0.47 \pm 1.79\times10^{-3}$	$-4.22 \pm 3.44\times10^{-1}$
$-T\Delta S$ (kcal mol^{-1})	-9.84	-3.76
K_a (M^{-1})	$3.56\times10^{7} \pm 1.86\times10^{6}$	$7.18\times10^{5} \pm 1.49\times10^{5}$
K_d (nM^{-1})	28.60 ± 1.6	$1{,}430 \pm 0.30$
***n* (binding sites)**	$0.35 \pm 8.41\times10^{-4}$	$0.53 \pm 3.25\times10^{-2}$

Abbreviations: K_a, equilibrium association constant; K_d, equilibrium dissociation constant.

A Gibb's free energy value (ΔG) <0 means the interaction is exergonic and energetically favourable. Therefore, smaller ΔG values correspond to higher binding affinities, signifying that less work is required to achieve an interaction between the protein and the ligand.[274] ΔG was calculated as -10.31 kcal mol^{-1} for MS_{Pa}-SB002 and -7.98 kcal mol^{-1} for ICL_{Pa}-SB002, see **table 30**. Enthalpic and entropic terms quantify ΔG (depicted in **equation 16** of **chapter 2**). The enthalpic term (ΔH) is a direct measure of the heat or energy associated with forming a macromolecular complex at a given temperature. ΔH is the number and strength of bonds broken and created during the molecular interaction. Hydrogen bonding and Van der Waals forces are the primary contributions to ΔH, and hydrogen bonding corresponds to a better binding affinity as the binding is more exothermic than those involved in Van der Waals forces.[274] ΔH for MS_{Pa}-SB002 was -0.47 kcal mol^{-1} and was -4.22 kcal mol^{-1} for ICL_{Pa}-SB002. This is generally low for

biomolecular interactions of approved drugs, where is it common to see ΔH values around -30 kcal mol^{-1}.[269]

The entropic term (ΔS), conversely, gives an indication of hydrophobic interactions and changes in protein conformation upon binding. Favourable entropic binding affinities are derived primarily from hydrophobic interactions.[275] An example of a hydrophobic interaction is the release of tightly bound water upon ligand binding in the binding pocket. Unfavourable entropy usually results from an overall decrease in the degrees of freedom of the protein or ligand when interacting. This means that the protein has undergone a large conformational change or that the ligand is very flexible.[276] -TΔS was -9.84 kcal mol^{-1} for MS_{Pa}-SB002, and was -3.76 kcal mol^{-1} for ICL_{Pa}-SB002. The differences in thermodynamic parameters calculated for MS_{Pa}-SB002 and ICL_{Pa}-SB002 are represented visually in **figure 34**.

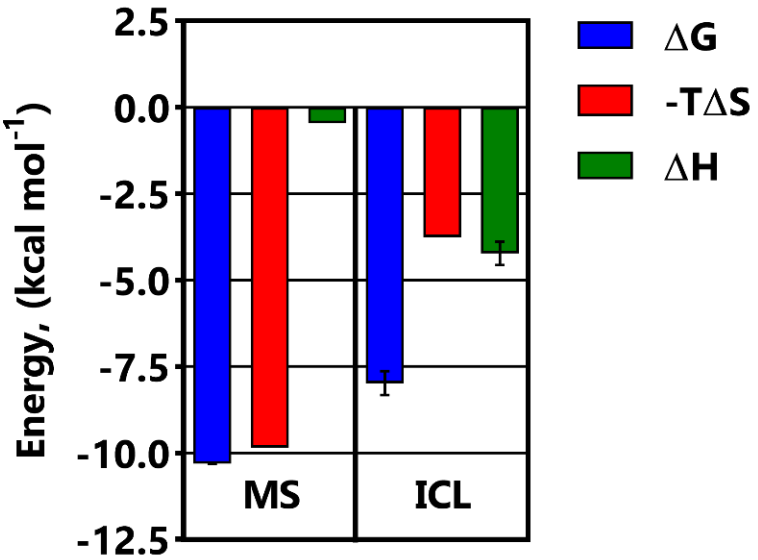

Figure 34. Thermodynamic parameters of MS_{Pa}-SB002 and ICL_{Pa}-SB002. The thermodynamic interactions and the proportions by which enthalpy (ΔH) and entropy (-TΔS) contribute to Gibb's free energy (ΔG) of binding are shown for MS_{Pa}-SB002 **(left)** and ICL_{Pa}-SB002 **(right)** as determined by isothermal titration calorimetry. MS_{Pa}-SB002 binding is driven largely by entropy, whereas ICL_{Pa}-SB002 binding is driven equally by entropy and enthalpy.

The K_d constants for MS_{Pa}-SB002 and ICL_{Pa}-SB002 were calculated as 28.6 nM and 1.43 μM, respectively. The number of binding sites (*n*) in the proteins was also calculated from the molar ratio of protein to ligand near to the inflection point of the binding isotherm (**figure 33**). Because I performed a reverse titration, SB002 was in excess early in the experiment. If there is more than one binding site in the protein, then both sites will be occupied by the ligand and will contribute to ΔH (*e.g.* $H_{site\ 1} + H_{site\ 2}$).[270] Once enough protein has been added to interact with all of the ligands in the cell (after the inflection point in the binding isotherm), then some ligand molecules in weaker interactions leave the second binding site to occupy the stronger first site.[277]

The inflection points of the isotherms were estimated visually and calculated from the binding isotherm at the molar ratios of 0.35 and 0.53 for MS_{Pa}-SB002 and ICL_{Pa}-SB002, respectively. Therefore, the prevailing binding stoichiometry is two molecules of SB002 for one molecule of ICL_{Pa} in two identical binding sites in the protein. For MS_{Pa}, n = 0.35, suggesting a ratio of 2.85 molecules of SB002 for every one molecule of MS_{Pa}, which cannot be accurate. The error present in the calculated value of n is most likely due to errors in the measured concentration of MS_{Pa}, or if the measured concentration was correct, that a proportion of the protein sample was inactive or unfolded. If we assume an n of 0.5 (2:1 ligand: protein ratio) for MS_{Pa}, we can calculate (using **equation 18** in **chapter 2**) that approximately 70% of the total concentration of MS_{Pa} was active in the syringe, which altered the actual active MS_{Pa} concentration in the syringe to 77 μM. It is worth noting that in a standard titration (ligand titrated into protein), it might be possible to observe a 1:1 stoichiometry (n = 1) as the protein is in excess at the start of the experiment, but due to experimental design constraints, namely solubility, this was not possible with SB002.

Overall, SB002 displays a higher binding affinity for MS_{Pa} than ICL_{Pa}, which correlates with the previous kinetic data. The interaction between MS_{Pa} and SB002 is largely driven by entropy, whereas the interaction between ICL_{Pa} and SB002 is driven more equally by enthalpy and entropy. This has interesting implications for the molecular binding mechanism of SB002 to the two proteins. For MS_{Pa}, with a favourable entropic term (-9.84 kcal mol^{-1}), upon binding, there could be some displacement of water molecules tightly-bound to the protein in a hydrophobic binding pocket. For ICL_{Pa}, there are similar events of hydrogen bonding or Van der Waals interaction events (ΔH) as potential conformational changes or water displacement events (-TΔS) upon ligand binding.

ITC may not tell us the exact binding pocket of the ligand in the protein, but the calculated thermodynamic parameters do have important consequences in drug discovery. When moving from hit to lead validation for a drug candidate, chemically modifying compounds to optimise the enthalpic term, while much more challenging than chemically optimising the entropic term (through the addition of hydrophobic groups), can result in much better binding affinity.[274] More favourable ΔH values signify better non-covalent bonding between the protein and the ligand as well. In fact, over the course of hit to lead optimisation, the entropic term of a compound usually improves as the drug discovery programme proceeds.[274] However, there is a limit to the improvement that can be gained from increasing the hydrophobic nature of a compound, as aqueous solubility is eventually compromised. Ultimately, high-resolution structural data is required to gain the most insight into binding.

4.9 Crystallisation of protein-ligand complexes

Obtaining an X-ray crystal structure of a protein-ligand complex is a conclusive validation of a binding event because it allows for the direct visualisation of protein and ligand interactions at atomic resolution.[269] Both of the protein purification methods for the target enzymes satisfied the requirements for protein crystallisation; namely, they yielded highly pure protein (>95%) and highly soluble protein in at high concentrations.[230] Gels from SDS-PAGE analyses are shown in results **chapter 3** and **appendix 3** for MS_{Pa} and ICL_{Pa}, respectively. Both glyoxylate shunt enzymes from *P. aeruginosa* have been successfully crystallised in their native forms in the Welch laboratory; malate synthase G by myself (PDB entry 5OAS) and isocitrate lyase by Audrey Crousilles (PDB entry 61GO). SB002's mechanisms of action on the target enzymes were also unclear. I endeavoured to obtain crystal structures with the ligand bound for these reasons.

4.9.1 MS_{Pa}-SB002 soaking

I reasoned from kinetic data that it was possible that SB002 competes with acetyl coenzyme A for binding in MS_{Pa}. In an MS_{Mt} crystal structure (PDB entry 2GQ3), acetyl coenzyme A interacts with several amino acids near the entrance of the active site.[181] In our computational analysis of putative drug binding sites in MS_{Pa} in results **chapter 3**, the acetyl coenzyme A binding site was among the highest-scoring druggable sites.

Ligand soaking experiments with MS_{Pa} were undertaken because I had already established a crystallisation system. I presumed I had a crystal form suitable for ligand soaking, *i.e.* that my proposed binding site (the acetyl coenzyme A binding pocket) was exposed to solvent channels and would be accessible to the ligand. Another requirement for ligand soaking is that the protein does not undergo a large conformational change upon ligand binding, which would cause the crystal to crack.[278] These two requirements allow for the ligand to diffuse into the crystal while preserving the crystal's integrity, which ensures higher quality data collection.

Purified MS_{Pa} (146 μM) was brought to a state of supersaturation, which allowed for small aggregates (nuclei) to form spontaneously to spur crystal growth. The degree of supersaturation was controlled by the precipitating agents in the crystallisation mixture (PEG 4000 and glycerol), which served to immobilise water and increase the effective protein concentration, as well as the salt in the mixture ($AmSO_4$), which improved protein solubility. Controlled supersaturation levels allowed the protein in solution to support crystalline growth rather than produce additional crystal nuclei by shifting into the metastable zone of saturation.[279] Crystalline growth in this zone was slow enough to form medium-sized crystals of 100-200 μm in length in three-five days. As a

crystal's total scattering power depends on its volume, the crystal needed to be large enough to harvest into loops and collect diffraction data manually.[280]

I diluted a stock of SB002 in DMSO into a solution of cryoprotectant and added 0.5 μL of this ligand-cryoprotectant mixture directly to the crystallisation drops to minimise crystal manipulation. SB002 had a final concentration of 1 mM and 6.25% DMSO per drop. All time points after 1 hour resulted in visual deterioration of the crystals, a sign that they were sensitive to the solvent (not shown). Therefore, I harvested and collected data for a "control" apo crystal (not shown), "instant soak" crystals, and crystals soaked for ten minutes and 30 minutes to determine diffraction and ligand occupancy, see **table 31**.

The best "instant soak" crystal diffracted to a resolution of 2.05 Å, the best of the crystals soaked for 10 minutes diffracted to 1.87 Å, and the crystals soaked for 30 minutes did not diffract, see **table 31**. The structures were solved using molecular replacement with the apo structure (PDB entry 5OAS). The data processing, model quality, and electron densities were all scrutinised by Dr Paul Brear from the Crystallographic X-ray facility before proceeding. When we compared the models and electron densities after initial refinement to that of the apo model, we did not see clear differences between the calculated electron densities. Any unmodelled electron density in the soaked crystal structures was solely indicative of water molecules. Also, aligning the soaked MS_{Pa} models with the apo model did not reveal any differences between the tertiary structures (not shown).

One reason for the absence of ligand electron density in the soaked crystals could be that the binding site was inaccessible to the ligand in that particular crystal form because there was a flexible portion of the protein that interfered with the site, or that crystal packing contacts within the crystal obstructed the site. I expected the ligand binding site to be the acetyl coenzyme A binding site, which was accessible to solvent channels in the apo structure; however, it is conceivable that the *true* binding site could be elsewhere in the protein and not actually accessible to the ligand.

Another conceivable reason for the absence of electron density for SB002 was due to low ligand occupancy in the crystals. In order to visualise a ligand in the calculated electron density map, at least 50% of all the binding sites in the crystal should be occupied by the ligand. Ideally, this occupancy should be closer to 90% for certainty in placing the correct pose of the ligand.[278] Low SB002 occupancy was either caused by insufficient ligand diffusion in the cryoprotectant mixture or by inadequate soaking times relative to the crystals' sizes. 10-20 μm crystals can reach 80% occupancy in fewer than 30 seconds, and these shorter soak times evidently minimise damage to the crystals.[278] Soaking smaller crystals was not practical in my situation because they were more

Table 31. Data collection statistics for MS_{Pa}-SB002 soaking experiments.[a]

Protein	MS_{Pa}			
Crystallisation conditions	146 µM protein 25 mM ammonium sulphate 13−17% (v/v) glycerol 20−27% (w/v) polyethylene glycol 4000			
Soaking conditions	**1 mM SB002, 6.25% DMSO + 93.75% cryoprotectant** (24% ethylene glycol + 76% mother liquor) per drop			
Soaking times	0 minutes (instant harvest)		10 minutes	30 minutes
Pre-soaked crystals			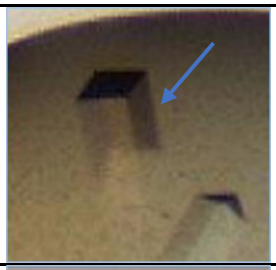	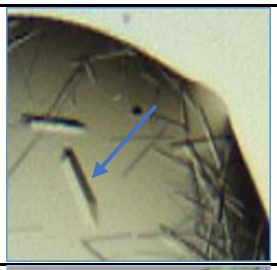
Harvested crystals	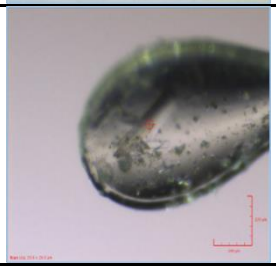		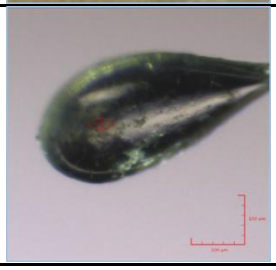	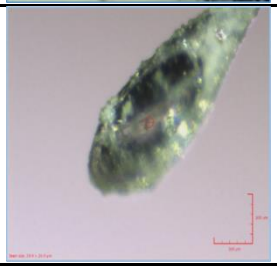
Approximate crystal length	~200 µm		~125 µm	~175 µm
Crystal system	orthorhombic		orthorhombic	orthorhombic
X-ray source	DLS MX-I03		DLS MX-I03	DLS MX-I03
Wavelength (Å)	0.9763		0.9763	0.9763
Resolution (Å)	70.60-2.05		81.53-1.87	**No diffraction**
Total reflections	343,006 (16,099)		423,824 (19,335)	
Unique reflections	53,812 (2,459)		66,761 (3,195)	
Multiplicity	6.4 (6.5)		6.3 (6.1)	
Completeness	99.7% (92.1%)		99.9% (96.6%)	
Mean I/σ(I)	8.9 (2.3)		8.2 (1.8)	
$CC_{1/2}$	1.0 (0.6)		1.0 (0.5)	
R_{meas}	0.182 (1.826)		0.150 (1.396)	
Mosaic spread	 **0.27**		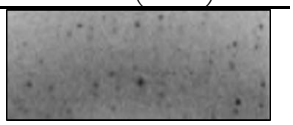 **0.44**	
Space group	$P2_1\ 2_1\ 2_1$		$P2_1\ 2_1\ 2_1$	
Unit cell parameters (Å, °)	A=70.47 B=81.88 C=139.38	α=90.00 β=90.00 γ=90.00	A=70.34 B=81.53 C=138.84	α=90.00 β=90.00 γ=90.00
Ligand	No clear ligand electron density		No clear ligand electron density	-

[a] Values in parenthesis are statistics for the highest resolution shell.

difficult to harvest manually, and I did not have access to crystal harvesting robotics or *in situ* data collection. These crystals (100-200 μm) could not tolerate high DMSO concentrations as indicated by damage accrued during soaking. This naturally dictated changes in any future soaking. Ultimately, though, I knew SB002 had poor aqueous solubility, and that I had a limited quantity of crystallisable MS_{Pa}, so I could not explore options like longer soaks with higher ligand concentrations and lower solvent concentrations. Consequently, I attempted co-crystallisation.

4.9.2 MS_{Pa}-SB002 co-crystallisation

SB002 dissolved in DMSO was added to 146 μM of purified MS_{Pa} to achieve a final ligand concentration of 300 μM and a protein to ligand ratio of 1:2. In general, it is advised to have the ligand concentration 10x higher than the K_d.[230] I thought this ligand concentration would be enough to fulfil the binding stoichiometry predicted by ITC, and I also reasoned that 1% DMSO was low enough not to affect the crystallisation dynamics. The protein and ligand mixture was left to incubate for ≥60 minutes on ice. The mixture was added to an optimisation plate, and the protein was again brought to supersaturation by mixing 200 nL of the reservoir solution with the protein in the drop.

The three best co-crystals diffracted to 1.29 Å, 1.33 Å, and 1.74 Å, which reflects crystal lattices with tight packing, see **table 32**. The structures were again solved using molecular replacement with my apo MS_{Pa} structure as the template (PDB entry 5OAS). Two crystals developed in a monoclinic crystal system (space group $P1\ 2_1\ 1$) with unit cell dimensions of a=65.27 Å, b=111.08 Å, c=98.25 Å and a=64.91 Å, b=111.0 Å, c=98.22 Å. Both crystals had two protomers in the asymmetric unit (ASU), related by an approximate non-crystallographic two-fold axis. The third crystal developed in an orthorhombic crystal system (space group $P2_1\ 2_1\ 2_1$) with unit cell dimensions of a=70.80 Å, b=81.50 Å, and c=137.22 Å and one protomer in the ASU. Again, the data processing, model quality, and electron densities were all confirmed by Dr Paul Brear before proceeding. When we compared all of the initial models and calculated electron densities after initial refinement to that of the apo model, we saw an improvement in the electron density quality for the monoclinic crystals, but we did not see any obvious electron density for the ligand. Unmodelled electron density in the co-crystal structures after refinement was solely indicative of water molecules. Also, aligning each structure with the apo structure again did not reveal any significant differences between the tertiary structures (not shown).

Co-crystallisation is known to result in varying ligand occupancies between crystals, as well as reduced ligand occupancy in general when compared with soaking.[278] I considered the possibility that the crystallisation conditions were not compatible with the optimal ligand binding conditions. Dr Xavier Chee from the Department of Pharmacology performed a thermal shift assay to find

Table 32. Data collection statistics of three co-crystals of MS_{Pa}-SB002.[a]

Protein	MS_{Pa}					
Crystallisation conditions	146 µM protein 300 µM SB002 (2:1 ligand: protein) 1% DMSO 25 mM ammonium sulphate 13−17% (v/v) glycerol 23−27% (w/v) PEG 4000					
Co-crystals	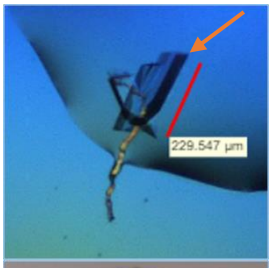		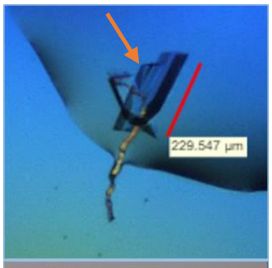		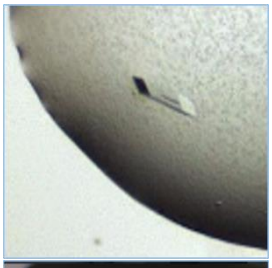	
Harvested co-crystals	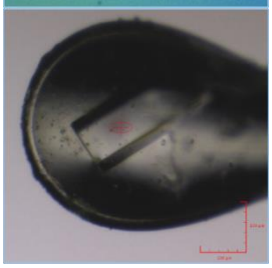		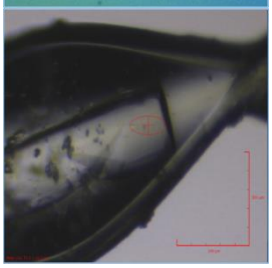		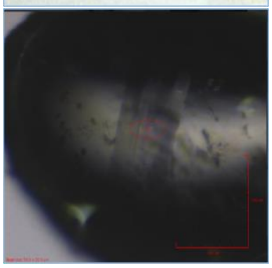	
Approximate crystal length	~225 µm		~ 225 µm		~200 µm	
Crystal system	monoclinic		monoclinic		orthorhombic	
X-ray source	DLS MX-I03		DLS MX-I03		DLS MX-I03	
Wavelength (Å)	0.9763		0.9763		0.9763	
Resolution (Å)	55.54-1.29		111.00-1.33		70.80-1.74	
Total reflections	1,084,450 (32,526)		950,173 (26,852)		519,623 (22,436)	
Unique reflections	337,198 (13,966)		303,930 (12,332)		82,221 (3,982)	
Multiplicity	3.2 (2.3)		3.2 (2.2)		6.3 (5.0)	
Completeness	98.4% (81.8%)		97.6% (79.4%)		100% (98.2%)	
Mean I/σ(I)	11.6 (1.0)		10.4 (1.0)		13.1 (1.1)	
$CC_{1/2}$	1.0 (0.5)		1.0 (0.7)		1.0 (0.5)	
R_{meas}	0.056 (1.110)		0.055 (0.956)		0.065 (1.702)	
Mosaic spread	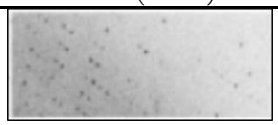		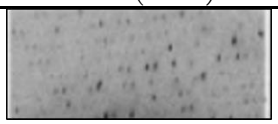		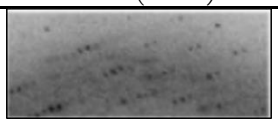	
	0.25		**0.36**		**0.58**	
Space group	*P*1 2_1 1		*P*1 2_1 1		*P*2_1 2_1 2_1	
Unit cell parameters (Å, °)	A=65.27 B=111.08 C=98.25	α=90.00 β=102.00 γ=90.00	A=64.91 B=111.0 C=98.22	α=90.00 β=101.74 γ=90.00	A=70.80 B=81.50 C=137.22	α=90.00 β=90.00 γ=90.00
Ligand	No clear ligand electron density		No clear ligand electron density		No clear ligand electron density	

[a] Values in parenthesis are statistics for the highest resolution shell. **Abbreviations:** DMSO, dimethyl sulfoxide; PEG, polyethylene glycol.

the binding conditions most stable against thermal denaturation. We tested MS_{Pa} and 1 mM SB002 in various buffers, pH values, and with or without 10 mM $MgCl_2$ and $NaSO_4$. The analysis showed the greatest thermal stability for MS_{Pa}-SB002 was at a pH of 7.5 in KH_2PO_4 buffer with 10 mM $MgCl_2$ added, followed by Tris buffer, pH 7.5, with 10 mM $MgCl_2$ added (data not shown). Therefore, I set out to find different co-crystallisation conditions that would encourage ligand binding.

Concentrations of SB002 were added to 75 and 146 μM of MS_{Pa} in 50 mM KH_2PO_4 buffer with 10 mM $MgCl_2$ and incubated for ≥60 minutes on ice before samples were added to industry screening matrices. The screens were repeated with 1 mM glyoxylate added to the protein-ligand mixture in the event it would also stabilise ligand binding. In the second co-crystallisation attempt of MS_{Pa} and SB002, there was no crystal formation in any condition after eight days; however, the best outcomes are displayed in **table 33**.

In the first condition listed in **table 33** is what appears to be microcrystalline material (crystals smaller than 20 μm), which are difficult to differentiate from precipitate unless polarising optics are used to detect birefringence.[281] Either way, because the contents of the drop are light in colour, it signalled that the protein was not denatured. Other conditions contained small (<50 μm), poor quality crystals, or spherulites, which are spherical masses of semi-crystalline material and a sign that the crystallisation kinetics are too rapid to form crystals.[282]

Furthermore, when the substrate glyoxylate was added to the mixture, no apparent improvement was observed, with the best of drops containing either spherulites or phase separation, which is indicative of a protein-rich phase that separated from the original drop solution.[279] Some of the chemicals appeared in common between these conditions from the secondary screen. One of them was PEG, although at different molecular weights, while another was calcium salt that had either acetate or chloride as the anion moiety. The pH of the solutions ranged from pH 6.0 to pH 8.5. The theoretical pI of MS_{Pa} is 5.47, which could explain why the largest crystals formed in the drop with a pH of 6.0.[201]

Despite the promising formation of microcrystalline material in some of the screens, the conditions were recalcitrant to optimisation attempts. SB002 was hindering the formation of the crystal lattice somehow, perhaps because the binding site was near to a critical point for crystal packing in the protein. Cases have been reported where additive molecules have made crucial interactions between protein molecules in the crystal that helps the secure the formation of the lattice.[283–285] Such small molecules sometimes have a physiological basis for their presence, but others simply provide essential or at least helpful crosslinks within the crystal. Perhaps in the future, some of these additives could be utilised to co-crystallise MS_{Pa} and SB002 successfully.

Table 33. Images of MS_{Pa}-SB002 co-crystallisation drops after eight days. Images and UV-filtered images were captured by Rock Imager 1000 automated imaging system.

Conditions	Images	UV images (280 nm)	Classification
75 µM protein 300 µM SB002 1% DMSO 0.1 M Tris pH 8.5 8% (w/v) PEG 8000	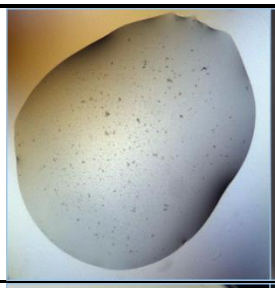	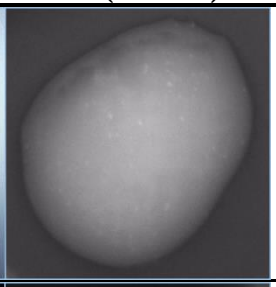	Light precipitation or Microcrystals
146 µM protein 5 mM SB002 0.5% DMSO 0.1 M MES pH 6.0 0.2 M calcium chloride 20% (w/v) PEG 6000	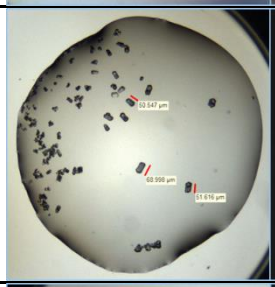	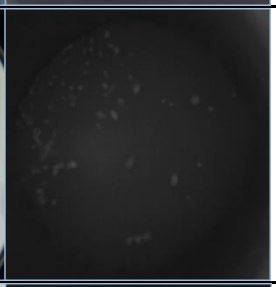	Small crystals (50 µm), not suitable for diffraction
146 µM protein 5 mM SB002 0.5% DMSO 0.1 M Tris pH 7.0 0.2 M calcium acetate 20% (w/v) PEG 3000	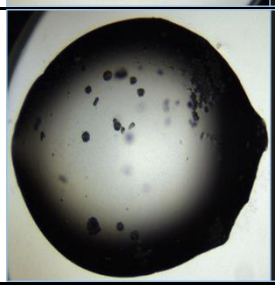	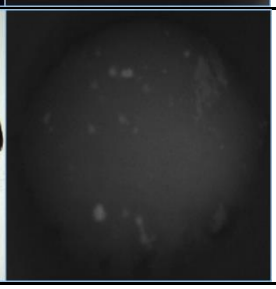	Spherulites
146 µM protein 5 mM SB002 1 mM glyoxylate 0.5% DMSO 0.1 M Imidazole pH 8.0 0.2 M calcium acetate 10% (w/v) PEG 8000	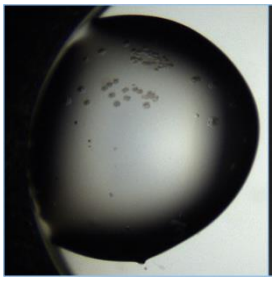	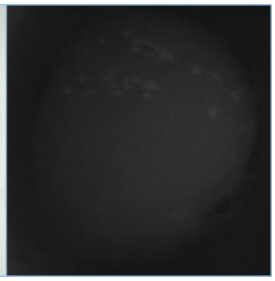	Phase separation
146 µM protein 5 mM SB002 1 mM glyoxylate 0.5% DMSO 0.1 M HEPES pH 7.5 0.2 M calcium chloride 28% (w/v) PEG 400	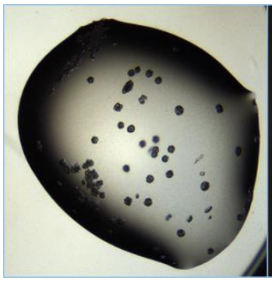	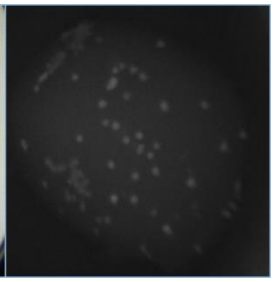	Spherulites

Abbreviations: DMSO, dimethyl sulfoxide; PEG, polyethylene glycol.

4.9.3 ICL_{Pa}-SB002 co-crystallisation

ICL_{Pa} has been shown to function as a biological tetramer.[174] Its oligomeric status, along with an uncompetitive SB002's binding mode, led me to believe that co-crystallisation would yield better results than soaking because the protein might require a conformational change during ligand binding. SB002 was added to purified ICL_{Pa} (340 μM or 170 μM) to achieve a final ligand concentration of 800 μM in 3% DMSO and approximate protein to ligand ratios of 1:2 and 1:4. I anticipated this ligand concentration would fulfil the binding stoichiometry predicted by ITC in a previous section.

Multiple chemically-distinct conditions produced crystals after two-five days. Various co-crystal morphologies formed in several of the conditions, but I prioritised the co-crystals containing a bipyramid morphology and a length between 100-200 μm to harvest for data collection. I thought these crystals would have tighter crystal packing as a result of more internal order, and that they tend to diffract to a higher resolution than other crystal morphologies like plates or needles. **Table 34** displays the two best diffracting co-crystals from this experiment. These crystals diffracted to 1.93 Å and 2.63 Å with unit cell dimensions of a=78.69 Å, b=111.55 Å, c=897.34 Å and a=80.93 Å, b=114.99 Å, c=895.10 Å, respectively. Both co-crystals had a c-axis of nearly 900 Å in length. Single macromolecules are not usually >200 Å in any single dimension.[286] ICL_{Pa} was crystallising in this morphology with several protomers in the ASU.

Large unit cells often fail to diffract to high resolutions and are sensitive to radiation damage due to unusually high solvent content.[287] Diffraction patterns of large unit cells also show spots that lie very close to each other on the detector, which defines high mosaicity, or the angular measure of the degree of long-range order of the unit cells within a crystal.[288] Lower mosaicity indicates better-ordered crystals that tend to result in better diffraction.[289] Because of the high mosaicity in the diffraction patterns, see **table 35**, and the large calculated unit cell, Dr Paul Brear again assisted me in processing the data and solving the structure of the 1.93 Å crystal through molecular replacement with the native ICL_{Pa} solved by the Welch laboratory (PDB entry 6G1O). The model resulted in an ordered core but was very disordered in the C and N termini regions (not shown). Despite this, we could not discern any electron density for SB002 in the modelled protein core after several attempts at refinement.

I repeated the co-crystallisation screens with larger amounts of ligand (achieved by increasing SB002 stock concentrations using sonication at 30°C and 60°C) so that the final SB002 concentration added to the drop was 6 mM with 0.5% DMSO. Many crystals formed in the same conditions as when 800 μM SB002 was added, which was surprising because of the large increase in ligand concentration. The best of these crystals is shown in **table 34** (3rd column) and diffracted

Table 34. Data collection statistics of three co-crystals of ICL_{Pa}-SB002.[a]

Protein	ICL_{Pa}		
Crystallisation conditions	340 µM protein 800 µM SB002 3% DMSO 25% w/v PEG 1500 0.1 M MIB buffer, pH 5.0	340 µM protein 800 µM SB002 3% DMSO 0.1 M Na_3 Citrate 20% w/v PEG 4000 5% v/v isopropanol	340 µM protein 6 mM SB002 1% DMSO 25% w/v PEG 1500 0.1 M SPG buffer, pH 8.0
Crystals		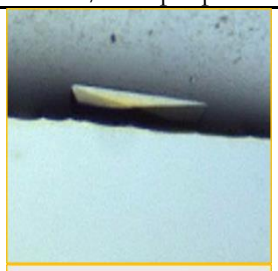	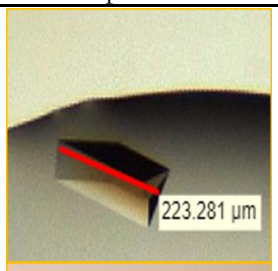
Harvested crystals	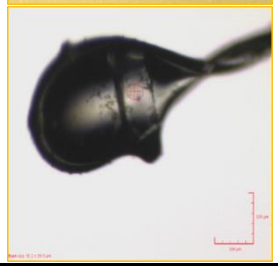	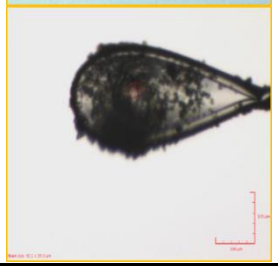	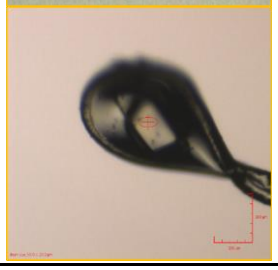
Crystal length	~200 µm	~150 µm	~225 µm
Crystal system	orthorhombic	orthorhombic	orthorhombic
X-ray source	DLS MX-I04	DLS MX-I04	DLS MX-I03
Wavelength (Å)	0.9795	0.9795	0.9762
Resolution (Å)	66.25-1.93	114.05-2.63	64.36-1.81
Total reflections	1,343,265 (11,506)	812,923 (37,736)	1,732,296 (32,691)
Unique reflections	269,193 (7,115)	125,249 (6,077)	106,740 (5,309)
Multiplicity	5.0 (1.6)	6.5 (6.2)	16.2 (6.2)
Completeness	89.2% (47.6%)	99.9% (98.1%)	100% (100%)
Mean I/σ(I)	8.7 (0.9)	5.8 (1.6)	13.1 (2.2)
$CC_{1/2}$	1.0 (0.4)	1.0 (0.6)	1.0 (0.5)
R_{meas}	0.102 (0.853)	0.201 (1.373)	0.170 (0.887)
Mosaic spread	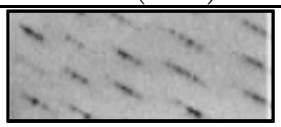 **1.24**	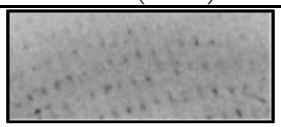 **0.45**	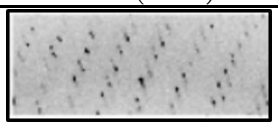 **0.75**
Space group	*I*2 2 2	*I*2 2 2	*P*2 2 2_1
Unit cell parameters (Å, °)	A=78.69 α=90.00 B=113.55 β=90.00 C=897.34 γ=90.00	A=80.93 α=90.00 B=114.99 β=90.00 C=895.10 γ=90.00	A =79.32 α=90.00 B = 113.86 β=90.00 C =128.72 γ=90.00
Comments	Large unit cell; no ligand electron density	Large unit cell; no ligand electron density	Poor data for MR; irregular intensities

[a] Values in parenthesis are statistics for the highest resolution shell. **Abbreviations:** DMSO, dimethyl sulfoxide; MIB, sodium **m**alonate: **i**midazole: **b**oric acid buffer in molar ratios of 2:3:3; PEG, polyethylene glycol; SPG, **s**uccinic acid: sodium dihydrogen **p**hosphate: **g**lycine buffer in molar ratios of 2:7:7.

to 1.81 Å with unit cell dimensions of a=79.32 Å, b=113.86 Å, c=128.72 Å and two protomers in the ASU. I solved the structure via molecular replacement, but the resulting model had large portions of the chains missing. The refinement statistics (R_{flags}) were ≥0.38 and did not decrease despite progress made to the model during refinement cycles. Before proceeding, Dr Paul Brear attempted to refine using different crystallographic software programmes such as BALBES,[290] but could not decrease the R_{flags} and progress any further. We compared the model and electron density after initial refinement to that of the apo model, and predictably, we did not see any electron density for the ligand.

Translational noncrystallographic symmetry (NCS) arises if more than two copies of the same structural motif in the asymmetric unit of the crystal are present in a similar orientation.[291] This results in abnormalities in the distribution of reflection intensities in the reciprocal space and in difficulties in assigning correct symmetries at the data processing stage.[292] Solution of these structures is often possible, although it usually requires a high degree of competence and perseverance in testing various, potentially plausible symmetry interpretations.[230] Therefore, I consulted Professor Ben Luisi, with whom I tried expanding the symmetry operations to *I*2 2 2 and *P*1 space groups, but the R_{flags} still did not decrease upon refinement in CCP4's Refmac.

In the *I*2 2 2 space group, the unit cell was again redefined with an axis of 900 Å. Twinning is not possible in orthorhombic space groups, but there were unusual intensity statistics in the dataset, and there could be several reasons for the departure of the intensity statistics from normality. Possible reasons include over-merging pseudo-symmetric or twinned data, intensity to amplitude conversion problems, as well as simply bad data quality.[293] Analysing the Patterson function in Phenix's Xtriage[294] in the dataset revealed a significant off-origin peak that was 37.28% of the origin peak, which indicates pseudo-translational symmetry. The chance of finding a peak of this height randomly in a structure without pseudo-translational symmetry was equal to 4.39×10^{-04}, according to this analysis. The detected translational NCS was most likely also responsible for the elevated intensity ratio. If the structure is solved, abnormal intensity statistics can lead to higher R-factors (R_{flags}) in refinement.[286]

Crystal morphology, including various twinned forms, is often directly related to pH, but the irregular intensity statistics were observed across a pH range of 5.0-8.0 in the datasets of the ICL_{Pa} co-crystals presented here, see **table 34**. Still, these experiments provided a good starting point for future work. I was able to obtain crystals that diffracted to at least 2.0 Å in the presence of SB002. Diffraction to 3.0 Å and beyond provides the resolution of specific interactions necessary to relate these interactions to biological function. However, we could not detect SB002 binding in the solved structures, and more advanced techniques are required for further crystal

optimisation. Crystallisation is a difficult and unpredictable stage of structural determination and remains a hit-or-miss proposition fundamentally.

4.10 Discussion

In this work, I evaluated novel 2-aminopyridine compounds for their potential as dual inhibitors of the glyoxylate shunt in *Pseudomonas aeruginosa. P. aeruginosa* infections are notoriously difficult to treat as this species has a plethora of intrinsic resistance mechanisms, including the impermeable Gram-negative outer membrane. There is undoubtedly an urgent need for new therapeutic leads. The glyoxylate shunt has been demonstrated as essential for *P. aeruginosa* to establish an infection *in vivo*, and it is well understood that the glyoxylate shunt is required for the bacteria to thrive in conditions with poor nutrient conditions.[167]

Research endeavours to find species-specific inhibitors in the equally clinically challenging *Mycobacterium tuberculosis* have yielded successes through structural-based approaches. Building on structural information of a critical anion-π interaction provided from these structure-based studies on MS_{Mt},[242,263] Dr Sean Bartlett synthesised a collection of small molecules based off of the structural and electronic features of the MS_{Mt} PDKA inhibitors as well as a hit compound from a HTS campaign against *P. aeruginosa* in acetate media that could be used to verify this hypothesis. Of the 2-aminopyridines, only SB002 (4-Cl) and SB023 (4-CN) were capable of inhibiting *P. aeruginosa* PAO1 growth completely in minimal medium with acetate as a sole carbon source. This inhibition was not observed in LB medium, further validating that the glyoxylate shunt is conditionally expressed under carbon-poor nutrient conditions. It also verifies that these inhibitors were selective and cell-permeable through the Gram-negative cell envelope.

SB002 was the only compound to display complete dual inhibition against the purified glyoxylate shunt enzymes. SB023 and SB026 (4-F) displayed partial dual inhibition as well, but among these two compounds, only SB023 was able to inhibit MS_{Pa} activity completely. I then expanded on the inhibition by using enzyme kinetics to determine the mode of inhibition of SB002 and SB023 on MS_{Pa} and SB002 on ICL_{Pa}. According to the Lineweaver-Burk plots, SB002 and SB023 displayed mixed inhibition of MS_{Pa} with a preference towards uncompetitive inhibition regarding substrate glyoxylate, which was inferred by comparing calculated K_i and K_i' values. SB002 and SB023 displayed mixed inhibition with a preference for competitive inhibition regarding co-substrate acetyl coenzyme A. This finding correlated with the analysis of MS_{Pa} druggability in results **chapter 3**.

SB002 also displayed mixed/noncompetitive inhibition of ICL_{Pa}, according to the Lineweaver-Burk analysis, but the data from the substrate *versus* enzyme velocity plots showed that the mode of inhibition was better suited to uncompetitive inhibition. This means that SB002 binds with a stronger affinity to the enzyme-substrate complex than the free enzyme. According to Crousilles *et al.,* there is a flexible loop between β-4 and β-5 in the ICL_{Pa} crystal structure poised 6 Å away from the active site. The loop contains the general catalytic base, Cys222. In the ICL_{Mt} crystal structure, the loop is positioned inwards, closing off access to the active site, and is presumably involved in catalysis.[174] This provides insight into a possible binding scenario. When isocitrate and SB002 are both present, the substrate might bind to ICL_{Pa} first, closing the active cleft. SB002 is left to bind to another enzyme location and halt isocitrate cleavage.

Using ITC, I validated SB002 as a dual inhibitor by measuring the thermodynamics of direct binding to the target enzymes. ITC revealed that SB002 binds to MS_{Pa} with a better affinity than ICL_{Pa}, which correlates with the results from kinetic analyses. This is not what was reported in the original study that identified this compound in a high throughput screening.[194] The reason for this difference in affinity could have to do with the activity of the protein purification batches, or it could be providing insight into the mechanism of action against ICL_{Pa}, but otherwise, I have no explanation for this.

Extensive soaking and co-crystallisation attempts were undertaken to try and further validate ligand binding and to determine the binding pockets and poses of SB002 in both enzymes. I was successful in obtaining robust ICL_{Pa} and MS_{Pa} crystals, but I could not obtain a structure of either of the ligand-protein complexes. The main issue with MS_{Pa} soaking was the crystal's sensitivity to DMSO. Higher solvent concentrations caused disorder in the crystal, resulting in crystal disintegration in the worst of cases and reduced data quality in the best of cases. SB002 displayed solubility in other solvents, like methanol, but was not very soluble in water, physiological buffers, or previous crystallisation conditions, which made the SB002 concentration the limiting factor in soaking attempts.

MS_{Pa} co-crystallisation was arguably even more unproductive than soaking because SB002 appeared to prevent crystal formation. Rational attempts to acquire co-crystallisation hits using sparse screening were employed, including reducing the concentration of DMSO, matching the ligand-protein ratio guided by the ITC results, and screening for hits that were congruent with the physiological conditions of ligand binding, as suggested by kinetics and thermal shift experiments. Either SB002 was interfering with important crystallisation contacts required for crystal packing, or the crystallisation conditions were prohibiting ligand binding.

While SB002 binding to ICL_{Pa} was conducive to crystallisation, it caused abnormal diffraction intensities and high mosaicity in the diffraction patterns, which complicated symmetry calculations and resulted in a massive unit cell, predicted to have 7-8 protomers present. Because this was not a straightforward case, I enlisted help from more experienced crystallographers, but the consensus was to continue rational co-crystallisation screening to find a crystal system which supported ligand binding and was more conducive to data processing and downstream model refinement.

According to the literature, extensive optimisation by trial and error is common when trying to obtain co-crystal structures.[278,279,281,284,293,295] There are a few gems of wisdom (mostly from experienced crystallographers) that endorse the chances of obtaining a crystal structure with the ligand bound. One example is to understand the protein quality with which one is working (*i.e.* solubility, stability and prior hit crystallisation conditions).[295] Another example is to use a high ligand concentrations (≥1 mM final concentration) for soaking or co-crystallisation, particular in cases where weaker binding (K_d in the mM range) is expected.[278] A final example is to mimic what is understood about the physiological binding conditions,[284] but in the end, the success of a co-crystal structure cannot be predicted and varies widely depending on the protein, the protein batch, and even the day.[282]

Table 35. Physicochemical properties of 2-aminopyridines.

	SB001	SB002[a]	SB022	SB023	SB026	SB029	2-AP
MW (Daltons)	415.29	370.83	404.39	361.40	354.38	394.43	128.56
cLog*P* $_{\text{octanol/water}}$	3.91	3.74	4.02	2.99	2.78	1.96	1.13
H-bond donors	2	2	2	2	2	3	1
H-bond acceptors	5	5	5	6	5	7	2

[a] Values reported for SB002 also apply to isomeric SB032. Properties were calculated using ChemBioDraw Ultra 13.0 (PerkinElmer). **Abbreviations:** 2-AP, 2-amino-4-chloropyridine; cLogP, calculated partition coefficient; H-bond, hydrogen bond; MW, molecular weight.

In the absence of a co-crystal structure to definitively support my proposed molecular mechanism of action, I examined the physicochemical properties of the synthesised compound library to attempt to correlate the structure-activity relationships (SAR). The analysis (shown in **table 35**) revealed that they are all compliant with Lipinski's rule of five (RO5), in that they have a molecular weight <500 Daltons, <5 hydrogen bond donors, <10 hydrogen bond acceptors, a calculated octanol-water partition coefficient, cLog*P*, <5, and <10 rotatable bonds.[296,297] Complying with the RO5 is a useful metric of how "drug-like" a compound is. Compounds that conform to the RO5 are associated with 90% of orally active drugs that have achieved phase II clinical status in the drug development pipeline.[296] The RO5 was deliberately created by Pfizer to

be a conservative predictor in an era where medicinal and combinatorial chemistry produced too many compounds with very poor physicochemical properties. This information is a decent starting point for understanding hit compounds and is useful in designing inhibitors to which the pharmaceutical industry still adheres and simultaneously rejects.[298,299]

Personal communication with Prashanthi Medarametla from the University of Eastern Finland suggested that when subjected to general molecular docking, SB002 interacts with MS_{Pa} in the acetyl coenzyme A binding pocket. Because we could not confirm this through X-ray crystallography, the pharmacophores based on the functional groups present in SB002 and SB023 are only predictions, **see figure 35.**

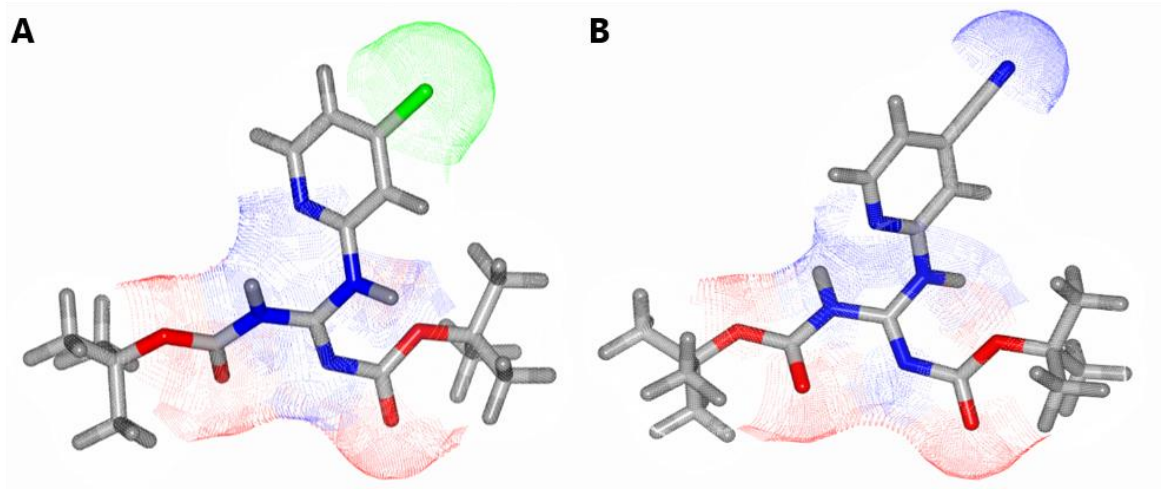

Figure 35. Predicted ligand pharmacophores for SB002 and SB023. Functional groups are shown in a coloured dot surface based on atom type. Nitrogen atoms are coloured in blue and comprise a guanidine moiety in the centre of the structures. The two ester functional groups that are a part of the Boc protecting groups are coloured in red. **(A)** SB002's chlorine substitution is coloured in green. **(B)** SB023's nitrile substitution is coloured blue.

2-AP showed no target nor whole-cell inhibition throughout my experiments, meaning the guanidine moiety and the Boc protecting groups are important for SB002 and SB023 binding to the target enzymes as well as penetrating *P. aeruginosa*'s outer membrane. Both compounds contain guanidine moieties, which have been associated with antibacterial activities, including the inhibition of *P. aeruginosa*.[300] In fact, six out of the eight hits from Pfizer's *P. aeruginosa* whole-cell screening campaign in acetate medium contained guanidine groups.[194] Most guanidine derivatives are strong bases and this underpins their biological interactions. Under physiological conditions, the guanidine group exists mainly in its protonated form, which may afford interactions with the target enzymes. Another option is that it could be binding to the bacterial outer membrane on the negatively-charged polysaccharide layer, causing cell death.[301,302] Additionally, the Boc groups could also be important to maintain the overall shape rather than just the chemical binding, such as

providing an electronegative balance to the chemical scaffold, but I could find no evidence of intentionally using a Boc protecting group as a part of a pharmacophore for biological activity, antibacterial or otherwise.

Finally, the electron withdrawing groups at the heterocyclic 4th positions are likely responsible for the inhibition. They might activate the guanidine binding activity to enhance its interaction with any amine groups present in the cell membrane. The nitrile substituent on SB023 is a short, polarised triple bond, resulting in a small steric demand on the molecular scaffold.[303] For comparison, the C-N unit is 8x smaller than a methyl group.[304,305] Nitriles often play a key role as hydrogen bond acceptors in active pharmaceuticals, and arylnitriles are one of the most common of these pharmaceuticals.[306] SAR studies have shown that para-substituted arylnitriles in the 4th position were instrumental in hydrogen bonding to arginine residues and that these crystal structures show the nitrile projecting into narrow crevices in the binding pocket to make polar interactions or hydrogen bonds in a sterically congested environment.[307,308] SB002, on the other hand, is an arylchloride, which has a weaker dipole moment on the rest of the molecule than the arylnitrile. This substitution (4-Cl) is very electronegative; however, and can cause the inductive withdrawal of electrons from the carbons in the benzene ring depending on the position of the halide substituent.[309]

It is important to note that the dual inhibitory activity of SB023 reported in this chapter is incongruent with the *in vitro* inhibition of ICL_{Pa} to explain its observed MIC value. This indicates that although the predicted affinity based on the chemical scaffold was generally confirmed, the reasons behind the whole-cell activity of SB023 most likely lies elsewhere. I have shown that these compounds inhibit the glyoxylate shunt enzymes, but a more conservative explanation is that a direct dual or polypharmacology explain the observed MIC values by hitting other *P. aeruginosa* targets. However, it is also possible that the observed MIC values are a result of a synergistic effect that includes their activities against ICL and MS and on other enzymes.

This study provided an example of how a designed, multi-targeted approach to early antibacterial drug discovery, particularly in a clinically important pathogen, is a good starting point for medicinal chemistry modifications. In the future, instead of ICL or MS, other enzymes could make alternative targets for the functional inhibition of the glyoxylate shunt. For instance, an indirect means of inhibition of the glyoxylate shunt is through inhibiting the enzymes of the polyhydroxybutyrate cycle since this metabolic route can produce acetyl coenzyme A in a manner that circumvents the link between glycolysis and the TCA cycle.[310,311] Another example is inhibiting the CbrAB two-component system, or Crc, in *P. aeruginosa*, which is a post-transcriptional global

regulator of carbon metabolism. Inhibiting this system would block the initiation of translation and could impact carbon utilisation in *P. aeruginosa*.[312]

5. Results and discussion

The antibacterial potential of SB002 and SB023: hit to lead optimisation

5.1 Background

A screening programme for new antibacterial compounds can result in several hits, but not all of them will have equally desirable qualities. It is essential to evaluate and prioritise their potential before settling on a single hit as suitable for development into a lead compound.[313] This process is known as hit to lead optimisation. Antibacterial drug discovery encompasses the same goals as all drug discovery; to develop therapies that are efficacious and safe.[81] An antibiotic hit must bind to its target and must be important for growth inhibition of the pathogen of interest. However, antibacterial drugs are unique in that they require chemistry which allows them to pass the cellular envelope (outer membrane, periplasm, and cell membrane) in Gram-negative bacteria.[80] Potential antibacterial candidates must specifically kill bacterial cells while being innocuous to eukaryotic cells, which is determined by assessing mammalian cytotoxicity.

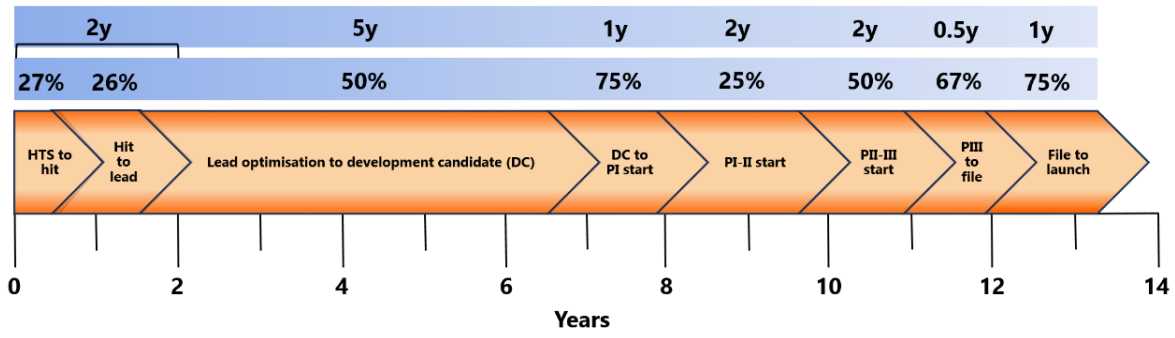

Figure 36. Timeline of antibacterial drug development. The corresponding timelines and success rates for each stage of antibacterial drug discovery and development pipeline are shown. Lead optimisation is the most arduous stage. Figure modified from Payne *et al.*, 2007.[110]

Determining *in vitro* drug metabolism is a significant pharmacokinetic parameter as the majority of drugs are metabolised in the liver, and intrinsic clearance determined *in vitro* can be used to predict *in vivo* drug clearance.[314,315] Significant drug-drug interactions can also arise from the inhibition of cytochrome P450-mediated clearance mechanisms in the liver and can negatively impact the clinical and commercial viability of potential medicines. This impact ranges from labelling requirements for relatively minor interactions to non-approval or withdrawal from the

market for more serious cases.[316] Therefore, it is important to consider drug metabolism, as well as mammalian cytotoxicity, early on in development when evaluating the potential of hit compounds in lead optimisation.

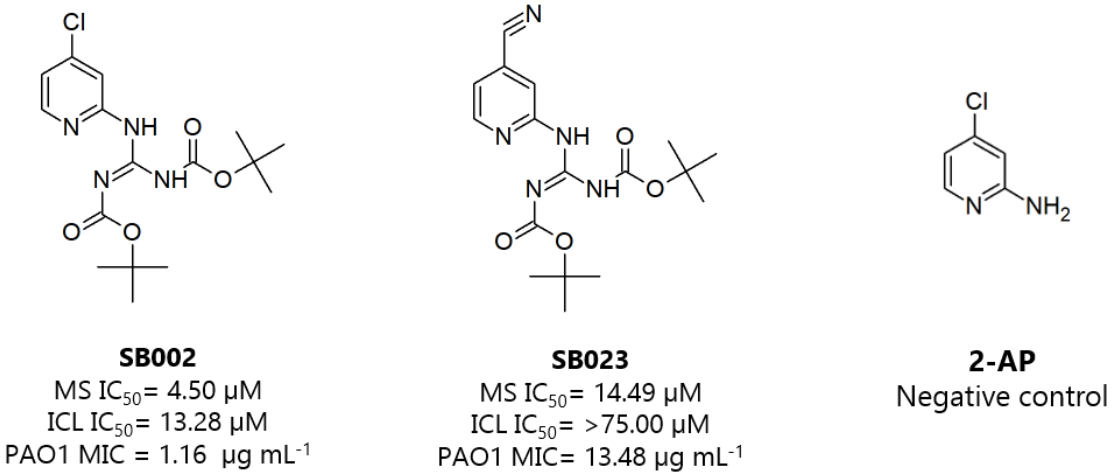

Figure 37. The hit compounds tested in this study. SB002 and SB023 displayed potent inhibition against the glyoxylate shunt enzymes from *Pseudomonas aeruginosa* and prevented PAO1 growth in acetate. Therefore, their potentials as antibacterial lead candidates were evaluated in this chapter. 2-amino-4-chloropyridine (2-AP) was used as a negative control.

In this chapter, I set out with three experimental objectives. First, I hoped to elucidate more about the antibacterial specificity and mechanism of the hit compounds, SB002 and SB023 (**figure 37**), defined in **chapter 4**. I attempted this by evaluating their antibacterial effects on *P. aeruginosa* grown in different carbon sources, a multidrug efflux pump mutant of *P. aeruginosa*, and on the ESKAPE pathogen panel. Second, I assessed the hit compounds for *in vitro* cytotoxicity using four human cell lines and one murine cell line. Third, I evaluated the hit compounds for *in vitro* drug metabolism and pharmacokinetics (DMPK), specifically their intrinsic metabolic clearance in liver microsomes of humans and preclinical species, as well as for any inhibition of the main human cytochrome P450 enzymes. These goals were meant to support a general assessment of SB002 and SB023 and their potential of satisfying the requirements for defining hit to lead compounds.

5.2 SB002 and SB023 display bactericidal activity

First, I expanded on the antibacterial evaluation of hit compounds detailed in **section 4.3** of **chapter 4** by incubating *P. aeruginosa* PAO1 with SB002 and SB023 and plotting turbidity measurements ($OD_{600\ nm}$) over time to observe growth kinetics. Untreated PAO1 reached exponential phase in M9 acetate after 4 hours and stationary phase after 10 hours (**figure 38A**).

PAO1 treated with 1.16 μg mL^{-1} SB002 resulted in a severe growth lag while PAO1 treated with 2.32 μg mL^{-1} SB002 or 50 μg mL^{-1} of gentamicin, a bactericidal aminoglycoside, resulted in no growth. After incubation, the samples were serially diluted and added to M9 acetate agar plates to determine if the compounds were bacteriostatic or bactericidal. **Figure 38B** shows colony forming units after 24 hours at 37°C. Agar plates with gentamicin-treated PAO1 and 2.32 μg mL^{-1} SB002-treated PAO1 showed no recoverable colonies, indicating that SB002 is bactericidal at relevant doses.

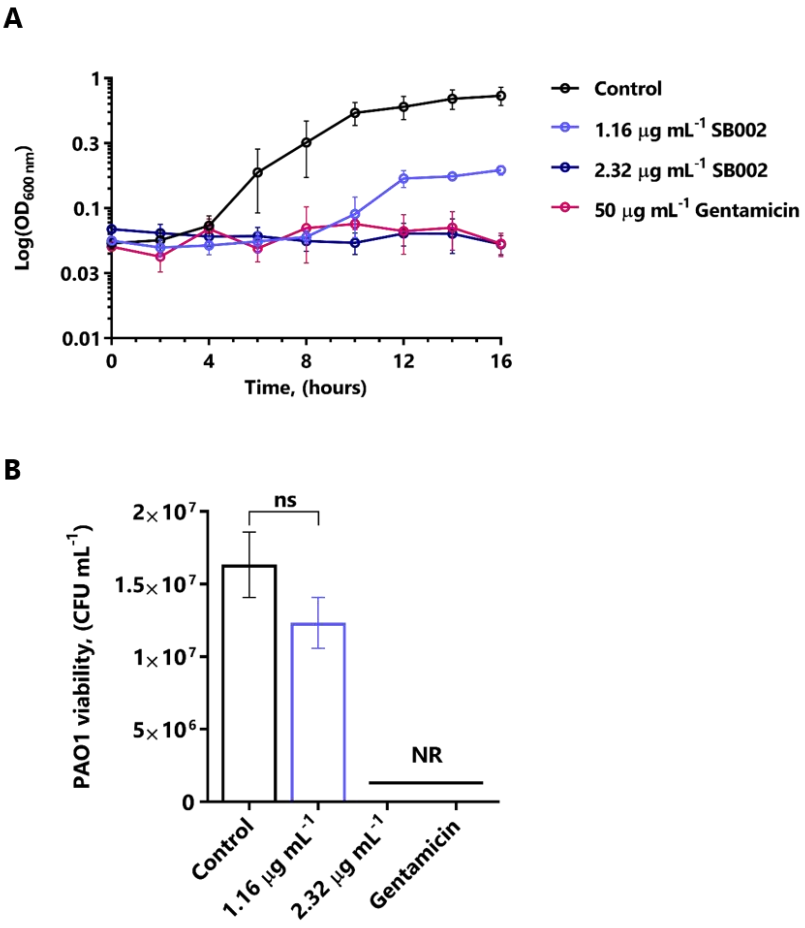

Figure 38. Growth kinetics of PAO1 inhibition by SB002. (A) Growth curves of PAO1 grown in acetate medium in the absence of (black) and presence of 50 μg mL^{-1} of gentamicin (magenta), 1.16 μg mL^{-1} SB002 (powder blue), and 2.32 μg mL^{-1} SB002 (navy blue). **(B)** PAO1 viable CFUs from the growth curve samples. Values marked with ns are not significantly different ($p>0.05$; $n=3$). **Abbreviations:** CFU, colony forming units; NR, no recovered colonies; OD, optical density.

The same experiment was repeated with SB023. Untreated PAO1 again reached exponential phase in M9 acetate after 4 hours and stationary phase after 10 hours. In the presence of 2.3 μg mL^{-1} SB023, there was a slight lag in overall PAO1 growth when compared with the untreated control. There was an even larger growth lag when 18.1 μg mL^{-1} SB023 was added, and no growth was observed when either 50 μg mL^{-1} gentamicin or 36.1 μg mL^{-1} SB023 were added. After incubation, I serially diluted these samples and plated them on fresh M9 acetate agar plates. After 24 hours incubation, there were no recoverable colonies from the 36.1 μg mL^{-1} SB023 sample, indicating that SB023 is also a bactericidal agent at relevant doses. When exponential-phase PAO1 cells were challenged by adding hit compounds, there was no effect on growth or viability (data not shown).

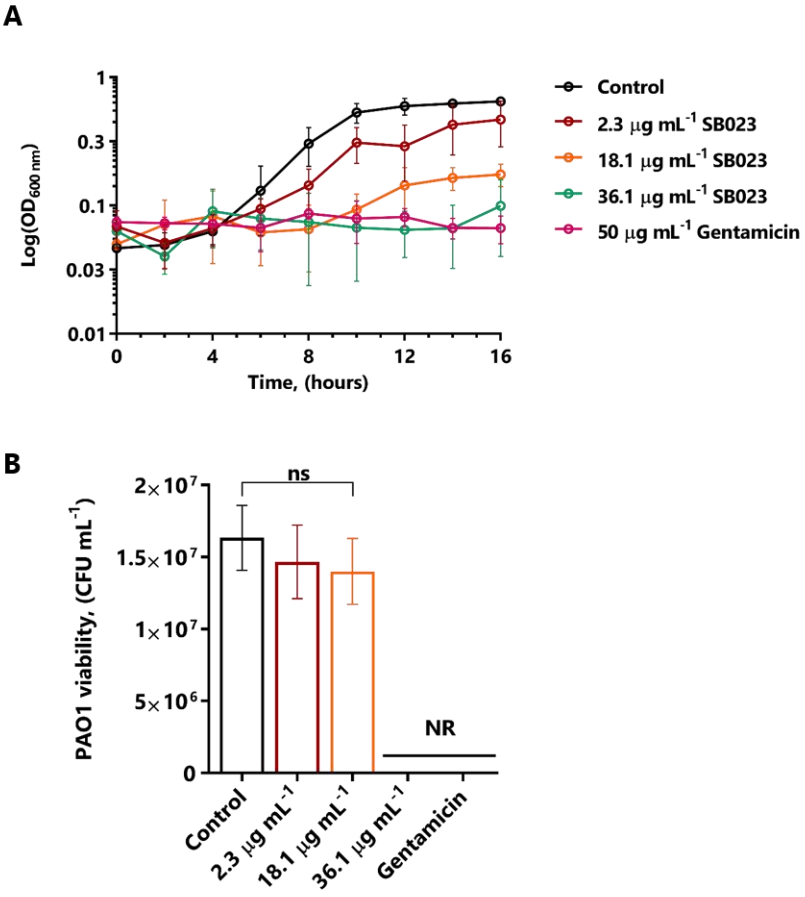

Figure 39. Growth kinetics of PAO1 inhibition by SB023. (A) Growth curves of PAO1 in minimal medium with acetate in the absence of (black) and presence of 50 μg mL^{-1} gentamicin (magenta), 2.3 μg mL^{-1} SB023 (maroon), 18.1 μg mL^{-1} SB023 (orange), and 36.1 μg mL^{-1} SB023 (turquoise). **(B)** PAO1 viable CFUs from the growth curve samples. Values marked with ns are not significantly different ($p>0.05$; $n=3$). **Abbreviations:** CFU, colony forming units; NR, no recovered colonies; OD, optical density.

Bactericidal antibiotics, regardless of their original target, commonly induce oxidative stress by disrupting metabolite flux into the TCA cycle and reducing the amount of NADH present in the cell.[317] A decline in NADH fuels the formation of oxide anions (O_2^-) by the cell's electron transport chain. O_2^- then damages iron-sulphur clusters and frees ferrous iron to be oxidised via the Fenton reaction, which results in the formation of hydroxyl radicals (•OH). Build-up of •OH culminates in damage to DNA, proteins and lipids, which eventually results in cell death.[318] The glyoxylate shunt has been linked to oxidative stress tolerance in *P. aeruginosa*. Mutants deficient in the glyoxylate shunt displayed metabolic phenotypes favouring aerobic denitrification, which decreases the amount of oxygen consumption without dropping the total ATP yield.[317] According to this finding, SB002 and SB023 inhibit the glyoxylate shunt and relinquish PAO1's protection from •OH damage and cell death.

5.3 SB023 exhibits broad-spectrum antibacterial activity

As the glyoxylate shunt enzymes are present in many medically relevant bacteria, I assayed the hit compounds on the ESKAPE pathogen panel to assess their broad spectrum applications. Antibacterial assays were completed in Dr Päivi Tammela's Bioactivity Screening Laboratory at the University of Helsinki during a research secondment. MIC assays were performed initially using Mueller Hinton broth (MHB) medium following the CLSI broth microdilution protocol for antimicrobial testing.[197]

Assays were then repeated on the pathogens that displayed robust growth (Z' values > 0.75) in M9 minimal medium supplemented with 0.5% acetate. The ESKAPE pathogen panel is listed in **table 36** along with the amino acid identities of the glyoxylate shunt enzymes in the ESKAPE pathogens compared with *Pseudomonas aeruginosa* PAO1. During this secondment, I realised the SB002 sample had lost most of its antibacterial activity, even against PAO1. This was presumably due to chemical degradation, which was later confirmed through NMR, the spectrum of which is in **appendix 4**. Therefore, the results presented in **table 36** are the MICs for SB023 in MHB and M9 acetate media. SB023 could not inhibit the growth of any ESKAPE pathogen nor PAO1 in MHB at 27.11 μg mL^{-1} (75 μM), which was as expected in rich medium. Of the ESKAPE pathogens, *S. aureus* and *E. faecium* are Gram-positive bacteria that do not possess genes encoding the glyoxylate shunt enzymes.[319] Absence of the shunt may relate to the specific growth conditions in which these species flourish and cause infection. For example, many *S. aureus* infections are associated with the blood-stream, which provides high concentrations of glucose (5 mM-50 mM) available for infective bacteria.[320] Therefore, *S. aureus* and *E. faecium* could not grow in a medium where acetate was supplied as the sole carbon source. When I repeated the antibacterial assay in

M9 acetate, I increased the test concentrations of SB023 to 72.28 μg mL^{-1} (200 μM). PAO1 inhibition was observed at 36 μg mL^{-1}, which confirmed that PAO1 was consistently susceptible to SB023, even from different laboratories. *E. coli* was also susceptible to SB023 at a MIC of 9 μg mL^{-1}, and *A. baumannii* was susceptible at 72.28 μg mL^{-1}.

Table 36. SB023 antibacterial activity against the ESKAPE pathogen panel. Amino acid sequence identities of isocitrate lyase and malate synthase G from *Pseudomonas aeruginosa* PAO1 are compared with those present in the ESKAPE pathogen panel, along with MICs against ESKAPE pathogens for SB023.

	Amino acid identity[b] (%)		SB023 MIC (μg mL^{-1})	
Bacterial species	**MS_{Pa}**	**ICL_{Pa}**	**MHB**	**M9 Ac**
***E**nterobacter aerogenes* 13048	25%	28%	>27.11	>72.28
***S**taphylococcus aureus* 29213	N/A	N/A	>27.11	n.d.
***K**lebsiella pneumoniae* 700603	24%	28%	>27.11	>72.28
***A**cinetobacter baumannii* 19606	65%	75%	>27.11	72.28
***P**seudomonas aeruginosa* 27853	100%	100%	>27.11	>72.28
***E**nterococcus faecium* 35667	N/A	N/A	>27.11	n.d.
Pseudomonas aeruginosa (PAO1)[a]	100%	100%	>27.11	36.04
Escherichia coli 25922	59%	27%	>27.11	9.04

[a] *Pseudomonas aeruginosa* PAO1 strain was from the University of Helsinki.
[b] Amino acid sequence identities were determined by the protein-protein algorithm BLAST.[231]
Abbreviations: Ac, acetate; MHB, Mueller Hinton Broth; MIC; minimum inhibitory concentration; N/A, not applicable; n.d., not determined; *Pa*, *Pseudomonas aeruginosa* PAO1.

No inhibition was observed for all other microorganisms, despite growing robustly on acetate and hence utilising the glyoxylate shunt enzymes. For the *P. aeruginosa* clinical isolate, perhaps there was a barrier to cell entry such as active multidrug efflux pumps. For the remaining pathogens, *E. aerogenes* and *K. pneumoniae*, the shunt enzymes' amino acid similarity with PAO1's were no higher than 28%, which could explain the lack of inhibition, especially if SB023 binds in an allosteric pocket that is subject to more amino acid variability than in the conserved protein catalytic cores. Successful SB023 inhibition of *A. baumannii* and *E. coli*, however, expands the compound's antibacterial spectrum, supports the hypothesis that the glyoxylate shunt is an attractive antibacterial target, and represents new ways to address the need for new antibacterial agents.

5.4 Antibacterial activity is altered in the absence of multidrug efflux pumps

From the MIC assays, it was clear that the hit compounds were cell permeable, but I was conscious of the threat of spontaneous mutations that could give rise to resistance. One of the

major acquired resistance mechanisms is increased drug efflux from mutations in multidrug efflux pumps.[111] If *P. aeruginosa*, which is already characterised by a poorly-permeable outer membrane, benefits from increased efflux, then a serious risk of resistance can develop, even though the hit compounds have multiple targets. *Pseudomonas aeruginosa* YM64, a mutant strain of PAO1 lacking all four major *mex* operons encoding the Mex multicomponent efflux pumps (MexAB-OprM, MexEF-OprN, MexCD-OprJ, and MexXY-OprM) was used to explore any possible enhancement of the antibacterial activity of the hit compounds in the absence of said multidrug efflux pumps.[153] First, robust growth of YM64 was confirmed in M9 minimal medium supplemented with 0.5% acetate before subjecting the strain to incubation with the hit compounds. YM64 did not show a significant change in susceptibility to 6.25 μM (2.32 μg mL^{-1}) SB002 when compared with PAO1 treated with the same SB002 concentration, suggesting it is not a substrate of these efflux pump systems, see **figure 40**.

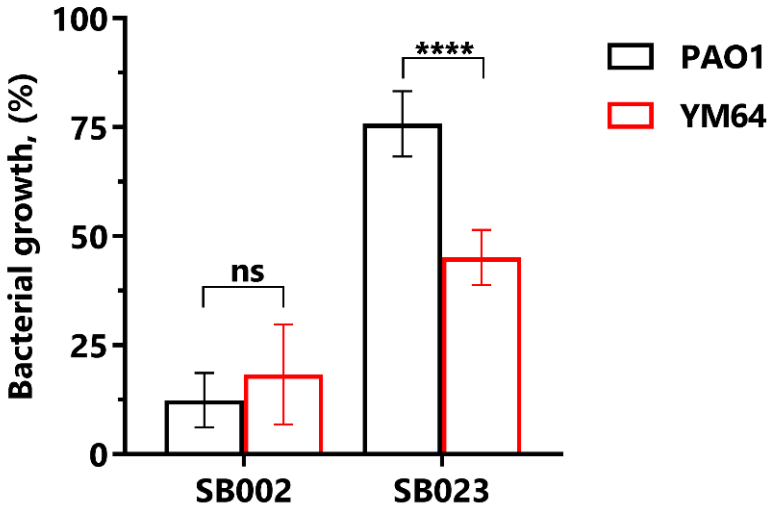

Figure 40. Comparison of PAO1 and YM64 growth in the presence of hits. YM64 showed increased susceptibility to SB023 compared with PAO1, while there was no difference in growth between PAO1 and YM64 when exposed to SB002. Compounds were tested at 6.25 μM. Values marked with **** are significantly different [ns = not significant ($p>0.05$); **** = $p<0.0001$; $n=4$].

Conversely, YM64 showed a significantly increased susceptibility to 6.25 μM (2.26 μg mL^{-1}) of SB023 when compared with PAO1 treated with the same concentration of SB023. This means that SB023 might be a substrate for any of the four Mex multidrug efflux pumps present in *P. aeruginosa* PAO1, which could eventually confer resistance. The resistance-nodulation-division (RND) family of efflux pumps present in Gram-negative bacteria are thought to function as a detoxification mechanism for the cell from heavy metals and detergents present in the environment.[321] MexAB-OprM and MexXY-OprM efflux pumps, in particular, contribute to the

intrinsic multidrug resistance in *P. aeruginosa*.[155] The MexXY efflux system is a well-known determinant of aminoglycoside resistance, and MexAB system contributes to intrinsic resistance of fluoroquinolones, tetracycline, chloramphenicol, and carbenicillin.[322]

Perhaps for SB002, there is an alternative mechanism of entering the cell that avoids the efflux pump systems, such as passively through porins or actively through substrate-specific β-barrel transport systems.[111] OprD and OprO are porins from the outer-membrane carboxylate channel (Occ) family, for example, that function as "nonspecific" entry and exit points for antibiotic-like molecules and are responsible for transporting neutral and basic amino acids such as arginine, lysine, and histidine.[59,152] The guanidine moiety present in SB002 and SB023 is also present in the arginine side chain, so it is conceivable that these compounds could mimic arginine uptake. OprD expression, like many other PAO1 porins, varies based on growth media or exposure to metals like copper or zinc. In one instance, an in-frame deletion allowed for normal porin expression and arginine uptake while simultaneously conferring carbapenem resistance.[148]

5.5 Antibacterial activity is likely achieved through "network pharmacology"

When exposed to a variety of carbon sources, *P. aeruginosa* can rewire its central metabolism to adapt. PAO1 growth in all types of minimal media was robust whether the bacteria had access to acetate, glucose, succinate or propionate as the building blocks for gluconeogenesis. M9 and MOPS (3-(N-Morpholino) Propane-Sulfonic Acid) were both tried as bases for minimal media, see **table 37.** The full differences between the recipes of M9 and MOPS are detailed in **chapter 2**, but MOPS is comprised of a more complex nutrient profile with added minerals like iron, copper and zinc.[323]

P. aeruginosa has a two-component CzcSR system that is activated after exposure to metals, which in turn, induces efflux pumps to extrude any excess metals. An increase in metals in the medium alters the expression of different membrane porins. For example, the presence of copper and zinc decrease OprD expression, iron decreases OprG and OprE expression, and magnesium decreases OprH. This can influence how the hit compounds gain entry into the cell.[324] This may explain the differences in the MICs in M9 and MOPS media, particularly concerning acetate. A notable surprise is the fact that the compounds inhibit PAO1 growth in the presence of glucose equal to, if not slightly better than, acetate. This is not what was reported in Fahnoe *et al.*'s work, and I have no explanation for why this discrepancy exists, other than the fact that the hit compounds must have off-target effects on other metabolic enzymes. A study on *P. aeruginosa* ^{13}C-metabolic flux indicated that strains grown in glucose still exhibit significant flux through the

glyoxylate shunt, but this does not fully explain why the inhibition is equally potent in glucose as in acetate.[325]

Table 37. MICs values of hit compounds in various carbon sources.

	MIC (μg mL^{-1})	
Media and carbon source	**SB002**	**SB023**
M9 acetate (0.5%; 60 mM)	1.16	13.52
M9 glucose (0.5%; 15 mM)	1.16	4.51
MOPS acetate (40 mM)	9.27	72.28
MOPS glucose (15 mM)	9.27	72.28
MOPS propionate (30 mM)	37.08	72.28
MOPS succinate (30 mM)	9.27	72.28

Propionate (C_3) is an abundant short-chain fatty acid and is metabolised by the methylisocitrate pathway in *P. aeruginosa*, resulting in molecules of pyruvate and succinate. Methylcitrate synthase (PrpC) catalyses the conversion of oxaloacetate, provided from the TCA cycle, and propionyl coenzyme A, provided from propionate as a nutrient source, into 2-methylcitrate and coenzyme A.[326] I tested SB002 for PrpC inhibition to confirm if the inhibition of bacterial growth observed in MOPS propionate medium could be observed enzymatically.[ii] Inhibition of PrpC enzyme activity was measured by quantifying thiol release from propionyl-CoA leading to the formation of TNB from DTNB measured at 412 nm. SB002 exhibited promiscuous activity by significantly inhibiting (50%) of methylcitrate synthase activity at 100 μM, while SB023 did not show significant inhibition at 100 μM, see **figure 41**.

The reason for the partial inhibition of PrpC by SB002 could be a consequence of similar active sites between PrpC and MS_{Pa}, which have to accommodate propionyl coenzyme A and acetyl coenzyme A, respectively. In MS_{Pa}, the proposed binding pocket for SB002 binding is in the acetyl coenzyme A binding pocket. However, no crystal structure of PrpC from *P. aeruginosa* has been deposited in the PDB, and the deposited structures from bacterial species like *M. tuberculosis*, *Salmonella typhimurium*, and *Coxiella burnetii* do not have propionyl coenzyme A or coenzyme A present to confirm this theory.

[ii] I tested PrpC instead of other metabolic enzymes involved in glucose metabolism because PrpC was readily available in the Welch laboratory and was conducive to the same kinetic assay conditions as MS_{Pa}.

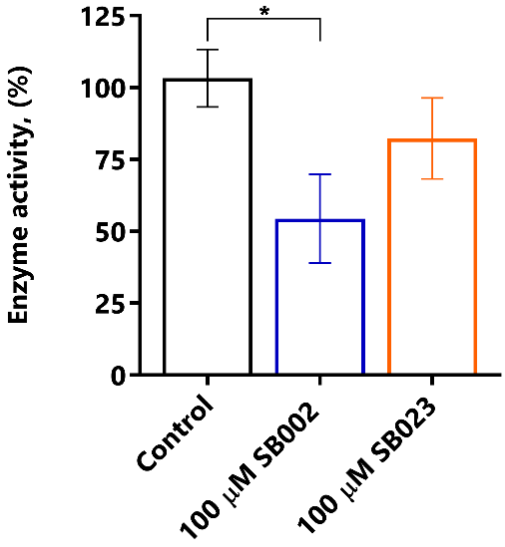

Figure 41. SB002 inhibition of 2-methylcitrate synthase. Enzyme activity of methylcitrate synthase was determined by measuring the enzyme's products, 2-methylcitrate and coenzyme A, using Ellman's reagent, which is similar to how malate synthase activity and inhibition was determined. SB002 (blue) inhibited enzyme activity significantly, and SB023 (orange) did not inhibit enzyme activity. Values marked with * are significantly different (* = $p<0.05$; $n=3$).

5.6 Cytotoxic assessment of SB002 and SB023

I assessed any mammalian cytotoxicity of SB002 and SB023 using a commercial luminescence-based assay during a research secondment in Dr Päivi Tammela's Bioactivity Screening Laboratory at the University of Helsinki. I evaluated any mammalian cytotoxicity of SB002 and SB023 using a commercial colourimetric-based assay in the Department of Pharmacology at the University of Cambridge.

Cytotoxicity of SB002, SB023 and 2-amino-4-chloropyridine (2-AP) was measured by quantifying ATP after 48-hour incubation with A-375, Hs27, and BALB/c cell lines. Cytotoxicity of SB002 and SB023 was estimated by measuring lactate dehydrogenase (LDH) release, correlating with cell membrane damage, after 4-hour incubation with A549 and U937. The highest concentration of the compounds tested was 100 μM in 0.5% DMSO. The first attempt at assessing SB002 cytotoxicity on A-375, Hs27 and BALB/c cells during the research secondment was unproductive, as it was later discovered that the quality of SB002 had been compromised due to chemical degradation, see **appendix 4**. Therefore, I am grateful to Viviana Gatta from the University of Helsinki for repeating the cytotoxicity assay on Hs27 cells with "fresh" SB002 for me. The results for SB002 reported in this section for A-375, and BALB/c cells are from the first attempt with the degraded material, and the reported Hs27 results are from the second attempt with newer material.

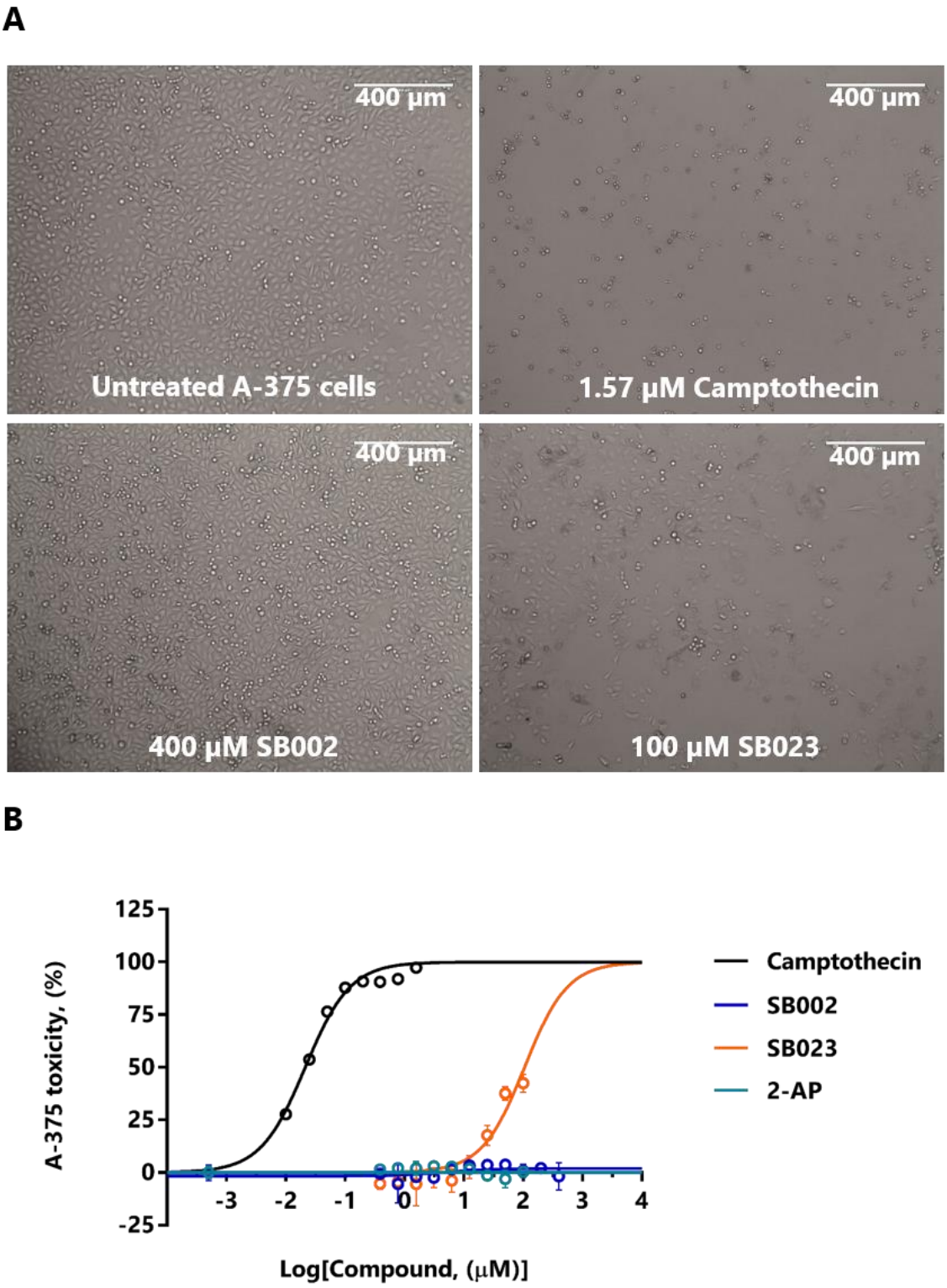

Figure 42. A-375 human malignant melanoma cytotoxicity. (A) Micrographs of control and treated A-375 cells after a 48-hour incubation. 40x images including (in clockwise order) untreated A-375 cells, and A-375 cells exposed to 1.57 µM camptothecin, 100 µM SB023, and 400 µM SB002. **(B)** Dose-response curves of A-375 cytotoxicity by 10 nM-1.57 µM positive control camptothecin (black), 0.39-400 µM SB002 (blue), 0.39-100 µM SB023 (orange), and 0.39-100 µM 2-amino-4-chloropyridine (2-AP) (teal). Toxicity was calculated from cell viability (n=3) relative to untreated controls and media only wells.

Microscopic images of A-375 (**figure 42A**), Hs27 (**figure 43A**) and BALB/c (**figure 44A**) cells showed >90% confluency in untreated wells. All images of cells treated with positive controls contained rounded, shrunken cells, which is a sign of apoptosis.[224] A-375 cells incubated with 1.57 μM camptothecin also showed reduced cell quantity compared with untreated cells (**figure 42A**). SB023-treated wells in all three cell lines displayed less confluence, as did SB002-treated Hs27 wells (**figures 42A-44A**).

In order to determine if the observed cytotoxic effects were specific effects of the compounds or non-specific factors, dose-response curves were generated for the test compounds and positive controls on all three cell lines (**figures 42B-44B**). In cells treated with 100 μM SB023, images show reduced cell quantities, but according to the dose responses, 60-80% of those cells were metabolically active. Full cytotoxicity profiles of the hit compounds for all five cell lines are presented in **table 38**.

Among the cell lines, A-375 was the most susceptible to incubation with SB023 at 100 μM, displaying 42% toxicity. U937 and Hs27 were the cell lines most susceptible to SB002 exposure at 100 μM, see **table 38**. Hs27 was susceptible to both hit compounds but was more sensitive to SB002 than SB023. BALB/c and A549 cells were the most resilient to exposure towards the hit compounds and did not show any dose-dependent susceptibility. There was, however, baseline toxicity of around 20-25% for SB023 in the case of BALB/c, see **figure 44B**, as well as for A549 and U937 (not shown). BALB/c cells are sensitive to contact inhibition from cell division, so they are an intrinsically more sensitive cell line.[224] 2-AP displayed no toxicity towards any cell lines, which was predicted because it does not have the guanidine moiety or Boc protecting groups present.

Because the compounds are lipophilic, they run the risk of diffusing through the cytoplasmic membrane, disrupting the structure of the different layers of polysaccharides, fatty acids and phospholipids. Guanidines are associated with membrane perturbation, so it is possible that any cytotoxic or anti-proliferative effects of the compounds were due to the presence of the guanidine moiety.[327]

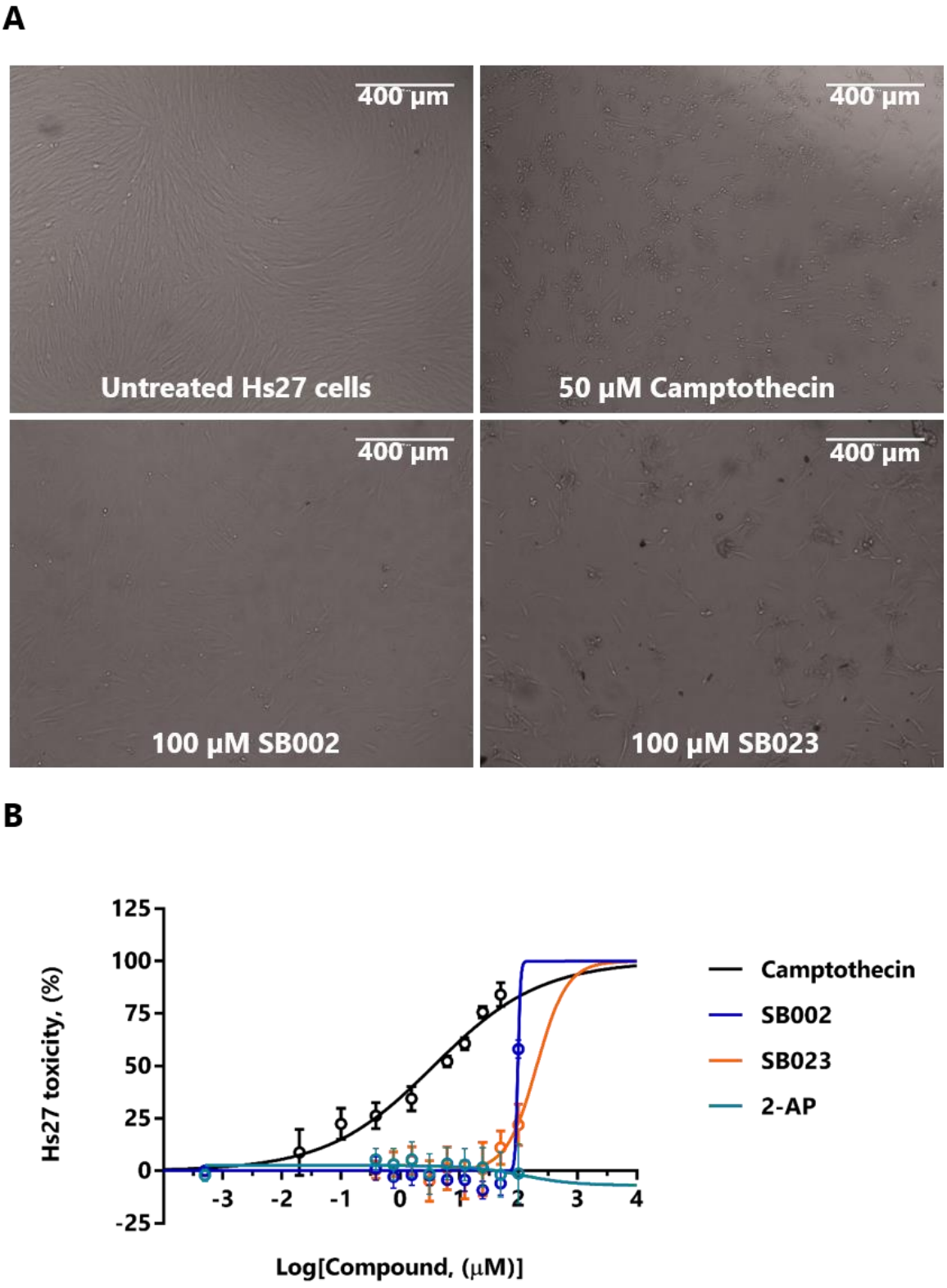

Figure 43. Hs27 human neonatal foreskin fibroblast cytotoxicity. (A) Micrographs of control and treated Hs27 cells after 48-hour incubation. 40x images include (in clockwise order) untreated Hs27 cells, and Hs27 cells exposed to 50 µM camptothecin, 100 µM SB023, and 100 µM SB002. **(B)** Dose-response curves of Hs27 cytotoxicity by 20 nM-50 µM of positive control camptothecin (black), 0.39-100 µM SB002, (blue), 0.39-100 µM SB023 (orange), and 0.39-100 µM 2-amino-4-chloropyridine (2-AP) (teal). Toxicity was calculated from cell viability (n=6) relative to untreated controls and media only wells.

Table 38. Cytotoxicity profiles of hit compounds against five cell lines.

		SB002	SB023	2-AP	Camptothecin[a]	Polymyxin B[b]
A-375	IC_{50} (μM)	>400[c]	105.60 ±1.14	>100	0.02 ±1.05	N/A
	Hill slope	n.d.	1.20 ±0.18	n.d.	1.15 ±0.07	N/A
	%Toxicity at 100 μM	0.82[c]	42.49	0.25	n.d.	N/A
Hs27	IC_{50} (μM)	98.42	>100	>100	3.69 ±1.12	N/A
	Hill slope	n.d.	1.70 ±0.61	n.d.	0.48 ±0.03	N/A
	%Toxicity at 100 μM	58.03	22.03	-1.21	n.d.	N/A
BALB/c	IC_{50} (μM)	>400[c]	>100	>100	N/A	533.60 ±1.03
	Hill slope	n.d.	n.d.	n.d.	N/A	4.73 ±0.53
	%Toxicity at 100 μM	-2.52[c]	23.36	-8.35	N/A	n.d.
A549	IC_{50} (μM)	>100	>100	n.d.	N/A	N/A
	Hill slope	n.d.	n.d.	n.d.	N/A	N/A
	%Toxicity at 100 μM	26.76	13.24	n.d.	N/A	N/A
U937	IC_{50} (μM)	18.18 ±1.45	>100	n.d.	N/A	N/A
	Hill slope	0.23 ±0.04	n.d.	n.d.	N/A	N/A
	%Toxicity at 100 μM	56.79	31.16	n.d.	N/A	N/A

[a] Camptothecin was used a positive control for both A-375 and Hs27 cell lines.
[b] Polymyxin B was used as a positive control for BALB/c.
[c] These results were of degraded SB002. **Abbreviations:** 2-AP, 2-amino-4-chloropyridine; BALB/c, BALB/c 3T3 Clone A31 cells; N/A, not applicable; n.d., not determined.

The difference in susceptibilities across cells lines, particularly in the case of A-375 compared with Hs27 and BALB/c could be due to different cellular markers expressed and compositions of the cellular plasma membranes as a result of their respective metabolic and differentiated cellular states.[328]

The assays did not indicate whether cell damage is occurring through apoptosis or necrosis. For instance, in the LDH assay, cells that did not release LDH might still have undergone apoptosis. The cell viability assay only gave certainty about whether the cells are metabolically active, and thus, alive; it did not elaborate on the mechanism of cell death. The duration of incubation is also important as apoptosis markers may only be expressed transiently, and this can influence cytotoxic determinations like LD_{50}.[329] Both the concentration of toxin and the duration of exposure contribute to the cytotoxic effect. Also, in the LDH assay, cells could be dying (releasing LDH) for reasons other than compound exposure, including temperature, mechanical rupturing of cells, which must be taken into consideration when interpreting results.

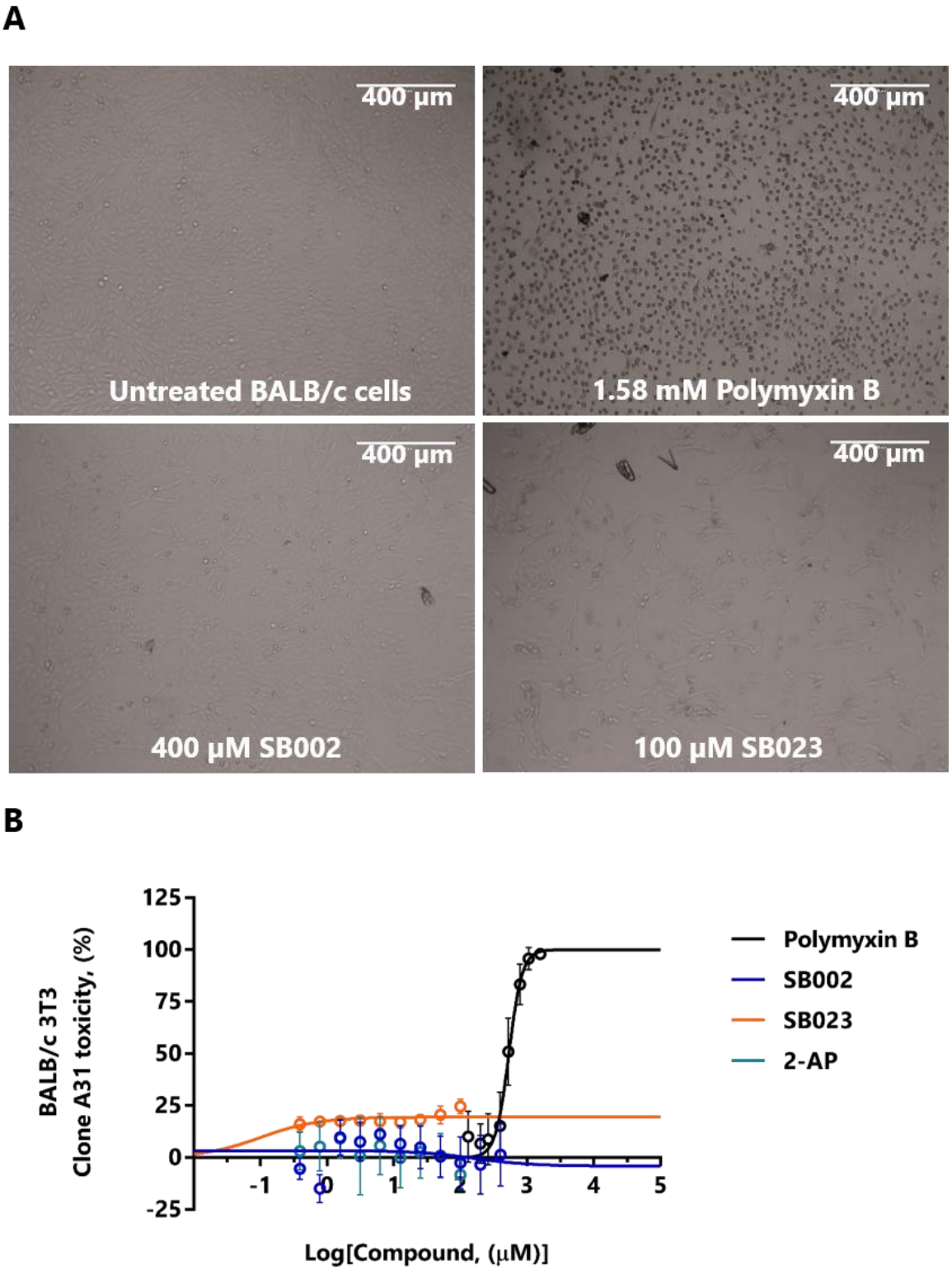

Figure 44. BALB/c 3T3 Clone A31 (BALB/c) mouse embryonic fibroblast cytotoxicity. (A) Micrographs of control and treated BALB/c cells after 48-hour incubation. 40x images include (in clockwise order) untreated BALB/c cells, and BALB/c cells exposed to 50 µM camptothecin, 100 µM SB023, and 400 µM SB002. **(B)** Dose-response curves of BALB/c cytotoxicity by 130 µM-1.58 mM of positive control polymyxin B (black), 0.39-400 µM of SB002 (blue), 0.39-100 µM SB023 (orange), and 0.39-100 µM 2-amino-4-chloropyridine (2-AP) (teal). Toxicity was calculated from cell viability (n=6) relative to untreated controls and media only wells.

Table 39. Therapeutic indexes of SB002 and SB023.

	SB002			SB023		
Cell line	**ED_{50}[a] (µM)**	**LD_{50} (µM)**	**Therapeutic index[b]**	**ED_{50}[a] (µM)**	**LD_{50} (µM)**	**Therapeutic index[b]**
A-375	1.05	n.d.	n.d.	8.84	105.60	11.95
A549	1.05	>100	n.d.	8.84	>100	n.d.
BALB/c	1.05	n.d.	n.d.	8.84	>100	n.d.
Hs27	1.05	98.42	93.73	8.84	204.80	23.17
U937	1.05	18.18	17.31	8.84	>100	n.d.

[a] The ED_{50} values were obtained from dose-response inhibition of *P. aeruginosa* in M9 acetate medium.
[b] Calculated by dividing LD_{50} by ED_{50}. **Abbreviations:** ED_{50}, dose at 50% efficacy; LD_{50}, dose at 50% cytotoxicity; n.d., not determined.

To make a meaningful judgment about whether the compounds were cytotoxic, I aligned the dose-response curves illustrating toxicity towards cell lines with the dose-response curves of PAO1 inhibition in M9 acetate medium. This created a visual comparison of the beneficial and adverse effects of SB002 and SB023. The concentration of compound which produced 50% of the adverse effect was divided by the concentration of compound which produced 50% of the beneficial effect, which gave a therapeutic index (TI), presenting a relationship between the minimum effective dose and the maximum tolerated dose *in vitro*.[330]

The dose-response curves of beneficial, *i.e.* antibacterial, and adverse, *i.e.* cytotoxic, effects of SB002 were compared using Hs27 and U937 cell lines. A black arrow indicates the area between the effective dose at 50% (ED50) and the lethal dose at 50% (LD50) in **figure 45A** and **B**. There was a wider TI for Hs27 (93.73) than U937 (17.31), see **table 39**. A high base absorbance signal (indicating >25% toxicity) among the concentrations of SB002-treated U937 cells could be responsible for the narrower TI. U937 is a suspension cell line, which means some cells were probably pipetted from the incubation plate into the assay plate, which added to the amount of LDH present in the assay plate. Attempts to optimise the assay included a centrifugation step, which I found to disrupt the cells and create mechanical cell lysis, which only increased the final spectroscopic signal.

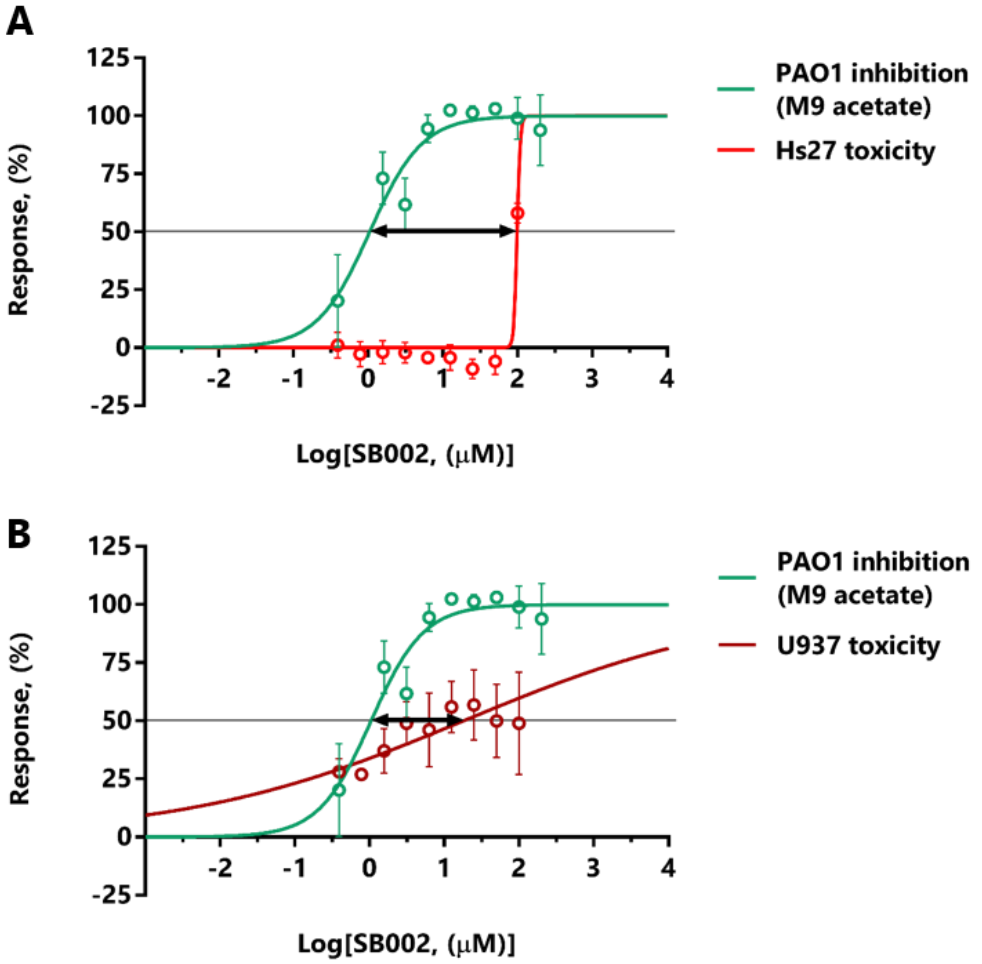

Figure 45. Therapeutic index of SB002. (A) Comparison of dose-response curves of *Pseudomonas aeruginosa* PAO1 inhibition in M9 acetate (turquoise) and toxicity towards Hs27 normal human fibroblasts (red) indicates a broad therapeutic window (black arrow) of 93.73. **(B)** Comparison of dose-response curves of *P. aeruginosa* PAO1 inhibition in M9 acetate (turquoise) and toxicity towards U937 human lymphocytes (maroon) indicates a narrower therapeutic window (black arrow) of 17.31.

The dose-response curves of the antibacterial and cytotoxic effects of SB023 were compared for A-375 and Hs27 cell lines. The area between the ED_{50} and the LD_{50} was analysed and indicated as a black arrow in **figure 46A** and **B**. There was a wider TI for Hs27 (23.17) than A-375 (11.95). Generally, if the dose required for the desired effect is high, the higher the exposure that is required to drive that effect, and the smaller the TI will be. The United States Food and Drug Administration defines narrow TI drugs as medicines that have less than a twofold difference in the minimum toxic concentration and minimum effective concentration, and which often require blood-level monitoring that is patient-specific.[330] An ideal therapeutic index depends on the clinical situation but should be several-fold higher than the dose required for efficacy if the drug behaves with suboptimal pharmacokinetics.

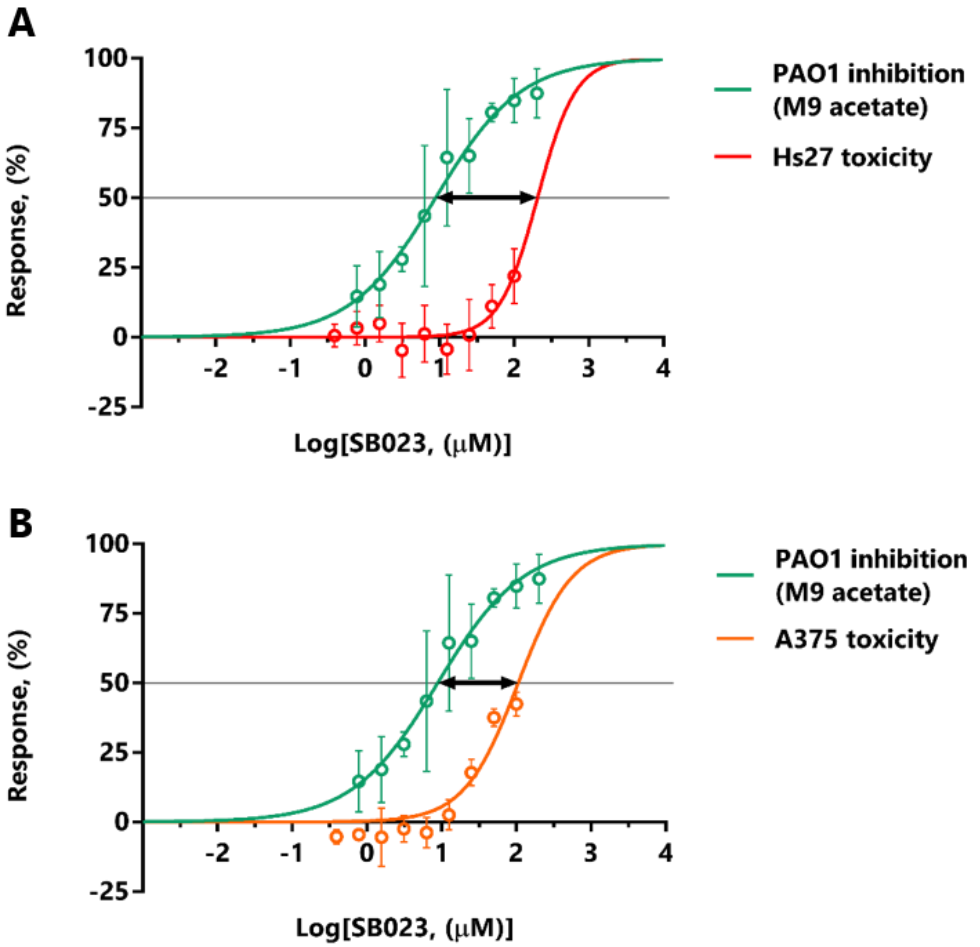

Figure 46. Therapeutic index of SB023. (A) Comparison of dose-response curves of *Pseudomonas aeruginosa* PAO1 inhibition in M9 acetate (turquoise) and toxicity towards Hs27 normal human fibroblasts (red) indicates a narrow therapeutic window (black arrow) of 23.17. **(B)** Comparison of dose-response curves of *P. aeruginosa* PAO1 inhibition in M9 acetate (turquoise) and toxicity towards A-375 human malignant melanoma (orange) indicates an even narrower therapeutic window (black arrow) of 11.95.

Progression of drug candidates that have narrow therapeutic indexes through the development process for non-life-threatening indications may be justified to explore a new therapeutic mechanism (also known as proof-of-mechanism studies). These studies must use limited dose exposure durations and ideally use sensitive biomarkers to monitor target modulation.[331] Overall, SB002 and SB023 were tested on two normal cell lines and three cancerous cell lines for any anti-proliferative and cytotoxic effects. Both SB002 and SB023 exerted low cytotoxicity on Hs27, A549, and U937 cells in concentration ranges relevant to therapeutic concentrations for the observed bactericidal effects. SB002 is particularly promising in the case of Hs27, where it has a therapeutic index of 93.73. SB023 additionally exhibited low toxicity towards A-375 melanoma cells and BALB/c 3T3 Clone A31 mouse embryonic fibroblasts. 2-AP exhibited no toxicity.

5.7 CYP450 metabolism of hit compounds

The *in vitro* metabolic clearances of the hit compounds were determined in liver microsomes from human and preclinical species during a research secondment in the Drug Metabolism and Pharmacokinetics (DMPK) department at Aptuit in Verona, Italy. Cytochrome P450s (CYP450) are a family of isoforms concentrated in the liver that play an important role in the oxidative metabolism of nearly 60% of all drugs we consume.[332] Relevant concentrations of test compounds and controls were incubated with human liver microsomes (HLM), rat liver microsomes (RLM) and mouse liver microsomes (MLM) to represent theoretical amounts of test molecules in the blood not bound to plasma proteins.

HLM, RLM and MLM were able to metabolise all three compounds (note: SB002 was not tested on MLM due to the limited quantity of sample available), see **figure 47**. The rate of parent compound depletion during the microsomal incubation was plotted as the natural log of the percentage of analyte remaining *versus* time and was used to calculate the compounds' intrinsic clearance, predicted hepatic clearance, and predicted *in vivo* hepatic clearance, see **table 40**. For SB002, 64%, and 51% of the parent compound was remaining at the end of 45-minute incubations with HLM and RLM, respectively. For SB023, 62%, 27%, and 30% was remaining after 45 minutes with HLM, RLM, and MLM, respectively. For 2-AP, 53%, 85%, and 35% was remaining after 45 minutes with HLM, RLM, and MLM, respectively (**figure 47**). By contrast, both positive controls were completely cleared at the end of the incubation period in all species, excluding dextromorphan incubated with HLM (**figure 47A**).

The clearance rates for the test compounds displayed interspecies variation. The values for intrinsic clearance (in $\mu L\ min^{-1}\ mg^{-1}$) of the hit compounds incubated with HLM were 2-AP > SB023 > SB002. Intrinsic clearance values of hits incubated with RLM were SB023 > SB002 > 2-AP, and in MLM, clearance values were SB023 > 2-AP see **table 40**. SB002 was metabolised faster when incubated with RLM (27.27 $\mu L\ min^{-1}\ mg^{-1}$) than with HLM (17.27 $\mu L\ min^{-1}\ mg^{-1}$).

SB023 was metabolised faster when incubated with RLM (53.93 $\mu L\ min^{-1}\ mg^{-1}$) and MLM (55.88 $\mu L\ min^{-1}\ mg^{-1}$) than when incubated with HLM (19.09 $\mu L\ min^{-1}\ mg^{-1}$), so SB023 was metabolised faster than SB002 by both HLM and RLM. For 2-AP, clearance was highest in MLM (48.37 $\mu L\ min^{-1}\ mg^{-1}$) and lowest in RLM (6.33 $\mu L\ min^{-1}\ mg^{-1}$).

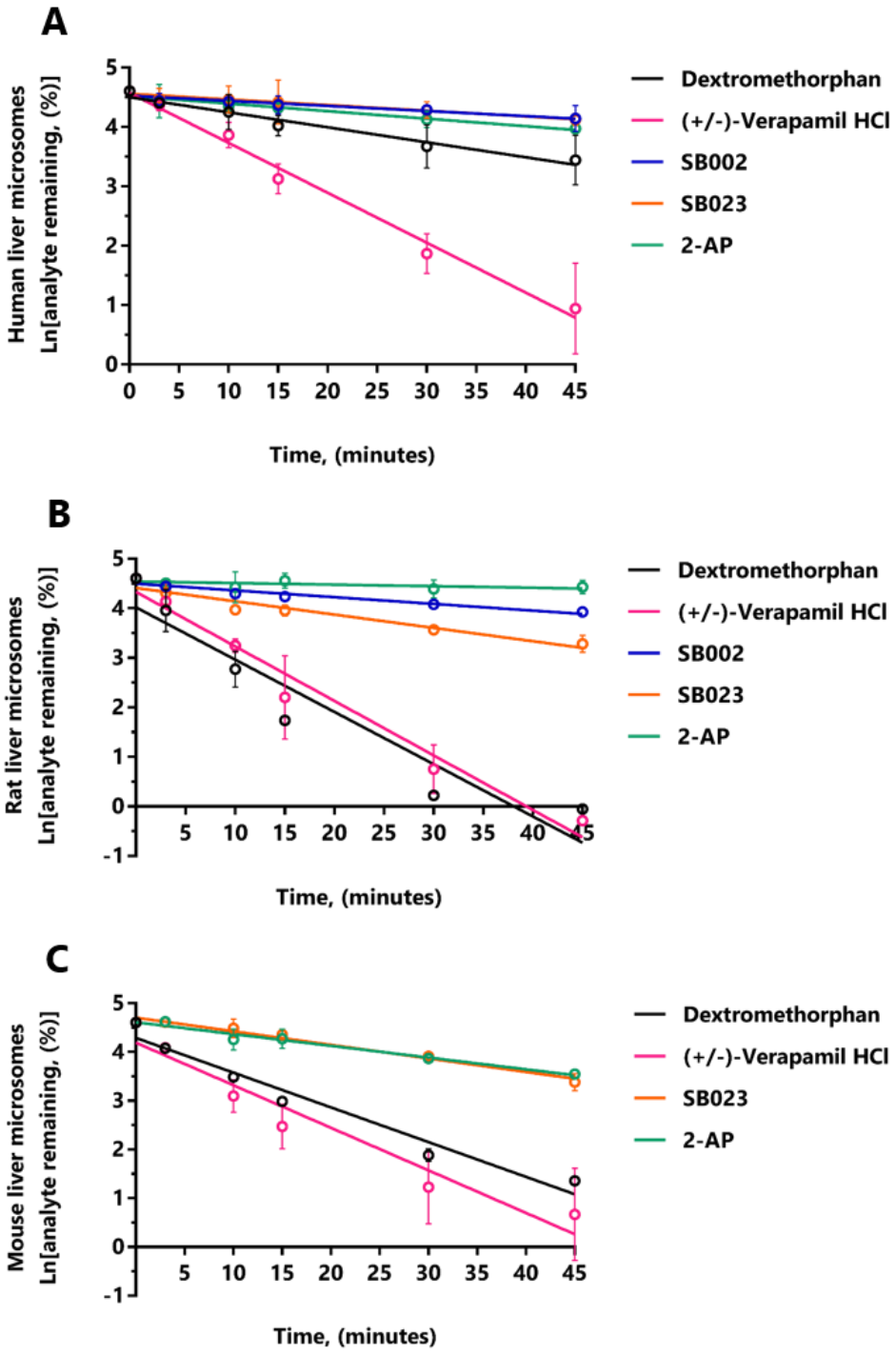

Figure 47. Metabolic clearance of SB002, SB023 and 2-AP in liver microsomes. All compounds were quantified by LC-MS/MS from 45-minute incubations with **(A)** human liver microsomes **(B)** rat liver microsomes and **(C)** mouse liver microsomes. The % analyte remaining at each time point was calculated by dividing the peak area by the peak area of the LC-MS/MS internal standard and % was determined based on the analyte remaining at time 0. % of analyte remaining was transformed to the natural log (ln) so that clearance could be derived from the slope of the linear regression.

Table 40. Calculated *in vitro* and predicted *in vivo* clearance parameters of hit compounds.

		Slope	R^2	Cl_{int} (µL min^{-1} mg^{-1})	$Cl_{h,\ int}$ (mL min^{-1} kg^{-1})	Cl_h (mL min^{-1} kg^{-1})	Half-life (min.)
Human LM	**SB002**	0.009	0.91	17.27	23.31	10.96	80.50
	SB023	0.010	0.96	19.09	25.75	11.48	72.85
	2-AP	0.013	0.95	25.44	34.33	12.91	54.65
	Dex.	0.025	0.97	50.66	68.36	15.89	27.45
	Ver.	0.084	0.99	168.64	227.54	18.97	8.25
Rat LM	**SB002**	0.014	0.93	27.27	62.99	36.18	50.99
	SB023	0.027	0.93	53.93	124.58	50.53	25.78
	2-AP	0.003	0.44	6.33	14.63	12.48	219.58
	Dex.	0.106	0.90	211.88	489.44	72.42	6.56
	Ver.	0.110	0.97	220.91	510.29	72.86	6.29
Mouse LM	**SB002**	n.d.	n.d.	n.d.	n.d.	n.d.	n.d.
	SB023	0.028	0.93	55.88	205.40	64.95	24.88
	2-AP	0.028	0.98	48.37	177.78	61.91	28.74
	Dex.	0.071	0.96	143.02	525.60	80.46	9.72
	Ver.	0.087	0.94	175.24	644.00	82.79	7.93

Abbreviations: 2-AP, 2-amino-4-chloropyridine; Cl_{int}, calculated intrinsic clearance in liver microsomes; $Cl_{h,\ int}$, calculated intrinsic hepatic clearance; Cl_h calculated *in vivo* hepatic clearance; Dex, dextromethorphan; LM, liver microsomes; Ver, verapamil.

The variation in microsomal metabolism carried through to the calculated hepatic and *in vivo* intrinsic clearances, where I considered the effect of scaling intrinsic clearance by average body mass and blood flow of each organism, see **table 40**. From the calculated hepatic clearance and blood flow, an extraction ratio was also determined for each compound. All compounds including positive controls had extraction ratios >0.70, which means the compounds are rapidly and wholely cleared from the blood by the liver, and their clearance is heavily dependent on the rate of blood flow.[333]

5.8 Evaluating CYP450 inhibition of hit compounds

Once I established that the hit compounds were CYP450 substrates, I also tested them for CYP450 inhibition in human liver microsomes during the same research secondment in Aptuit's DMPK department. CYP450 inhibition points to potential drug-drug interactions that occur when a molecule competes with a drug for the same enzyme receptor site. The more potent molecule will predominate, resulting in the decreased metabolism of the other. For most drugs, CYP450 inhibition leads to increased serum levels of their un-metabolised form, increasing the potential for toxicity. For drugs whose pharmacological activity requires biotransformation from a pro-drug form, inhibition also can lead to decreased drug efficacy.[316]

CYP450 inhibition was determined by quantifying the amounts of the CYP450 probes' products via LC-MS/MS analysis when human liver microsomes were incubated with the test compounds, probe compounds, and known inhibitors. The dose-response curves are shown in **figure 48**, and the IC_{50} values from the dose-response curves are displayed in **table 41**. SB002, SB023 and 2-AP inhibited none of the isozymes, with IC_{50} values well above the highest concentration tested (100 μM). SB002 displayed a slight inhibition of CYP2C19 (**figure 48D**), with a calculated IC_{50} value of 126.20 μM. By contrast, all positive controls inhibited CYP450s with sigmoidal data distributions and with IC_{50} values in the nanomolar to submicromolar range (**table 41**).

Table 41. CYP450 inhibition. Parameters were determined from best nonlinear regressions using GraphPad Prism version 7.04.

CYP		SB002	SB023	2-AP	Positive control[a]
1A2	**IC_{50} (μM)**	>100	>100	>100	1.55 ± 1.16
	Hill slope	-0.27 ± 0.14	-0.33 ± 0.23	-0.14 ± 0.02	-0.73 ± 0.07
2C8	**IC_{50} (μM)**	>100	>100	>100	2.28 ± 1.14
	Hill slope	n.d.	n.d.	n.d.	-1.09 ± 0.14
2C9	**IC_{50} (μM)**	>100	>100	>100	1.47 ± 1.81
	Hill slope	n.d.	n.d.	n.d.	-0.38 ± 0.09
2C19	**IC_{50} (μM)**	126.20 ± 1.10	n.d.	n.d.	0.54 ± 1.92
	Hill slope	-0.35 ± 0.12	n.d.	n.d.	-0.57 ± 0.24
2D6	**IC_{50} (μM)**	>100	>100	>100	0.09 ± 1.23
	Hill slope	n.d.	n.d.	n.d.	-0.62 ± 0.08
3A4-ATR	**IC_{50} (μM)**	>100	>100	n.d.	0.03 ± 1.11
	Hill slope	n.d.	n.d.	n.d.	-0.83 ± 0.07
3A4-NIF	**IC_{50} (μM)**	>100	>100	n.d.	0.02 ± 1.29
	Hill slope	n.d.	-0.22 ± 0.04	n.d.	-0.52 ± 0.07
3A4-MDZ	**IC_{50} (μM)**	>100	>100	>100	0.02 ± 1.16
	Hill slope	n.d.	n.d.	n.d.	-0.75 ± 0.09

[a] Positive controls; 1A2: fluvoxamine; 2C8: quercetin; 2C9: sulfaphenazole; 2C19: ticlopidine; 2D6: quinidine; 3A4-ATR, 3A4-NIF, and3A4-MDZ: ketoconazole.
Abbreviations: 2-AP, 2-amino-4-chloropyridine; ATR, atorvastatin; CYP, cytochrome P450; MDZ, midazolam; n.d., not determined; NIF, nifedipine.

The probe for CYP2C19 could not be detected in the first instance during incubations with SB023 and 2-AP because the constitutive expression of CYP450 genes fluctuates in the human population.[315] When we used a new batch of liver microsomes, we detected the probe (diclofenac), but due to limited quantity of hit compounds available, we could not repeat the assays during the secondment on that particular isozyme.

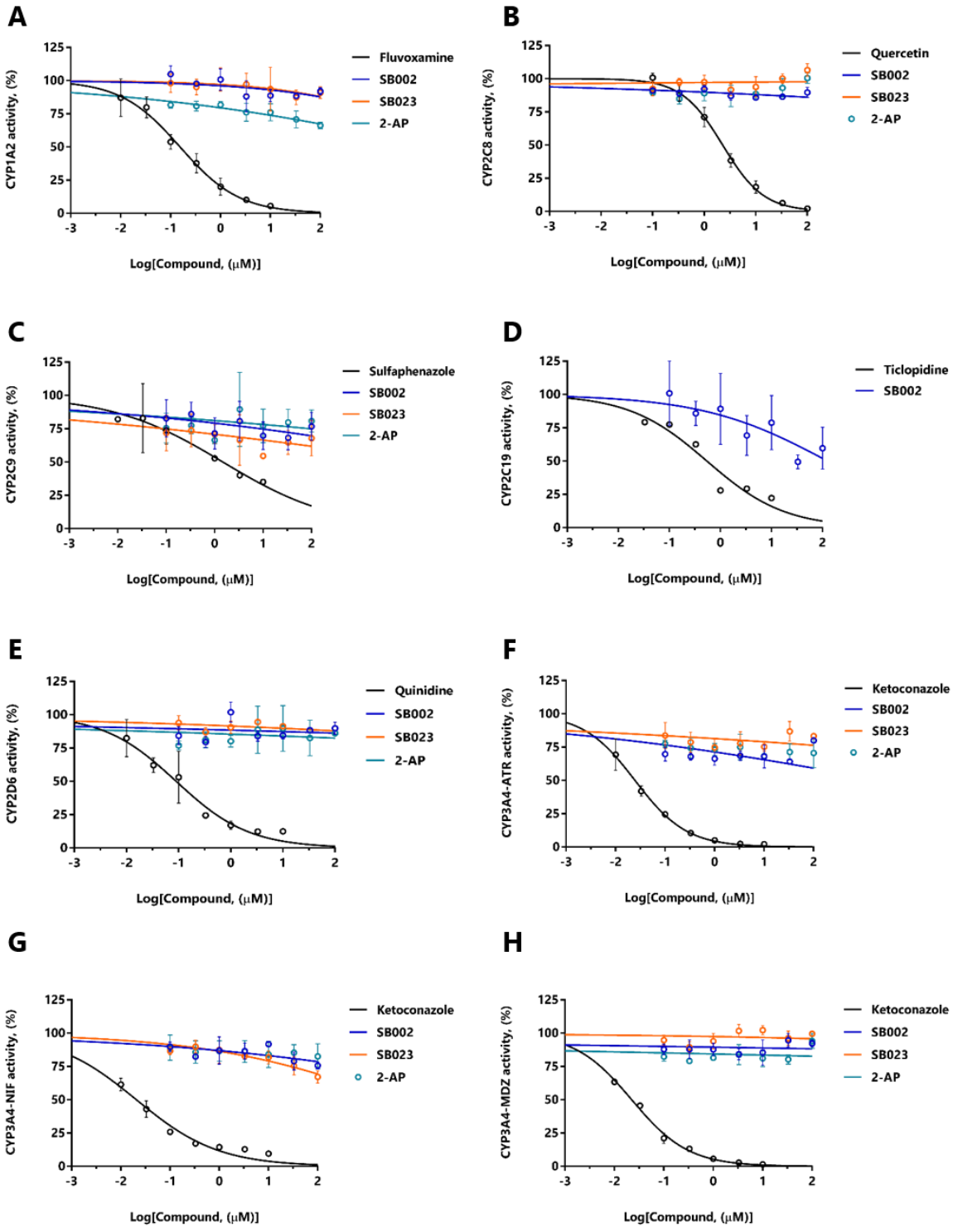

Figure 48. Dose-response inhibition of CYP450 isozymes. SB002 (blue), SB023 (orange), 2-amino-4-chloropyridine (teal) and relevant positive controls (black) were tested for their inhibition of: **(A)** CYP1A2 (positive control: fluvoxamine), **(B)** CYP2C8 (positive control: quercetin), **(C)** CYP2C9 (positive control: sulfaphenazole), **(D)** CYP2C19 (positive control: ticlopidine), **(E)** CYP2D6 (positive control: quinidine), **(F)** CYP3A4 binding site 1 (ATR) (positive control: ketoconazole), **(G)** CYP3A4 binding site 2 (NIF) (positive control: ketoconazole), **(H)** CYP3A4 binding site 3 (MDZ) (positive control: ketoconazole).

Biochemically, the lack of inhibitory activity simply meant that the hit compounds were not able to bind irreversibly to any of the CYP450s to inhibit oxidation of the known substrates. We know from the previous section that the hit compounds are metabolised by CYP450s, so these results indicate the hits did not bind CYP450s with a similar affinity as the known substrates and therefore did not offer competitive inhibition. Pharmacologically, however, the absence of CYP450 inhibition means that the probability of causing drug-drug interactions is markedly reduced, and it signals the ability to progress further in the drug development pipeline.[334]

5.9 Discussion

The two primary reasons behind the failure of hit to lead candidates in drug discovery and development are lacking efficacy and safety profiles.[82] This study is the first to report SB002 and SB023 in the context of hit to lead optimisation as putative antibacterial compounds for *Pseudomonas aeruginosa*. SB002 and SB023 displayed bactericidal activity towards *P. aeruginosa*, which is congruent with the glyoxylate shunt's function to protect against oxidative stress. When I expanded the pathogen screening, SB023 was not effective against a *P. aeruginosa* clinical isolate or *K. pneumoniae*, and showed limited inhibition of *A. baumannii*. This could have to do with the difference in the regulation of the glyoxylate shunt in these organisms, or it could be a permeability issue. Comparing the genomes between PAO1 and ATCC 27853, the differences are due to the accessory genes from prophages and genomic islands that suggest biofilm maturation and virulence-related genes in the clinical isolate.[335] The YM64 mutant did not show increased susceptibility to SB002, yet was more susceptible to SB023, which means that an up-regulation in any of the major Mex efflux pumps could decrease the intracellular SB023 concentration.

SB002 and SB023 also showed variability in their efficacy when carbon sources were altered, which could be that off-target effects or a more complex network are behind inhibition. A slight inhibitory activity was observed in minimal medium supplemented with propionate, so I tested the hits against 2-methylcitrate synthase, one of the enzymes in the 2-methylcitrate pathway that allows bacterial growth on C_3 sources, like propionate.[326] This experiment confirmed that the inhibition of bacterial growth in propionate was partially occurring as a result of direct interaction with one of the enzymes in the pathway and that the compounds were displaying a degree of promiscuity. The promiscuity could be intrinsic to the compounds' antibacterial efficiency.

Antibacterial compounds have been an exception to Lipinski's RO5 and occupy a unique chemical space. They typically deviate from the rules towards higher molecular weights and increased polarities, which reflect the requirement to penetrate the outer membranes of Gram-negative bacteria.[149] An analysis of the physicochemical properties of 147 compounds active

against Gram-negative bacteria revealed that compared with the average properties of compounds in the Comprehensive Medicinal Chemistry (CMC) database, the average MW, H-bond donors, and H-bond acceptors of antibacterial agents were higher, while the cLogP was lower.[149] The calculated physicochemical properties of SB002, SB023 and 2-AP are listed in **table 42**, along with the averages from the study for reference. Approved antibacterial drugs effective against *Pseudomonas aeruginosa* revealed an even narrower physicochemical range, with molecular weights below 600 Da and a lipophilicity average well below 0. This is nearly 4-fold more polar than SB002 and SB023.

Table 42. Comparison of physicochemical properties of hits and antibiotics.

	CMC	Gram-	SB002	SB023	2-AP
MW (g mol^{-1})	338	414	370.8	361.4	128.6
cLogP $_{\text{octanol/water}}$	2.7	-0.1	3.7	3.0	1.1
H-bond donors	1.6	5.1	2	2	1
H-bond acceptors	4.9	9.4	5	6	2

Properties were calculated using ChemBioDraw Ultra 13.0 (PerkinElmer). CMC and Gram-negative properties were obtained from O'Shea, 2008.[149]
Abbreviations: 2-AP, 2-amino-4-chloropyridine; CMC, Comprehensive Medicinal Chemistry database; Gram-, Gram-negative antibiotics; H-bond, hydrogen bond; cLog*P*, calculated partition coefficient; MW, molecular weight.

The likelihood of binding to multiple targets doubles above the value of cLog*P* = 3.75.[297,336] Lipophilicity represents the molecular desolvation when transferring from aqueous phases to cell membranes and protein sites, which are hydrophobic in nature.[297] Promiscuity is the number of hits where >30% inhibition was found at a concentration of 10 μM, and promiscuity is controlled by lipophilicity and ionisation state of the drug.[297]

It is important to understand the pharmacophore of the hit compounds for medicinal chemistry optimisation, which is a crucial step in hit to lead optimisation. The structure-activity relationships of the hit compounds are not yet confirmed by co-crystal structures with the target enzymes, but were rationally discussed in **chapter 4**. 2-AP showed no target nor whole-cell inhibition in these studies, meaning the guanidine moiety and/or the Boc protecting groups most likely are important for binding to the target enzymes as well as getting through *P. aeruginosa*'s outer membrane. Although rare, there are instances of approved drugs containing a guanidine moiety, including the aminoglycoside, streptomycin.[337] Despite this rarity, there are several examples in the literature of guanidine-containing compounds that exhibit antibacterial activity.[301,327,338–341] Indeed, six out of the eight hits from Pfizer's *P. aeruginosa* whole-cell screening campaign contained guanidine groups.[194] Another example is a rational approach to improve aminoglycoside antibiotics conducted by modifying the chemical scaffold and replacing the amine or hydroxy groups with

guanidine groups. This resulted in guanidine-modified amikacin with improved affinity and a lower MIC for *P. aeruginosa*.[342] In 2018, a patent was filed for a guanidine-derivative that displayed potent inhibition against *P. aeruginosa* and low toxicity to A-549 lung epithelial cells.[300] Another example is the muraymycin compounds, which have a lipophilic side chain and a guanidine group that are required to inhibit the peptidoglycan biosynthesis pathway in *P. aeruginosa*.[343]

Most of the biological properties of guanidine derivatives are related to their strong basicity in water with a pKa of 13.8.[344] Under physiological conditions, the guanidine group exists mainly in its protonated form, which may allow for interaction with the target enzymes.[345] Another option is that it could be responsible for binding to the bacterial outer membrane on the negatively-charged polysaccharide layer, causing cell death.[346] The electron-withdrawing groups present in the hit compounds might enhance guanidine's binding activity with phosphate and sulphate groups present on the cell membrane through charge pairing and hydrogen bonds.[347]

Despite the successful performance of the compounds overall, there were issues with chemical stability during this study. I observed a total loss of antibacterial activity on a degraded sample of SB002. Removal of the Boc protecting groups was most likely responsible for the loss of activity and most likely occurred by protonation from the residual water present in DMSO (a hygroscopic solvent), which was accelerated by heat during my attempts to improve compound solubility (personal communication with Dr Sean Bartlett). In fact, it has been published that Boc protecting groups can be removed using H_2O and a microwave (170°C) in 2-3 minutes.[348] It is a requirement of drugs, in general, to remain stable for prolonged periods due to administration requirements based on the dosing window,[321] so this is a major drawback when considering the potential of SB002 and SB023 as antibacterial lead compounds.

The next stage in hit to lead optimisation is to improve upon the medicinal chemistry of the hits. An obvious chemical modification to perform on SB002 and SB023 is to replace the Boc protecting groups with a functional group that behaves similarly either chemically or sterically. Possible chemical shape modifications are being explored using *in silico* methods by Prashanthi Medarametla from the University of Eastern Finland. She is currently conducting a shape screening study on my MS_{Pa} crystal structure (PDB entry 5AOS), which is a virtual screening methodology that considers the shape and steric chemistry of a molecule, which could be important depending on the shape and amino acids in the binding pocket of interest.[349]

The other requirement for a lead candidate is safety. Lipinski's RO5 are meant to be guidelines based on successful lead candidates that reach Phase II in the drug development pipeline and display good murine bioavailability. By definition, RO5-compliant lead candidates have already passed rigorous toxicology and clinical safety hurdles.[296] This was promising as SB002 and SB023

were RO5-compliant. SB002 and SB023 did not exhibit profound cytotoxicity towards any of the mammalian cells I tested, but compared side-by-side with the antibacterial dose-response curves, revealed a narrow potential therapeutic range (<100), according to preclinical development standards.[331]

There are approved antibiotics with narrow TIs that require patient monitoring when administered, including the aminoglycosides, gentamicin and amikacin, or the lipopeptide, vancomycin, as well as polymyxin B.[350] This indicates that the candidate's safety is considered on a case by case basis when there is a clear efficacy with drug-like, physicochemical properties.

SB002 and SB023 were metabolised by CYP450s in human liver microsomes with moderate half-lives of 81 and 72 minutes, respectively. The results indicate that SB002 and SB023 are direct substrates of CYP450 isozymes. Analysing *in vitro* metabolic clearance does not indicate which isozyme is responsible for the compound's metabolism; however, the clearance rates themselves and the *in vivo* considerations are important for progressing in the drug development pipeline. The *in vivo* predictions should be approached with caution, though, because whenever pooled liver microsomal activities are measured, the assumption is that every enzyme represents the average population's activity.[351] I observed differences in hit compounds' metabolism between HLM and RLM/MLM, which gives insight into future *in vivo* work, specifically that using murine models as pharmacokinetic/pharmacodynamic representations for human models might not be accurate.[315]

2-AP itself is a chemical fragment of SB002 and SB023, and CYP450-mediated N-hydroxylation of the primary amine in the ortho position would theoretically be more stable and therefore slower to metabolise than its meta or para counterparts. Slower metabolism is linked to increased accrual in the liver and likely increases the chances for toxicity *in vivo*.[352] 2-AP is a precursor for the manufacture of a select few drugs on the market, including Sulphapyridine, a sulphonamide antibiotic that is no longer prescribed for human treatment due to bacterial resistance.[353] The hit compounds are metabolised by CYP450s in liver microsomes but do not inhibit CYP450s compared with known inhibitors. This is a routine test for *in vitro* DMPK studies and is indicative of potential drug-drug interactions.

Despite the advantages, *in vitro* models have an important downside in that the host immune system is ignored during antibacterial evaluation. For instance, in an *in vitro* pharmacodynamic study, ticarcillin performed better at reducing log CFU of *Pseudomonas aeruginosa* than in a murine thigh infection model.[354] In animal models, the action and efficacy of the drug can be evaluated at the place of infection, and the reaction of the immune system can be monitored, which delivers more precise results, provided a realistic human pharmacokinetic profile

is present. Free drug concentrations need to sometimes remain above the MIC level for this type of assessment, which is why assessing cytotoxicity is so important.[355]

Overall, SB002 and SB023 display promise as potential lead candidates for antibacterial development. Further work will involve chemical optimisation, as well as testing a range of doses for *in vivo* pharmacodynamics in preclinical species. The methodology required in moving from hit to lead candidate selection depends on the screening technology used to identify the hit compounds. Hit evolution is a technique for hit optimisation where analogues of the original hits are synthesised and tested for potency or an improved lead-like profile. Structure-activity relationship (SAR) studies are then used for chemical optimisation and lead selection.[313] The work presented here provides data for proof-of-principle studies, but there will be a substantial challenge in the future of how to convert SB002 and SB023 into leads while retaining their current cellular activities.

6. Conclusions

The adaptation of *Pseudomonas aeruginosa* to its environment is responsible for a significant proportion of hospital-acquired infections worldwide. These infections are notoriously difficult to treat because they often exhibit resistance to one or more antibiotics. Despite the critical need for new antibiotics to mitigate these hospital-acquired infections, the pharmaceutical industry has struggled to replace antibiotics as they inevitably become obsolete due to antibiotic resistance. *P. aeruginosa* can thrive in diverse infection scenarios by rewiring its central metabolism, and a prominent example of this is in the airways of cystic fibrosis patients, where the bacterium uses the glyoxylate shunt to metabolise fatty acids (degraded from lung surfactant into acetyl coenzyme A) for biomass production.[356] It has been proven that without a functional glyoxylate shunt, *P. aeruginosa* is unable to grow on fatty acids or acetate that are the main nutrient sources in the CF airways.[357]

The glyoxylate shunt has potential as a new antibacterial target in *P. aeruginosa*. The glyoxylate shunt is a part of central metabolism and therefore, conditionally important for the bacteria. There is also evidence to support that, besides carbon fixation, the glyoxylate shunt has been implicated in virulence and is essential for establishing pulmonary infections in mammalian systems. There are no known mammalian orthologues of the glyoxylate shunt, meaning the target is selective. Additionally, successfully targeting the glyoxylate shunt could be possibly broad spectrum as it is present in many pathogenic bacteria. Finally, the glyoxylate shunt contains two enzymes: isocitrate lyase and malate synthase G, which targeting simultaneously could provide an antibacterial agent that theoretically delays the development of resistance. Being able to create new strategies of antibacterial intervention for *P. aeruginosa* infections would greatly improve a patient's prognosis.

Appreciating the conditional importance of the glyoxylate shunt in establishing and sustaining *P. aeruginosa* infection scenarios, the first objective of this study was to characterise the second enzyme of the glyoxylate shunt, malate synthase G, from *Pseudomonas aeruginosa* and assess its suitability as a target for drug discovery and development. Recent work has demonstrated the tractability of this enzyme as a drug target in other pathogens, but remarkably little has been documented about its biochemistry in *P. aeruginosa*. I overexpressed and purified MS_{Pa} and determined the first X-ray crystal structure at 1.62 Å resolution. I found that the secondary structures were very similar between malate synthases from other pathogens, which led to highly similar tertiary structures among pathogenic bacteria as well.

Data derived from a computational analysis of the crystal structure revealed two sites in the enzyme that were theoretically promising for binding of drug-like molecules. One site was highly hydrophobic and was buried deep in the protein, while the other site was more hydrophilic and spanned the entrance of the active site, which contained the amino acids responsible for acetyl coenzyme A binding. Another computational analysis mapped the likely physiological hydration network within the protein and illustrated the thermodynamic properties of the predicted hydration sites. This examination further supported the "druggability" of malate synthase, as it elaborated on the energetically favourable and unfavourable hydration sites within the predicted drug binding sites. I also found that the events in the enzyme's active site could be monitored non-invasively using intrinsic tryptophan fluorescence as a probe. I quantified magnesium binding as a co-factor and confirmed its necessity as a co-factor in enzyme catalysis. The structural and mechanistic information deriving from this study will support the design of improved inhibitors of malate synthase G in *P. aeruginosa*.

The second objective of this study was to identify dual inhibitors of the glyoxylate shunt in *P. aeruginosa*. Compounds were synthesised that combined the structural features of a known family of π-anion inhibitors of malate synthase G in *Mycobacterium tuberculosis*, and a 2-aminopyridine hit from a high throughput screening campaign against *P. aeruginosa* grown in acetate. This resulted in eight novel 2-aminopyridine derivatives, which I screened for their potential as dual inhibitors using enzyme kinetics and bacterial MIC assays. From this investigation, a hit compound was confirmed, SB002, which inhibited *P. aeruginosa* PAO1 growth in acetate medium, as well as abolished the enzyme activities of both shunt enzymes with low micromolar potencies. A second hit compound emerged from this study; SB023, a cyano derivative of SB002. SB023 inhibited PAO1 growth and MS_{Pa} activity completely, and which partially inhibited ICL_{Pa} activity with MICs and IC_{50} values in the low micromolar range. These experiments confirmed the hypothesis that these designed inhibitors were selective and cell-permeable. However, the other 2-aminopyridine derivatives underperformed as inhibitors, which did not follow initial predictions that their potencies would increase as the electronegativity of their aromatic substitutions increased.

The precise molecular mechanism of the two hit compounds was not yet clear, but I elucidated more information about the mechanism of inhibition upon further kinetic analysis. Both SB002 and SB023 displayed mixed inhibition of malate synthase, with a preference towards uncompetitive inhibition regarding substrate glyoxylate and competitive inhibition regarding co-substrate acetyl coenzyme A. SB002 displayed uncompetitive inhibition of isocitrate lyase. I validated SB002 as a dual inhibitor using isothermal titration calorimetry, which resulted in dissociation constants equal to 28 nM and 1 μM for malate synthase and isocitrate lyase,

respectively. ITC also revealed that the thermodynamics driving inhibitor binding was different for both shunt enzymes. The favourable energy of binding was strongly driven by entropy for malate synthase. While releasing less heat, the binding of SB002 to isocitrate lyase was driven more equally by enthalpy and entropy.

Although I could not obtain co-crystal structures to determine the exact binding poses and confirm the structure-activity relationships of the inhibitors, SB002 and SB023, I proposed an alternative analysis based on ligand chemistry. The hit compounds contain unique functional groups, such as guanidine groups and Boc protecting groups that were not present in the negative control, which illustrated that these functional groups were important for binding to the target enzymes as well as cellular uptake *P. aeruginosa*'s outer membrane. Guanidine groups are well known for their biological properties. At physiological pH, guanidine exists as a protonated, highly stable cation, which allows for many biological interactions, particularly forming hydrogen bonds with negatively-charged ions, like the phosphates in the cell's polysaccharide layer. Despite this conjecture, the molecular mechanism by which SB002 and SB023 are interacting with both glyoxylate shunt enzymes remains unanswered. This study resulted in the identification of novel dual inhibitors of the glyoxylate shunt and highlighted intriguing differences in the mechanisms behind their inhibition.

The final objective of this study was to evaluate the hit compounds to determine their potential as lead antibacterial candidates for *Pseudomonas aeruginosa* infections in the context of the pharmaceutical discovery and development pipeline. The first requirement for a successful antibacterial candidate is efficacy, so more insight about the antibacterial action of the hit compounds was elucidated. SB002 and SB023 exhibited bactericidal activity, which corresponds with the notion that the glyoxylate shunt serves to protect against oxidative stress in *P. aeruginosa*.[317]

When I expanded the pathogen screen to include the ESKAPE pathogen panel, SB023 was not effective against a *P. aeruginosa* clinical isolate or *K. pneumoniae*, but did reduce *A. baumannii* and *E. coli* growth, further expanding its activity spectrum. The incongruity of inhibition among these pathogens might be due to the different regulation of the glyoxylate shunt in these organisms, which, in turn, affects their expression levels and available binding sites.[166] Another possibility for reduced activity, particularly in the *P. aeruginosa* clinical isolate could be decreased permeability derived from increased efflux pump expression or decreased porin expression. A mutant of *P. aeruginosa* deficient in the genes encoding the four major Mex multidrug efflux pumps did not show increased susceptibility to SB002, yet was more susceptible to SB023, which means that SB023 is a likely substrate for one of these efflux pumps. Up-regulation of any of the efflux pumps could

rapidly decrease the intracellular SB023 concentrations and reduce its efficacy, which is an important consideration if the compound were to progress in its current chemical form.

SB002 and SB023 also showed variability in their antibacterial efficacies when I altered the carbon sources in the growth media. This indicated that off-target effects were present, or that a more complex network was responsible for the inhibition. For example, inhibitory activity was observed in medium supplemented with propionate for both compounds, so I tested the hits on 2-methylcitrate synthase, which is one of the enzymes in the 2-methylcitrate pathway that allows bacterial growth on propionate. I tested on 2-methylcitrate synthase to confirm that the inhibition was occurring as a result of direct interaction with the enzymes in the pathway. SB002 displayed promiscuity by partially inhibiting 2-methylcitrate synthase, but it seemed that the promiscuity was intrinsic to the compounds' therapeutic efficiency as SB002 consistently performed better than SB023.

The other requirement for a lead candidate is that it must be safe for eukaryotic cells. From the cytotoxicity evaluation, SB002 and SB023 did not exhibit cytotoxicity towards any of the mammalian cells, but when the toxicity data were compared side-by-side with the antibacterial dose-response curves, they revealed a relatively narrow potential therapeutic range according to preclinical development standards. There are approved antibiotics with narrow therapeutic indices, which indicates that safety is considered as a case by case basis when the compounds exhibit clear efficacy.

SB002 and SB023 were metabolised by CYP450s in human liver microsomes with moderate half-lives of 81 and 72 minutes, respectively. These results indicated that SB002 and SB023 were direct substrates of CYP450 isozymes. The hit compounds also exhibited no irreversible inhibition of CYP450s compared with known inhibitors, which decreases the likelihood of drug-drug interactions in the future. The hepatic clearance rates and the *in vivo* extrapolations are important considerations for progressing in the drug development pipeline before subjecting the hit compounds to *in vivo* efficacy testing. I also observed differences in the hit compounds' metabolism between human liver microsomes and the liver microsomes of preclinical species, which gives insight into how the inhibitors might behave in future *in vivo* work. Specifically, using murine models as pharmacokinetic/pharmacodynamic representations for human models might not be totally accurate.

Consequently, the hit compounds performed successfully in the *in vitro* efficacy and safety assessments. Despite this success, there were issues with chemical stability during this study. I observed a total loss of antibacterial activity on a degraded sample of SB002. Removal of the Boc protecting groups through protonation from residual water present in DMSO, especially in the

presence of heat, is what most likely occurred. Evidence of stability issues leads into the next stage in the hit to lead optimisation, which is to improve upon the medicinal chemistry of the hits. An obvious chemical modification to perform on SB002 and SB023 is to replace the Boc protecting groups with a functional group that either interacts similarly, chemically or sterically.

Overall, this work provided a proof of concept for the glyoxylate shunt as a target for antibacterial intervention in *Pseudomonas aeruginosa*. MS_{Pa} was biochemically characterised and delivered structural and mechanistic information that will support the design of MS inhibitors in the future. SB002 and SB023 were identified and validated as selective and cell-permeable inhibitors of the glyoxylate shunt in *Pseudomonas aeruginosa*, and both hit compounds displayed promise in *in vitro* safety and efficacy analyses. Continuing work should endeavour to chemically optimise the compounds to improve their stability, solubility, and to define structure-activity relationships while retaining their current cellular activity and permeability.

7. References

1. World Health Organization. Health care-associated infections fact sheet. (2010). Available at: http://www.who.int/gpsc/country_work/gpsc_ccisc_fact_sheet.en.pdf.
2. Magill, S. S., Edwards, J. R., Bamberg, W., Beldavs, Z. G., Dumyati, G., Kainer, M. A., Lynfield, R., Maloney, M., McAllister-Hollod, L., Nadle, J., Ray, S. M., Thompson, D. L., Wilson, L. E. & Fridkin, S. K. Multistate Point-Prevalence Survey of Health Care–Associated Infections. *N. Engl. J. Med.* **370**, 1198–1208 (2014).
3. National Institute for Health and Care Excellence. Healthcare-associated infections: prevention and control. (2019). Available at: https://www.nice.org.uk/guidance/qs61/resources/infection-prevention-and-control-2098782603205.
4. Viale, P., Giannella, M., Tedeschi, S. & Lewis, R. Treatment of MDR-Gram negative infections in the 21st century: a never ending threat for clinicians. *Curr. Opin. Pharmacol.* **24**, 30–37 (2015).
5. Peleg, A. Y. & Hooper, D. C. Hospital-Acquired Infections Due to Gram-Negative Bacteria. *N. Engl. J. Med.* **362**, 1804–1813 (2010).
6. Rice, L. B. Federal Funding for the Study of Antimicrobial Resistance in Nosocomial Pathogens: No ESKAPE. *J. Infect. Dis.* **197**, 1079–1081 (2008).
7. Boucher, H. W., Talbot, G. H., Benjamin, D. K., Bradley, J., Guidos, R. J., Jones, R. N., Murray, B. E., Bonomo, R. A. & Gilbert, D. 10 x '20 Progress-Development of New Drugs Active Against Gram-Negative Bacilli: An Update From the Infectious Diseases Society of America. *Clin. Infect. Dis.* **56**, 1685–1694 (2013).
8. Hersh, A. L., Newland, J. G., Beekmann, S. E., Polgreen, P. M. & Gilbert, D. N. Unmet medical need in infectious diseases. *Clin. Infect. Dis.* **54**, 1677–1678 (2012).
9. Tacconelli, E., Carrara, E., Savoldi, A., Kattula, D., Burkert, F. & Tacconelli. Global Priority List of Antibiotic-Resistant Bacteria to guide Research, Discovery, and Development of New Antibiotics. *World Health Organization* 1–7 (2017). Available at: http://wwwa.who.int/medicines/publications/WHO-PPL-Short_Summary_25Feb-ET_NM_WHO.pdf?ua=1.
10. O'Neill, J. Antimicrobial Resistance: Tackling a crisis for the health and wealth of nations. *Review on Antimicrobial Resistance* (2014). Available at: https://amr-review.org/sites/default/files/AMR Review Paper Tackling a crisis for the health and wealth of nations_1.pdf.

11. U.S. Department of Health and Human Services Centers for Disease Control and Prevention. Antibiotic Resistance Threats in United States, 2013. (2013). Available at: https://www.cdc.gov/drugresistance/threat-report-2013/pdf/ar-threats-2013-508.pdf#page=13.
12. Cassini, A., Högberg, L. D., Plachouras, D., Quattrocchi, A., Hoxha, A., Simonsen, G. S., Colomb-Cotinat, M., Kretzschmar, M. E., Devleesschauwer, B., Cecchini, M., Ouakrim, D. A., Oliveira, T. C., Struelens, M. J., Suetens, C., Monnet, D. L., Strauss, R., Mertens, K., Struyf, T., Catry, B., *et al.* Attributable deaths and disability-adjusted life-years caused by infections with antibiotic-resistant bacteria in the EU and the European Economic Area in 2015: a population-level modelling analysis. *Lancet Infect. Dis.* **19**, 56–66 (2019).
13. Laxminarayan, R. & Chaudhury, R. R. Antibiotic Resistance in India: Drivers and Opportunities for Action. *PLOS Med.* **13**, e1001974 (2016).
14. O'Neill, J. Tackling drug-resistant infections globally: final report and recommendations. *Review on Antimicrobial Resistance* (2016). Available at: https://amr-review.org/sites/default/files/160525_Final paper_with cover.pdf
15. Laxminarayan, R., Matsoso, P., Pant, S., Brower, C., Røttingen, J.-A., Klugman, K. & Davies, S. Access to effective antimicrobials: a worldwide challenge. *Lancet* **387**, 168–175 (2016).
16. Moellering, R. C. Past, Present, and Future of Antimicrobial Agents. *Am. J. Med.* **99**, 6A-11S (1995).
17. Gould, I. M. Antibiotic resistance: the perfect storm. *Int. J. Antimicrob. Agents* **34**, S2–S5 (2009).
18. Alanis, A. J. Resistance to Antibiotics: Are We in the Post-Antibiotic Era? *Arch. Med. Res.* **36**, 697–705 (2005).
19. Tan, S. Y. & Tatsumura, Y. Alexander Fleming (1881–1955): Discoverer of penicillin. *Singapore Med. J.* **56**, 366–367 (2015).
20. Baldry, P. E. *The Battle Against Bacteria.* (Cambridge University Press, 1965).
21. S, S. Zur Frage der salvarsanresistenten Leus. *Arch Derm Syph* **147**, 116–130 (1924).
22. Stekel, D. Antibiotic resistance pre-dates penicillin. *Nature* **562**, 192 (2018).
23. Hall, B. G. & Barlow, M. Evolution of the serine β-lactamases: Past, present and future. *Drug Resist. Updat.* **7**, 111–123 (2004).
24. Baltz, R. H. Renaissance in antibacterial discovery from actinomycetes. *Curr. Opin. Pharmacol.* **8**, 557–563 (2008).
25. Spellberg, B., Bartlett, J. G. & Gilbert, D. N. The Future of Antibiotics and Resistance. *N.*

Engl. J. Med. **368**, 299–302 (2013).

26. D'Costa, V. M., King, C. E., Kalan, L., Morar, M., Sung, W. W. L., Schwarz, C., Froese, D., Zazula, G., Calmels, F., Debruyne, R., Golding, G. B., Poinar, H. N. & Wright, G. D. Antibiotic resistance is ancient. *Nature* **477**, 457–461 (2011).
27. Hughes, V. M. & Datta, N. Conjugative plasmids in bacteria of the 'pre-antibiotic' era. *Nature* **302**, 725–726 (1983).
28. Andersson, D. I. The biological cost of mutational antibiotic resistance: any practical conclusions? *Curr. Opin. Microbiol.* **9**, 461–465 (2006).
29. D'Costa, V. M., McGrann, K. M., Hughes, D. W. & Wright, G. D. Sampling the Antibiotic Resistome. *Science.* **311**, 374–378 (2006).
30. Wright, G. D. The antibiotic resistome: The nexus of chemical and genetic diversity. *Nat. Rev. Microbiol.* **5**, 175–186 (2007).
31. Wright, G. D. Antibiotic resistance in the environment: A link to the clinic? *Curr. Opin. Microbiol.* **13**, 589–594 (2010).
32. Perry, J. A., Westman, E. L. & Wright, G. D. The antibiotic resistome: what's new? *Curr. Opin. Microbiol.* **21**, 45–50 (2014).
33. Forsberg, K. J., Patel, S., Gibson, M. K., Lauber, C. L., Knight, R., Fierer, N. & Dantas, G. Bacterial phylogeny structures soil resistomes across habitats. *Nature* **509**, 612–616 (2014).
34. Holmes, A. H., Moore, L. S. P., Sundsfjord, A., Steinbakk, M., Regmi, S., Karkey, A., Guerin, P. J. & Piddock, L. J. V. Understanding the mechanisms and drivers of antimicrobial resistance. *Lancet* **387**, 176–187 (2016).
35. Ventola, C. L. The Antibiotic Resistance: part 1: causes and treats. *J. Formul. Manag.* **40**, 277–283 (2015).
36. Suda, K. J., Hicks, L. A., Roberts, R. M., Hunkler, R. J. & Danziger, L. H. A national evaluation of antibiotic expenditures by healthcare setting in the United States, 2009. *J. Antimicrob. Chemother.* **68**, 715–718 (2013).
37. Van Boeckel, T. P., Gandra, S., Ashok, A., Caudron, Q., Grenfell, B. T., Levin, S. A. & Laxminarayan, R. Global antibiotic consumption 2000 to 2010: an analysis of national pharmaceutical sales data. *Lancet Infect. Dis.* **14**, 742–750 (2014).
38. Li, Y., Xu, J., Wang, F., Wang, B., Liu, L., Hou, W., Fan, H., Tong, Y., Zhang, J. & Lu, Z. Overprescribing in China, driven by financial incentives, results in very high use of antibiotics, injections, and corticosteroids. *Health Aff.* **31**, 1075–1082 (2012).
39. Mcdonnell, T. & Group, N. Antibiotic Overuse: The Influence of Social Norms. *J. Am. Coll. Surg.* **207**, 265–275 (2008).

40. Davies, J. Origins and evolution of antibiotic resistance. *Microbiologia* **12**, 9–16 (1996).
41. Morgan, D. J., Okeke, I. N., Laxminarayan, R. & Perencevich, E. N. Non prescription use of antibiotics a worldwide systematic review. *Lancet Infect. Dis.* **11**, 692–701 (2013).
42. European Commission. *Special Eurobarometer 445 'Antimicrobial Resistance'*. (Springer International Publishing, 2016). doi:10.2875/446879
43. Andersson, D. I. & Hughes, D. Microbiological effects of sublethal levels of antibiotics. *Nat. Rev. Microbiol.* **12**, 465–478 (2014).
44. Bryskier, A. *Antimicrobial Agents: Antibacterials and Antifungals*. (American Society of Microbiology, 2005).
45. Gorbach, S. L. Antimicrobial Use in Animal Feed-Time to Stop. *N. Engl. J. Med.* **345**, 1202–1203 (2001).
46. Palumbi, S. R. Humans as the World's Greatest Evolutionary Force. *Science.* **293**, 1786–1790 (2001).
47. Lewis, K. Platforms for antibiotic discovery. *Nat. Rev. Drug Discov.* **12**, 371–387 (2013).
48. Bonomo, R. A. New Delhi metallo-β-lactamase and multidrug resistance: A global SOS? *Clin. Infect. Dis.* **52**, 485–487 (2011).
49. Dortet, L., Poirel, L. & Nordmann, P. Worldwide Dissemination of the NDM-Type Carbapenemases in Gram-Negative Bacteria. *Biomed Res. Int.* **2014**, 1–12 (2014).
50. Matos-Tocasca, M., De la Cruz-Ku, G., Auccacusi, E., Fernandez-Salas, D., García-Ahuanari, T. & Valcarcel-Valdivia, B. Extensively Drug-Resistant Tuberculosis: Report and Literature Review on Two Cases Requiring Prolonged Treatment. *Am. J. Case Rep.* **17**, 819–826 (2016).
51. Krapp, F., Ozer, E. A., Qi, C. & Hauser, A. R. Case Report of an Extensively Drug-Resistant *Klebsiella pneumoniae* Infection With Genomic Characterization of the Strain and Review of Similar Cases in the United States. *Open Forum Infect. Dis.* **5**, 1–5 (2018).
52. Deplano, A., Denis, O., Poirel, L., Hocquet, D., Nonhoff, C., Byl, B., Nordmann, P., Vincent, J. L. & Struelens, M. J. Molecular Characterization of an Epidemic Clone of Panantibiotic-Resistant *Pseudomonas aeruginosa*. *J. Clin. Microbiol.* **43**, 1198–1204 (2005).
53. Lolans, K., Queenan, A. M., Bush, K., Sahud, A. & Quinn, J. P. First Nosocomial Outbreak of *Pseudomonas aeruginosa* Producing an Integron-Borne Metallo-Beta-Lactamase (VIM-2) in the United States. *Antimicrob. Agents Chemother.* **49**, 3538–3540 (2005).
54. Cabeen, M. T. & Jacobs-Wagner, C. Bacterial cell shape. *Nat. Rev. Microbiol.* **3**, 601–610 (2005).
55. Delcour, A. H. Outer membrane permeability and antibiotic resistance. *Biochim. Biophys.*

Acta - Proteins Proteomics **1794**, 808–816 (2009).

56. Exner, M., Bhattacharya, S., Christiansen, B., Gebel, J., Goroncy-Bermes, P., Hartemann, P., Heeg, P., Ilschner, C., Kramer, A., Larson, E., Merkens, W., Mielke, M., Oltmanns, P., Ross, B., Rotter, M., Schmithausen, R. M., Sonntag, H.-G. & Trautmann, M. Antibiotic resistance: What is so special about multidrug-resistant Gram-negative bacteria? *GMS Hyg. Infect. Control* **12**, 1–24 (2017).
57. Lin, J., Nishino, K., Roberts, M. C., Tolmasky, M., Aminov, R. I. & Zhang, L. Mechanisms of antibiotic resistance. *Front. Microbiol.* **6**, 42–51 (2015).
58. Sørensen, S. J., Bailey, M., Hansen, L. H., Kroer, N. & Wuertz, S. Studying plasmid horizontal transfer in situ: a critical review. *Nat. Rev. Microbiol.* **3**, 700–710 (2005).
59. Alekshun, M. N. & Levy, S. B. Molecular Mechanisms of Antibacterial Multidrug Resistance. *Cell* **128**, 1037–1050 (2007).
60. Giedraitienė, A., Vitkauskienė, A., Naginienė, R. & Pavilonis, A. Antibiotic Resistance Mechanisms of Clinically Important Bacteria. *Medicina (B. Aires).* **47**, 19 (2011).
61. Woodford, N. & Ellington, M. J. The emergence of antibiotic resistance by mutation. *Clin. Microbiol. Infect.* **13**, 5–18 (2007).
62. Lambert, P. A. Bacterial resistance to antibiotics: Modified target sites. *Adv. Drug Deliv. Rev.* **57**, 1471–1485 (2005).
63. Nikaido, H. & Pagès, J.-M. Broad-specificity efflux pumps and their role in multidrug resistance of Gram-negative bacteria. *FEMS Microbiol. Rev.* **36**, 340–363 (2012).
64. Wright, G. Bacterial resistance to antibiotics: Enzymatic degradation and modification. *Adv. Drug Deliv. Rev.* **57**, 1451–1470 (2005).
65. Kumaer, A. & Schweizer, H. Bacterial resistance to antibiotics: Active efflux and reduced uptake. *Adv. Drug Deliv. Rev.* **57**, 1486–1513 (2005).
66. Masi, M., Réfregiers, M., Pos, K. M. & Pagès, J.-M. Mechanisms of envelope permeability and antibiotic influx and efflux in Gram-negative bacteria. *Nat. Microbiol.* **2**, 17001 (2017).
67. Blair, J. M. A., Webber, M. A., Baylay, A. J., Ogbolu, D. O. & Piddock, L. J. V. Molecular mechanisms of antibiotic resistance. *Nat. Rev. Microbiol.* **13**, 42–51 (2015).
68. Drlica, K. & Malik, M. Fluoroquinolones: Action and Resistance. *Curr. Top. Med. Chem.* **3**, 249–282 (2003).
69. Palmer, A. C. & Kishony, R. Opposing effects of target overexpression reveal drug mechanisms. *Nat. Commun.* **5**, 4296 (2014).
70. Yelin, I. & Kishony, R. Antibiotic Resistance. *Cell* **172**, 1136-1136.e1 (2018).
71. Katayama, Y., Ito, T. & Hiramatsu, K. A New Class of Genetic Element, Staphylococcus

Cassette Chromosome mec, Encodes Methicillin Resistance in *Staphylococcus aureus*. *Antimicrob. Agents Chemother.* **44**, 1549–1555 (2000).

72. Wright, G. D. Molecular mechanisms of antibiotic resistance. *Chem. Commun.* **47**, 4055 (2011).
73. Munita, J. M. & Arias, C. A. Mechanisms of Antibiotic Resistance. *Virulence Mech. Bact. Pathog. Fifth Ed.* **4**, 481–511 (2016).
74. Fernandez, L. & Hancock, R. E. W. Adaptive and Mutational Resistance: Role of Porins and Efflux Pumps in Drug Resistance. *Clin. Microbiol. Rev.* **25**, 661–681 (2012).
75. Warner, D. M., Shafer, W. M. & Jerse, A. E. Clinically relevant mutations that cause derepression of the *Neisseria gonorrhoeae* MtrC-MtrD-MtrE Efflux pump system confer different levels of antimicrobial resistance and in vivo fitness. *Mol. Microbiol.* **70**, 462–478 (2008).
76. Stewart, P. S. & Costerton, J. W. Antibiotic resistance of bacteria in biofilms. *Lancet* **358**, 135–138 (2001).
77. Bohnert, J. A., Schuster, S., Seeger, M. A., Fahnrich, E., Pos, K. M. & Kern, W. V. Site-Directed Mutagenesis Reveals Putative Substrate Binding Residues in the *Escherichia coli* RND Efflux Pump AcrB. *J. Bacteriol.* **190**, 8225–8229 (2008).
78. Sabnis, A., Ledger, E. V. K., Pader, V. & Edwards, A. M. Antibiotic interceptors: Creating safe spaces for bacteria. *PLOS Pathog.* **14**, 1–6 (2018).
79. Coates, A., Hu, Y., Bax, R. & Page, C. The future challenges facing the development of new antimicrobial drugs. *Nat. Rev. Drug Discov.* **1**, 895–910 (2002).
80. Hughes, D. & Karlén, A. Discovery and preclinical development of new antibiotics. *Ups. J. Med. Sci.* **119**, 162–169 (2014).
81. Hughes, J., Rees, S., Kalindjian, S. & Philpott, K. Principles of early drug discovery. *Br. J. Pharmacol.* **162**, 1239–1249 (2011).
82. Kola, I. & Landis, J. Can the pharmaceutical industry reduce attrition rates? *Nat. Rev. Drug Discov.* **3**, 711–715 (2004).
83. Silver, L. L. Appropriate Targets for Antibacterial Drugs. *Cold Spring Harb. Perspect. Med.* **6**, 1–6 (2016).
84. Lange, R., Locher, H., Wyss, P. & Then, R. The Targets of Currently Used Antibacterial Agents: Lessons for Drug Discovery. *Curr. Pharm. Des.* **13**, 3140–3154 (2007).
85. Kohanski, M. A., Dwyer, D. J. & Collins, J. J. How antibiotics kill bacteria: from targets to networks. *Nat. Rev. Microbiol.* **8**, 423–435 (2010).
86. Gould, K. Antibiotics: from prehistory to the present day. *J. Antimicrob. Chemother.* **71**, 572–

575 (2016).

87. Marston, H. D., Dixon, D. M., Knisely, J. M., Palmore, T. N. & Fauci, A. S. Antimicrobial Resistance. *JAMA* **316**, 1193 (2016).
88. Howell, L. Global Risks 2013. *World Economic Forum* (2013). Available at: http://www3.weforum.org/docs/WEF_GlobalRisks_Report_2013.pdf.
89. Butler, M. S., Blaskovich, M. A. & Cooper, M. A. Antibiotics in the clinical pipeline at the end of 2015. *J. Antibiot.* **70**, 3–24 (2017).
90. Hamad, B. The antibiotics market. *Nat. Rev. Drug Discov.* **9**, 675–676 (2010).
91. Kresse, H., Belsey, M. J. & Rovini, H. The antibacterial drugs market. *Nat. Rev. Drug Discov.* **6**, 19–20 (2007).
92. Dixit, R. & David, F. S. Market watch: Trends in pharmaceutical company R&D spending: 2005–2015. *Nat. Rev. Drug Discov.* **16**, 376–376 (2017).
93. Paul, S. M., Mytelka, D. S., Dunwiddie, C. T., Persinger, C. C., Munos, B. H., Lindborg, S. R. & Schacht, A. L. How to improve R&D productivity: the pharmaceutical industry's grand challenge. *Nat. Rev. Drug Discov.* **9**, 203–214 (2010).
94. Lewis, K. New approaches to antimicrobial discovery. *Biochem. Pharmacol.* **134**, 87–98 (2017).
95. Fair, R. J. & Tor, Y. Antibiotics and Bacterial Resistance in the 21st Century. *Perspect. Medicin. Chem.* **6**, 25-64 (2014).
96. Medical Research Council. UKRI 'One Health' AMR research priorities showcased in Parliament today. (2019). Available at: https://mrc.ukri.org/news/browse/ukri-one-health-amr-research-priorities-showcased-in-parliament-today/.
97. Outterson, K., Powers, J. H., Daniel, G. W. & McClellan, M. B. Repairing The Broken Market For Antibiotic Innovation. *Health Aff.* **34**, 277–285 (2015).
98. Kelly, R., Zoubiane, G., Walsh, D., Ward, R. & Goossens, H. Public funding for research on antibacterial resistance in the JPIAMR countries, the European Commission, and related European Union agencies: a systematic observational analysis. *Lancet Infect. Dis.* **16**, 431–440 (2016).
99. Eichberg, M. J. Public Funding of Clinical-Stage Antibiotic Development in the United States and European Union. *Heal. Secur.* **13**, 156–165 (2015).
100. Simpkin, V. L., Renwick, M. J., Kelly, R. & Mossialos, E. Incentivising innovation in antibiotic drug discovery and development: progress, challenges and next steps. *J. Antibiot.* **70**, 1087–1096 (2017).
101. Wanted: a reward for antibiotic development. *Nat. Biotechnol.* **36**, 555–555 (2018).
102. Sciarretta, K., Røttingen, J.-A., Opalska, A., Van Hengel, A. J. & Larsen, J. Economic

Incentives for Antibacterial Drug Development: Literature Review and Considerations From the Transatlantic Task Force on Antimicrobial Resistance. *Clin. Infect. Dis.* **63**, 1470–1474 (2016).

103. Rex, J. H., Goldberger, M., Eisenstein, B. I. & Harney, C. The evolution of the regulatory framework for antibacterial agents. *Ann. N. Y. Acad. Sci.* **1323**, 11–21 (2014).
104. Spellberg, B. The future of antibiotics. *Crit. Care* **18**, 228 (2014).
105. Donlan, R. M. & Costerton, J. W. Biofilms: Survival Mechanisms of Clinically Relevant Microorganisms. *Clin. Microbiol. Rev.* **15**, 167–193 (2002).
106. Ochman, H., Lawrence, J. G. & Groisman, E. A. Lateral gene transfer and the nature of bacterial innovation. *Nature* **405**, 299–304 (2000).
107. Green, E. R. & Mecsas, J. Bacterial Secretion Systems: An Overview. in *Virulence Mechanisms of Bacterial Pathogens* **4**, 215–239 (American Society of Microbiology, 2016).
108. Fischbach, M. A. & Walsh, C. T. Antibiotics for Emerging Pathogens. *Science.* **325**, 1089–1093 (2009).
109. Wright, P. M., Seiple, I. B. & Myers, A. G. The Evolving Role of Chemical Synthesis in Antibacterial Drug Discovery. *Angew. Chemie Int. Ed.* **53**, 8840–8869 (2014).
110. Payne, D. J., Gwynn, M. N., Holmes, D. J. & Pompliano, D. L. Drugs for bad bugs: confronting the challenges of antibacterial discovery. *Nat. Rev. Drug Discov.* **6**, 29–40 (2007).
111. Tommasi, R., Brown, D. G., Walkup, G. K., Manchester, J. I. & Miller, A. A. ESKAPEing the labyrinth of antibacterial discovery. *Nat. Rev. Drug Discov.* **14**, 529–542 (2015).
112. Coates, A. R., Halls, G. & Hu, Y. Novel classes of antibiotics or more of the same? *Br. J. Pharmacol.* **163**, 184–194 (2011).
113. Dunman, P. M. & Tomaras, A. P. Translational deficiencies in antibacterial discovery and new screening paradigms. *Curr. Opin. Microbiol.* **27**, 108–113 (2015).
114. Silver, L. L. Multi-targeting by monotherapeutic antibacterials. *Nat. Rev. Drug Discov.* **6**, 41–55 (2007).
115. Tomaras, A. P., McPherson, C. J., Kuhn, M., Carifa, A., Mullins, L., George, D., Desbonnet, C., Eidem, T. M., Montgomery, J. I., Brown, M. F., Reilly, U., Miller, A. A. & O'Donnell, J. P. LpxC Inhibitors as New Antibacterial Agents and Tools for Studying Regulation of Lipid A Biosynthesis in Gram-Negative Pathogens. *MBio* **5**, 1–13 (2014).
116. Spellberg, B. & Rex, J. H. The value of single-pathogen antibacterial agents. *Nat. Rev. Drug Discov.* **12**, 963–963 (2013).
117. Gengenbacher, M. & Dick, T. Antibacterial Drug Discovery: Doing It Right. *Chem. Biol.* **22**, 5–6 (2015).

118. Buckland, D. Antimicrobial resistance and the race to find new antibiotics. *Prescriber* **28**, 12–15 (2017).

119. Patyar, S., Prakash, A. & Medhi, B. Dual inhibition: a novel promising pharmacological approach for different disease conditions. *J. Pharm. Pharmacol.* **63**, 459–471 (2011).

120. Temml, V., Garscha, U., Romp, E., Schubert, G., Gerstmeier, J., Kutil, Z., Matuszczak, B., Waltenberger, B., Stuppner, H., Werz, O. & Schuster, D. Discovery of the first dual inhibitor of the 5-lipoxygenase-activating protein and soluble epoxide hydrolase using pharmacophore-based virtual screening. *Sci. Rep.* **7**, 42751 (2017).

121. Phillips, J. W., Goetz, M. A., Smith, S. K., Zink, D. L., Polishook, J., Onishi, R., Salowe, S., Wiltsie, J., Allocco, J., Sigmund, J., Dorso, K., Lee, S., Skwish, S., de la Cruz, M., Martín, J., Vicente, F., Genilloud, O., Lu, J., Painter, R. E., *et al.* Discovery of Kibdelomycin, A Potent New Class of Bacterial Type II Topoisomerase Inhibitor by Chemical-Genetic Profiling in *Staphylococcus aureus*. *Chem. Biol.* **18**, 955–965 (2011).

122. Hopkins, A. L. Network pharmacology: the next paradigm in drug discovery. *Nat. Chem. Biol.* **4**, 682–690 (2008).

123. Harry, R. Etymologia: *Pseudomonas*. *Emerg. Infect. Dis.* **18**, 1241–1241 (2012).

124. Tümmler, B., Wiehlmann, L., Klockgether, J. & Cramer, N. Advances in understanding *Pseudomonas*. *F1000Prime Rep.* **6**, 1–9 (2014).

125. Klockgether, J., Cramer, N., Wiehlmann, L., Davenport, C. F. & Tümmler, B. *Pseudomonas aeruginosa* Genomic Structure and Diversity. *Front. Microbiol.* **2**, 1–18 (2011).

126. Römling, U., Schmidt, K. D. & Tümmler, B. Large genome rearrangements discovered by the detailed analysis of 21 *Pseudomonas aeruginosa* clone C isolates found in environment and disease habitats. *J. Mol. Biol.* **271**, 386–404 (1997).

127. Raymond, C. K., Sims, E. H., Kas, A., Spencer, D. H., Kutyavin, T. V., Ivey, R. G., Zhou, Y., Kaul, R., Clendenning, J. B. & Olson, M. V. Genetic Variation at the O-Antigen Biosynthetic Locus in *Pseudomonas aeruginosa*. *J. Bacteriol.* **184**, 3614–3622 (2002).

128. Smith, E. E., Sims, E. H., Spencer, D. H., Kaul, R. & Olson, M. V. Evidence for Diversifying Selection at the Pyoverdine Locus of *Pseudomonas aeruginosa*. *J. Bacteriol.* **187**, 2138–2147 (2005).

129. Mesaros, N., Nordmann, P., Plésiat, P., Roussel-Delvallez, M., Van Eldere, J., Glupczynski, Y., Van Laethem, Y., Jacobs, F., Lebecque, P., Malfroot, A., Tulkens, P. M. & Van Bambeke, F. *Pseudomonas aeruginosa*: resistance and therapeutic options at the turn of the new millennium. *Clin. Microbiol. Infect.* **13**, 560–578 (2007).

130. de Bentzmann, S. & Plésiat, P. The *Pseudomonas aeruginosa* opportunistic pathogen and

human infections. *Environ. Microbiol.* **13**, 1655–1665 (2011).

131. Lister, P. D., Wolter, D. J. & Hanson, N. D. Antibacterial-Resistant *Pseudomonas aeruginosa*: Clinical Impact and Complex Regulation of Chromosomally Encoded Resistance Mechanisms. *Clin. Microbiol. Rev.* **22**, 582–610 (2009).

132. Obritsch, M. D., Fish, D. N., MacLaren, R. & Jung, R. Nosocomial Infections Due to Multidrug-Resistant *Pseudomonas aeruginosa*: Epidemiology and Treatment Options. *Pharmacotherapy* **25**, 1353–1364 (2005).

133. Weinstein, R. A., Gaynes, R. & Edwards, J. R. Overview of Nosocomial Infections Caused by Gram-Negative Bacilli. *Clin. Infect. Dis.* **41**, 848–854 (2005).

134. Estahbanati, H. K., Kashani, P. P. & Ghanaatpisheh, F. Frequency of *Pseudomonas aeruginosa* serotypes in burn wound infections and their resistance to antibiotics. *Burns* **28**, 340–348 (2002).

135. Kalil, A. C., Metersky, M. L., Klompas, M., Muscedere, J., Sweeney, D. A., Palmer, L. B., Napolitano, L. M., O'Grady, N. P., Bartlett, J. G., Carratalà, J., El Solh, A. A., Ewig, S., Fey, P. D., File, T. M., Restrepo, M. I., Roberts, J. A., Waterer, G. W., Cruse, P., Knight, S. L., *et al.* Management of Adults With Hospital-acquired and Ventilator-associated Pneumonia: 2016 Clinical Practice Guidelines by the Infectious Diseases Society of America and the American Thoracic Society. *Clin. Infect. Dis.* **63**, e61–e111 (2016).

136. Döring, G. & Gulbins, E. Cystic fibrosis and innate immunity: how chloride channel mutations provoke lung disease. *Cell. Microbiol.* **11**, 208–216 (2009).

137. Palmer, K. L., Aye, L. M. & Whiteley, M. Nutritional Cues Control *Pseudomonas aeruginosa* Multicellular Behavior in Cystic Fibrosis Sputum. *J. Bacteriol.* **189**, 8079–8087 (2007).

138. Frizzell, R. A. & Hanrahan, J. W. Physiology of Epithelial Chloride and Fluid Secretion. *Cold Spring Harb. Perspect. Med.* **2**, a009563–a009563 (2012).

139. Cheng, S. H., Gregory, R. J., Marshall, J., Paul, S., Souza, D. W., White, G. A., O'Riordan, C. R. & Smith, A. E. Defective intracellular transport and processing of CFTR is the molecular basis of most cystic fibrosis. *Cell* **63**, 827–834 (1990).

140. Paranjape, S. M. & Mogayzel, P. J. Cystic Fibrosis. *Pediatr. Rev.* **35**, 194–205 (2014).

141. Klepac-Ceraj, V., Lemon, K. P., Martin, T. R., Allgaier, M., Kembel, S. W., Knapp, A. A., Lory, S., Brodie, E. L., Lynch, S. V., Bohannan, B. J. M., Green, J. L., Maurer, B. A. & Kolter, R. Relationship between cystic fibrosis respiratory tract bacterial communities and age, genotype, antibiotics and *Pseudomonas aeruginosa*. *Environ. Microbiol.* **12**, 1293–1303 (2010).

142. Hogardt, M. & Heesemann, J. Adaptation of *Pseudomonas aeruginosa* during persistence in the

cystic fibrosis lung. *Int. J. Med. Microbiol.* **300**, 557–562 (2010).

143. Kim, E.-J. Iron deficiency leads to inhibition of oxygen transfer and enhanced formation of virulence factors in cultures of *Pseudomonas aeruginosa* PAO1. *Microbiology* **149**, 2627–2634 (2003).

144. Lyczak, J. B., Cannon, C. L. & Pier, G. B. Establishment of *Pseudomonas aeruginosa* infection: lessons from a versatile opportunist. *Microbes Infect.* **2**, 1051–1060 (2000).

145. Miller, R. M., Tomaras, A. P., Barker, A. P., Voelker, D. R., Chan, E. D., Vasil, A. I. & Vasil, M. L. *Pseudomonas aeruginosa* Twitching Motility-Mediated Chemotaxis towards Phospholipids and Fatty Acids: Specificity and Metabolic Requirements. *J. Bacteriol.* **190**, 4038–4049 (2008).

146. Son, M. S., Matthews, W. J., Kang, Y., Nguyen, D. T. & Hoang, T. T. In Vivo Evidence of *Pseudomonas aeruginosa* Nutrient Acquisition and Pathogenesis in the Lungs of Cystic Fibrosis Patients. *Infect. Immun.* **75**, 5313–5324 (2007).

147. Bonomo, R. A. & Szabo, D. Mechanisms of Multidrug Resistance in *Acinetobacter* Species and *Pseudomonas aeruginosa*. *Clin. Infect. Dis.* **43**, S49–S56 (2006).

148. Chevalier, S., Bouffartigues, E., Bodilis, J., Maillot, O., Lesouhaitier, O., Feuilloley, M. G. J., Orange, N., Dufour, A. & Cornelis, P. Structure, function and regulation of *Pseudomonas aeruginosa* porins. *FEMS Microbiol. Rev.* **41**, 698–722 (2017).

149. O'Shea, R. & Moser, H. E. Physicochemical Properties of Antibacterial Compounds: Implications for Drug Discovery. *J. Med. Chem.* **51**, 2871–2878 (2008).

150. Woodruff, W. A., Parr, T. R., Hancock, R. E. W., Hanne, L. F., Nicas, T. I. & Iglewski, B. H. Expression in *Escherichia coli* and function of *Pseudomonas aeruginosa* outer membrane porin protein F. *J. Bacteriol.* **167**, 473–479 (1986).

151. Livermore, D. M. Of *Pseudomonas*, porins, pumps and carbapenems. *J. Antimicrob. Chemother.* **47**, 247–250 (2001).

152. Trias, J. & Nikaido, H. Protein D2 Channel of the *Pseudomonas aeruginosa* Outer Membrane Has a Binding Site for Basic Amino Acids and Peptides *. *J. Biol. Chem.* **265**, 15680–15684 (1990).

153. Morita, Y. Construction of a series of mutants lacking all of the four major mex operons for multidrug efflux pumps or possessing each one of the operons from *Pseudomonas aeruginosa* PAO1: MexCD-OprJ is an inducible pump. *FEMS Microbiol. Lett.* **202**, 139–143 (2001).

154. Singh, S. B., Young, K. & Silver, L. L. What is an "ideal" antibiotic? Discovery challenges and path forward. *Biochem. Pharmacol.* **133**, 63–73 (2017).

155. Morita, Y., Tomida, J. & Kawamura, Y. MexXY multidrug efflux system of *Pseudomonas aeruginosa*. *Front. Microbiol.* **3**, 1–13 (2012).

156. Driffield, K., Miller, K., Bostock, J. M., O'Neill, A. J. & Chopra, I. Increased mutability of *Pseudomonas aeruginosa* in biofilms. *J. Antimicrob. Chemother.* **61**, 1053–1056 (2008).

157. Krebs, H. A. & Lowenstein, J. M. in. *Metab. Pathways* **1**, 129–192 (1960).

158. Krebs, H. A. The history of the tricarboxylic acid cycle. *Perspect. Biol. Med.* **14**, 154–172 (1970).

159. Berg, J., Tymoczko, J. & Stryer, L. The Citric Acid Cycle. in *Biochemistry* (W.H. Freemand and Company, 2002).

160. Campbell, J. J. R. & Stokes, F. N. Tricarboxylic Acid Cycle in *Pseudomonas aeruginosa*. *J. Biol. Chem.* **190**, 853–858 (1951).

161. Lee, S. A., Gallagher, L. A., Thongdee, M., Staudinger, B. J., Lippman, S., Singh, P. K. & Manoil, C. General and condition-specific essential functions of *Pseudomonas aeruginosa*. *Proc. Natl. Acad. Sci.* **112**, 5189–5194 (2015).

162. Temple, L. M., Sage, A. E., Schweizer, H. P. & Phibbs, P. V. Carbohydrate Catabolism in *Pseudomonas aeruginosa*. in *Pseudomonas* 35–72 (Springer US, 1998). doi:10.1007/978-1-4899-0120-0_2

163. Lessie, T. G. & Phibbs, P. V. Alternative Pathways of Carbohydrate Utilization in Pseudomonads. *Annu. Rev. Microbiol.* **38**, 359–388 (1984).

164. Garrett, R. H. & Grisham, C. M. *Biochemistry*. (Brooks/Cole, 2008).

165. Sun, Z., Kang, Y., Norris, M. H., Troyer, R. M., Son, M. S., Schweizer, H. P., Dow, S. W. & Hoang, T. T. Blocking Phosphatidylcholine Utilization in *Pseudomonas aeruginosa*, via Mutagenesis of Fatty Acid, Glycerol and Choline Degradation Pathways, Confirms the Importance of This Nutrient Source In Vivo. *PLoS One* **9**, e103778 (2014).

166. Dolan, S. K. & Welch, M. The Glyoxylate Shunt, 60 Years On. *Annu. Rev. Microbiol.* **72**, 309–330 (2018).

167. Kornberg, H. L. & Krebs, H. A. Synthesis of cell constituents from C2-units by a modified tricarboxylic acid cycle. *Nature* **179**, 988–991 (1957).

168. Hearn, E. M., Patel, D. R., Lepore, B. W., Indic, M. & van den Berg, B. Transmembrane passage of hydrophobic compounds through a protein channel wall. *Nature* **458**, 367–370 (2009).

169. Beeckmans, S. Glyoxylate Cycle. in *Encyclopedia of Microbiology* 159–179 (Elsevier, 2009). doi:10.1016/B978-012373944-5.00075-4

170. Lorenz, M. C. & Fink, G. R. Life and Death in a Macrophage: Role of the Glyoxylate Cycle

in Virulence. *Eukaryot. Cell* **1**, 657–662 (2002).

171. Kornberg, H. L. & N.B., M. Synthesis of C4-dicarboxylic acids from acetate by a glyoxylate bypass of the tricarboxylic acid cycle. *Biochim. Biophys. Acta - Gen. Subj.* **24**, 651–653 (1957).
172. Kornberg, H. L. The Role and Control of the Glyoxylate Cycle in Escherichia coli. *Biochem. J.* **99**, 1–11 (1966).
173. Dunn, M. F., Ramirez-Trujillo, J. A. & Hernandez-Lucas, I. Major roles of isocitrate lyase and malate synthase in bacterial and fungal pathogenesis. *Microbiology* **155**, 3166–3175 (2009).
174. Crousilles, A., Dolan, S. K., Brear, P., Chirgadze, D. Y. & Welch, M. Gluconeogenic precursor availability regulates flux through the glyoxylate shunt in *Pseudomonas aeruginosa*. *J. Biol. Chem.* **293**, 14260–14269 (2018).
175. Maloy, S. R. & Nunn, W. D. Genetic Regulation of the Glyoxylate Shunt in *Escherichia coli* K-12. *J. Bacteriol.* **149**, 173–180 (1982).
176. LaPorte, D. C. & Koshland, D. E. Phosphorylation of isocitrate dehydrogenase as a demonstration of enhanced sensitivity in covalent regulation. *Nature* **305**, 286–290 (1983).
177. Quartararo, C. E., Hadi, T., Cahill, S. M. & Blanchard, J. S. Solvent Isotope-Induced Equilibrium Perturbation for Isocitrate Lyase. *Biochemistry* **52**, 9286–9293 (2013).
178. Britton, K. L., Abeysinghe, I. S. B., Baker, P. J., Barynin, V., Diehl, P., Langridge, S. J., McFadden, B. A., Sedelnikova, S. E., Stillman, T. J., Weeradechapon, K. & Rice, D. W. The structure and domain organization of *Escherichia coli* isocitrate lyase. *Acta Crystallogr. Sect. D Biol. Crystallogr.* **57**, 1209–1218 (2001).
179. Sharma, V., Sharma, S., Hoener zu Bentrup, K., McKinney, J. D., Russell, D. G., Jacobs, W. R. & Sacchettini, J. C. Structure of isocitrate lyase, a persistence factor of *Mycobacterium tuberculosis*. *Nat. Struct. Biol.* **7**, 663–668 (2000).
180. Gainey, L. D. S., Connerton, I. F., Lewis, E. H., Turner, G. & Ballance, D. J. Characterization of the glyoxysomal isocitrate lyase genes of *Aspergillus nidulans* (acuD) and *Neurospora crassa* (acu-3). *Curr. Genet.* **21**, 43–47 (1992).
181. Anstrom, D. M. & Remington, S. J. The product complex of *M. tuberculosis* malate synthase revisited. *Protein Sci.* **15**, 2002–2007 (2006).
182. Lohman, J. R., Olson, A. C. & Remington, S. J. Atomic resolution structures of *Escherichia coli* and *Bacillus anthracis* malate synthase A: Comparison with isoform G and implications for structure-based drug discovery. *Protein Sci.* **17**, 1935–1945 (2008).
183. Molina, I., Pellicer, M.-T., Badia, J., Aguilar, J. & Baldoma, L. Molecular Characterization of *Escherichia coli* Malate Synthase G. Differentiation with the Malate Synthase A Isoenzyme.

Eur. J. Biochem. **224**, 541–548 (1994).

184. Kumar, R. & Bhakuni, V. A functionally active dimer of *Mycobacterium tuberculosis* Malate synthase G. *Eur. Biophys. J.* **39**, 1557–1562 (2010).

185. Howard, B. R., Endrizzi, J. A. & Remington, S. J. Crystal Structure of *Escherichia coli* Malate Synthase G Complexed with Magnesium and Glyoxylate at 2.0 Å Resolution: Mechanistic Implications. *Biochemistry* **39**, 3156–3168 (2000).

186. Anstrom, D. M., Kallio, K. & Remington, S. J. Structure of the *Escherichia coli* malate synthase G: pyruvate: acetyl-coenzyme A abortive ternary complex at 1.95 Å resolution. *Protein Sci.* **12**, 1822–1832 (2003).

187. Smith, C. V., Huang, C., Miczak, A., Russell, D. G., Sacchettini, J. C. & Höner zu Bentrup, K. Biochemical and Structural Studies of Malate Synthase from *Mycobacterium tuberculosis*. *J. Biol. Chem.* **278**, 1735–1743 (2003).

188. Grishaev, A., Tugarinov, V., Kay, L. E., Trewhella, J. & Bax, A. Refined solution structure of the 82-kDa enzyme malate synthase G from joint NMR and synchrotron SAXS restraints. *J. Biomol. NMR* **40**, 95–106 (2008).

189. Lindsey, T. L., Hagins, J. M., Sokol, P. A. & Silo-Suh, L. A. Virulence determinants from a cystic fibrosis isolate of *Pseudomonas aeruginosa* include isocitrate lyase. *Microbiology* **154**, 1616–1627 (2008).

190. Chung, J. C. S., Rzhepishevska, O., Ramstedt, M. & Welch, M. Type III secretion system expression in oxygen-limited *Pseudomonas aeruginosa* cultures is stimulated by isocitrate lyase activity. *Open Biol.* **3**, 120131 (2013).

191. Puckett, S., Trujillo, C., Wang, Z., Eoh, H., Ioerger, T. R., Krieger, I., Sacchettini, J., Schnappinger, D., Rhee, K. Y. & Ehrt, S. Glyoxylate detoxification is an essential function of malate synthase required for carbon assimilation in *Mycobacterium tuberculosis*. *Proc. Natl. Acad. Sci.* **114**, E2225–E2232 (2017).

192. Nandakumar, M., Nathan, C. & Rhee, K. Y. Isocitrate lyase mediates broad antibiotic tolerance in *Mycobacterium tuberculosis*. *Nat. Commun.* **5**, 4306 (2014).

193. Muñoz-Elías, E. J. & McKinney, J. D. *Mycobacterium tuberculosis* isocitrate lyases 1 and 2 are jointly required for in vivo growth and virulence. *Nat. Med.* **11**, 638–644 (2005).

194. Fahnoe, K. C., Flanagan, M. E., Gibson, G., Shanmugasundaram, V., Che, Y. & Tomaras, A. P. Non-Traditional Antibacterial Screening Approaches for the Identification of Novel Inhibitors of the Glyoxylate Shunt in Gram-Negative Pathogens. *PLoS One* **7**, e51732 (2012).

195. Miroux, B. & Walker, J. E. Over-production of Proteins in Escherichia coli: Mutant Hosts

that Allow Synthesis of some Membrane Proteins and Globular Proteins at High Levels. *J. Mol. Biol.* **260**, 289–298 (1996).

196. Roucourt, B., Minnebo, N., Augustijns, P., Hertveldt, K., Volckaert, G. & Lavigne, R. Biochemical characterization of malate synthase G of *P. aeruginosa*. *BMC Biochem.* **10**, 20 (2009).
197. CLSI. Performance Standards for Antimicrobial Susceptibility Testing. (2019). Available at: https://clsi.org/media/2663/m100ed29.pdf.
198. Kahlmeter, G., Brown, D. F. J., Goldstein, F. W., MacGowan, A. P., Mouton, J. W., Odenholt, I., Rodloff, A., Soussy, C.-J., Steinbakk, M., Soriano, F. & Stetsiouk, O. European Committee on Antimicrobial Susceptibility Testing (EUCAST) Technical Notes on antimicrobial susceptibility testing. *Clin. Microbiol. Infect.* **12**, 501–503 (2006).
199. Thomas, P., Sekhar, A. C., Upreti, R., Mujawar, M. M. & Pasha, S. S. Optimization of single plate-serial dilution spotting (SP-SDS) with sample anchoring as an assured method for bacterial and yeast cfu enumeration and single colony isolation from diverse samples. *Biotechnol. Reports* **8**, 45–55 (2015).
200. Pfeiffer, H. G. & Liebhafsky, H. A. The origins of Beer's law. *J. Chem. Educ.* **28**, 123 (1951).
201. Gasteiger, E., Hoogland, C., Gattiker, A., Duvaud, S., Wilkins, M. R., Appel, R. D. & Bairoch, A. Protein Identification and Analysis Tools on the ExPASy Server in *The Proteomics Protocols Handbook* 571–607 (Humana Press, 2005). doi:10.1385/1-59259-890-0:571
202. de Winter, J. C. F. Using the student's t-test with extremely small sample sizes. *Pract. Assessment, Res. Eval.* **18**, 1–12 (2013).
203. Riener, C. K., Kada, G. & Gruber, H. J. Quick measurement of protein sulfhydryls with Ellman's reagent and with 4,4'-dithiodipyridine. *Anal. Bioanal. Chem.* **373**, 266–276 (2002).
204. Eyer, P., Worek, F., Kiderlen, D., Sinko, G., Stuglin, A., Simeon-Rudolf, V. & Reiner, E. Molar absorption coefficients for the reduced Ellman reagent: reassessment. *Anal. Biochem.* **312**, 224–227 (2003).
205. English, B. P., Min, W., van Oijen, A. M., Lee, K. T., Luo, G., Sun, H., Cherayil, B. J., Kou, S. C. & Xie, X. S. Ever-fluctuating single enzyme molecules: Michaelis-Menten equation revisited. *Nat. Chem. Biol.* **2**, 87–94 (2006).
206. Jambovane, S., Duin, E. C., Kim, S.-K. & Hong, J. W. Determination of Kinetic Parameters, K_m and k_{cat}, with a Single Experiment on a Chip. *Anal. Chem.* **81**, 3239–3245 (2009).
207. Hammes, G. G. & Wu, C. W. Kinetics of Allosteric Enzymes. *Annu. Rev. Biophys. Bioeng.* **3**, 1–33 (1974).

208. Berg, J., Tymoczko, J. & Stryer, L. *Biochemistry*. *Biochemistry* (W.H. Freemand and Company, 2002).

209. Giachetti, E., Pinzauti, G., Bonaccorsi, R. & Vanni, P. Isocitrate lyase from *Pinus pinea*. Characterization of its true substrate and the action of magnesium ions. *Eur. J. Biochem.* **172**, 85–91 (1988).

210. Johnson, K. A. A century of enzyme kinetic analysis, 1913 to 2013. *FEBS Lett.* **587**, 2753–2766 (2013).

211. Berg, J., Tymoczko, J. & Stryer, L. Enzymes: Basic Concepts and Kinetics in *Biochemistry* (W.H. Freemand and Company, 2002).

212. Strelow, J., Dewe, W., Iversen, P. W., Brooks, H. B., Radding, J. A., McGee, J. & Weidner, J. Mechanism of Action Assays for Enzymes. *Assay Guidance Manual* 1–27 (2004).

213. Keller, S., Vargas, C., Zhao, H., Piszczek, G., Brautigam, C. A. & Schuck, P. High-Precision Isothermal Titration Calorimetry with Automated Peak-Shape Analysis. *Anal. Chem.* **84**, 5066–5073 (2012).

214. Holdgate, G. A. & Ward, W. H. J. Measurements of binding thermodynamics in drug discovery. *Drug Discov. Today* **10**, 1543–1550 (2005).

215. Keizer, J. Nonlinear fluorescence quenching and the origin of positive curvature in Stern-Volmer plots. *J. Am. Chem. Soc.* **105**, 1494–1498 (1983).

216. Dahlquist, F. W. The meaning of scatchard and hill plots. in *Methods in Enzymology* 270–299 (Elsevier Science Publishing Co Inc, 1978). doi:10.1016/S0076-6879(78)48015-2

217. Winter, G., Waterman, D. G., Parkhurst, J. M., Brewster, A. S., Gildea, R. J., Gerstel, M., Fuentes-Montero, L., Vollmar, M., Michels-Clark, T., Young, I. D., Sauter, N. K. & Evans, G. DIALS : implementation and evaluation of a new integration package. *Acta Crystallogr. Sect. D Struct. Biol.* **74**, 85–97 (2018).

218. McCoy, A. J., Grosse-Kunstleve, R. W., Adams, P. D., Winn, M. D., Storoni, L. C. & Read, R. J. Phaser crystallographic software. *J. Appl. Crystallogr.* **40**, 658–674 (2007).

219. Murshudov, G. N., Skubák, P., Lebedev, A. A., Pannu, N. S., Steiner, R. A., Nicholls, R. A., Winn, M. D., Long, F. & Vagin, A. A. REFMAC 5 for the refinement of macromolecular crystal structures. *Acta Crystallogr. Sect. D Biol. Crystallogr.* **67**, 355–367 (2011).

220. Emsley, P. & Cowtan, K. Coot : model-building tools for molecular graphics. *Acta Crystallogr. Sect. D Biol. Crystallogr.* **60**, 2126–2132 (2004).

221. Sastry, G. M., Adzhigirey, M., Day, T., Annabhimoju, R. & Sherman, W. Protein and ligand preparation: parameters, protocols, and influence on virtual screening enrichments. *J. Comput. Aided. Mol. Des.* **27**, 221–234 (2013).

222. Halgren, T. A. Identifying and Characterizing Binding Sites and Assessing Druggability. *J. Chem. Inf. Model.* **49**, 377–389 (2009).

223. Abel, R., Young, T., Farid, R., Berne, B. J. & Friesner, R. A. Role of the Active-Site Solvent in the Thermodynamics of Factor Xa Ligand Binding. *J. Am. Chem. Soc.* **130**, 2817–2831 (2008).

224. Dopico, A., ATCC & Invitrogen. Cell Culture Basics. *Chemical Senses* **39**, (2014).

225. Landman, D., Georgescu, C., Martin, D. A. & Quale, J. Polymyxins Revisited. *Clin. Microbiol. Rev.* **21**, 449–465 (2008).

226. Wilkinson, G. R. & Shand, D. G. A physiological approach to hepatic clearance. *Clin. Pharmacol. Ther.* **18**, 377–390 (1975).

227. Dong, J. & Park, M. S. Discussions on the hepatic well-stirred model: Re-derivation from the dispersion model and re-analysis of the lidocaine data. *Eur. J. Pharm. Sci.* **124**, 46–60 (2018).

228. Furge, L. L. & Guengerich, F. P. Cytochrome P450 enzymes in drug metabolism and chemical toxicology: An introduction. *Biochem. Mol. Biol. Educ.* **34**, 66–74 (2006).

229. Wingfield, P. T. Overview of the Purification of Recombinant Proteins in *Current Protocols in Protein Science* **5**, 6.1.1-6.1.35 (John Wiley & Sons, Inc., 2015).

230. Wlodawer, A., Minor, W., Dauter, Z. & Jaskolski, M. Protein crystallography for aspiring crystallographers or how to avoid pitfalls and traps in macromolecular structure determination. *FEBS J.* **280**, 5705–5736 (2013).

231. Goujon, M., McWilliam, H., Li, W., Valentin, F., Squizzato, S., Paern, J. & Lopez, R. A new bioinformatics analysis tools framework at EMBL-EBI. *Nucleic Acids Res.* **38**, W695–W699 (2010).

232. Sievers, F., Wilm, A., Dineen, D., Gibson, T. J., Karplus, K., Li, W., Lopez, R., McWilliam, H., Remmert, M., Soding, J., Thompson, J. D. & Higgins, D. G. Fast, scalable generation of high-quality protein multiple sequence alignments using Clustal Omega. *Mol. Syst. Biol.* **7**, 539–539 (2014).

233. Waterhouse, A. M., Procter, J. B., Martin, D. M. A., Clamp, M. & Barton, G. J. Jalview Version 2--a multiple sequence alignment editor and analysis workbench. *Bioinformatics* **25**, 1189–1191 (2009).

234. Duggan, P. F. The Reaction of Glyoxylate With Tris Buffer Under Physiological Conditions. *Ir. J. Med. Sci.* 163–168 (1964).

235. Andrae, U., Singh, J. & Ziegler-Skylakakis, K. Pyruvate and Related α-ketoacids Protect Mammalian Cells in Culture Against Hydrogen Peroxide-Induced Cytotoxicity. *Toxicol. Lett.*

28, 93–98 (1985).

236. Bar-Even, A., Noor, E., Savir, Y., Liebermeister, W., Davidi, D., Tawfik, D. S. & Milo, R. The Moderately Efficient Enzyme: Evolutionary and Physicochemical Trends Shaping Enzyme Parameters. *Biochemistry* **50**, 4402–4410 (2011).
237. Quartararo, C. E., Hazra, S., Hadi, T. & Blanchard, J. S. Structural, Kinetic and Chemical Mechanism of Isocitrate Dehydrogenase-1 from *Mycobacterium tuberculosis*. *Biochemistry* **52**, 1765–1775 (2013).
238. Cornish-Bowden, A. Analysis and interpretation of enzyme kinetic data. *Perspect. Sci.* **1**, 121–125 (2014).
239. Quartararo, C. E. & Blanchard, J. S. Kinetic and Chemical Mechanism of Malate Synthase from *Mycobacterium tuberculosis*. *Biochemistry* **50**, 6879–6887 (2011).
240. Reinscheid, D. J., Eikmanns, B. J. & Sahm, H. Malate synthase from *Corynebacterium glutamicum*: sequence analysis of the gene and biochemical characterization of the enzyme. *Microbiology* **140**, 3099–3108 (1994).
241. Huang, H., Krieger, I. V, Parai, M. K., Gawandi, V. B. & Sacchettini, J. C. *Mycobacterium tuberculosis* Malate Synthase Structures with Fragments Reveal a Portal for Substrate/Product Exchange. *J. Biol. Chem.* **291**, 27421–27432 (2016).
242. Krieger, I. V., Freundlich, J. S., Gawandi, V. B., Roberts, J. P., Gawandi, V. B., Sun, Q., Owen, J. L., Fraile, M. T., Huss, S. I., Lavandera, J.-L., Ioerger, T. R. & Sacchettini, J. C. Structure-Guided Discovery of Phenyl-diketo Acids as Potent Inhibitors of *M. tuberculosis* Malate Synthase. *Chem. Biol.* **19**, 1556–1567 (2012).
243. Royer, C. A., Mann, C. J. & Matthews, C. R. Resolution of the fluorescence equilibrium unfolding profile of trp aporepressor using single tryptophan mutants. *Protein Sci.* **2**, 1844–1852 (1993).
244. Lukat, G. S., Stock, A. M. & Stock, J. B. Divalent metal ion binding to the CheY protein and its significance to phosphotransfer in bacterial chemotaxis. *Biochemistry* **29**, 5436–5442 (1990).
245. Gashaw, I., Ellinghaus, P., Sommer, A. & Asadullah, K. What makes a good drug target? *Drug Discov. Today* **16**, 1037–1043 (2011).
246. Schmidtke, P. & Barril, X. Understanding and Predicting Druggability. A High-Throughput Method for Detection of Drug Binding Sites. *J. Med. Chem.* **53**, 5858–5867 (2010).
247. Halgren, T. New Method for Fast and Accurate Binding-site Identification and Analysis. *Chem. Biol. Drug Des.* **69**, 146–148 (2007).
248. Ellenbarger, J. F., Krieger, I. V., Huang, H., Gómez-Coca, S., Ioerger, T. R., Sacchettini, J.

C., Wheeler, S. E. & Dunbar, K. R. Anion-π Interactions in Computer-Aided Drug Design: Modeling the Inhibition of Malate Synthase by Phenyl-Diketo Acids. *J. Chem. Inf. Model.* **58**, 2085–2091 (2018).

249. Wang, L., Berne, B. J. & Friesner, R. A. Ligand binding to protein-binding pockets with wet and dry regions. *Proc. Natl. Acad. Sci.* **108**, 1326–1330 (2011).
250. Crousilles, A., Maunders, E., Bartlett, S., Fan, C., Ukor, E.-F., Abdelhamid, Y., Baker, Y., Floto, A., Spring, D. R. & Welch, M. Which microbial factors really are important in *Pseudomonas aeruginosa* infections? *Future Microbiol.* **10**, 1825–1836 (2015).
251. Luan, H. H. & Medzhitov, R. Food Fight: Role of Itaconate and Other Metabolites in Antimicrobial Defense. *Cell Metab.* **24**, 379–387 (2016).
252. McFadden, B. A. & Purohit, S. Itaconate, an isocitrate lyase-directed inhibitor in *Pseudomonas indigofera*. *J. Bacteriol.* **131**, 136–144 (1977).
253. Sasikaran, J., Ziemski, M., Zadora, P. K., Fleig, A. & Berg, I. A. Bacterial itaconate degradation promotes pathogenicity. *Nat. Chem. Biol.* **10**, 371–377 (2014).
254. Myler, P. J. & Stacy, R. A New Drug for an Old Bug. *Chem. Biol.* **19**, 1499–1500 (2012).
255. Ko, Y. H. & McFadden, B. A. Alkylation of isocitrate lyase from *Escherichia coli* by 3-bromopyruvate. *Arch. Biochem. Biophys.* **278**, 373–380 (1990).
256. Schloss, J. V & Cleland, W. W. Inhibition of isocitrate lyase by 3-nitropropionate, a reaction-intermediate analog. *Biochemistry* **21**, 4420–4427 (1982).
257. Lee, Y. V., Wahab, H. A. & Choong, Y. S. Potential inhibitors for isocitrate lyase of *Mycobacterium tuberculosis* and Non- *M. tuberculosis*: A summary. *Biomed Res. Int.* **2015**, (2015).
258. Moynihan, M. M. & Murkin, A. S. Cysteine Is the General Base That Serves in Catalysis by Isocitrate Lyase and in Mechanism-Based Inhibition by 3-Nitropropionate. *Biochemistry* **53**, 178–187 (2014).
259. Ray, S., Kreitler, D. F., Gulick, A. M. & Murkin, A. S. The Nitro Group as a Masked Electrophile in Covalent Enzyme Inhibition. *ACS Chem. Biol.* **13**, 1470–1473 (2018).
260. Alston, T. A., Mela, L. & Bright, H. J. 3-Nitropropionate, the toxic substance of Indigofera, is a suicide inactivator of succinate dehydrogenase. *Proc. Natl. Acad. Sci.* **74**, 3767–3771 (1977).
261. Pham, T. V., Murkin, A. S., Moynihan, M. M., Harris, L., Tyler, P. C., Shetty, N., Sacchettini, J. C., Huang, H. & Meek, T. D. Mechanism-based inactivator of isocitrate lyases 1 and 2 from *Mycobacterium tuberculosis*. *Proc. Natl. Acad. Sci.* **114**, 7617–7622 (2017).
262. Lucas, X., Bauzá, A., Frontera, A. & Quiñonero, D. A thorough anion–π interaction study in biomolecules: on the importance of cooperativity effects. *Chem. Sci.* **7**, 1038–1050 (2016).

263. Bauzá, A., Quiñonero, D., Deyà, P. M. & Frontera, A. Long-Range Effects in Anion-π Interactions: Their Crucial Role in the Inhibition Mechanism of *Mycobacterium Tuberculosis* Malate Synthase. *Chem. - A Eur. J.* **20**, 6985–6990 (2014).

264. Prinz, H. Hill coefficients, dose–response curves and allosteric mechanisms. *J. Chem. Biol.* **3**, 37–44 (2010).

265. Shoichet, B. K. Interpreting Steep Dose-Response Curves in Early Inhibitor Discovery. *J. Med. Chem.* **49**, 7274–7277 (2006).

266. Lineweaver, H. & Burk, D. The Determination of Enzyme Dissociation Constants. *J. Am. Chem. Soc.* **56**, 658–666 (1934).

267. Sharma, R. Enzyme Inhibition: Mechanisms and Scope in *Enzyme Inhibition and Bioapplications* (ed. Sharma, R.) 3–36 (InTech, 2012).

268. Crousilles, A., Dolan, S. K., Brear, P., Chirgadze, D. Y. & Welch, M. Gluconeogenic precursor availability regulates flux through the glyoxylate shunt in *Pseudomonas aeruginosa*. *J. Biol. Chem.* **293**, 14260–14269 (2018).

269. Renaud, J.-P., Chung, C., Danielson, U. H., Egner, U., Hennig, M., Hubbard, R. E. & Nar, H. Biophysics in drug discovery: impact, challenges and opportunities. *Nat. Rev. Drug Discov.* **15**, 679–698 (2016).

270. Liang, Y. Applications of isothermal titration calorimetry in protein science. *Acta Biochim. Biophys. Sin. (Shanghai).* **40**, 565–576 (2008).

271. Wiseman, T., Williston, S., Brandts, J. F. & Lung-Nan, L. Rapid Measurement of Binding Constants and Heats of Binding Using a New Titration Calorimeter. *Anal. Biochem.* **179**, 131–137 (1989).

272. Freyer, M. W. & Lewis, E. A. Isothermal Titration Calorimetry: Experimental Design, Data Analysis, and Probing Macromolecule/Ligand Binding and Kinetic Interactions. in *Methods in Cell Biology* **84**, 79–113 (Elsevier Inc., 2008).

273. Du, X., Li, Y., Xia, Y.-L., Ai, S.-M., Liang, J., Sang, P., Ji, X.-L. & Liu, S.-Q. Insights into Protein–Ligand Interactions: Mechanisms, Models, and Methods. *Int. J. Mol. Sci.* **17**, 144 (2016).

274. Ladbury, J. E., Klebe, G. & Freire, E. Adding calorimetric data to decision making in lead discovery: a hot tip. *Nat. Rev. Drug Discov.* **9**, 23–27 (2010).

275. Brien, R. O., Markova, N. & Holdgate, G. A. Thermodynamics in Drug Discovery in *Applied Biophysics for Drug Discovery* (John Wiley & Sons, Ltd., 2017).

276. Williams, G., Ferenczy, G. G., Ulander, J. & Keserű, G. M. Binding thermodynamics discriminates fragments from druglike compounds: a thermodynamic description of

fragment-based drug discovery. *Drug Discov. Today* **22**, 681–689 (2017).

277. Herrera, I. & Winnik, M. A. Differential Binding Models for Direct and Reverse Isothermal Titration Calorimetry. *J. Phys. Chem. B* **120**, 2077–2086 (2016).
278. Müller, I. Guidelines for the successful generation of protein–ligand complex crystals. *Acta Crystallogr. Sect. D Struct. Biol.* **73**, 79–92 (2017).
279. Chirgadze, D. *Protein crystallisation in action*. (2001). Available at: http://www.xray.bioc.cam.ac.uk/xray_resources/whitepapers/pdf/xtal-in-action.pdf.
280. Snell, E. H., Bellamy, H. D. & Borgstahl, G. E. O. Macromolecular Crystal Quality in *Methods in Enzymology* **368**, 268–288 (2003).
281. Russo Krauss, I., Merlino, A., Vergara, A. & Sica, F. An Overview of Biological Macromolecule Crystallization. *Int. J. Mol. Sci.* **14**, 11643–11691 (2013).
282. Luft, J. R., Wolfley, J. R. & Snell, E. H. What's in a Drop? Correlating Observations and Outcomes to Guide Macromolecular Crystallization Experiments. *Cryst. Growth Des.* **11**, 651–663 (2011).
283. McPherson, A. & Cudney, B. Searching for silver bullets: An alternative strategy for crystallizing macromolecules. *J. Struct. Biol.* **156**, 387–406 (2006).
284. McPherson, A. & Gavira, J. A. Introduction to protein crystallization. *Acta Crystallogr. Sect. F Struct. Biol. Commun.* **70**, 2–20 (2014).
285. Larson, S. B., Day, J. S., Nguyen, C., Cudney, R. & McPherson, A. Progress in the Development of an Alternative Approach to Macromolecular Crystallization. *Cryst. Growth Des.* **8**, 3038–3052 (2008).
286. Dauter, Z. & Wlodawer, A. On the accuracy of unit-cell parameters in protein crystallography. *Acta Crystallogr. Sect. D Biol. Crystallogr.* **71**, 2217–2226 (2015).
287. Murali, R. & Burnett, R. M. X-ray crystallography of very large unit cells. *Curr. Opin. Struct. Biol.* **1**, 997–1001 (1991).
288. Holton, J. M. & Frankel, K. A. The minimum crystal size needed for a complete diffraction data set. *Acta Crystallogr. Sect. D Biol. Crystallogr.* **66**, 393–408 (2010).
289. Pflugrath, J. W. The finer things in X-ray diffraction data collection. *Acta Crystallogr. Sect. D Biol. Crystallogr.* **55**, 1718–1725 (1999).
290. Long, F., Vagin, A. A., Young, P. & Murshudov, G. N. BALBES: a molecular-replacement pipeline. *Acta Crystallogr. Sect. D Biol. Crystallogr.* **64**, 125–132 (2008).
291. Read, R. J., Adams, P. D. & McCoy, A. J. Intensity statistics in the presence of translational noncrystallographic symmetry. *Acta Crystallogr. Sect. D Biol. Crystallogr.* **69**, 176–183 (2013).
292. Powell, H. R. X-ray data processing. *Biosci. Rep.* **37**, BSR20170227 (2017).

293. Pflugrath, J. W. Practical macromolecular cryocrystallography. *Acta Crystallogr. Sect. F Struct. Biol. Commun.* **71**, 622–642 (2015).

294. Adams, P. D., Afonine, P. V., Bunkóczi, G., Chen, V. B., Davis, I. W., Echols, N., Headd, J. J., Hung, L.-W., Kapral, G. J., Grosse-Kunstleve, R. W., McCoy, A. J., Moriarty, N. W., Oeffner, R., Read, R. J., Richardson, D. C., Richardson, J. S., Terwilliger, T. C. & Zwart, P. H. PHENIX : a comprehensive Python-based system for macromolecular structure solution. *Acta Crystallogr. Sect. D Biol. Crystallogr.* **66**, 213–221 (2010).

295. Hassell, A. M., An, G., Bledsoe, R. K., Bynum, J. M., Carter, H. L., Deng, S.-J. J., Gampe, R. T., Grisard, T. E., Madauss, K. P., Nolte, R. T., Rocque, W. J., Wang, L., Weaver, K. L., Williams, S. P., Wisely, G. B., Xu, R. & Shewchuk, L. M. Crystallization of protein–ligand complexes. *Acta Crystallogr. Sect. D Biol. Crystallogr.* **63**, 72–79 (2007).

296. Lipinski, C. A. Lead- and drug-like compounds: the rule-of-five revolution. *Drug Discov. Today Technol.* **1**, 337–341 (2004).

297. Leeson, P. D. & Springthorpe, B. The influence of drug-like concepts on decision-making in medicinal chemistry. *Nat. Rev. Drug Discov.* **6**, 881–890 (2007).

298. The Pew Charitable Trusts. A Scientific Roadmap for Antibiotic Discovery. (2016). Available at: https://www.pewtrusts.org/-/media/assets/2016/05/ascientificroadmapforantibioticdiscovery.pdf.

299. Schneider, G. Automating drug discovery. *Nat. Rev. Drug Discov.* **17**, 97–113 (2017).

300. Saeed, A., Bosch, A., Bettiol, M., Nossa González, D., Erben, M. & Lamberti, Y. Novel Guanidine Compound against Multidrug-Resistant Cystic Fibrosis-Associated Bacterial Species. *Molecules* **23**, 1158 (2018).

301. Berlinck, R. G. S. & Stelamar, R. The Chemistry and Biology of Guanidine Natural Products. *Nat. Prod. Rep.* 1–87 (2015).

302. Sączewski, F. & Balewski, Ł. Biological activities of guanidine compounds, 2008 – 2012 update. *Expert Opin. Ther. Pat.* **23**, 965–995 (2013).

303. Le Questel, J., Berthelot, M. & Laurence, C. Hydrogen-bond acceptor properties of nitriles: a combined crystallographic and ab initio theoretical investigation. *J. Phys. Org. Chem.* **13**, 347–358 (2000).

304. Eliel, E. L. & Wilen, S. H. *Stereochemistry of Organic Compounds*. *Journal of Chemical Education* (Wiley-Blackwell, 1994).

305. *The Cyano Group*. (John Wiley & Sons, Ltd., 1970). doi:10.1002/9780470771242

306. Fleming, F. F., Yao, L., Ravikumar, P. C., Funk, L. & Shook, B. C. Nitrile-Containing Pharmaceuticals: Efficacious Roles of the Nitrile Pharmacophore. *J. Med. Chem.* **53**, 7902–

7917 (2010).

307. Bohl, C. E., Gao, W., Miller, D. D., Bell, C. E. & Dalton, J. T. Structural basis for antagonism and resistance of bicalutamide in prostate cancer. *Proc. Natl. Acad. Sci.* **102**, 6201–6206 (2005).

308. Li, J. J., Iula, D. M., Nguyen, M. N., Hu, L.-Y., Dettling, D., Johnson, T. R., Du, D. Y., Shanmugasundaram, V., Van Camp, J. A., Wang, Z., Harter, W. G., Yue, W.-S., Boys, M. L., Wade, K. J., Drummond, E. M., Samas, B. M., Lefker, B. A., Hoge, G. S., Lovdahl, M. J., *et al.* Rational Design and Synthesis of 4-((1 R ,2 R)-2-Hydroxycyclohexyl)-2(trifluoromethyl)benzonitrile (PF-998425), a Novel, Nonsteroidal Androgen Receptor Antagonist Devoid of Phototoxicity for Dermatological Indications. *J. Med. Chem.* **51**, 7010–7014 (2008).

309. Hoffman, R. V. *Organic Chemistry*. (John Wiley & Sons, Inc., 2004). doi:10.1002/0471648736

310. Purohit, H., Cheema, S., Lal, S., Raut, C. & Kalia, V. In Search of Drug Targets for *Mycobacterium tuberculosis*. *Infect. Disord. - Drug Targets* **7**, 245–250 (2007).

311. Catone, M. V., Ruiz, J. A., Castellanos, M., Segura, D., Espin, G. & López, N. I. High Polyhydroxybutyrate Production in *Pseudomonas extremaustralis* Is Associated with Differential Expression of Horizontally Acquired and Core Genome Polyhydroxyalkanoate Synthase Genes. *PLoS One* **9**, e98873 (2014).

312. Morales, G., Linares, J. F., Beloso, A., Albar, J. P., Martinez, J. L. & Rojo, F. The *Pseudomonas putida* Crc Global Regulator Controls the Expression of Genes from Several Chromosomal Catabolic Pathways for Aromatic Compounds. *J. Bacteriol.* **186**, 1337–1344 (2004).

313. Keserű, G. M. & Makara, G. M. Hit discovery and hit-to-lead approaches. *Drug Discov. Today* **11**, 741–748 (2006).

314. Wang, L., Chiang, C., Liang, H., Wu, H., Feng, W., Quinney, S. K., Li, J. & Li, L. How to Choose In Vitro Systems to Predict In Vivo Drug Clearance: A System Pharmacology Perspective. *Biomed Res. Int.* **2015**, 1–9 (2015).

315. Gao, J., Wang, J., Gao, N., Tian, X., Zhou, J., Fang, Y., Zhang, H.-F., Wen, Q., Jia, L.-J., Zou, D. & Qiao, H.-L. Prediction of cytochrome P450-mediated drug clearance in humans based on the measured activities of selected CYPs. *Biosci. Rep.* **37**, BSR20171161 (2017).

316. Zambon, S., Fontana, S. & Kajbaf, M. Evaluation of Cytochrome P450 Inhibition Assays Using Human Liver Microsomes by a Casette Analysis /LC-MS/MS. *Drug Metab. Lett.* **4**, 120–128 (2010).

317. Ahn, S., Jung, J., Jang, I.-A., Madsen, E. L. & Park, W. Role of Glyoxylate Shunt in Oxidative Stress Response. *J. Biol. Chem.* **291**, 11928–11938 (2016).

318. Kohanski, M. A., Dwyer, D. J., Hayete, B., Lawrence, C. A. & Collins, J. J. A Common Mechanism of Cellular Death Induced by Bactericidal Antibiotics. *Cell* **130**, 797–810 (2007).

319. Richardson, A. R., Somerville, G. A. & Sonenshein, A. L. Regulating the Intersection of Metabolism and Pathogenesis in Gram-positive Bacteria. *Microbiol. Spectr.* **3**, 1–14 (2015).

320. Vitko, N. P., Grosser, M. R., Khatri, D., Lance, T. R. & Richardson, A. R. Expanded Glucose Import Capability Affords *Staphylococcus aureus* Optimized Glycolytic Flux During Infection. *MBio* **7**, 1–11 (2016).

321. Yılmaz, Ç. & Özcengiz, G. Antibiotics: Pharmacokinetics, toxicity, resistance and multidrug efflux pumps. *Biochem. Pharmacol.* **133**, 43–62 (2017).

322. Morita, Y., Tomida, J. & Kawamura, Y. Efflux-mediated fluoroquinolone resistance in the multidrug-resistant *Pseudomonas aeruginosa* clinical isolate PA7: identification of a novel MexS variant involved in upregulation of the mexEF-oprN multidrug efflux operon. *Front. Microbiol.* **6**, 1–9 (2015).

323. LaBauve, A. E. & Wargo, M. J. Growth and Laboratory Maintenance of *Pseudomonas aeruginosa*. *Curr. Protoc. Microbiol.* **31**, 477–479 (2012).

324. Hancock, R. E. W. & Brinkman, F. S. L. Function of *Pseudomonas* Porins in Uptake and Efflux. *Annu. Rev. Microbiol.* **56**, 17–38 (2002).

325. Berger, A., Dohnt, K., Tielen, P., Jahn, D., Becker, J. & Wittmann, C. Robustness and plasticity of metabolic pathway flux among uropathogenic isolates of *Pseudomonas aeruginosa*. *PLoS One* **9**, (2014).

326. Dolan, S. K., Wijaya, A., Geddis, S. M., Spring, D. R., Silva-Rocha, R. & Welch, M. Loving the poison: the methylcitrate cycle and bacterial pathogenesis. *Microbiology* **164**, 251–259 (2018).

327. Andreev, K., Bianchi, C., Laursen, J. S., Citterio, L., Hein-Kristensen, L., Gram, L., Kuzmenko, I., Olsen, C. A. & Gidalevitz, D. Guanidino groups greatly enhance the action of antimicrobial peptidomimetics against bacterial cytoplasmic membranes. *Biochim. Biophys. Acta - Biomembr.* **1838**, 2492–2502 (2014).

328. Andrade, R., Crisol, L., Prado, R., Boyano, M. D., Arluzea, J. & Aréchaga, J. Plasma membrane and nuclear envelope integrity during the blebbing stage of apoptosis: a time-lapse study. *Biol. Cell* **102**, 25–35 (2010).

329. Promega Corporation. *CellTiter-Glo Lumiescent Cell Viability Assay. Pharmacology and Therapeutics* (2015).

330. Muller, P. Y. & Milton, M. N. The determination and interpretation of the therapeutic index in drug development. *Nat. Rev. Drug Discov.* **11**, 751–761 (2012).

331. Blix, H. S., Viktil, K. K., Moger, T. A. & Reikvam, A. Drugs with narrow therapeutic index as indicators in the risk management of hospitalised patients. *Pharm. Pract.* **8**, 50–55 (2010).

332. Lin,J H & Lu,A Y. Inhibition and induction of cytochrome P450 and the clinical implications. *Clin. Pharmacokinet.* **35**, 361–390 (1998).

333. Taneja, I., Karsauliya, K., Rashid, M., Sonkar, A. K., Rama Raju, K. S., Singh, S. K., Das, M., Wahajuddin, M. & Singh, S. P. Species differences between rat and human in vitro metabolite profile, in vivo predicted clearance, CYP450 inhibition and CYP450 isoforms that metabolize benzanthrone: Implications in risk assessment. *Food Chem. Toxicol.* **111**, 94–101 (2018).

334. Kerns, E. & Di, L. Pharmaceutical profiling in drug discovery. *Drug Discov. Today* **8**, 316–323 (2003).

335. Cao, H., Lai, Y., Bougouffa, S., Xu, Z. & Yan, A. Comparative genome and transcriptome analysis reveals distinctive surface characteristics and unique physiological potentials of *Pseudomonas aeruginosa* ATCC 27853. *BMC Genomics* **18**, 459 (2017).

336. Hopkins, A. L. Predicting promiscuity. *Nat. News Views* **462**, 167–168 (2009).

337. Moussa, A. Two Functional Guanidine Groups Are Responsible For the Biological Activity of Streptomycin and Functionally Equivalent Molecules. *J. Chromatogr. Sep. Tech.* **05**, 5–7 (2014).

338. Said, M., Badshah, A., Shah, N., Khan, H., Murtaza, G., Vabre, B., Zargarian, D. & Khan, M. Antitumor, Antioxidant and Antimicrobial Studies of Substituted Pyridylguanidines. *Molecules* **18**, 10378–10396 (2013).

339. Rotondo, C. M., Marrone, L., Goodfellow, V. J., Ghavami, A., Labbé, G., Spencer, J., Dmitrienko, G. I. & Siemann, S. Arginine-containing peptides as potent inhibitors of VIM-2 metallo-β-lactamase. *Biochim. Biophys. Acta - Gen. Subj.* **1850**, 2228–2238 (2015).

340. Montalvão, S., Leino, T. O., Kiuru, P. S., Lillsunde, K.-E., Yli-Kauhaluoma, J. & Tammela, P. Synthesis and Biological Evaluation of 2-Aminobenzothiazole and Benzimidazole Analogs Based on the Clathrodin Structure. *Arch. Pharm. (Weinheim).* **349**, 137–149 (2016).

341. Kaul, M., Parhi, A. K., Zhang, Y., LaVoie, E. J., Tuske, S., Arnold, E., Kerrigan, J. E. & Pilch, D. S. A Bactericidal Guanidinomethyl Biaryl That Alters the Dynamics of Bacterial FtsZ Polymerization. *J. Med. Chem.* **55**, 10160–10176 (2012).

342. Fair, R. J., Hensler, M. E., Thienphrapa, W., Dam, Q. N., Nizet, V. & Tor, Y. Selectively Guanidinylated Aminoglycosides as Antibiotics. *ChemMedChem* **7**, 1237–1244 (2012).

343. Takeoka, Y., Tanino, T., Sekiguchi, M., Yonezawa, S., Sakagami, M., Takahashi, F., Togame, H., Tanaka, Y., Takemoto, H., Ichikawa, S. & Matsuda, A. Expansion of Antibacterial

Spectrum of Muraymycins toward *Pseudomonas aeruginosa*. *ACS Med. Chem. Lett.* **5**, 556–560 (2014).

344. Raczyńska, E. D., Cyrański, M. K., Gutowski, M., Rak, J., Gal, J. F., Maria, P. C., Darowska, M. & Duczmal, K. Consequences of proton transfer in guanidine. *J. Phys. Org. Chem.* **16**, 91–106 (2003).
345. Schug, K. A. & Lindner, W. Noncovalent Binding between Guanidinium and Anionic Groups: Focus on Biological- and Synthetic-Based Arginine/Guanidinium Interactions with Phosph[on]ate and Sulf[on]ate Residues. *Chem. Rev.* **105**, 67–114 (2005).
346. Zamperini, C., Maccari, G., Deodato, D., Pasero, C., D'Agostino, I., Orofino, F., De Luca, F., Dreassi, E., Docquier, J. D. & Botta, M. Identification, synthesis and biological activity of alkyl-guanidine oligomers as potent antibacterial agents. *Sci. Rep.* **7**, 8251 (2017).
347. Wexselblatt, E., Esko, J. D. & Tor, Y. On Guanidinium and Cellular Uptake. *J. Org. Chem.* **79**, 6766–6774 (2014).
348. Thaqi, A., McCluskey, A. & Scott, J. L. A mild Boc deprotection and the importance of a free carboxylate. *Tetrahedron Lett.* **49**, 6962–6964 (2008).
349. Cappel, D., Dixon, S. L., Sherman, W. & Duan, J. Exploring conformational search protocols for ligand-based virtual screening and 3-D QSAR modeling. *J. Comput. Aided. Mol. Des.* **29**, 165–182 (2015).
350. Kovacevic, T., Avram, S., Milakovic, D., Spiric, N. & Kovacevic, P. Therapeutic monitoring of amikacin and gentamicin in critically and noncritically ill patients. *J. Basic Clin. Pharm.* **7**, 65 (2016).
351. T'jollyn, H., Snoeys, J., Van Bocxlaer, J., De Bock, L., Annaert, P., Van Peer, A., Allegaert, K., Mannens, G., Vermeulen, A. & Boussery, K. Strategies for Determining Correct Cytochrome P450 Contributions in Hepatic Clearance Predictions: In Vitro–In Vivo Extrapolation as Modelling Approach and Tramadol as Proof-of Concept Compound. *Eur. J. Drug Metab. Pharmacokinet.* **42**, 537–543 (2017).
352. Seger, S. T., Rydberg, P. & Olsen, L. Mechanism of the N-Hydroxylation of Primary and Secondary Amines by Cytochrome P450. *Chem. Res. Toxicol.* **28**, 597–603 (2015).
353. Technical Resources International, I. *Aminopyridines*. **52**, (2002).
354. White, R. L. What In Vitro Models of Infection Can and Cannot Do. *Pharmacotherapy* **21**, 292S-301S (2001).
355. Barger, A. Pharmacological indices in antibiotic therapy. *J. Antimicrob. Chemother.* **52**, 893–898 (2003).
356. Wu, X., Siehnel, R. J., Garudathri, J., Staudinger, B. J., Hisert, K. B., Ozer, E. A., Hauser,

A. R., Eng, J. K., Manoil, C., Singh, P. K. & Bruce, J. E. In Vivo Proteome of *Pseudomonas aeruginosa* in Airways of Cystic Fibrosis Patients. *J. Proteome Res.* 2601-2612 (2019).

357. Rossi, E., Falcone, M., Molin, S. & Johansen, H. K. High-resolution in situ transcriptomics of *Pseudomonas aeruginosa* unveils genotype independent patho-phenotypes in cystic fibrosis lungs. *Nat. Commun.* **9**, 1–13 (2018).

8. Appendices

Appendix 1: Extracted information from MS_{Pa} PDB deposition

The percentile ranks, Ramachandran plot, Polygon chart, and data collection and refinement statistics show the final results of solving the structure of MS_{Pa} after deposition in the PDB.

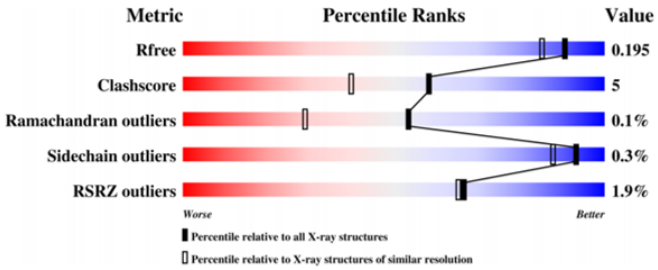

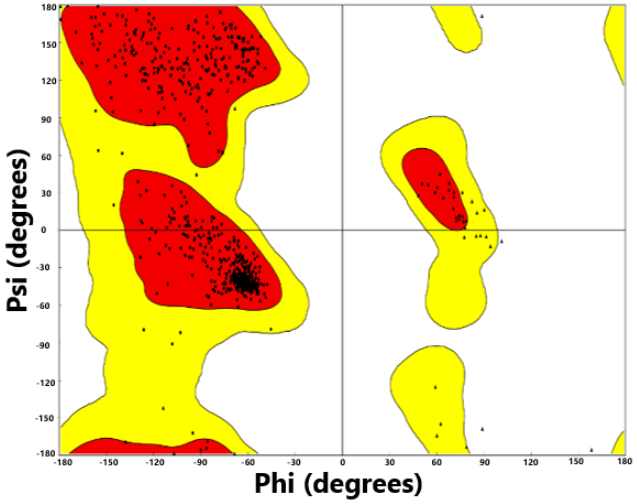

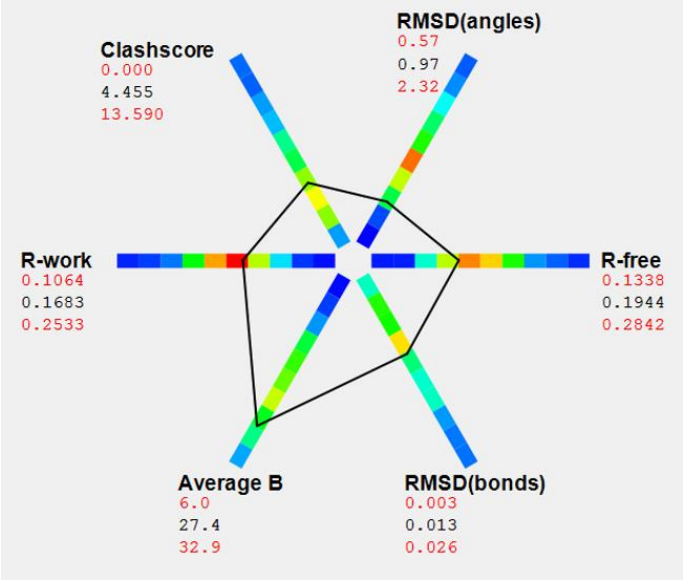

Table 43. Summary of data collection and refinement statistics for MS_{Pa}.

Data Collection[α]	
X-ray source	DLS MX-I03
wavelength (Å)	0.97625
resolution range (Å)	71.17-1.62
# total reflections	556009 (9988)
# unique reflections	96326 (3151)
multiplicity	5.8 (3.2)
completeness (%)	94.5 (69.9)
mean I/σ(I)	11.75 (1.47)
R_{sym}	0.066 (0.912)
R_{meas}	0.079 (1.080)
$CC_{1/2}$	1 (0.5)
space group	$P2_12_12_1$
unit cell	
a (Å)	71.17
b (Å)	81.20
c (Å)	137.57
$\alpha = \beta = \gamma$ (°)	90
# molecules per asymmetric unit	1
Refinement	
R_{work} (%)	16.7
R_{free} (%)	19.6
no. of atoms	
protein	6350
glycerol	4
1,2-ethanediol	15
ions	2
water	691
root-mean-square deviation	
bond lengths (Å)	0.0008
bond angles (°)	0.897
Wilson B factor (Å^2)	19.6
average B factor (Å^2)	
overall	27.30
protein	25.49
glycerol	56.28
1,2-ethanediol	60.92
ions	54.90
water	38.76
Ramachandran analysis	
favoured (%)	98
allowed (%)	12
outliers (%)	0.1
rotamer outliers (%)	0.3
MolProbity Clashscore	5
PDB entry	5OAS

[α] Values for highest resolution shell are given in parenthesis.

Appendix 2: Thermodynamic parameters of MS_{Pa} from WaterMap.

Table 44. Full thermodynamic parameters of hydration sites from WaterMap. WaterMap hydration sites and thermodynamic parameters for the water molecules shown in **figure 18B** and **C**: enthalpy (ΔH), entropy (-TΔS) and Gibbs free energy (ΔG).

Site number	ΔH	-TΔS	ΔG
8	-25.40	5.94	-19.46
82	0.68	4.05	4.73
135	0.60	3.38	3.98
140	-0.91	3.47	2.56
156	-4.42	3.39	-1.03
218	1.62	2.85	4.47
406	1.19	2.53	3.72
407	3.35	2.40	5.75
568	0.35	2.00	2.35
736	-1.23	1.53	0.30
832	-0.40	1.35	0.95
1039	-3.50	1.47	-2.03
1092	0.59	1.04	1.63
1279	5.75	1.09	6.84
1286	5.40	1.14	6.54
1434	4.34	0.88	5.22
1601	0.56	0.88	1.44

Appendix 3: ICL_{Pa} purification and activity.

Analysis after purification of His_6-tagged ICL indicates that it corresponds to the estimate molecular mass (59 kDa) compared with the molecular mass ladder. Kinetic analysis of purified ICL revealed that 1) the protein was enzymatically active and 2) that it behaved as a Michaelis-Menten enzyme, which was important for testing small molecule inhibitors.

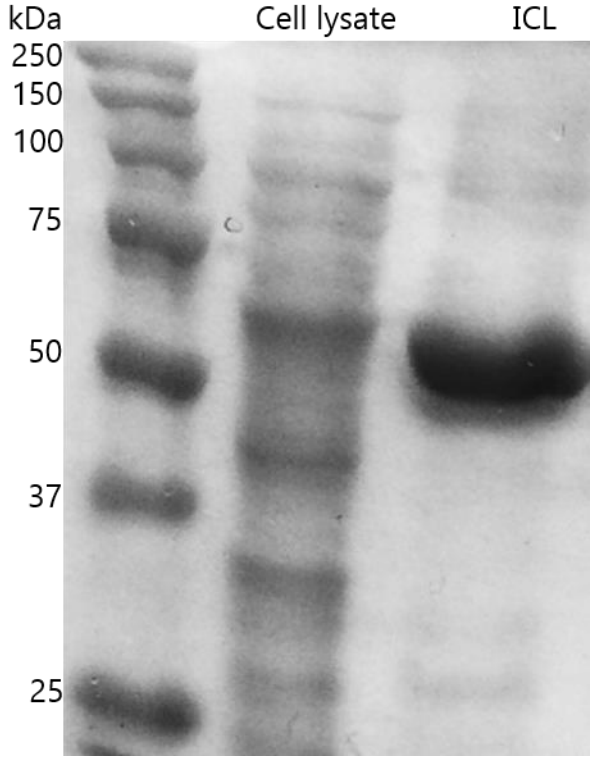

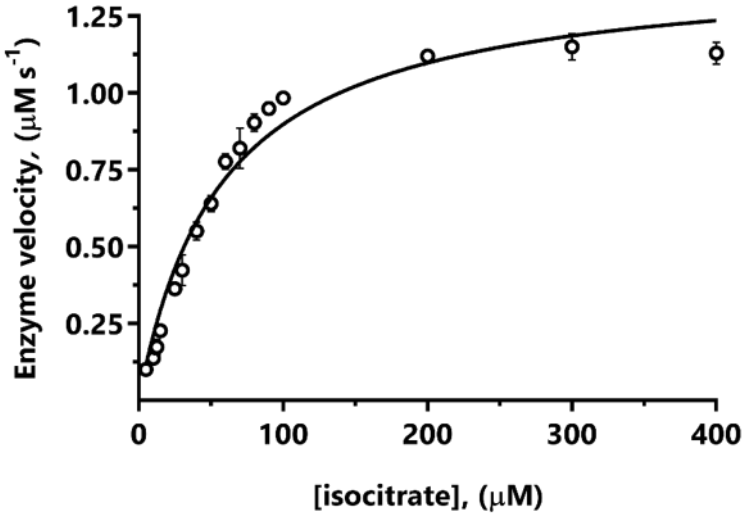

Appendix 4: NMR spectra of SB002.

The Department of Chemistry NMR service analysed a sample of SB002 (40mM) for signs of chemical degradation. SB002 was previously dissolved in DMSO and was vortexed and heated (60°C) to increase solubility. Stocks were then kept at -20°C. The DMSO caused solvent swamping, as the hydrogens in DMSO influenced the NMR signal in the 1-3 ppm region, which is just where the hydrogen atoms in the methyl groups on the Boc groups would appear. The bottom graph illustrates the intensity of the chemical shifts over time, indicating that the chemical structure did not change after 48 hours at 25°C. It had already degraded, as indicated by the loss of antibacterial activity.